Simulating Gain and Absorption Spectra of InAs/GaAs Quantum Dot Material

Ben René Jakobs

A thesis submitted as partial fulfilment for the degree of Doctor of Philosophy

Cardiff University

October 2025

Abstract

Quantum dot structures were numerically and experimentally investigated for the purpose of modelling absorption and gain spectra for varying biases. Such models already exist for bulk or quantum well materials and are widely used to simulate photonic integrated circuits.

The 8-band k.p approximation was implemented to simulate InAs quantum dots. The strain tensor and the piezoelectric potential were identified, leading to detailed descriptions of the energy levels and wavefunction of individual dots. By extrapolating the results from the simulations of individual dots the absorption of quantum dot epitaxial structures was simulated. Excellent agreement was achieved between simulation results and measured absorption, assuming the individual dots are asymmetric or two growth modes are present.

A rate equation model was used in combination with a commercially available diode solver to identify the occupation probabilities of dot states. From this, modal gain was simulated, and a calibration of recombination lifetimes was employed to yield good experimental agreement.

The temperature induced shift in the absorption spectrum was measured and quantified. Including temperature dependent recombination lifetimes into the gain model, the modal gain spectrum for three different samples at various temperatures was simulated. Good agreement was obtained between simulations and measurements.

The impact of an electric field on different dot structures was investigated, revealing inconsistencies in their responsiveness to an electric field. In comparison to simulations, insights into the dimensions and material composition of the individual dots were obtained.

The model was expanded to simulate the gain of doped dot structures. p-type modulation showed increased gain and differential gain. The presence of a n-dopant in individual quantum dots was simulated, showing an increase in transition energy and a reduction in wavefunction overlaps. The overall impact of the n-dopant on the modal gain was simulated to be minimal.

To my family, Luna, Kim, Monique and Rudi

Acknowledgements

I would like to thank Professor Peter M. Smowton for having taken me on as a PhD student and for his support during my PhD. I'm also grateful to the members of the OPTO group, especially Dr. Lydia Jarvis, Dr. Curtis Hentschel and Dr. Craig Alford for their help with training me and getting the measurement kit to work.

I would also like to thank Photon Design for financially supporting this project. Especially to Dr. Dominic Gallagher, I'm extremely grateful for the weekly meetings and the useful discussion that have been conducted during those meetings. I would also like to express my gratitude to Joel Lowther whose keen mathematical and physical insight have been incredibly helpful throughout my PhD.

I have been incredibly lucky to have been part of a Cohort, without which this endeavour wouldn't have nearly been as fun as it ended up being. Thrown together by sheer luck I have found people that I now call my closest friends. The lunchtime and conference shenanigans have been a delightful break.

I am eternally indebted to my family, whose support has been unwavering, not only during my PhD, but also during the journey that has allowed to get me there. I can honestly say that this wouldn't have been possible without them. Thank you all, I'm beyond lucky to be able to call you my family.

I'm also incredibly lucky to have found a close partner in Kate during my time in Cardiff. Thank you for your company, it has brought me more than joy on days that otherwise would simply have sucked.

Table of Contents

Table of Figures:

1. Introduction

1.1. Thesis Rationale

For the last four decades quantum dots (QDs) have been intensely researched as they have demonstrated huge potential for the use as active material in optoelectronic devices. Theoretical predictions of the optical properties of spatially confined charge carriers go as far back as the 1930s [1]. In the 1970s the first thin films to exhibit one-dimensional charge carrier confinement was demonstrated [2]. The first physical structures confining charge carriers in all three dimensions were fabricated in the 1990s, realizing the manipulation of the emission spectrum of a material by reducing its physical size to a few tens of nanometres [3]. With this came the promise to engineer materials to different specifications by "simply" altering the extent of its spatial confinement, i.e., the same material could be used for different tasks by making the structure smaller or larger. Further advancements in growth and fabrication techniques in the field of semiconductors have uncovered additional advantages of QDs that have led to improved photonic device performance [4].

The use of QD active material in diode lasers led to a significant reduction in threshold current density, with a record of 19 A/cm^2 for continuous wave lasing; demonstrating drastic improvements over their quantum well (QW) counterparts [5]. The reduction of threshold current density leads to the fabrication of more efficient lasing devices. Additionally, operation temperatures of QD lasers up to 220 °C were observed [6], which is significantly higher than the required 80 °C operational functional temperature set by, for example, data centres [7]. Achieving higher operational temperature as well as high temperature stability eliminates the need to cool the devices, which if implemented would dramatically reduce the energy and water demand of data centres. Additionally, QD active material based lasers shown advantageous properties such as a lowered linewidth enhancement factor (LEF[1]) and a reduced linewidth [8]. Essentially, QDs present improved operational frequency stability.

---

[1] The LEF is an indicator of the stability of the output signal for changes in carrier density, quantifying the likelihood of the appearance of undesired effects such as broad linewidth, chirp, optical feedback induced coherence collapse, or filamentation in broad area lasers and amplifiers

QDs are less sensitive to crystalline defects than bulk or QW structures, which makes them ideal candidates for heteroepitaxial integration and operation under non-ideal conditions [4]. QDs are less susceptible to defects, specifically dark-line defects (DLD[2]), which are a common failure mechanism in semiconductor laser devices [9]. As a result, QDs as active material in lasers lead to a significant increase in device lifetime [4]. Besides operationally induced defects, QDs are also more tolerant to defects appearing during the growth of the dot material, including antiphase boundary (APB) defects, misfit (MD) and threading (TD) dislocations, or thermal cracks. This allows QDs to be grown directly on different substrates, a feature the semiconductor industry relies on, where desirable device properties are engineered through epitaxial structure modifications. The tolerance of QDs to these dislocations increases the pool of materials that can be used. Specifically, the integration of QDs on silicon substrates is highly sought after [10]. Silicon based devices can be found in most contemporary electronic devices, an ever-growing demand to improve their functionality and their efficiency led to the emergence of the field of silicon photonics; a field that promises faster data transfer, lower energy consumption, and increased device functionality [11].

The “holy grail” of silicon photonics is an on-chip light source [12], which was achieved using QDs. This is a major advantage over bulk or QW material, as the silicon industry relies on well-established manufacturing processes, which can be taken advantage of, if a seamless integration on silicon is achieved. QD lasers directly grown on Si achieved threshold current densities as low as 62.5 A/cm^2 [13]. Furthermore, lifetime tests were conducted and within five years, QD lasers on Si have seen a four-fold increase in device lifetime [4]. These advantageous characteristics of QDs grown on Si are not restricted to lasers; other photonic devices, such as modulators or detectors are predicted to benefit from heterogenous integration of QDs [14].

Despite presenting a multitude of advantages over other less confined materials, QD based photonic devices have yet to be commercialised. Arguably, one reason for the lack of commercially available QD devices is the absence of a readily available

---

[2] DLDs are regions of low radiative recombination. These defects are caused during the growth and / or processing of the device and expand during device operation until failure. The specific process causing to the expansion of DLDs during operation is strongly suppressed in QD structures.

simulation tool. Simulating is an important element in many process flows, allowing the design, analysis, and optimisation of QD based photonic devices prior to fabrication. For less confined structures (QW or bulk photonic structures, for example [15,16]) there is a wide selection of such tools; which have led to a plethora of scientific publications and advances in the field of optoelectronics. The key advantage of these simulation tools is that by analysing changes in the material composition or device geometry prior to fabrication, the user is able to drastically reduce the number of process iterations [17]. Thus, speeding up the development phase of the device and reducing the fabrication cost of the final product. In essence the final device can be designed and optimised using these modelling tools and can then be fabricated. Nowadays most, if not all, companies and research groups in the field of compound semiconductor photonics rely on at least one such tool for the development of their products and design of devices for research purposes. Tools such as Photon Design, Lumerical, or COMSOL will be familiar to most researchers in the field of optoelectronics.

The aim of this work is to establish a QD simulation tool that is easy to use and does not require enhanced computational power. The strength of such a tool is to allow the user to predict the impact that variations to the structure of the photonic device have on the final functionality. Especially with QDs, small variations to, for example, the epitaxial layers can have drastic and difficult to predict effects on the functionality of the device. Simulation is only valuable, however, if it replicates the behaviour of devices. Consequently, the implemented model was validated against experimental data.

This project aims to create a reliable QD simulation model with functionality comparable to commercially available bulk or QW simulation software. In doing so, the model will enable users to relate the epitaxial structure of grown QDs to the final functionality of QD based photonic devices. Additionally, this work seeks to expand the understanding of QD photonic devices and their interactions with external stimuli.

1.2. Thesis Structure

Chapter 2 introduces the background knowledge for this work, specifically the theory behind QDs and the microscopy techniques commonly used to visualise individual dots. The focus then shifts to a discussion of different simulation techniques capable of describing confined charge carriers in individual dots; highlighting the accuracy and the computational costs of each model. Macroscopic properties, such as absorption and gain, of QD material are then described. The identification of gain and absorption relies on parameters which are extracted from commercially available photonic software models and the necessary background theory used by the model is presented.

Chapter 3 focuses on the numerical implementation and experimental methods used in this work. Three distinct solvers are described, and their implementation is discussed. Firstly, the continuum mechanical model for strain within a QD is described, implemented using a staggered grid, to identify the strain tensor for zinc blende material. Secondly, the identification method of the piezoelectric effect, resulting from internal strain, is discussed. Thirdly a detailed description of the 8-band k.p theory is given and a method of eliminating spurious solutions is highlighted. The identification of the momentum matrix element for the 8-band k.p model is described. Additionally, the rate equation model used to simulate the occupation probability in individual QDs is described. The focus then shifts to experimental work used to validate the simulations; specifically the method used to measure modal gain and absorption spectra under varying biases is detailed.

The simulation results of the different solvers discussed in Chapter 3 are presented in Chapter 4. The implemented individual dot solvers are validated through comparison to the Literature. The method of obtaining the modal absorption is discussed, detailing how the simulation results of individual dots are used to describe the absorption of entire epitaxial structures. The importance of calibrating the model to measurements is highlighted, allowing the replication of the modal absorption spectra of three different epitaxial structures. The modelling routine of the modal absorption is extended to allow the simulation of modal gain. This required further calibration of the lifetimes used for identification of the occupation probabilities of the dot energy states. The simulated gain of three different epitaxial structures is then compared to gain measurements.

In Chapter 5, the effects of temperature on the gain and absorption spectra of dot structures are simulated and measured. Sample dependent parameters are identified to match the shift in energy as a function of temperature to measurements. The identified Varshni parameters and the established gain model from Chapter 4 is then used to simulate the gain at four different temperatures for different injection currents for three samples. Temperature dependent spontaneous photon transition lifetime was identified through calibration. Furthermore, the effects of an applied electric field was analysed. The response of the energy and wavefunction of a confined charge carriers in QDs to an electric field was simulated for dots of varying dimensions and material composition. The shift caused by an applied reverse bias is then both simulated and measured. Additionally, the impact of different doping strategies for QD is discussed. The change in modal gain due to p-type modulation doping is investigated, as well as the changes in transition energy of individual dots due to direct n-doping and their subsequent impact on modal gain.

The final chapter gives a conclusion of the work done and proposes potential future investigations which could be of interest.

2. Background Theory

This chapter introduces the definition of the quantum confinement effect and its impact on the confined charge carriers. The dimensions, shapes, and material compositions of self-assembled QDs are discussed highlighting the strong variations in the descriptions presented in the Literature. Different simulation techniques, used for the identification of energy levels and wavefunctions of confined charge carriers are discussed to identify a suitable candidate to efficiently and accurately describe the charge carriers of individual QDs. The identification of gain and absorption, requires the simulation of the electromagnetic wave and the propagation of charge carriers under varying biases, within the semiconductor structure. This is achieved using commercially available software, which solves the carrier continuity equation as well as Maxwell's equations. A description of the underlying physics used by the commercial software is presented.

The simulations in Section 2.5 were completed using Photon Design's laser diode solver software package Harold.

2.1. What Makes a Dot Quantum?

A QD is a semiconductor crystal containing charge carriers which are confined in all three dimensions [18]. The size of QDs can range from a couple nanometres to a few tens of nanometres. At those dimensions quantum effects start to become dominant. The scale at which such effects are observable can be identified by the de-Broglie wavelength of the charge carriers of the structure.

$$\lambda = \frac{h}{\sqrt{3m_e^* k_b T}} \tag{2.1}$$

where λ is the de-Broglie wavelength, h is Planck's constant, m_e^* is the effective mass of the charge carrier, k_b is Boltzmann's constant, and T is the temperature. Applying Equation 2.1 to, for example, a confined electron in indium arsenide at room temperature, a wavelength of ~67 nm is obtained, indicating the size at which quantum effects will start to significantly alter the band structure of this material. A schematic visualisation of the spatial confinement of a QD can be seen in Figure 2.1. The effect of quantum confinement leads to the appearance of well-defined atomic-like energy levels. Whereas bulk materials have energy levels that are so closely spaced that they appear to be a continuous range of energies.

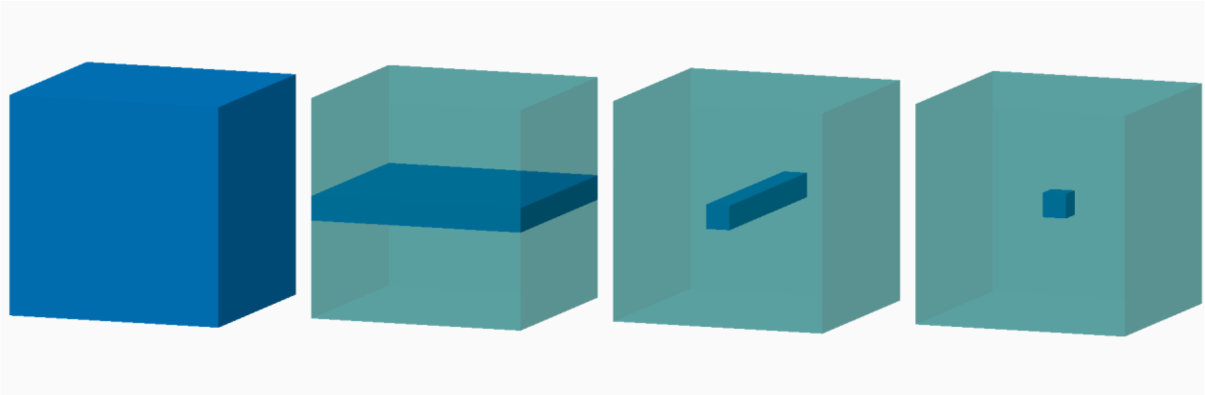

Figure 2.1: Schematic depiction of bulk, 1D confinement (quantum well), 2D confinement (quantum wire), and 3D confinement (quantum dot), from left to right, respectively.

The density of states is commonly used to quantify the distribution of allowed energy states in a semiconductor material. A high DOS indicates a high number of states available to be occupied at a given energy. A zero DOS means that at that energy no states can be occupied. Confinement can be used to significantly alter the DOS. The effect of confinement, under various degrees of confinement, on the DOS is portrayed in Figure 2.2. The energy spacing of QD state can be tailored based on the dimensions and material composition of the dot. A direct advantage of wide energy spacing occurs when the energy between states is larger than the thermal energy, ~25 meV at room temperature, effectively reducing temperature induced transitions between states.

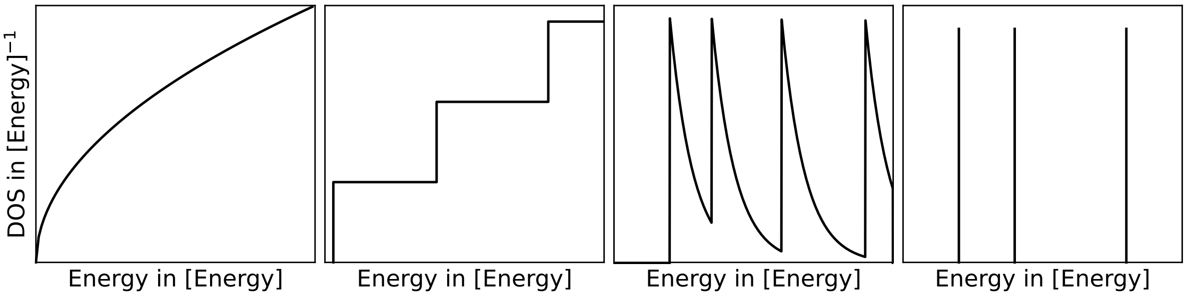

Figure 2.2: Schematic representation of the changes in DOS due to confinement effects, for bulk, 1D confinement, 2D confinement, and 3D confinement, from left to right, respectively.

This project focuses on dots grown following the self-assembled method, which is achieved using physical or chemical vapour deposition. Historically, the first self-assembled dot structures were grown using molecular beam epitaxy (MBE). MBE allows for high control of monoatomic layer growth. Metal-organic chemical vapour deposition (MOCVD) is another common technique for the growth of QDs [19]. The disadvantage of MOCVD is that it has less control over the thickness of the layer deposited than MBE. Additionally, MBE is compatible with a method (Reflection High Energy Electron Diffraction) able to investigate the onset of dot formation during growth [20]. The advantage of MOCVD is that the growth is substantially quicker, and the growth conditions are less strict, leading to shorter down time of the equipment [21]. Additionally, higher uniformity across the wafer, or multiple wafers is typically achieved under MOCVD growth. The exact formation of the dots follows the Stranski-Krastanow growth mode (SK), which describes the nucleation of islands after the thickness of the deposited material has passed the critical thickness conditions [22]. Small variations in the substrate material or material deposited immediately below the dots lead to variations in the material composition, strain distribution, and size of the QDs. This variation in the dot growth introduces an additional challenge in simulating dot structures. Specifically, it is difficult to validate the model if the actual form of the individual dots is unknown. Thus raising the question, what do QDs actually look like?

2.2. Visualisation of Quantum Dots

The dimensions, shape, and material composition of the individual dots need to be identified to accurately model the confined charge carriers. A simple self-assembled dot description is obtained based on material distribution of two lattice mismatched materials, i.e., the dot sits on top of another material. However, due to the SK nucleation process the description of the dot should also include a wetting layer (WL) [23]. This layer is commonly assumed to be made of the same material as the QD. The formed dots and WL are then covered by a capping material. A possible epitaxial structure is schematically depicted in Figure 2.3. The barrier is commonly made of multiple layers chosen to facilitate the transport of charge carriers through the structure, and / or improve the confinement of the optical mode to the QD material. The well layers are commonly added to improve the growth of QDs [24] and to aid carrier capture into the dots [25].

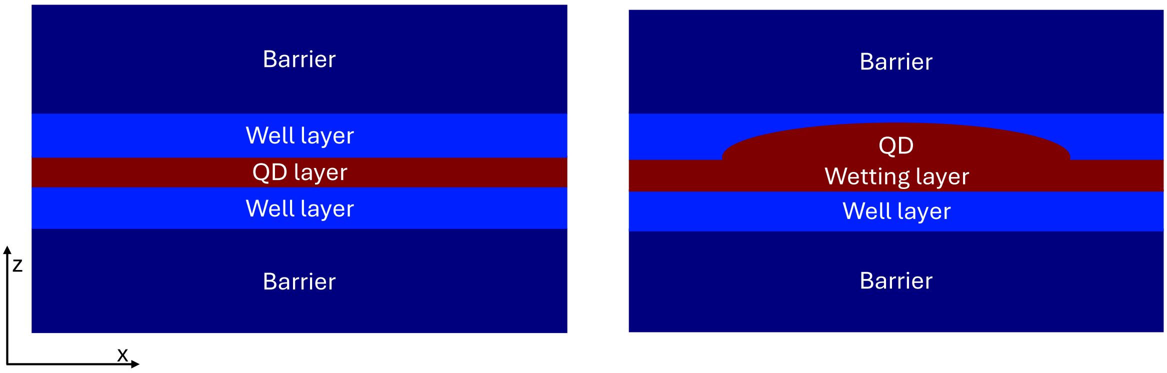

Figure 2.3 Schematic depiction of the QD epitaxial structure (left). Schematic depiction of the QD layer, highlighting the material description of an individual dot (right).

The simplest possible structure can be created out of two distinct materials, however a realistic quantum dot system is significantly more complex, either because more than two materials are used for the growth, and / or because of material segregation during growth and material mixing during growth and post-growth processing. The actual identification of the width, height, shape and material composition of dot structures requires complex microscopy techniques and is widely contested as the growth of quantum dots is extremely sensitive to small variations in MBE or MOCVD growth conditions. An additional difficulty in visualising individual dots is caused by Indium segregation and material mixing during the growth [26–28]. Different models have been proposed to describe the distribution of InAs QDs grown on GaAs, for example the Blokland model [28], which describes the dot by a high InAs concentration right at the top of the dot with diminishing InAs concentration at the bottom and the sides of the dot, or the Giddings description [27], which describes the dot using a Gaussian distribution with high Indium concentration at the centre of the dot. A numerical investigation into the impact of the indium distribution on the transition energies of the dot is given by Tanaka et al. (2016) [29], who emphasized the importance of using a model that incorporates a non-homogeneous InAs composition, as this allowed a match between simulations and experimental results.

2.2.1. Seeing Quantum Dots

Multiple microscopy techniques had been used to observe singular QDs, including, but not limited to, atomic force microscopy (AFM), cross-sectional scanning tunnelling microscopy (XSTM), or transmission electron microscopy (TEM), each method possessing their own advantages and disadvantages. AFM, for example, is commonly used as it allows to scan over a relatively wide area of a range of a few μm^2. An example AFM picture of uncapped InAs dots grown on GaAs is depicted in Figure 2.4.

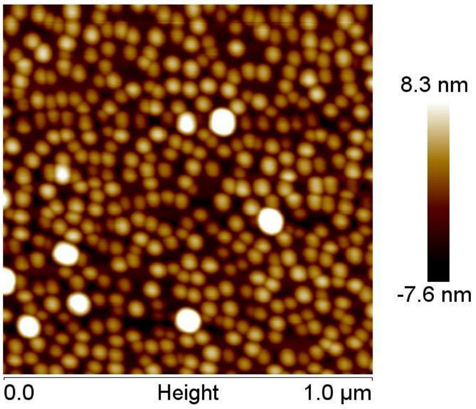

Figure 2.4: AFM picture of an uncapped InAs QDs grown on GaAs.

AFM works by dragging a needle tip over or close to the surface of the samples, therefore AFM can only be used for dots that are exposed and are not covered by a capping layer. This method can thus only lead to accurate measurements under the assumptions that during the capping process, or during any other post-growth processes, the dimensions, shape, or material composition of the QD do not change. This assumption is a severe over-simplification and thus cannot be used to identify the true shape or dimensions of the QD. However, AFM can be used to determine the dot density [30,31]. Although the shape and dimensions of the dots change during the capping process, this should not significantly affect the number of dots formed during QD material deposition.

The microscopy techniques that allow the analysis of capped QDs are XSTM or TEM; these methods, or slight variations to them, have been regularly used to analyse different dot systems. During TEM electrons are transmitted through the structure, leading to scattering of the electrons. The sample acts as a grating through which the electrons travel, creating a diffraction pattern. By analysing the diffraction pattern structural information of the material can be extracted [32]. A disadvantage of the TEM is that it commonly overestimates dot dimensions [33,34]. A more accurate description of the dot dimensions can be achieved using XSTM. Similarly to AFM, XSTM scans the surface of an object. The dimensions of the dot are identified by exposing a plane of the structure perpendicular to the heterostructure growth plane, which is achieved by cleaving the sample in ultra-high vacuum [35] or extracting a thin foil using focused ion beam. The downside of this is that the position of the cross section relative to the dot structure is random. This adds an additional statistical uncertainty as it is impossible to know if the cross section of the individual dot is representative of the dot ensemble. Due to the complications associated with each microscopy technique, it is common practice to use two complementary methods to give a reliable description of the composition, dot density, and dimensions of the individual dots in an ensemble.

2.2.2. Comparison of Dot Emission Spectra, Dimensions, and Shape

Early QD research focused on the identification of dot dimensions, shapes, and emission spectrum. An attempt at comparing different results from different groups was made, by analysing dot samples grown using pure InAs material on GaAs. While the spectrum measurements were not taken at the same temperature, the shift in emission spectra due to temperature variations was accounted for following the work done by Mal et al. (2018) [36]. Their work quantified the spectral shift due to variations in temperature. Although, the variations due to temperature can be sample dependent, the general trend was identified by Mal et al. (2018), which allowed for a rudimentary comparison of emission spectra, whose PL spectra were measured at different temperatures.

Blokland et al. (2009) [28] conducted XSTM measurements of InAs on GaAs QDs and estimated a dot height of 8.1 ± 0.4 nm and dot width of 27.5 ± 4 nm for seemingly lens-shaped dots. In contrast, measurements by Gaan et al. (2010) [37], also using XSTM, presented dot dimensions of 10.5 ± 0.5 nm wide and 2.9 ± 0.2 nm height for lens-shaped dots. While significantly smaller than the dots measured by Blokland et al. (2009), the aspect ratios of 0.29 for Blokland et al. (2009) and 0.28 for Gaan et al. (2010) are similar. Additional measurements were done by Giddings et al. (2011) [27], who relied on XSTM and atom probe tomography. They reported dots of 16.7 ± 2 nm width and 2.3 nm height, presenting a similar height as Gaan et al. (2010) but significantly wider dots, leading to an aspect ratio of 0.14. While variations in dot dimensions can be attributed to different growth conditions, it is the emission wavelength associated with the reported dot structure that is of interest. The energy of the identified peak PL spectra for Giddings et al. (2011) was 93 meV larger than the energy of the PL peak of Gaan et al. (2010), even though the volume occupied by the Giddings' dots was more than that of Gaan's. A PL peak at higher energies is expected for smaller dots. Similar disagreements were observed when comparing the results presented by Murray et al. (1999) [38] and Heitz et al. (2000) [39], with an energy difference of 117 meV at the same temperature, or comparing Blokland et al. (2009) [28] and Offermans et al. (2005) [40], presenting an energy difference of 60 meV. Besides the seemingly inconsistent relation between dot volume and emission spectra, multiple different shapes were reported. Lens-shaped dots were presented by Blokland et al. (2009), and Gaan et al. (2010), whereas pyramid-shaped dots were reported by Heitz et al. (2000), Giddings et al. (2010), discussed flat disk-shaped dots, and Mal et al. (2018), and Offermans et al. (2005), reported truncated pyramid-shaped dots.

The above paragraph describes just a few of the reported measurements for dot dimensions and emission spectra, specifically focusing on work done using pure InAs dot material capped by GaAs, however it highlights the complexity of QD growth and characterisation. The discrepancies that can be found in the Literature additionally underlines the need for a robust model that can be used to compare how our theoretical understanding agrees with measurements. It does make validating a created QD model more difficult as the material composition of the dot structure cannot be known a priori. Therefore a model can only be deemed reliable if it has been validated using experimental measurements.

2.3. Simulating Energy Levels in Quantum Dots

A vast portion of contemporary photonic technology can be simulated using the classical description of light by solving Maxwell's equation and implementing carrier rate equation models. However, due to the increasing sensitivity and the shrinking size of emerging technologies, classical descriptions fail to correctly incorporate quantum effects. Schrödinger's equation needs to be used to correctly describe these effects. The problem lies with the complexity of Schrödinger's equation; only very few systems can be solved analytically, most requiring significant computational resources. QD based photonic devices commonly incorporate between 10^{10} to 10^{11} QDs, each containing 10^4 to 10^5 atoms. Thus, an exact solution is currently impossible, as the

Hilbert space increases exponentially with the number of atoms in each dot [41]. Therefore, to be able to apply Schrödinger's equation to QDs an appropriate approximation is necessary. A wide range of approximations to the Schrödinger equation had been studied. The most commonly discussed methods in the Literature are the single band effective mass model, the multi-band k.p model, the empirical tight binding (ETB) model, and the pseudopotential model. Each of these models apply approximations to the Schrödinger equation of different complexity. With increasing complexity more and more details of the underlying physics is incorporated into the simulation, however at the cost of increasing the required computational resources.

Computational resources refer to the computational power or simulation time. The aim of this project is to create a model than can be used on standard computers without requiring the simulations to run over multiple days. Ideally, the implemented model accurately describes the QD system obtaining the description without requiring vast amounts of computational time or power. This, however, is not feasible, and a compromise between accuracy and computational resource was made. Therefore, the most suitable approximation to Schrödinger's equation needed to be identified. An input to the Schrödinger equation is the confining potential, which depends on the strain of the system. Therefore, the use of an appropriate strain model is discussed. Furthermore, a short description of the four most common models for the identification of energy levels and wavefunctions of confined carriers in QDs is given below, highlighting the advantages and disadvantages of each model.

2.3.1. Strain in Quantum Dots

Self-assembled QDs form due to internal stress caused by the difference in lattice constant of the grown material. The presence of strain impacts the charge carriers in semiconductor material [42]. Therefore, a detailed description of strain is necessary to simulate charge carriers in QDs. The continuum mechanical model (CM) is a reliable and efficient method that leads to an appropriate description of the strain contained in a dot structure [43]. This model was derived by minimizing the total strain energy of the system, leading to a set of coupled differential equations. This set of equations can be discretised and the resulting strain is used in the identification of the confinement potential of the carriers in the QD [44]. An alternative model, based on the valence force field (VFF) description, gives an atomistic description of strain in a given QD structure, making it in theory more accurate than the continuous model. However, the additional complexity, and therefore additional computation resources, does not justify the small increase in accuracy, as concluded by Stier et al. (1998), who directly compared the two models [43]. In addition, the choice of strain solver will depend on the model chosen for the electronic structure calculations. The model for strain and electronic structure should both present either a continuum or an atomistic approach. For example, if an atomistic choice for the strain solver is chosen, information on the strain will be lost when transitioning to the continuous electronic structure model [45].

2.3.2. Single Band Effective Mass Model

One of the simplest methods used to describe the behaviour of carriers in semiconductor structures is the effective mass approximation. This model relies on the description of the carriers based on a single defining constant, termed the effective mass. This model identifies energy levels and wavefunction of confined carriers by adjusting the mass in Schrödinger's equation describing the material system. Electron-electron interactions and other underlying physics are accounted for by fitting the effective mass to experimental measurements [46]. The inherent downside is that this method is dependent on experimental results, meaning that the simulations are only suitable for a small range of dot structures, for which the effective mass needs to be experimentally identified [47,48]. However, this model is still used to obtain preliminary results when trying to research phenomena whose effects on the energy levels and wavefunctions of the confined carriers are larger than the variations on energy levels caused by the incorporation of a more complex model. The effective mass approximation allows, for example, the prediction of trends caused by material mixing, change in dimension, composition, and strain, as well as other effects that change the confining potential profile, such as doping or electric fields [49,50].

2.3.3. Multi-band k.p Model

A continuation to the single-band effective mass model is the incorporation of additional bands which are energetically closely spaced. This is especially necessary for diamond or zinc blende semiconductors, which possess sub-bands in the VB that are separated by less than 0.5 eV. Due to the close proximity band mixing effects arise [51]. The multi-band model identifies charge carrier characteristics across multiple bands. Each band is represented by atomic like orbital functions, called Bloch functions [48]. This approach transforms the Schrödinger equation into a coupled partial differential equation, which can be discretised and solved. The identified solutions represent the wavefunction and the available energy levels of the confined carriers, described by a linear combination of the used Bloch functions [52–54].

The advantage of the multi-band model is that it is conceptually simple, easy to implement, and still allows the incorporation of a wide range of underlying physical phenomena, such as confinement, strain, piezo- and pyroelectricity, band-coupling, and -splitting, for seemingly arbitrary material combinations and dot shapes. Furthermore, it features significantly improved accuracy, specifically the identification of the energy level separation in the VB and the CB, and the ability to find solutions for material structures by relying on the bulk material parameters, thus allowing improved a priori simulations in comparison to the effective mass model.

However, the downside is that multi-band models require more computational resources. The identification of energy levels and wavefunctions is done by constructing and solving an eigenmatrix, whose description is given by the approximated Schrödinger equation[3]. The computational power needed to solve this eigenproblem is dependent on the size and sparsity of the eigenmatrix. Contemporary eigen solvers, such as the Lanczos algorithm, have a computational complexity, which is linearly dependent on the number of non-zero values in the eigenmatrix [54]. Thus, the computational resources needed are directly linked to the size of the descriptive matrix. The descriptive Hamiltonian of the 8-band k.p model is at least 8 times larger than the single-band effective mass, and will therefore require at least 8 times more time or computing power than the effective mass model.

2.3.4. Empirical Tight Binding Model

A more accurate description of the underlying crystalline structure can be obtained by applying the empirical tight binding (ETB) model. Similar to the k.p model, the ETB model relies on a set of functions whose linear combination can be used to describe

---

[3] N.B. This is not just for the multi-band model, but for any approximation to the Schrödinger equation.

the behaviour of confined carriers. The difference is the set of wavefunctions used. The ETB model relies on atomic orbitals allowing, in theory, atomistic precision [55,56]. The ETB model generates a descriptive Hamiltonian, which is composed of diagonal terms, describing the orbital atomic eigen energies, and off-diagonal terms, which quantify the interactions between atomic neighbours. Mittelstädt et al. (2022) [52] directly compared the k.p model and the ETB model. Their work highlighted the increased accuracy of the ETB and the accompanied increase of computational resource, resulting in a 20 fold increase of computational time for simulations run on the same processor. The identified transition energy for a 2.2 nm high and 20 nm wide dot varied by 70 meV between the 8-band k.p model and the ETB model.

A disadvantage of the ETB model is the unavailability of universally acceptable input parameters, which are used to describe the materials in the structure of interest. Thus, even though the ETB model is in theory more accurate than the k.p model, it is difficult to identify the right material parameters needed, which in turn, might make the model less reliable [57], unless a rigorous identification of the parameters is done [58,59]. This restricts the ETB model to material systems that have been rigorously experimentally investigated.

2.3.5. More Accuracy

The full picture of interactions between particles is described by Schrödinger's equation, thus an exact description of confined carriers is theoretically possible by applying Schrödinger's equation to a QD structure. This equation would then incorporate the interactions between the outer electrons and their core atoms, as well as the interactions between electrons, which would require vast computational resources. High performance computers, which possess increased computational power by coupling multiple processor units working in parallel on individual parts of the same problem, can be used for solving the Hamiltonian obtained by the Schrödinger equation. However, it is still strongly restricted to extremely small systems [60]. Even applying pseudopotential approximations, incorporating electron-electron and electron-core effects, which rely on averaging these effects and describing them by an effective potential, and do indeed give a better description of the physics at play, require vast computational power for relatively small systems [61]. The increase of accuracy stems from the additional information between atomic sites as well as the interaction amongst electrons, given by the Hamiltonian, however, it is that additional information, which drastically increases the resulting eigenproblem making it computationally demanding [62].

2.3.6. Which Model Should Be Used?

The above segments give a brief description of multiple methods to identify energy levels and wavefunctions of confined charge carriers. A detailed description of these carriers is required to create a reliable model of the available energy spectrum of a given QD ensemble. However, the task of this project is not only to obtain a detailed description of a dot system, but also to create a model that can be readily used. Therefore the model requires both a rigorous and fast description of the physics at play. Table 2.1 gives a succinct overview of the different numerical models.

Table 2.1: Summary table of different numerical models investigated

Method:	**Effective Mass Approximation**	**8-band k.p Model**	**Empirical Tight Binding**	**Pseudopotential Approximation**
Accuracy (relative)	Low	Moderate-high	High	Very high
Computational Cost (relative)	Very Low	Moderate	High	Very high
What Drives the Accuracy	Parabolic bands, single effective mass, no atomistic detail	Multiband coupling, non-parabolicity	Atomic resolution	Full atomic wavefunctions, accurate band structure
What Drives the Cost	Simple partial differential equation, continuum geometry	Larg Hamiltonian, additional bands	Larger Hamiltonian, description using atomic orbitals	Even larger Hamiltonian, expensive diagonalization as more physics is included

Based on the above summary, the 8-band k.p model[4] was identified as the most suitable model, allowing the incorporation of a wide range of physical effects without requiring a vast amount of computational resources. This conclusion is further supported by the application of the 8-band k.p model in commercially available software [63,64].

2.4. From Dot to Device

Once the energy levels and wavefunctions of individual confined carriers are known the characteristics of an ensemble of dots can be identified. These characteristics are referred to as macroscopic properties, and describe how the entire structure interacts with light. Absorption, spontaneous emission, and gain are examples of macroscopic properties. Knowing these properties can give preliminary insights into the functionality of the final QD device, for example, knowing the gain spectrum of the epitaxial structure leads to insights into the emission wavelength of the laser fabricated from that structure.

There are multiple different techniques that can be used to identify these macroscopic properties. Similar to choosing the right individual dot solver, the process to identify the macroscopic properties was identified based on the compromise between accuracy and speed. A detailed description of the different levels of accuracy achievable with various modelling approaches is discussed in “Photonics of Quantum-Dot Nanomaterials and Devices” by Ortwin Hess and Edeltraud Gehrig (2012) [18]. In their work, the authors identify four levels of descriptions: phenomenological rate equations, the semiclassical laser theory based on Maxwell-Bloch equations, quantum luminescence equations, and a fully quantum-theoretical description. Each successive level increases in both complexity and accuracy [18]. The level chosen for this project is the “most simple” level, based on rate equation models. The models rely on spatially and temporally averaged quantities for light and matter, which are represented using photon numbers and carrier densities. The identification of gain and absorption play an important role in the rate equation model. The process of identifying modal absorption and modal gain, follows the treatment of dot material discussed in Chapter 9 of

---

[4] N.B. A special case of the multi-band model.

“Quantum Confined Laser Devices” by Peter Blood (2015) [65], the main points are reproduced below.

2.4.1. Light Interaction with Individual Dots

The dimensions of dots are smaller than the wavelength of the light with which they interact. Therefore, dot-light interactions are treated equivalently to atom-light interactions. This assumption turns the dot into a dimensionless point whose interaction with light is quantified via an optical cross section. The optical cross section is given as,

$$\sigma(\hbar\omega) = \left(\frac{\pi\omega}{c\epsilon_0 n}\right) M_{dip}^2 L(\hbar\omega) \tag{2.2}$$

Where ω is the frequency of the light, c is the speed of light, ϵ_0 is the permittivity of free space, n is the refractive index of the material, and $L(\hbar\omega)$ is the homogeneous broadening. The homogeneous broadening affects each dot equally and describes the absorption and emission of light with frequencies not at the resonant frequency. The homogeneous broadening is expressed using a Lorentzian distribution function, given by the following equation,

$$L(\hbar\omega) = \frac{1}{\pi}\frac{\Gamma}{(\hbar\omega - \hbar\omega_0)^2 + \Gamma^2} \tag{2.3}$$

Where ω is the angular frequency of the incident light, ω_0 is the angular frequency of the transition, and Γ is the full-width at half-maximum (FWHM). The final term of the optical cross section is the dipole matrix element, M_{dip} and is expressed by the following equation,

$$M_{dip} = -e\int_{-\infty}^{+\infty} \Psi_i^*(\vec{\boldsymbol{r}})\hat{x}\Psi_f(\vec{\boldsymbol{r}})d\vec{\boldsymbol{r}} \tag{2.4}$$

Where e is the elementary charge, $\Psi_{i,f}(\vec{\boldsymbol{r}})$ is the wavefunction of the initial or final state of the transition, and $\hat{x}$ is the position operation. In the context of QDs the wavefunctions describe the confined carriers and are identified using an appropriate Schrödinger solver.

2.4.2. Modal Absorption and Gain

The gain and absorption can both be seen as the fractional change in photon flux due to optical transitions between a single pair of states, as the light is propagating through the material. The fractional change in flux of identical dots can be expressed as,

$$\frac{\Delta\Phi(\hbar\omega)}{\Phi(\hbar\omega)} = -N_d\sigma(\hbar\omega)[f(\hbar\omega_i) - f(\hbar\omega_f)] \tag{2.5}$$

where $\Delta\Phi$ is the change in photon flux Φ, N_d is the density of dots that the incident light encounters, and $f(\hbar\omega_{i,f})$ is the occupation probability of a carrier in the initial, i, or final state, f. The angular frequency of the initial and final state are such that $\omega = \omega_i - \omega_f$.

Two more factors play an important role to the identification of variation on the photon flux within a given material, the degeneracy of the energy levels with which the light interacts and the selection rules, which determine the allowed transitions. Two states are said to be degenerate if they share the same energy. The degeneracy is dependent on the approximation of the Schrödinger equation used to describe the system, the 8-band k.p model has a degeneracy of 2, due to spin.

Optical transitions only manifest between states of equivalent spin. Additionally, the wavefunction overlap of the initial and final state is an indicator of which transitions occur and which do not. If the overlap is 0, no transition will be possible between these states. In the case of the simple harmonic oscillation, transitions only occur between states of equally excited states, i.e., states with the same principal quantum number, as they present non-zero wavefunction overlaps. For more accurate descriptive models, that might not be the case, leading to transitions which would traditionally be labelled “forbidden”.

Equation (2.5) was established for identical dots, however, due to the conditions under which the dots are grown, the final dot material will contain dots of different dot dimensions and materiel compositions. Therefore, the expression quantifying the relative change of the photon flux of a given dot ensemble and for a given dot, m, within that ensemble is given as,

$$\frac{\Delta\Phi(\hbar\omega)}{\Phi(\hbar\omega)} = -\gamma_{trans}N_d \int \sigma(E_m, \hbar\omega)P(E_m)\big[f\big(\hbar\omega_{i,m}\big) - f\big(\hbar\omega_{f,m}\big)\big]\mathrm{d}E_m \tag{2.6}$$

where $P(E_m)$ is the probability distribution describing the energy distribution of the dot ensemble, for a given energy E_m. The degeneracy of the transitions is given by γ_{trans}.

Designing photonic components requires the knowledge of the distribution of the light within the structure. As changes in the photon flux can only occur when the light travels through the active material, the overlap of the optical mode with the active layer must be known to determine the mode-dependent gain and absorption of a given structure. This, in turn, leads to the final expression for the modal gain of a dot ensemble, given by,

$$G(\hbar\omega) = \frac{\gamma_{trans}\sigma_{0E}N_d}{w_{mode}} \int L(E_m, \hbar\omega)P(E_m)\left[f(E_{f,m}) - f(E_{i,m})\right]dE_m \qquad (2.7)$$

where w_{mode} is the modal width, quantifying the width of a fictitious rectangle of uniform energy representing the mode in question, such that the energy within the rectangle equals that of the total energy of the mode it is describing. $L(E_m,\ \hbar\omega)$ is the homogeneous broadening, for a given transition energy $\hbar\omega$, as given by Equation 2.3. For absorption the electrons transition from the VB to the CB and a good approximation can be obtained by assuming that the VB is fully occupied and the CB is empty, i.e., $f(E_{i,m})$ is 1 and $f(E_{f,m})$ is 0. Leading to the following expression for the modal absorption, where the minus sign has been dropped,

$$A(\hbar\omega) = \frac{\gamma_{trans}\sigma_{0E}N_d}{w_{mode}} \int L(E_m, \hbar\omega)P(E_m)dE_m \qquad (2.8)$$

2.5. Full Device Description

The aim of this project is to simulate entire epitaxial structures, which can be several micrometres thick and encapsulate a multitude of different layers of various thicknesses and materials. An example QD epitaxial structure is given in Figure 2.5. The investigation of the effects of no, forward, and reverse bias on the whole epitaxial stack is accomplished using Photon Design's software. Specifically, FIMMWAVE and Harold are used to identify the confining modes of the structure, and to identify the band structure of the epitaxial layers under various biases, respectively. These will be described in the following sections.

Material	Height (nm)	Repetition
GaAs	300	
GaAs	2.5	x10
$Al_{0.3}Ga_{0.7}As$	2.5	
$Al_{0.3}Ga_{0.7}As$	1430	
GaAs	1	x12
$Al_{0.3}Ga_{0.7}As$	1	
GaAs	42.5	x7
$In_{0.16}Ga_{0.84}As$	5	
InAs (QD)	3 ML	
$In_{0.16}Ga_{0.84}As$	2	
GaAs	42.5	
GaAs	1	x12
$Al_{0.3}Ga_{0.7}As$	1	
$Al_{0.3}Ga_{0.7}As$	1430	
GaAs	2.5	x10
$Al_{0.3}Ga_{0.7}As$	2.5	
GaAs	200	

Figure 2.5: Description of a QD epitaxial structure. (ML ≡ monolayer)

2.5.1. Identification of Optical Modes

As detailed by section 2.4.2, the distribution of light within a device impacts its functionality. It is therefore pertinent to know the mode field profiles of the device. The mode profiles simulated through FIMMWAVE are used to identify the optical confinement and the mode width. This software allows the application of the finite difference model (FDM) to identify the solutions of Maxwell's equations. The software takes as input the epitaxial layer thicknesses, waveguide dimensions, boundary conditions, and wavelength of interest. For dot layers it is assumed that the material used for dot growth is spread evenly over the entire area of the structure, leading to an individual layer of given thickness covering the entire device, instead of multiple dots distributed across the device. The given structure is discretised and the electric and magnetic fields are solved using Maxwell's equations at each mesh point. The software accesses necessary material information at different frequencies from its extensive material database. Once the solver is set, having selected an appropriate mesh, the normalized electric and magnetic field components at each grid point are identified. The appropriate optical mode is chosen from the list of potential solutions, an example is depicted in Figure 2.6. The mode is selected based on its position within the epitaxial structure and its polarisation.

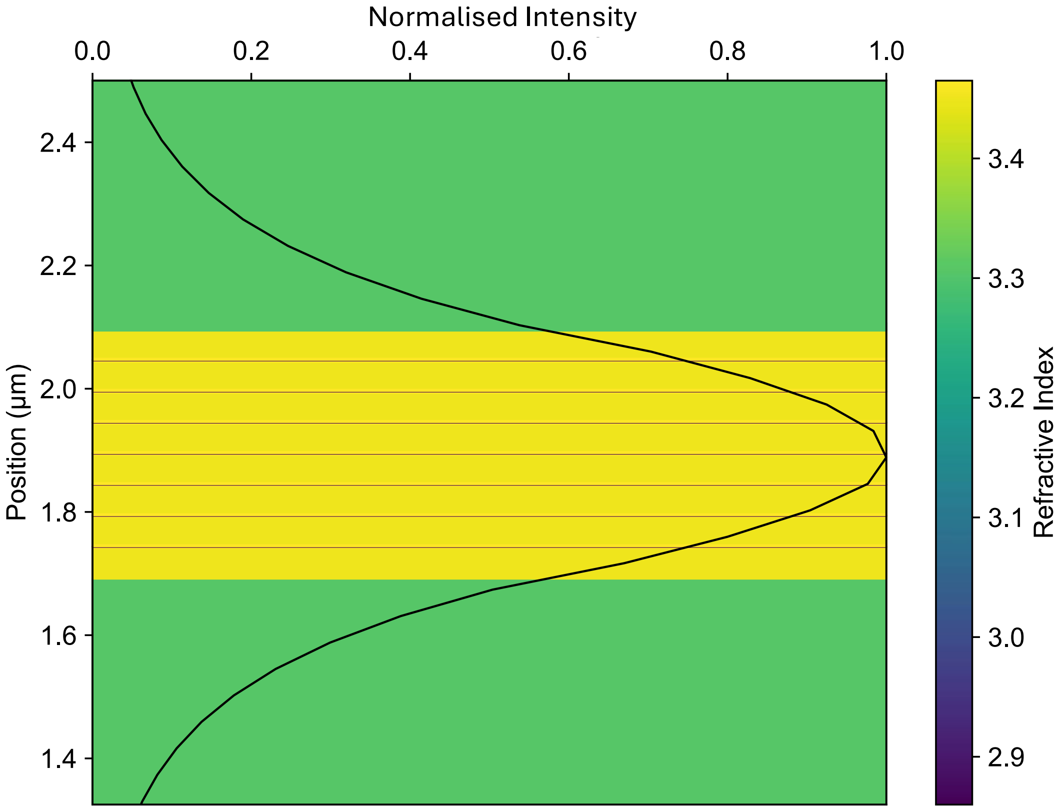

Figure 2.6: Schematic depiction of the refractive index of the different layers within an example epitaxial stack. The black line represents the 1D profile of the normalised intensity of the first TE mode in the epitaxial structure.

Once the optical mode is identified the optical mode width, w_{mode}, can be obtained using the following expression,

$$\mathrm{w_{mode}} = \frac{\int_{-\infty}^{+\infty} E^2(z)dz}{E_{pk}^2} \tag{2.9}$$

Where $E(z)$ is magnitude of the electric field along the direction of growth, with peak value E_{pk}. Assuming the optical field is constant over the width of the active material, L_d, the confinement factor, Γ, can be obtained from the mode width,

$$\Gamma = \frac{L_d}{w_{mode}} \tag{2.10}$$

The confinement factor quantifies the fraction of energy coupled to the gain medium.

2.5.2. Band Structure Description

For the identification of gain the transport of carriers through the individual layers of the epitaxial structure needs to be simulated. Specifically which states are being occupied by electrons and electron-holes under varying forward biases needs to be known to obtain an accurate gain description. The band structure of the full epitaxial structure is identified using a self-consistent Schrödinger-Poisson-current continuity solver with a 6-band k.p model for the VB and a parabolic band approximation for the CB. This model is implemented in Photon Design’s Harold software tool. The software relies on an extensive material database, which can be altered as required by the user. A flow chart as to how the Schrödinger-Poisson equations are solved for is depicted in Figure 2.7.

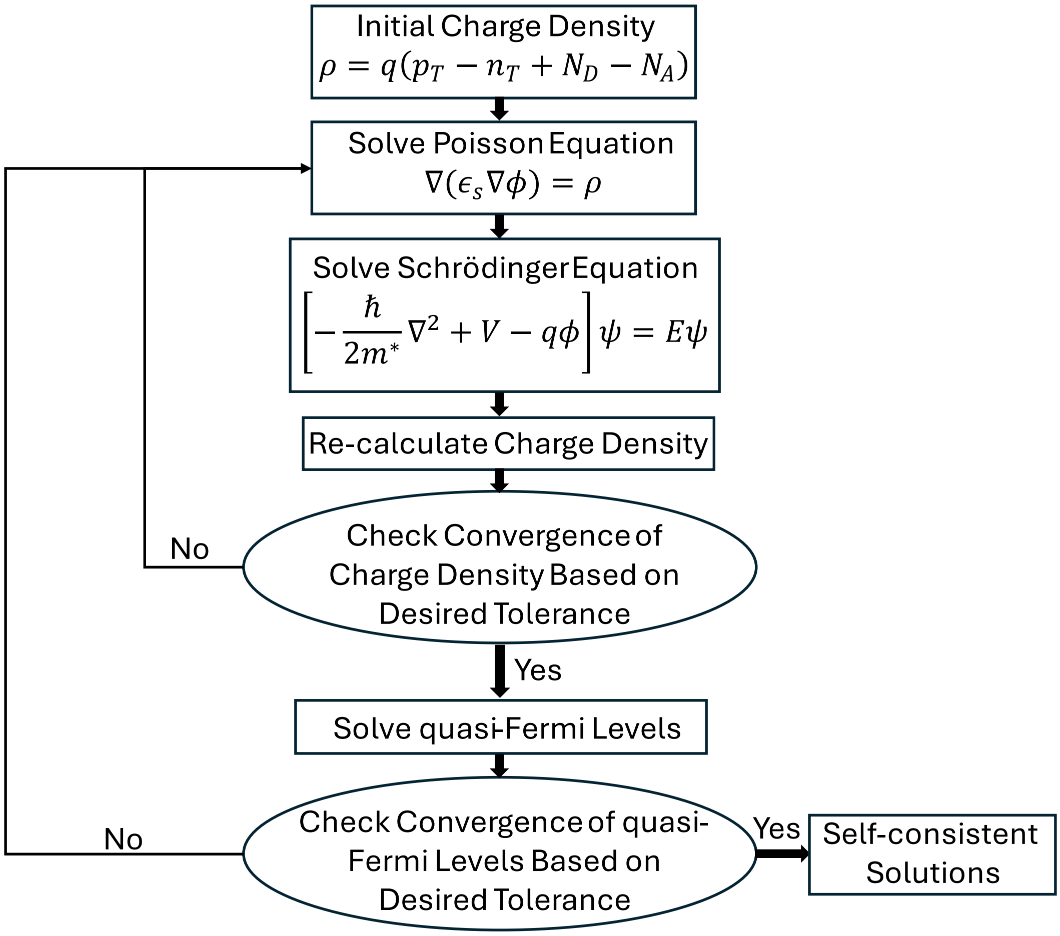

Figure 2.7: Flow chart diagram depicting the iteration scheme used to self-consistently solve the Schrödinger-Poisson equations.

Where ρ is the charge density distribution, q is the charge of the carriers, p_T is the total density of holes, n_T is the total density of the electrons, N_D and N_A are the doping densities of donors and acceptors, respectively. ϵ_s is the relative static dielectric constant, ϕ is the electrostatic potential. $\hbar$ is the reduced Planck constant, m^* is the effective mass of the carrier, and ψ and E are the wavefunction and the energy of the bound states for a given sub band.

In addition to Poisson's and Schrödinger's equation, the transport of the charge carriers, as they travel through the individual layers, needs to be identified. The layers of the structure are divided into two main categories, bulk regions, and quantum well regions, whose governing equations differ due to the appearance of confinement effects in the QWs. The continuity equations for the charge carriers for the bulk regions are expressed by the following equation,

$$\nabla \cdot \boldsymbol{j}_{n,p} \mp q\left(R^{SRH} + R^{Spon} + R^{Auger} + R^{net}_{n,p}\right) = 0 \tag{2.11}$$

Where $\boldsymbol{j}_{n,p}$ is the current density for electrons (n) and holes (p), and various recombination per unit volume, which are Shockley-Read-Hall, spontaneous, Auger, and net capture rate are represented by R^{SRH}, R^{Spon}, R^{Auger}, and $R^{net}_{n,p}$, respectively. Similarly for the quantum well regions the current capture and escape balance equations are given by

$$\nabla \cdot \boldsymbol{j}^{QW}_{n,p} \mp q\left(R^{SRH}_{QW} + R^{Spon}_{QW} + R^{Auger}_{QW} + R^{Stim} - \frac{1}{d_{QW}}\int_{QW} R^{net}_{n,p}\, dw\right) = 0 \tag{2.12}$$

with an additional recombination, which is the stimulated recombination, R^{Stim}. Stimulated emission also occurs in the bulk, but is considered negligible and is ignored in the software. The emission of light of the device is of interest, meaning that the generation of photons needs to be simulated, which is done using the photon rate equation,

$$(\bar{G} - \bar{B})S + \frac{\beta}{v_g}\int R^{Spont}_{QW}\, dV = 0 \tag{2.13}$$

where $\bar{G}$ is the gain, $\bar{B}$ is the total loss, for a given energy or wavelength, defined by the sum of the material absorption, α_m, and the internal loss, α_i, S is the average density of photon in the cavity, β represents the fraction of spontaneous emission that couples to the lasing mode and v_g is the group velocity of the wave. The above equation expresses the balance of loss and generation of photons as the device is being biased. Additionally, the propagation of the light through the structure needs to be evaluated, which is done using the waveguide equation,

$$\nabla^2 W + k_0^2(\epsilon - \beta_0^2)W = 0 \tag{2.14}$$

where W is the optical wave function, k_0^2 is the wave vector in vacuum at peak mode gain, ϵ is the complex optical dielectric constant, and β_0 is the propagation constant.

In what follows, the carrier densities in the bulk and QW layers are described as implemented in the commercial diode solver. These quantities must be know in order to determine the carrier density in the QDs, which is discussed in more detail in Section

3.2.3. The carrier densities for the bulk regions are identified using the Thomas-Fermi approximation, leading to,

$$n = N_c F_{\frac{1}{2}}\left(\frac{E_{f,n} - E_C}{k_B T}\right) \tag{2.15}$$

for electrons, and leading to,

$$p = N_v F_{\frac{1}{2}}\left(\frac{E_V - E_{f,p}}{k_B T}\right) \tag{2.16}$$

for holes. Where $F_{\frac{1}{2}}$ is the Fermi-Dirac integral of the order of ½, $E_{C,V}$ is the energy of the carrier of the well of the conduction or valence band, respectively, $E_{f,n,p}$ is the quasi-Fermi level of the CB or VB, respectively, T is the temperature, and k_B is the Boltzmann constant. With the Fermi-Dirac integral of the order of ½ is given by,

$$F_{\frac{1}{2}}(x) = \int_0^{\infty} \frac{\xi^{\frac{1}{2}} d\xi}{1 + e^{\xi - x}} \tag{2.17}$$

and the effective density of states in bulk regions, N_C and N_V in the CB and the VB, respectively is given by,

$$N_{C,V} = 2\left(\frac{2\pi m_{n,p} k_B T}{h^2}\right)^{\frac{3}{2}} \tag{2.18}$$

with $m_{n,p}$ being the effective mass of the electron or the hole, respectively. The model is setup such that only non-confined carriers contribute to the current, which include drift, diffusion and temperature effects.

For the QW regions the density of the charge carriers, n_{QW} is expressed as,

$$n_{QW} = k_B T \sum_j \rho_{j,QW} \log\left[1 + exp\left(\frac{E_{F,n_w} - E_j^0}{k_B T}\right)\right] \tag{2.19}$$

where E_{F,n_w} is the quasi-Fermi level for a given band, and $\rho_{j,QW}$ is the effective density of the confined charge carriers. The total density of states of the confined charge carriers, for every QW active layer, is expressed as,

$$\rho_j = \frac{m_j}{\pi \hbar^2 d_{act}} \tag{2.20}$$

with m_j being the effective mass of the charge carrier, and $d_{act}$is the thickness of the active region, which equals to the sum of the thickness of each active QW layer. The above expression is then used to identify the confined charge density for an individual QW layer using,

$$\rho_{j,QW} = \left(\frac{d_{act}}{d_w}\int_{QW}\left|\psi_j\right|^2 dw\right)\rho_i \tag{2.21}$$

where the total density of states is multiplied by the ratio of the total active layer thickness and the thickness of the individual QW, d_w and the wave overlap, expressed by the integral. An example simulation of the full epitaxial structure depicted in Figure 2.5 is portrayed in Figure 2.8, presenting the band edge of the CB and the VB and the quasi-Fermi level for the conduction band when the device is driven at 90 mA. The bands are aligned according to the material's affinity, which quantifies the energy difference between the vacuum level and the semiconductor CB. As can be seen in Figure 2.8, the band edges of the various material used in the epitaxial stack are depicted, with abrupt changes in band edge energy indicating material interfaces. Additionally, the quasi Fermi-level of the CB and the VB are separated, as is expected, under the influence of forward bias.

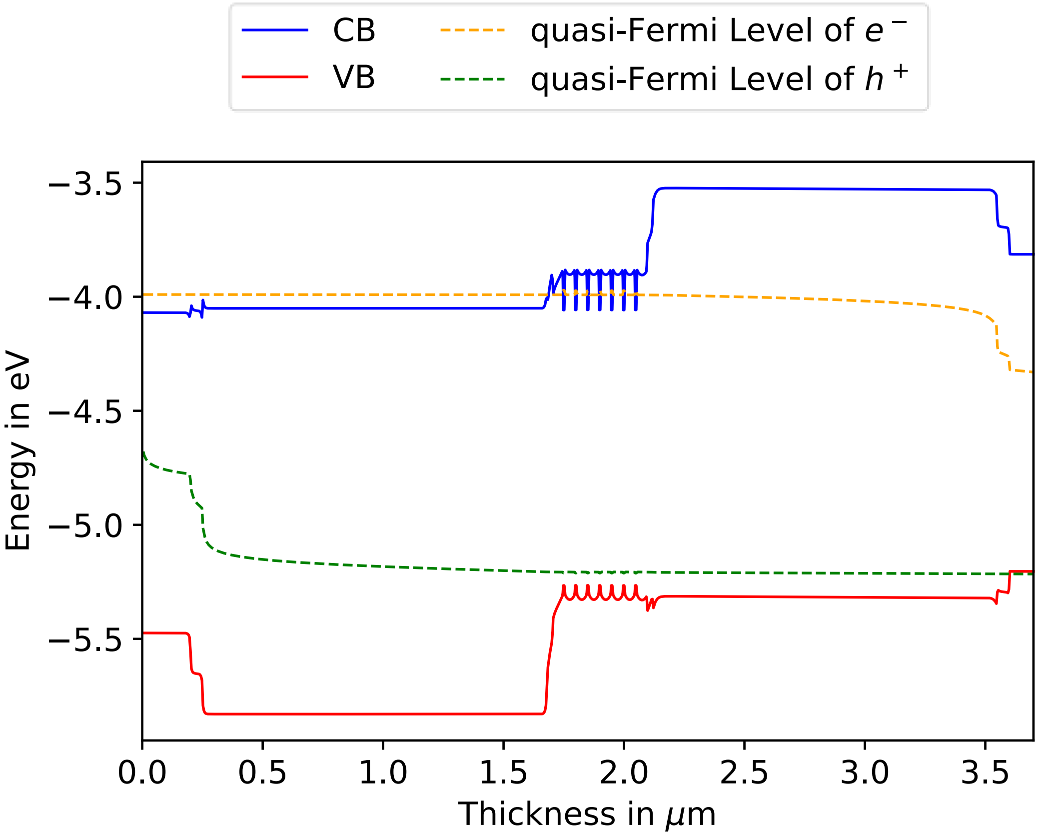

Figure 2.8: Depiction of the CB, VB, and quasi-Fermi level of the electron of an example epitaxial structure under forward bias as identified by Harold.

2.6. Summary

A brief introduction to QDs, pertaining to what they are, what they look like and how they can be grown, and observed is given in this Chapter. The difficulties that come with identifying the actual material composition, shape, and dimensions of QDs are highlighted. A discussion of different modelling techniques used to simulate the wavefunction and energy levels of confined carrier within an individual dot follows and leads to the conclusion that the multi-band k.p model is the most appropriate model to obtain an accurate simulation of the energy levels and wavefunction without the need for excessive computational resources. The focus then turns to modelling the whole epitaxial structure, needed for the identification of modal absorption and gain. This includes the identification of the mode profile and the description of the charge carrier using commercially available computational models.

3. Numerical Implementation and Experimental Technique

The first part of this chapter focuses on the numerical implementation of the continuous mechanical strain model, the 8-band k.p model, and Poisson's equation, for the identification of strain, energy and wavefunction of charge carriers, and the piezoelectric effect in individual QDs. The appearance of unphysical solutions in the 8-band k.p model is discussed as well as the approach to eliminate these solutions. Additionally, the rate equation model used for the description of the carrier transport inside the dots is described. The established rate equation identifies the occupation probability of the QD states for varying forward biases. The focus then shifts to the experimental methods used to identify the gain and absorption spectra for QD based material. The use of the segmented contact method (SCM) to identify the gain and absorption spectra is described. Modifications to the SCM setup are discussed, which allow the identification of the modal spectrum under reverse bias.

The mathematical description of the discretisation of the strain solver and the description of the momentum matrix element of the 8-band k.p model were derived by Joel Lowther from Photon Design.

The QD sample investigated in this chapter were grown by UCL and by IQE using an MBE reactor. The metal contacts on the SCM samples were deposited by Dr. Sara-Jayne Gillgrass. Further sample preparation, which included cleaving the metal plated wafer and wire-bonding the cleaved sample to a 16-pin header, to which the sample was glued onto using silver epoxy, was conducted by Susanna Power and Noor Albittar.

The setup used for the SCM was maintained by Dr. Richard Forrest. Dr. Chris Hodges, Dr Lydia Jarvis, Dr. Curtis Hentschel, and Dr. Craig Allford supported the implementation of the additional components required for the reverse bias measurements.

3.1. Continuum Elastic Model

The growth of self-assembled QDs inherently requires a difference in lattice constant between the QD material and the underlying material. This leads to a strained system. The strain impacts the confining potential of the charge carriers inside the QD. Thus, a dot system will only be appropriately described if the strain is correctly accounted for. To achieve this, the continuum elastic model has been implemented, chosen as it benefits from high accuracy and computational efficiency compared to atomistic or analytical models [44]. This model treats the stress and strain as a continuum, expressed using Hooke's law, given by Equation 3.1. The generalization of Hooke's law relates all directions of stress to all directions of strain, assuming elastic and linear deformation conditions.

$$\sigma_{ij} = C_{ijkl}\varepsilon_{kl} \tag{3.1}$$

σ_{ij} is the stress tensor, C_{ijkl} is the elastic stiffness tensor, of fourth rank, and ε_{kl} is the strain, i, j, k, and l indicate the direction of the stress and strain. They can be separated into normal strain/stress, with $i = j$, and $k = l$, with $i, j, k, l \in \{x, y, z\}$, or into shear strain/stress, $i \neq j$, and $k \neq l$. A two-dimensional visualisation is depicted in Figure 3.1.

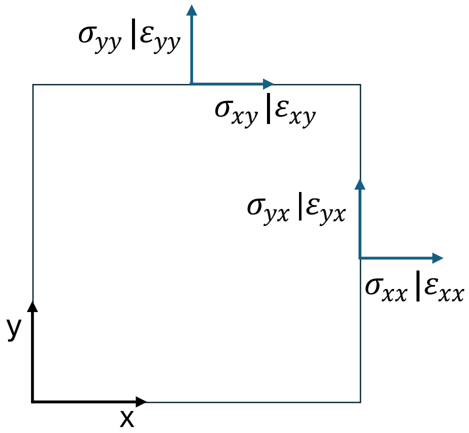

Figure 3.1: 2D representation of the stress, σ_{ij}, and strain, ε_{ij}, tensor.

For cubic crystalline materials, such as InAs, GaAs, and other zinc blende materials, the symmetry reduces the coefficients of C_{ijkl} to three independent elements, denoted C_{11}, C_{12}, and C_{44}. Taking advantage of the symmetries the strain, Equation 3.1 can be expressed as follows,

$$\begin{pmatrix} \sigma_{xx} \\ \sigma_{yy} \\ \sigma_{zz} \\ \sigma_{xy} \\ \sigma_{xz} \\ \sigma_{yz} \end{pmatrix} = \begin{pmatrix} C_{11} & C_{12} & C_{12} & 0 & 0 & 0 \\ C_{12} & C_{11} & C_{12} & 0 & 0 & 0 \\ C_{12} & C_{12} & C_{11} & 0 & 0 & 0 \\ 0 & 0 & 0 & 2C_{44} & 0 & 0 \\ 0 & 0 & 0 & 0 & 2C_{44} & 0 \\ 0 & 0 & 0 & 0 & 0 & 2C_{44} \end{pmatrix} \begin{pmatrix} \epsilon_{xx} \\ \epsilon_{yy} \\ \epsilon_{zz} \\ \epsilon_{xy} \\ \epsilon_{xz} \\ \epsilon_{yz} \end{pmatrix} \tag{3.2}$$

Under the conditions that the structure is in equilibrium and that there are no external forces acting on the structure, the equation of motions are identified from Equation 3.3,

$$\sum_i \frac{\partial \sigma_{ij}}{\partial x_i} = 0 \tag{3.3}$$

This leads to a system of coupled second-order partial derivatives, expressed by Equation 3.4, using $\partial_i = \frac{\partial}{\partial x_i}$,

$$\begin{cases} \sum_i \partial_i \sigma_{ix} = \partial_x \sigma_{xx} + \partial_y \sigma_{yx} + \partial_z \sigma_{zx} = 0 \\ \sum_i \partial_i \sigma_{iy} = \partial_x \sigma_{xy} + \partial_y \sigma_{yy} + \partial_z \sigma_{zy} = 0 \\ \sum_i \partial_i \sigma_{iz} = \partial_x \sigma_{xz} + \partial_y \sigma_{yz} + \partial_z \sigma_{zz} = 0 \end{cases} \tag{3.4}$$

Stress and strain originate from the displacement of atoms (or a cluster of atoms) from their equilibrium position. This displacement is a direct result from the lattice mismatch of the InAs dot material grown on material with a smaller lattice constant, e.g., GaAs. In bulk material the indium and arsenide atoms will naturally sit at a given position, when directly grown on a material of different lattice constant, for small enough lattice mismatch, the atoms adjust themselves according to the underlying material. The difference between the adjusted and original position is the displacement, $\vec{u}$. The strain is expressed as a function of displacement,

$$\varepsilon_{ij} = \frac{1}{2}\left(\partial_j u_i + \partial_i u_j\right) + \varepsilon_{0,ij} \tag{3.5}$$

Where u_i is the displacement in the x-, y-, or z-direction, and $\varepsilon_{0,ij}$ is the “initial” strain, given by,

$$\varepsilon_{0,ij} = \begin{cases} \frac{a_{sub} - a_{QD}}{a_{QD}}, & \text{(inside QD)} \\ 0 \quad , & \text{(outside QD)} \end{cases} \tag{3.6}$$

Where a_{sub} and a_{QD} are the lattice constants of the underlying layer material and the dot material, respectively. Using the expression of the strain as a function of displacement, the final equation of motion is given by the following system of coupled partial derivatives,

$$\begin{pmatrix} \partial_x C_{11}\partial_x + \partial_y C_{44}\partial_y + \partial_z C_{44}\partial_z & \partial_x C_{12}\partial_y + \partial_y C_{44}\partial_x & \partial_x C_{12}\partial_z + \partial_z C_{44}\partial_x \\ \partial_y C_{12}\partial_x + \partial_x C_{44}\partial_y & \partial_x C_{44}\partial_x + \partial_y C_{11}\partial_y + \partial_z C_{44}\partial_z & \partial_y C_{12}\partial_z + \partial_z C_{44}\partial_y \\ \partial_z C_{12}\partial_x + \partial_x C_{44}\partial_z & \partial_z C_{12}\partial_y + \partial_y C_{44}\partial_z & \partial_x C_{44}\partial_x + \partial_y C_{44}\partial_y + \partial_z C_{11}\partial_z \end{pmatrix} \begin{pmatrix} u_x \\ u_y \\ u_z \end{pmatrix} = \begin{pmatrix} -\partial_x C_{11}\varepsilon_{0,x} - \partial_x C_{12}\varepsilon_{0,y} - \partial_x C_{12}\varepsilon_{0,z} \\ -\partial_y C_{12}\varepsilon_{0,x} - \partial_y C_{11}\varepsilon_{0,y} - \partial_y C_{12}\varepsilon_{0,z} \\ -\partial_z C_{12}\varepsilon_{0,x} - \partial_z C_{12}\varepsilon_{0,y} - \partial_z C_{11}\varepsilon_{0,z} \end{pmatrix} \tag{3.7}$$

The above equation is then discretised using a staggered grid such that the strain at a given position, expressed as, $\varepsilon_{ij}^{\alpha,\beta,\gamma}$, where α, β, γ are spatial coordinates, is given by,

$$\varepsilon_{ii}^{\alpha,\beta,\gamma} = \frac{u_i^{\alpha+\frac{1}{2},\beta,\gamma} - u_i^{\alpha-\frac{1}{2},\beta,\gamma}}{\Delta_\alpha} + \varepsilon_{0,ii}^{\alpha,\beta,\gamma} \tag{3.8}$$

And,

$$\varepsilon_{ij}^{\alpha+\frac{1}{2},\beta+\frac{1}{2},\gamma} = \frac{1}{2}\left[\frac{u_i^{\alpha+\frac{1}{2},\beta+1,\gamma} - u_i^{\alpha+\frac{1}{2},\beta,\gamma}}{\Delta_\beta} + \frac{u_j^{\alpha+1,\beta+\frac{1}{2},\gamma} - u_j^{\alpha,\beta+\frac{1}{2},\gamma}}{\Delta_\alpha}\right] \tag{3.9}$$

This discretisation leads to strain components defined at different locations on the discretised mesh, as depicted in Figure 3.2.

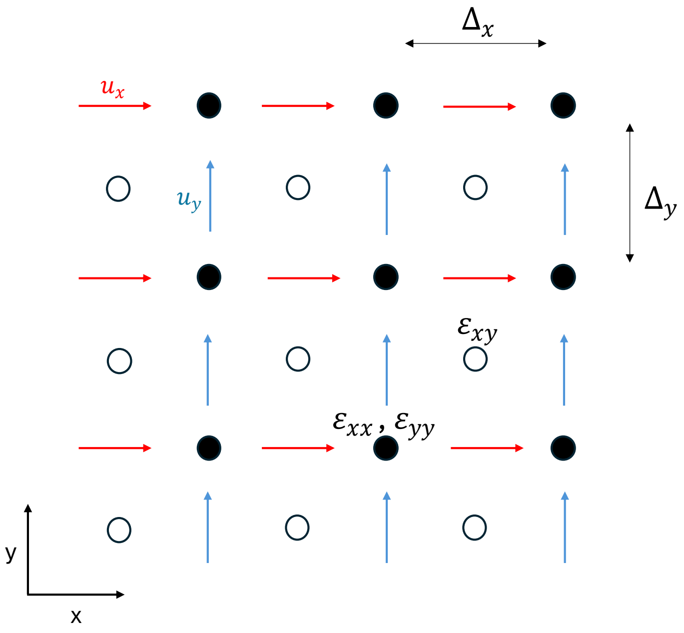

Figure 3.2: Schematic depiction of staggered mesh and location of displacement $u_{x,y}$, normal strain $\varepsilon_{xx,yy}$ and shear strain ε_{xy} on the mesh.

This would be inconvenient in the general case, however, since the off-diagonal components are not coupled to any other components, the stress tensor components can be identified at the same location as the corresponding strain components. Equation 3.3 can then be evaluated at the same location as the displacement field, $\vec{u}$. The staggered grid was chosen to better deal with changes in material. As the problem is inherently an inhomogeneous system, certain material parameters needed to be averaged at the material interfaces. For the implemented discretisation, only the C_{44} material parameter needed to be averaged, this was achieved using the following harmonic averaging scheme,

$$C_{44}\left(\alpha+\frac{1}{2},\beta+\frac{1}{2},\gamma\right)=\left[\frac{1}{4}\sum_{r=-1/2}^{1/2}\sum_{s=-1/2}^{1/2}C_{44}^{-1}(\alpha+r,\beta+s)\right]^{-1} \tag{3.10}$$

The discretised equation of motion, leads to a system of linear algebraic equations, which are solved using an open source linear algebra solver from Intel's oneAPI Math Kernel Library, designed to solve large sparse linear systems. Specifically, the Pardiso solver from Intel's oneMKL package is used. The solution of the system of linear algebraic equations describes the displacement of the strained material.

3.1.1. Piezoelectric Effect

When atoms of a crystal without inversion symmetry are displaced, dipole and quadrupole moments can be induced which create a piezoelectric polarization, $\boldsymbol{P}$. For such crystals the strain tensor induces a piezoelectric polarization. This equates to an effective polarization charge $\rho(\boldsymbol{r})=-\nabla\cdot\mathbf{P}(\mathbf{r})$, which in turn corresponds to an electrostatic potential, which has an effect on the confined carriers of the dot [66].

The piezoelectric potential depends on the strain via the linear piezoelectric tensor, e_{ij}. This tensor has only a single independent component for the case of zinc blende structures, leading to the following expression of linear piezoelectric polarization,

$$\boldsymbol{P}(\boldsymbol{r})=\begin{pmatrix}e_{14}&0&0\\0&e_{14}&0\\0&0&e_{14}\end{pmatrix}\begin{pmatrix}\varepsilon_{xy}\\\varepsilon_{xz}\\\varepsilon_{yz}\end{pmatrix} \tag{3.11}$$

where e_{14} is the spatially dependent piezoelectric material constant and ε_{ij} are the spatially dependent shear strain components. The above expression can then be used to identify a corresponding electrostatic potential, $\Phi(\boldsymbol{r})$, using Gauss' law, leading to the following Poisson's equation,

$$-\nabla \cdot \epsilon_0 \epsilon_r(\boldsymbol{r}) \nabla \Phi(\boldsymbol{r}) = -\nabla \cdot \boldsymbol{P}(\boldsymbol{r}) \tag{3.12}$$

where ϵ_0 is the vacuum dielectric constant and ϵ_r is the relative dielectric constant of the material. Terms which are quadratic in strain are included to give a more accurate description of the piezoelectric effect [67,68], and the corresponding polarization is given by,

$$\boldsymbol{P}(\boldsymbol{r}) = e_{14}\begin{pmatrix} \varepsilon_{xy} \\ \varepsilon_{xz} \\ \varepsilon_{yz} \end{pmatrix} + B_{114}\begin{pmatrix} \varepsilon_{xx}\varepsilon_{xy} \\ \varepsilon_{yy}\varepsilon_{xz} \\ \varepsilon_{zz}\varepsilon_{yz} \end{pmatrix} + B_{124}\begin{pmatrix} \left(\varepsilon_{yy} + \varepsilon_{zz}\right)\varepsilon_{xy} \\ (\varepsilon_{xx} + \varepsilon_{zz})\varepsilon_{xz} \\ \left(\varepsilon_{yy} + \varepsilon_{xx}\right)\varepsilon_{yz} \end{pmatrix} + B_{156}\begin{pmatrix} \varepsilon_{xz}\varepsilon_{yz} \\ \varepsilon_{xy}\varepsilon_{yz} \\ \varepsilon_{xy}\varepsilon_{xz} \end{pmatrix} \tag{3.13}$$

With the material dependent piezoelectric constants, e_{14}, B_{114}, B_{124}, and B_{156}. The corresponding electrostatic potential was obtained from Equation 3.12. The total polarisation is a sum of the linear and quadratic polarisation. The electrostatic potential was identified by solving Poisson's equation. This was achieved using a central finite difference scheme.

3.2. 8-band k.p Theory

The multi-band k.p model was developed to solve the time-independent Schrödinger equation, given by Equation 3.14, for semiconductor material.

$$\left[\frac{\boldsymbol{p}^2}{2m} + V(\boldsymbol{r})\right]\psi = E\psi \tag{3.14}$$

where $\boldsymbol{p}$ is the momentum, m is the mass, $V(\boldsymbol{r})$ is the potential, and ψ is the wavefunction of the system with a corresponding energy E.

The strength of the Luttinger-Kohn k.p theory is that it allows one to neglect atomistic effects that are only relevant on a sub-nanometre scale. This is achieved by preserving the symmetry properties of the crystal lattice to identify the electronic structure, allowing a piecewise or atomistic representation to be replaced by effective continuous equations described by empirical material parameters. This technique allows the analysis of structures at significantly larger length-scales, making numerical solutions significantly more efficient. Essentially, mesoscopic semiconductor structures, which enclose millions of atoms can be solved for, within good approximations, using only a few 1000 variables.

The Luttinger-Kohn k.p theory was originally designed for homogeneous material systems. The application of this theory to heterostructures, led to the appearance of unphysical descriptions of the confined charge carriers. Specifically, the boundary conditions connecting the envelope function across a material interface were strongly debated. This was settled by Burt, who established an exact envelope-function theory for heterogeneous semiconductor structures [69].

The envelope-function approximation identifies physical properties from the slowly varying envelope function. This eliminates the need to know the exact behaviour of the total wavefunction, which is also described by a rapidly varying part, acting over the scale of the crystal lattice. Special care has to be taken at the interface of materials. A detailed description of how the envelope function can still be applied to heterogeneous structures is given by Burt (1999) [48].

The Hamiltonian for the 8-band description includes the lowest band in the CB, and the three highest bands in the VB, the heavy-hole (HH), the light-hole (LH), and the spin-orbit split-off hole (SO), for spin up and spin down. Leading to the following basis set:

$$|S\downarrow\rangle, |X\uparrow\rangle, |Y\uparrow\rangle, |Z\uparrow\rangle, |S\downarrow\rangle, |X\downarrow\rangle, |Y\downarrow\rangle, |Z\downarrow\rangle. \tag{3.15}$$

$S, X, Y,$ and Z indicates that these functions share the same symmetry properties as the atomic orbitals, $1s$ for the description of the CB, and $2p_x$, $2p_y$, and $2p_z$ for the description of the VBs.

The resulting Hamiltonian can then be described by:

$$H = \begin{bmatrix} H_2 & 0 \\ 0 & H_2 \end{bmatrix} + \begin{bmatrix} H_1 & 0 \\ 0 & H_1 \end{bmatrix} + H_0 \tag{3.16}$$

where H_2 and H_1 are given as:

$$H_2 = \begin{bmatrix} Ak^2 & 0 & 0 & 0 \\ 0 & Lk_x^2 + M(k_y^2 + k_z^2) & Nk_xk_y & Nk_xk_z \\ 0 & Nk_xk_y & Lk_y^2 + M(k_x^2 + k_z^2) & Nk_yk_z \\ 0 & Nk_xk_z & Nk_yk_z & Lk_y + M(k_x^2 + k_z^2) \end{bmatrix},$$

$$H_1 = \begin{bmatrix} 0 & iPk_x - iP\sum_j \epsilon_{xj}k_j & iPk_y - iP\sum_j \epsilon_{yj}k_j & iPk_z - iP\sum_j \epsilon_{zj}k_j \\ -iPk_x + iP\sum_j \epsilon_{xj}k_j & 0 & 0 & 0 \\ -iPk_y + iP\sum_j \epsilon_{yj}k_j & 0 & 0 & 0 \\ -iPk_z + iP\sum_j \epsilon_{zj}k_j & 0 & 0 & 0 \end{bmatrix}.$$

Where the constant part of the Hamiltonian H_0 is given by

$$H_0 = \begin{bmatrix} G & \Gamma \\ \Gamma^* & G \end{bmatrix},$$

Where

$$G = \begin{bmatrix} E_c + a_c Tr(\varepsilon) & 0 & 0 & 0 \\ 0 & E_v{}' + l\varepsilon_{xx} + m(\varepsilon_{yy} + \varepsilon_{zz}) & n\varepsilon_{xy} - i\Delta/3 & n\varepsilon_{xz} \\ 0 & n\varepsilon_{xy} + i\Delta/3 & E_v{}' + l\varepsilon_{yy} + m(\varepsilon_{xx} + \varepsilon_{zz}) & n\varepsilon_{yz} \\ 0 & n\varepsilon_{xz} & n\varepsilon_{yz} & E_v{}' + l\varepsilon_{zz} + m(\varepsilon_{xx} + \varepsilon_{yy}) \end{bmatrix},$$

and,

$$\Gamma = \begin{bmatrix} 0 & 0 & 0 & 0 \\ 0 & 0 & 0 & \Delta/3 \\ 0 & 0 & 0 & -i\Delta/3 \\ 0 & -\Delta/3 & i\Delta/3 & 0 \end{bmatrix}.$$

Where $Tr(\varepsilon)$, is the trace of the strain tensor ε_{ij}. The parameters used to describe the above Hamiltonian are identified from the following equations,

$$A = \frac{\hbar}{2m_0}\left(\frac{m_0}{m_e^*} - \frac{E_p}{E_g}\frac{3E_g + 2\Delta}{3(E_g + \Delta)}\right),$$

$$L = \frac{P^2}{E_g} - \frac{\hbar^2}{2m_0}(\gamma_1 + 4\gamma_2),$$

$$M = -\frac{\hbar}{2m_0}(\gamma_1 - 2\gamma_2),$$

$$N = \frac{P^2}{E_0} - \frac{3\hbar^2}{m_0}\gamma_3,$$

$$k = k_x^2 + k_y^2 + k_z^2,$$

$$P = \sqrt{\frac{\hbar^2}{2m_0}E_p},$$

$$E_c = E_v + E_g,$$

$$E_v' = E_v - \Delta/3$$

$$l = 2b_v + a_v,$$

$$m = a_v - b_v,$$

$$n = \sqrt{3}d_v.$$

With $\hbar$ being the reduced Planck constant, m_0 is the mass of the free electron, m_e^* is the effective mass of an electron of a given material, E_g is the bandgap energy of a given material, E_p is the Kane parameter quantifying the interaction energy between the valence and the conduction band, Δ is the split-off energy, $\gamma_{1,2,3}$ are the Luttinger parameters, k is the wavevector, E_c is the energy of the CB edge, E_v is the energy of the VB edge, a_c is the deformation potential of the CB, a_v is the deformation potential of the valence band, b_v and d_v are the shear deformation potentials.

The above equations establish the Burt-Foreman description of the 8-band k.p Hamiltonian, leading to a set of linear equations describing the time-independent Schrödinger equation, given by Equation 3.14.

This set of equation was solved through transformation into an equivalent matrix representation. The first step of this transformation was to divide the structure of interest into a series of interconnected nodes. This was achieved by applying the second-order central finite difference approximation. Each node was described by the 8-band Schrödinger equation, leading to the final matrix representation. For the Burt-Foreman Hamiltonian, the diagonal terms were discretised as follows,

$$Qk_i^2 \rightarrow \hat{k}_i Q \hat{k}_i.$$

Where Q represents a spatially dependent Kane parameter or strain component, and $i = x, y, z$. Following the correct operator ordering established by Burt and Foreman, the upper triangular matrix elements of H_2 transform as follows,

$$N' k_i k_j \rightarrow \hat{k}_i N_+ \hat{k}_j + \hat{k}_j N_- \hat{k}_i.$$

Where $N_- = M - \hbar/2m_0$ and $N_+ = N' - N_-$. The lower triangular matrix elements were transformed as follows,

$$N' k_i k_j \rightarrow \hat{k}_j N_+ \hat{k}_i + \hat{k}_i N_- \hat{k}_j.$$

The elements of H_1 were transformed, for the upper triangular matrix elements, as follows,

$$iPk_i - iP \sum_j \varepsilon_{ij} k_j \rightarrow iP\hat{k}_i - iP \sum_j \varepsilon_{ij} \hat{k}_j,$$

and for the lower triangular matrix elements,

$$-iPk_i + iP \sum_j \varepsilon_{ij} k_j \rightarrow -i\hat{k}_i P + i \sum_j \hat{k}_j P \varepsilon_{ij}.$$

Under the assumption that there is no periodicity, as is the case for QDs, the $\hat{k}$ operation was replaced by the differential operator, $k_\alpha = -i\partial_\alpha$, where $\alpha = \{x, y, z\}$ [53].

3.2.1. Appearance and Elimination of Spurious Solutions

The 8-band k.p model is inherently haunted by the appearance of spurious solutions, also referred to as wing-band solutions [70]. These unphysical solutions are described either by an unphysical wavefunction (located inside the higher bandgap barrier material, or strongly fluctuating and noncontinuous) or by possessing an energy level that lies within the bandgap of the dot material. An example of spurious solutions is depicted in Figure 3.3, presenting the simulated solutions to a simple InAs QW surrounded by GaAs, whose probability distributions are non-continuous and are located deep inside the GaAs barrier. By changing the Kane parameter E_p, non-spurious solutions are obtained. Spurious solutions occur even when applying the corrected operator ordering. The cause of the appearance of spurious solutions is attributed to the failure of the 8-band k.p approximation to maintain the ellipticity of the Schrödinger equation [71]. The description of a physical system is ideally given by an elliptic differential equation, as this ensures that the obtained solutions are continuous. The failure to maintain the ellipticity can be accredited to either the inaccuracy of the 8-band k.p model, which is a second order perturbation approximation, the inaccurate discretisation of the identified partial differential equations, or the inaccurate identification of the material parameters describing the underlying structure. In this work we assume that the material parameters are ineffective. Therefore, minor changes to the material parameters were implemented that led to a spurious solution free 8-band k.p solver.

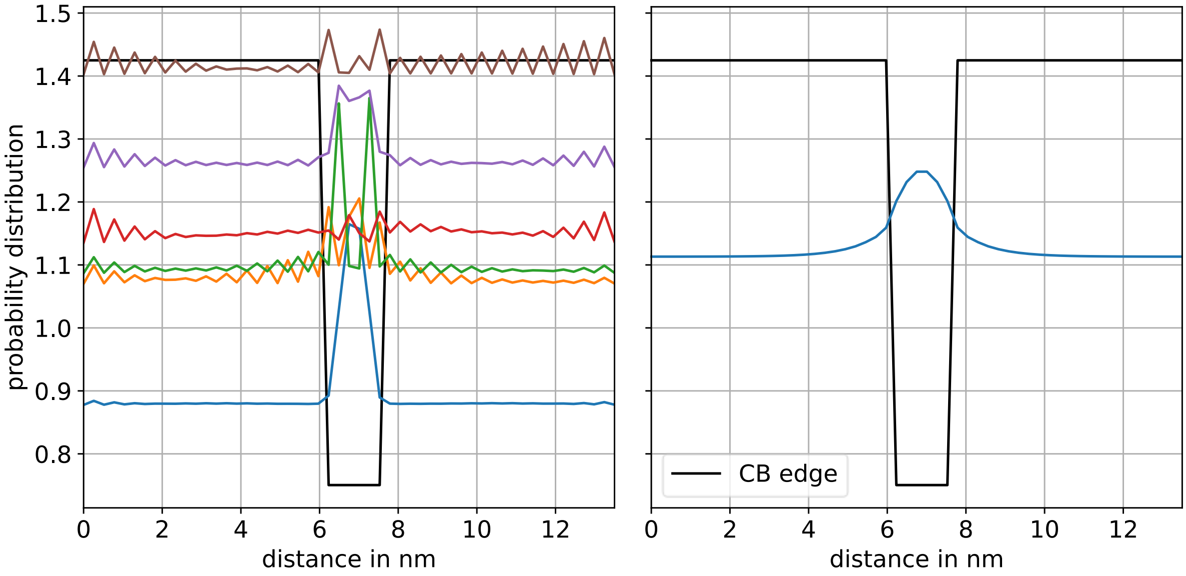

Figure 3.3: Depiction of spurious solutions for a 1.5 nm wide InAs QW surrounded by GaAs (left). Depiction of “correct” wavefunctions of the same QW structure, resulting from the elimination of spurious solutions by adjusting the E_p parameter (right).

Therefore to be able to achieve an accurate description of the confined charge carriers using the 8-and k.p model, the Hamiltonian needs to be correctly discretized, as given by the Burt-Foreman discretization scheme [72,73]. Additionally, to maintain the ellipticity of the differential equation the Kane parameter needs to be appropriately adjusted. The spurious solutions were eliminated by adjusting the Kane parameter, which describes the interaction strength between the VB states and the CB state, E_p [74], using the following equation,

$$E_p = \left(\frac{m_0}{m_e^*}\right)\left(\frac{3E_g\left(E_g + \Delta\right)}{3E_g + 2\Delta}\right). \tag{3.17}$$

Depending on the material system the above equation might still lead to spurious solutions [70], these can be avoided by multiplying the above expression of E_p by a factor of 0.9. The additional factor of 0.9 is to guarantee that the ellipticity of the partial differential equation is maintained even after it has been discretised.

Having to adjust the material parameters to obtain sensible solutions from the 8-band k.p model is a disadvantage, as this hinders the ability to identify an understanding of the confined carriers purely based on bulk material parameters. However, the 8-band k.p model is still of advantage when it comes to obtaining a better description of the energy levels and wavefunctions in QDs, than the effective mass model, and requires significantly less computational resources than the pseudopotential model, and the necessary material parameters are more readily available than those needed for the ETB. Both the effective mass and the spurious solution free 8-band model rely on the change of material parameters to correctly describe confined carriers; for the effective mass model it is the carrier mass, and for the 8-band model it is the Kane parameter. Despite that, the 8-band model still outperforms the effective mass model, as the Kane parameter is adjusted, in a known fashion, and can then be applied to various material systems, which is not the case for the effective mass model. Additionally, the effective mass model does not account for band mixing, while the herein implemented 8-band k.p model does. The scheme implemented to avoid spurious solutions effectively reduces the Kane parameter, which in turn reduces the confinement of the charge carriers.

3.2.2. Momentum Matrix Element for the 8-band k.p Model

The identification of the absorption and gain is dependent on the interaction of photons with the confined charge carriers. This type of process is widely studied and can be described using the dipole approximation. Essentially reducing the number of possible interactions that light can have with a material down to only interactions of light with multiple dipoles, i.e., pairs made out of a positive and negative charge which are spatially separated. In the case of semiconductor material, the positive and negative charge are the electron-hole and electron, respectively. In this view, only the descriptions of the negative and positive charge were necessary. Once the energies and wavefunctions of the charges were identified, the optical transitions between the states were evaluated by considering the interaction of the radiation field with the carriers. This interaction was described quantum mechanically using the vector potential $\boldsymbol{A}$. This vector potential was included in the time-dependent Schrödinger equation to quantify the interaction with the electromagnetic field [70].

$$i\hbar\partial_t\psi(\boldsymbol{r},t) = \widehat{H}\psi(\boldsymbol{r},t) = \left[\frac{\left(\widehat{\boldsymbol{p}} + e\boldsymbol{A}(\boldsymbol{r},t)\right)^2}{2m_0} + V(\boldsymbol{r})\right]\psi(\boldsymbol{r},t) \tag{3.18}$$

Where $\psi(\boldsymbol{r},t)$ is the time-dependent wavefunction and $V(\boldsymbol{r})$ is the crystal potential of the semiconductor structure. The vector potential of an electromagnetic field, quantified by a wave vector $\boldsymbol{k}$ and an angular frequency ω is given by,

$$\boldsymbol{A}(\boldsymbol{r},t) = Re\left[\boldsymbol{\epsilon}A_0e^{i(\boldsymbol{k}\cdot\boldsymbol{r}-\omega t)}\right] \tag{3.19}$$

In the optical limit $|\boldsymbol{r}| \ll 1/|\boldsymbol{k}|$, the vector potential transforms into,

$$\boldsymbol{A}(\boldsymbol{r},t) \approx \frac{1}{2}A_0\left(\boldsymbol{\epsilon}^*e^{i\omega t} + \boldsymbol{\epsilon}e^{-i\omega t}\right) \tag{3.20}$$

Where $\boldsymbol{\epsilon}$ accounts for general complex polarizations, describing the amplitude and phase of the wave's x-, y-, and z-polarization. In the linear response, where only terms of the order of $\boldsymbol{A}$ are non-zero, the time independent interaction Hamiltonian is identified as,

$$\widehat{H}_{int} = \frac{eA_0}{2m_0}\boldsymbol{\epsilon}\cdot\widehat{\boldsymbol{p}} \tag{3.21}$$

The transition rate between an initial state ψ_i and a final state ψ_f is then identified using,

$$\left|\langle\psi_i|\widehat{H}_{int}|\psi_f\rangle\right|^2 = A_0^2\left(\frac{e}{2m_0c}\right)^2\left|\langle\psi_i|\boldsymbol{\epsilon}\cdot\widehat{\boldsymbol{p}}|\psi_f\rangle\right|^2 \tag{3.22}$$

Where the term on the right in the vertical bars is the optical matrix element [75]. In the context of the 8-band k.p model, the wavefunctions are expressed as

$$\psi_n(\boldsymbol{r}) = \sum_{k=0}^{7}F_{n,k}(\boldsymbol{r})u_k(\boldsymbol{r}) \tag{3.23}$$

Where the wavefunction is given as the sum over the eight coupled sub-bands, with basis wavefunction u_k and their corresponding coefficient $F_{n,k}$, which make up the envelope function. Knowing that the charge carriers transition from the CB to the VB, and are described by Equation 3.23, the optical matrix elements can be evaluated as follows,

$$M_{cv} = |\langle\psi_c|\hat{e}\cdot\boldsymbol{p}|\psi_v\rangle|^2 \tag{3.24}$$

Where $\hat{e}$ is the direction of the polarisation, and $\boldsymbol{p}$ is the momentum operator, where c and v have been used to indicate whether the wavefunction describes a charge carrier in the CB or the VB, respectively. Substituting the wavefunctions into the expression inside the norm of Equation 3.24 leads to,

$$\begin{aligned}\langle\psi_c|\hat{e}\cdot\boldsymbol{p}|\psi_v\rangle &= \sum_{k=0}^{7}\sum_{l=0}^{7}\int d^3\boldsymbol{r}\left(F_{c,k}(\boldsymbol{r})u_k(\boldsymbol{r})\right)^{\dagger}(\hat{e}\cdot\boldsymbol{p})\left(F_{v,l}(\boldsymbol{r})u_l(\boldsymbol{r})\right)\\ &\approx \sum_{k=0}^{7}\sum_{l=0}^{7}\int_{unit\ cell} d^3\boldsymbol{r}u_k^{\dagger}(\boldsymbol{r})(\hat{e}\cdot\boldsymbol{p})u_l(\boldsymbol{r})\int d^3\boldsymbol{r}F_{c,k}^{\dagger}(\boldsymbol{r})F_{v,l}(\boldsymbol{r})\\ &= \sum_{k=0}^{7}\sum_{l=0}^{7}\langle u_k|\hat{e}\cdot\boldsymbol{p}|u_l\rangle\int d^3\boldsymbol{r}F_{c,k}^{\dagger}(\boldsymbol{r})F_{v,l}(\boldsymbol{r})\end{aligned}$$

Utilising the approximation that the envelope functions are slowly varying over the extent of a unit cell and taking advantage of the periodicity of the basis wavefunctions. The Burt-Foreman description of the 8-band k.p model relies on the atom-like basis set, given by Equation 3.15, which can be used to replace the $u_{k,l}$ values in the above expression. Using the Burt-Foreman basis set, most elements in the expression given by Equation 3.24 vanish due to symmetry, with the only non-zero elements being,

$$\langle S|p_x|X\rangle = \left\langle S\middle|p_y\middle|Y\right\rangle = \langle S|p_z|Z\rangle \equiv \frac{m_0}{\hbar}P \tag{3.25}$$

Where P is commonly related to the bulk matrix element, M_b, and the Kane parameter, E_p, as,

$$\frac{m_0^2}{\hbar^2}P^2 = 3M_b^2 = \frac{m_0}{2}E_p \tag{3.26}$$

For transverse magnetic (TM) polarisation, the direction of the polarisation is given in the z-directions, i.e., $\hat{e} = \hat{z}$, and the matrix element is expressed as,

$$M_{cv}^{TM} = |\langle\psi_c|p_z|\psi_v\rangle|^2 = \frac{m_0^2}{\hbar^2}P^2 \left|\int d^3\boldsymbol{r} \sum_{\sigma=\pm}\left[F_{c,S\sigma}^{\dagger}(\boldsymbol{r})F_{v,Z\sigma}(\boldsymbol{r}) + F_{c,Z\sigma}^{\dagger}(\boldsymbol{r})F_{v,S\sigma}(\boldsymbol{r})\right]\right|^2 \quad (3.27)$$

With the sum evaluated over the up and down spin of the carriers. For the transverse electric (TE) polarisation, the electric field is in the xy-plane. Here the z-direction is along the direction of growth of the material, and the x-, and y-direction are perpendicular to the direction of growth. Substituting in $\hat{e} = cos\phi\hat{x} + sin\phi\hat{y}$, the matrix element is expressed as,

$$\begin{aligned} M_{cv}^{TE} &= \left|\langle\psi_c|cos\phi p_x + sin\phi p_y|\psi_v\rangle\right|^2 \\ &= \frac{m_0^2}{\hbar^2}P^2 \left|\int d^3\boldsymbol{r} \sum_{\sigma=\pm}\left[F_{c,S\sigma}^{\dagger}(\boldsymbol{r})\left(cos\phi F_{v,X\sigma}(\boldsymbol{r}) + sin\phi F_{v,Y\sigma}(\boldsymbol{r})\right)\right.\right. \\ &\quad \left.\left. + \left(cos\phi F_{c,X\sigma}^{\dagger}(\boldsymbol{r}) + sin\phi F_{c,Y\sigma}^{\dagger}(\boldsymbol{r})\right)F_{v,S\sigma}(\boldsymbol{r})\right]\right|^2 \end{aligned}$$

In general, the dot distribution is random in the xy-plane. In this case, the expression of M_{cv}^{TE} needed to be averaged over the angle ϕ between the electric field and the x-axis of the dots. Leading to the final expression of the TE matrix element, expressed as,

$$M_{cv}^{TE} = \frac{m_0^2}{\hbar^2}P^2\frac{1}{2}\left\{\begin{array}{l} \left|\int d^3\boldsymbol{r} \sum_{\sigma=\pm} F_{c,S\sigma}^{\dagger}(\boldsymbol{r})F_{v,X\sigma}(\boldsymbol{r}) + F_{c,X\sigma}^{\dagger}(\boldsymbol{r})F_{v,S\sigma}(\boldsymbol{r})\right|^2 \\ + \left|\int d^3\boldsymbol{r} \sum_{\sigma=\pm} F_{c,S\sigma}^{\dagger}(\boldsymbol{r})F_{v,Y\sigma}(\boldsymbol{r}) + F_{c,Y\sigma}^{\dagger}(\boldsymbol{r})F_{v,S\sigma}(\boldsymbol{r})\right|^2 \end{array}\right\} \quad (3.28)$$

3.2.3. Identification of Occupation Probabilities of QD Levels

Similar to the transition dipole moment, the gain and absorption are directly dependent on the occupation probability of the conduction and valence band of the dots. While for the absorption a good approximation was obtained by assuming that no electrons are occupying the CB, a similarly easy assumption could not be implemented for the gain and an appropriate model was needed. A suitable model describing the electron distribution in the dots was established by O'Driscoll et al. (2010) [76]. This model relied on phonon-induced recombination for the capture and relaxation of carriers in dots, leading to a set of rate equations, quantifying the evolution of the carrier density as a function of recombination rates and carrier occupation probabilities of the dots and the surrounding material. The possible recombination are schematically depicted in Figure 3.4, for a single dot with only two available energy levels in the CB. For the hole states in the VB a Fermi-Dirac distribution is assumed, the necessary quasi-Fermi level is identified such that the individual dots are charge neutral. A detailed description of the identification of the holes in the VB is given in Section 4.2.3.

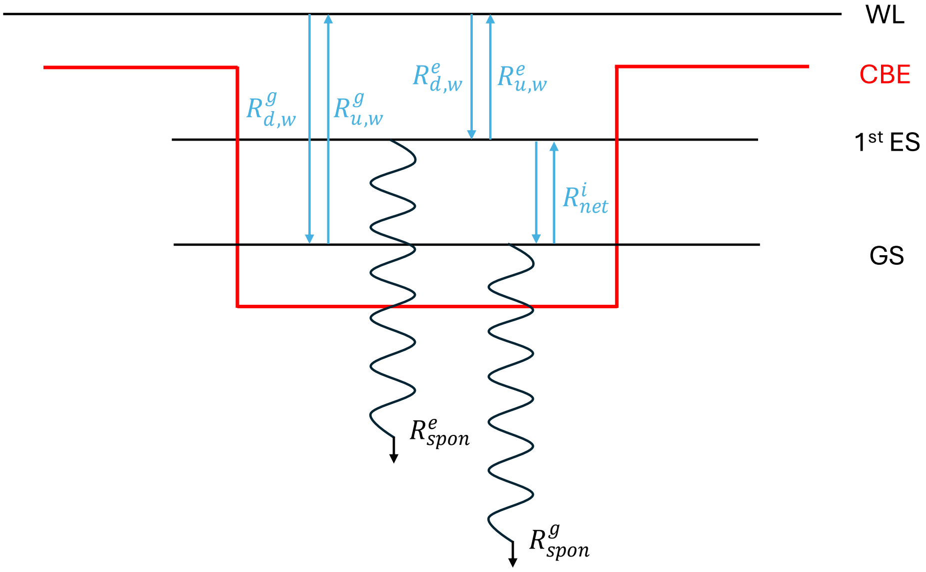

Figure 3.4: Schematic depiction of possible recombination amongst the energy level (black) of the WL and the GS and 1st ES of the QD, and the conduction band edge (CBE) (red).

Besides transitioning within the CB levels of the dot or the WL, the electron can also recombine with a hole from the VB of the dot and emit a photon, leading to radiative recombination. The assumption made by O'Driscoll et al. (2010) was that for every CB dot energy level occupied by an electron only the corresponding VB state was occupied by a hole. The rate equation for a given energy state is given by,

$$\frac{dn_i}{dt} = R^i_{d,w} f_w (1 - f_i) \gamma N_d - R^i_{u,w} (1 - f_w) f_i \gamma N_d - R^i_{spon} + R^i_{net} \tag{3.29}$$

where n_i is the carrier density for a given energy level, i, $R^i_{d,w}$ ~~$B^i_{d,u}$ is the rate constant accounting for the spontaneous emission and absorption of phonons, respectively~~ and

$R^i_{u,w}$ are the recombination rates accounting for the phonon-induced carrier capture of electrons between the dot states and the WL states. f_w is the occupation probability of the WL, γ is the degeneracy factor, N_d is the density of dots, f_i is the occupation probability of the i^{th} energy level, R^i_{spon} is the spontaneous emission rate and R^i_{net} is the net relaxation rate of recombination amongst dot states. The degeneracy factor, γ, for the 8-band k.p model is equal to 2, due to spin. The phonon rate constant for downward transitions, $R^i_{d,w}$, is dependent on the thermal phonon distribution, n^i_{th}, such that

$$R^i_{d,w} = \frac{1}{\tau_{WL\rightarrow QD}}\left(n^i_{th} + 1\right) \tag{3.30}$$

where $\tau_{WL\rightarrow QD}$ is the capture time between the WL and the dot states and n^i_{th} is given by the Bose-Einstein function,

$$n^i_{th} = \frac{1}{\exp\left(\frac{\hbar\omega_i}{k_B T}\right) - 1} \tag{3.31}$$

where $\hbar\omega_i$ is the energy separating the dot state and the WL energy, and T is the temperature. The rate constant for upward transitions, $R\cancel{B}^i_{u,w}$, given by,

$$R^i_{u,w} = \frac{1}{\tau_{WL\rightarrow QD}} n^i_{th} \tag{3.32}$$

The first two terms of Equation 3.29 are the result of the probability of a carrier transitioning from the WL into and out of the given dot level, respectively. The transition of an electron from the WL to the dot occurs only if the WL is occupied, given by f_w, and if the dot level is empty $1 - f_i$. Similarly for the transition from the dot to the WL, which can only occur if the dot level is occupied, given by f_i and if the WL state is empty, given by $1 - f_w$. The spontaneous emission rate is expressed as,

$$R^i_{spon} = \frac{2N_d}{\tau^i_{spon}} f_i \tag{3.33}$$

Where τ^i_{spon} is the spontaneous recombination lifetime for a dot. In the work done by O'Driscoll et al. (2010) [76] the spontaneous recombination lifetime was assumed identical for each dot level. The final term of Equation 3.29, the net recombination rate,

R_{net}^{i}, includes the emission and absorption of electrons recombining amongst dot energy levels, these recombination can only occur amongst states in the same dot. The intra dot recombination are directly dependent on the probability of an electron occupying a given energy level and the probability of the target energy level being empty. These probabilities can be expressed as a function of the possible microstates of the system, for a dot with two levels, the lower level i, occupied by k electrons, and a higher energy level, j, occupied by l electrons, the number of possible microstates is given by,

$$N_{(2-k),l} = \left[\frac{2!}{(2-k)!\,k!} f_i^{2-k}(1-f_i)^k\right] \times \left[\frac{2!}{(2-l)!\,l!} f_j^{l}\left(1-f_j\right)^{2-l}\right] \tag{3.34}$$

Therefore, if downward transitions amongst dot levels are allowed, they can only occur when the lower level is empty and the higher level is occupied, within the same dot. The downward transition rate can then be expressed as follows,

$$R_{(2-k),l} = \left\{\left[2\left(\frac{2-k}{2}\right)\frac{l}{2}\right]\left(\frac{1}{\tau_d^{21}}\right)\right\} N_{(2-k),l} \tag{3.35}$$

Where τ_d^{21} is the lifetime of the carrier occupying the higher energy level transitioning to the available lower energy level due to phonon interactions. The total downward transition rate is then given by the sum over all microstates (k, l). Following the same logic, the upward transition rate can be identified, where the higher energy level has at least one empty state and the lower energy state is occupied by at least one electron. The net recombination rate, R_{net}^{i}, is then given as the sum of all downward transitions of carriers into the i^{th} dot state minus the sum of all upward transitions out of the i^{th} dot state. The upward rate is inversely proportional to the τ_u^{12} lifetime of the transition. The lifetimes of these transitions are related to the lifetime for spontaneous phonon emission, τ_0^{12}, such that,

$$(\tau_u^{12})^{-1} = (\tau_0^{12})^{-1} n_{th}^{12}$$

And,

$$(\tau_d^{21})^{-1} = (\tau_0^{12})^{-1}(n_{th}^{12} + 1)$$

Under steady state conditions, the occupation probability of the energy levels of the CB in the dot can be identified. This leads to a set of coupled non-linear equations, whose roots are solved for using the Newton-Raphson method. The roots represent the occupation probabilities of the energy states in the CB of the dot, needed for the identification of gain. The number of roots to be solved for is equal to the number of available CB energy levels in the dot.

3.3. Measurements for Model Validation

The ability to simulate electro-optic devices allows to speed up their design, optimisation and fabrication [77,78]. However, they are only able to do so as they have proven to be able to replicate experimental measurements. Therefore, to be able to claim a functional model, it has to be validated. For the simulation of gain and absorption of QD material, this validation is done using the segmented contact method (SCM). The SCM is a gain and absorption measuring technique relying on the identification of amplified spontaneous emission (ASE) emitted from a given structure where the area of pumping is changed in a controlled fashion. Methods based on changing pump length allow the identification of modal gain and absorption for both the TE and TM polarization.

3.3.1. Gain Measurements

Gain is defined by the fractional change in energy in an optical mode over a unit distance of propagation [79], this is referred to as the modal gain, G. Multiple methods of measuring gain have been established and tested. They can generally be classified into two distinct groups, round trip methods, for example the Hakki and Paoli [80] method, or single pass methods, introduced for optical pumping by Shaklee and Leheny [81]. The round trip measurements suffer from complex techniques relating the measured gain to the intrinsic current [82]. This difficulty is avoided for single pass gain measurements, using the ASE emitted from the edge of the device. Round-trip amplifications have to be suppressed for this method to identify the net single pass modal gain $(G-\alpha_i)$, where α_i quantifies the internal optical mode loss, which is the optical attenuation due to scattering and free-carrier absorption loss [83]. Edge emitting single pass methods have the advantage of identifying both TE and TM polarization, and to extract true, unamplified, spontaneous emission spectrum, which can be used to measure the overall radiative quantum efficiency [84].

3.3.2. The Segmented Contact Method

The SCM is a single pass electrical excitation method for the identification of gain and absorption in semiconductor active material. Electrical excitation is favourable as this mimics the conditions of the final device [82]. Figure 3.5, gives a simplified view of the device used for SCM measurements, where the z-direction is the growth direction, the x-direction is the propagation direction along the axis of the waveguide, and the y-direction is the plane of the layers perpendicular to the axis.

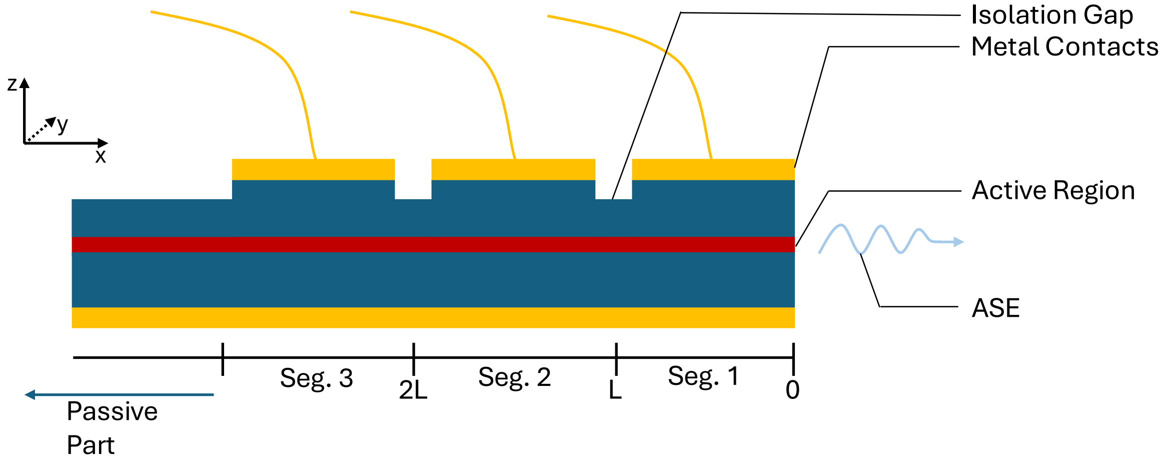

Figure 3.5: Schematical depiction of a device used for the SCM. Presenting three segments of length L that can be individually driven.

L indicates the length of a segment and the passive part is the extension of the sample, which is not pumped. The passive part needs to be long enough to absorb or scatter any light that might bounce back from the back edge facet. If reflection from the back facet remains, it can be further reduced by damaging the back facet, eliminating any and all roundtrip amplification. The isolation gap, which is a few μm long, was etched between the contacts to remove the highly conductive p-type GaAs contact layer, this reduces current leakage between neighbouring sections.

The total spontaneous emission rate for light of a certain polarization is expressed by I_{spon} per unit photon energy $(h\nu)$ per unit area in the plane of the layer, i.e., the xy-plane. With this, the emission rate within the waveguide at the end of a given stripe, originating from an element of thickness Δx after amplification over a distance x, can be expressed as follows,

$$I(x) = \beta I_{spon} e^{(G-\alpha_i)x} \Delta x \tag{3.36}$$

where β is the portion of spontaneous emission, which is coupled into the waveguide. Under the assumption that I_{spon} is uniform along the stripe, the total ASE for the given polarization created from a length L of pumped material per unit stripe width is given by,

$$I(L) = \int_0^L e^{(G-\alpha_i)x} dx = \beta I_{spon} \frac{e^{(G-\alpha_i)L} - 1}{G - \alpha_i} \tag{3.37}$$

The ASE signals $I(x)$ and $I(L)$ are given in units of photons per second per unit stripe width per unit energy interval. Equation 3.37 quantifies the internal ASE at the end of the device, thus, the ASE spectrum measured externally is given in arbitrary units by,

$$I_{meas}(L) = CI_{ext}(l) = C(1 - R)I(L) \tag{3.38}$$

where R is the reflectivity of the air semiconductor boundary at the end of the stripe and C is an extraction factor, which takes into account the light collection geometry, stripe width, spectrometer resolution, and the overall calibration factor of the measurement system. Having measured the ASE for a length L and $2L$, given by $I_{meas}(L)$ and $I_{meas}(2L)$, respectively, the net gain can be identified by rearranging Equations 3.37 and 3.38,

$$(G - \alpha_i) = \frac{1}{L} \ln \left[\frac{I_{meas}(2L)}{I_{meas}(L)} - 1 \right] \tag{3.39}$$

The same setup can be used to identify the absorption spectrum of the segmented material. This is done by pumping two segments individually. Under the condition that the device is uniform and that the current density in each section is equal. If only Segment 2 is pumped, the ASE at the interface between Segment 1 and 2 is identical to the ASE at the end of Segment 1 if Segment 1 is pumped individually, given as $I(L)$. When Segment 1 is unpumped, pumping Segment 2 allows the identification of ASE data for which a segment of the device is unpumped and absorbs part of the ASE. The ASE at the facet of Segment 1 is then given by the following equation.

$$I_{meas}(2) = C(1 - R)e^{(-A-\alpha_i)L} I_2(L) \tag{3.40}$$

Where A is the modal absorption of the unpumped gain medium. From the measured ASE of Segment 1, given by $I_{meas}(1) = C(1 - R)I(L)$, with $I(L) = I_2(L)$, the above equation can be rearranged to identify the total modal absorption of the gain material.

$$(A + \alpha_i) = \frac{1}{L} \ln \left[\frac{I_{meas}(1)}{I_{meas}(2)} \right] \tag{3.41}$$

Both the modal gain and absorption were obtained by measuring just two segments of the given sample, which makes this approach relatively quick and convenient compared to some of the other gain and absorption measurements. However, when using only two sections for the SCM care needs to be taken during sample preparation, testing, and alignment of the optical setup, as any misalignment or variation between the two measured segments leads to incorrect identifications of the absorption or gain. In this work the gain and absorption spectra of three distinct samples are identified. The segments of Sample A are 300 μm long and the segments of Sample B and Sample C are each 150 μm long. The difference in section length means that for equal current, the current density will be twice that in Sample B and C as the current density in Sample A.

3.3.3. Experimental Setup

Figure 3.6 depicts a schematic diagram of the experimental setup used for the SCM for the identification of modal gain and absorption. The device was affixed to a 16-pin header, which was mounted on a 6-axis stage. The 16-pin header could be heated, the temperature was controlled using a Thorlabs TC200 temperature controller. The device was then connected to an in-house built pulse generator, which was used to electrically pump the sections of the device. The PC controlled the pulse generators, creating the current running through the device. To avoid self-heating effects in the measurements the device needed to be driven at a low enough duty cycle, in the following work a duty cycle of 0.1 % was used, unless stated otherwise. This corresponds to a pulse width of 1 μs and a repetition rate of 1 kHz. Different sections were driven by manually switching the cables from one section to another. Once the sample was mounted, the device needed to be carefully aligned such that the only light being detected by the infrared camera was light that had propagated through the entire length of the stripe. The light was detected by a Xeva 320 series infrared camera (IR), able to measure light in the 0.9 – 1.7 μm wavelength range, which was controlled through the PC. The detection of stray light impacts the measured ASE and subsequently leads to incorrect gain and absorption measurements. To further reduce stray light an iris diaphragm was used as well as a slit at the entrance of the spectrometer.

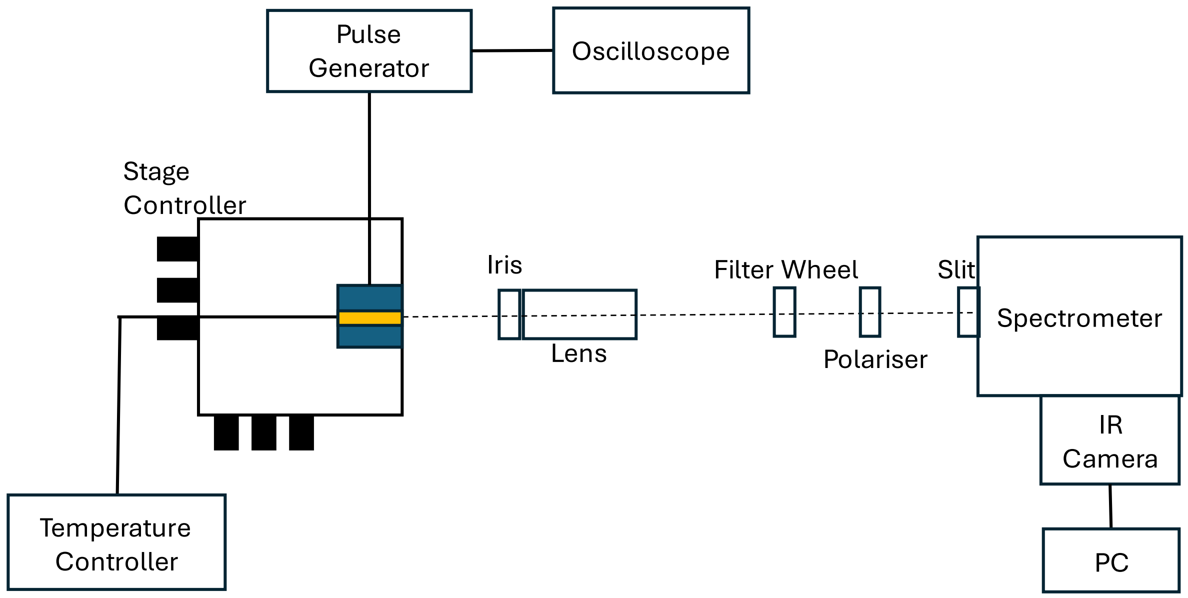

Figure 3.6: Schematical depiction of the setup used to perform the SCM.

By adjusting the micrometre knobs of the stage the device was aligned in the setup such that the output of the sample was maximised. However, to avoid oversaturation of the camera, a neutral density filter was used to adjust the strength of the ASE. The signal strength was given in counts. The camera works in the linear regime for a range between 400 to 2300 counts, exceeding this count could damage the detector, as well as skew the measurements. The polariser was set to allow only TE or TM light to enter the apparatus, for the following experiments only measurements of the TE ASE were of interest. The ASE was spectrally analysed using a monochromator, which used a diffraction grating to spatially separate the incoming ASE, which was controlled through the PC. The dispersed field strength of the ASE was displayed on the screen of the PC for a given wavelength on the x- and y-axis, respectively. The strength of the field was given in counts, leading to arbitrary units on the ASE spectrum and the integration time of the camera was set to 20 seconds.

3.3.4. Screening and Current Compensation

To ensure that the device was suitable for the SCM, two screening procedures were completed. The first one was the examination of the field profile of the emitted light of the driven device at the facet. This was to eliminate any devices, which suffered from defects that directly affect the emitted field profile, for example, defects at the facet or poor contact adhesion. A broad uninterrupted and symmetric field profile was desired, as this is an indicator of the absence of defects that might occur during sample preparation. A uniform field profile also indicated uniform propagation of the current through the structure. Example field profiles are depicted in Figure 3.7. The plot on the Left of Figure 3.7, depicts a sample with a desirable field profile, and could be used for SCMs. In contrast, in the graph on the Right of Figure 3.7, a field with an undesirable field profile is depicted, presenting a dip in the profile. This dip was most likely caused by a defect at the facet.

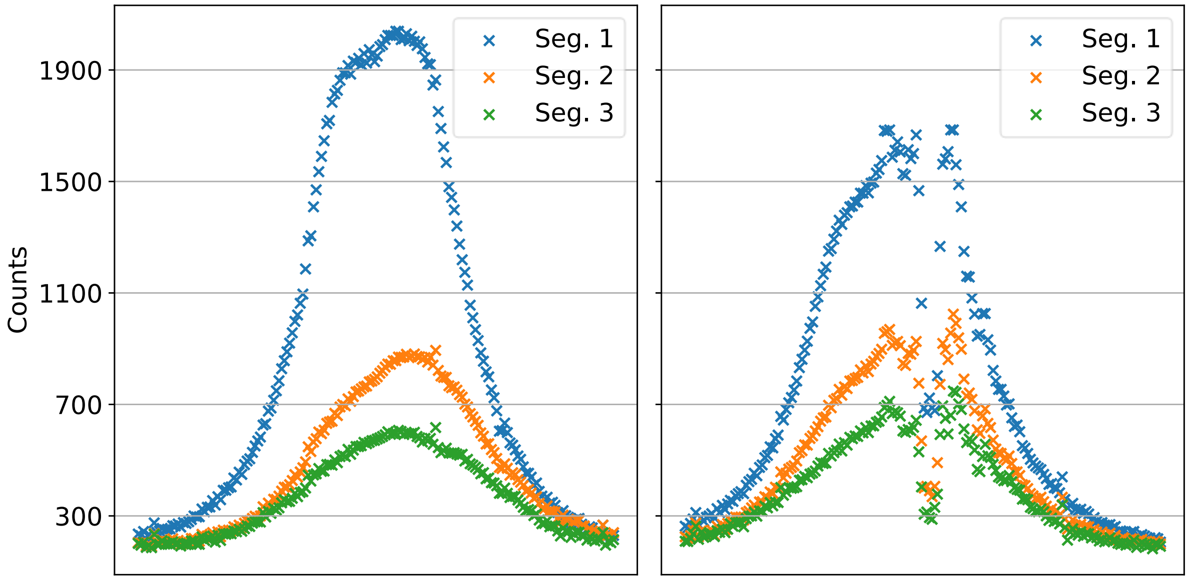

Figure 3.7: Depiction of the field profile of the different segments of a device screened for SCM.

To further analyse the material uniformity the current-volage (I-V) characteristics of the different segments of the QD device were measured. To be able to obtain a reasonable gain or absorption spectrum the I-V characteristics of at least two neighbouring sections had to match. Two segments whose I-Vs had a relative divergence of 3 % or less were deemed a match and could be used for the SCM. An example I-V characteristic can be seen in Figure 3.8, for the sections being individually driven.

Segment 1, deviates from segment 2 and 3 for currents less than 10 mA, this is most likely caused by the proximity of segment 1 to the edge of the sample. This deviation would not disqualify the use of Segment 1 and Segment 2 for SCMs, especially since the segments are nearly identical at currents larger than 20 mA.

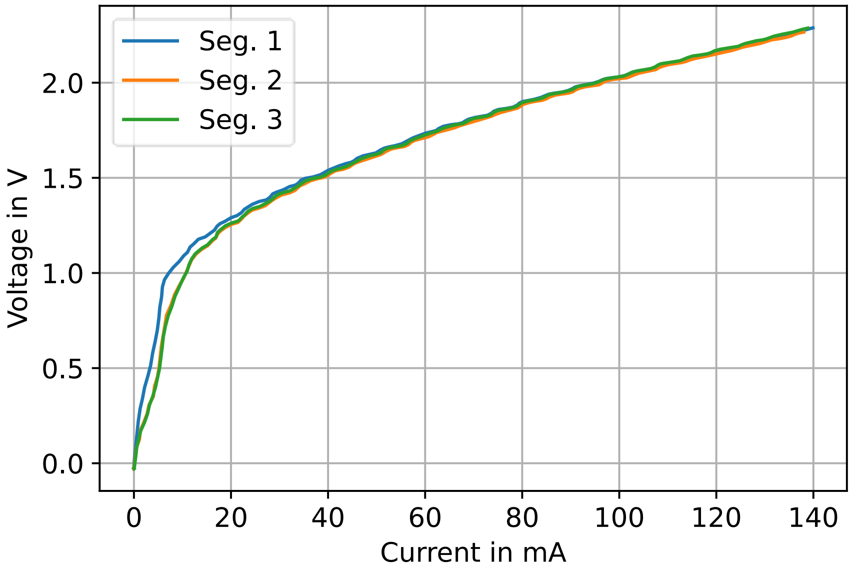

Figure 3.8: Representation of the I-V characteristics of different segments of a device screened for SCM.

The I-V characteristics were also used for current compensation, which is the process of translating the input current to an effective current. Where the effective or corrected current is the current that drives the recombination. The effective current was defined as the input current minus any leakage current[5]. While large intercontact resistance between segments and additionally grounding any segments which are not driven should in theory eliminate any leakage currents, this is not always the case. Thus, compensating for any leakage leads to a better description of the gain-current relation. In addition to identifying the effective current, this method was also used to guarantee that the two sections are effectively driven equally. The leakage current is identified based on the linear fit of the I-V curve before turn on, the leakage current is then expressed as,

---

[5] Leakage current in this context differs from the commonly referred to leakage current of minority carriers being pushed through the junction. Here it refers to current flowing that does not flow through the active region of the diode.

$$I_{leak} = m_{leak}V + c_{leak} \tag{3.42}$$

Where I_{leak} is the leakage current, m_{leak} and c_{leak} are the gradient and the intercept, respectively, and V is the voltage. An example of fitting Equation 3.42 to a measured I-V curve is given in the Left of Figure 3.9. The corrected current was identified by subtracting the leakage current from the measured current. For the SCM the input current was then identified by finding the measured input voltage for which the desired corrected current was closest to the measured input current. For example if the desired effective current was 50 mA (red cross in Figure 3.9), then the input current was 66.34 mA (black cross in Figure 3.9).

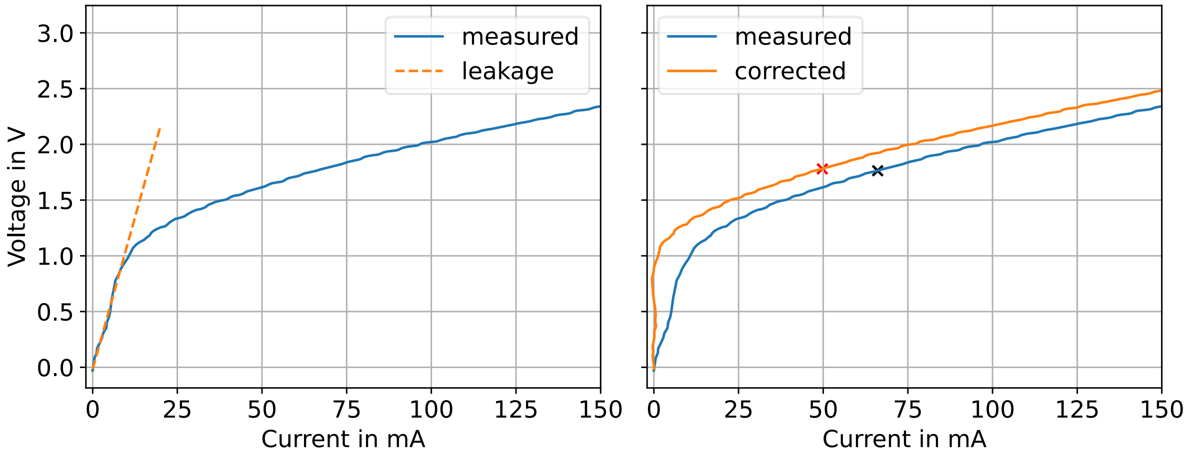

Figure 3.9: Representation of the measured I-V characteristic, including the fit identifying the leakage current (left), and the corrected current (right).

3.3.5. Result Validation

Due to the nature of the measurement, including several unknowns, such as the optimal alignment, or the uniformity of the material, the measurements needed to be validated a posteriori. This means that the same measurements needed to potentially be repeated multiple times before the correct alignment was identified. The region of the gain and absorption spectrum at energies below the bandgap energy of the active material was used to validate the measurements. In this region there should be no modal gain nor modal absorption, as no light is produced or absorbed by the active material at those energies. Meaning that at those energies the absorption and gain should converge to the internal loss of the sample. Thus, results that showed either modal gain or modal absorption at those energies were eliminated, as the setup was either misaligned, the current density was not equal in both segments, or the gain material was non-uniform. Additionally, at lower energies both the absorption and the gain should converge, thus in a scenario where for example the absorption converged to the internal loss, but the gain had not or the other way around, the results were eliminated, as there was either a problem with the alignment of the sample, a non-uniformity in the gain material, or unequal carrier densities in the two sections. An exemplar behaviour of gain and absorption spectrum converging to the internal loss of the material is given in Figure 3.10. The identified internal loss is 3 cm^{-1}.

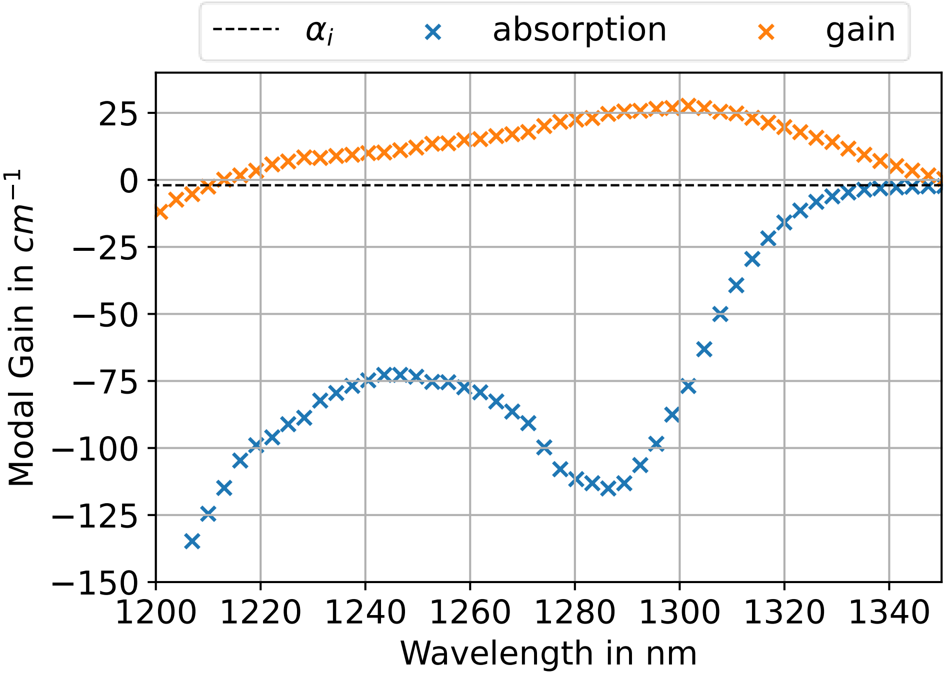

Figure 3.10: Depiction of ideal gain and absorption measurements, where the absorption is plotted as gain at no bias, and α_i is the internal loss.

An additional verification of the obtained measurements could be done by identifying the absorption of the same sample for different current densities. Although heating effects or carrier-carrier effects could affect the absorption spectrum, when the input current was only changed by a few tens of mA, the absorption spectrum should not change. Thus, obtaining equal absorption spectra for multiple current densities of the same sample could be used as an additional validation step. Furthermore, multiple devices from the same material could be tested, which should possess the same characteristics. Thus, retaking the same measurements from devices made from the same wafer could be used to further validate the measurements.

During the measurements the ASE of each segment was sampled for a given number of times. Based on this sampling the standard deviation on the ASE for each wavelength was identified. This standard deviation was then used as an estimate of the error on the ASE. When taking 300 samples the error on the ASE was too small to be visible when plotting the data. Using the propagation of errors formula [85], the error for the absorption and gain was evaluated from the error of the ASE spectra. This leads to error bars, for both the modal absorption and the modal gain, which were too small to be visible in the figures and have thus been disregarded.

3.3.6. Reverse Bias Measurements

In addition to forward and no bias, the absorption of QD material under reverse bias (RB) was measured. This was achieved using the SCM setup depicted in Figure 3.6 and including a RB source connected to the sample and the oscilloscope. An updated schematic of the SCM setup is given in Figure 3.11.

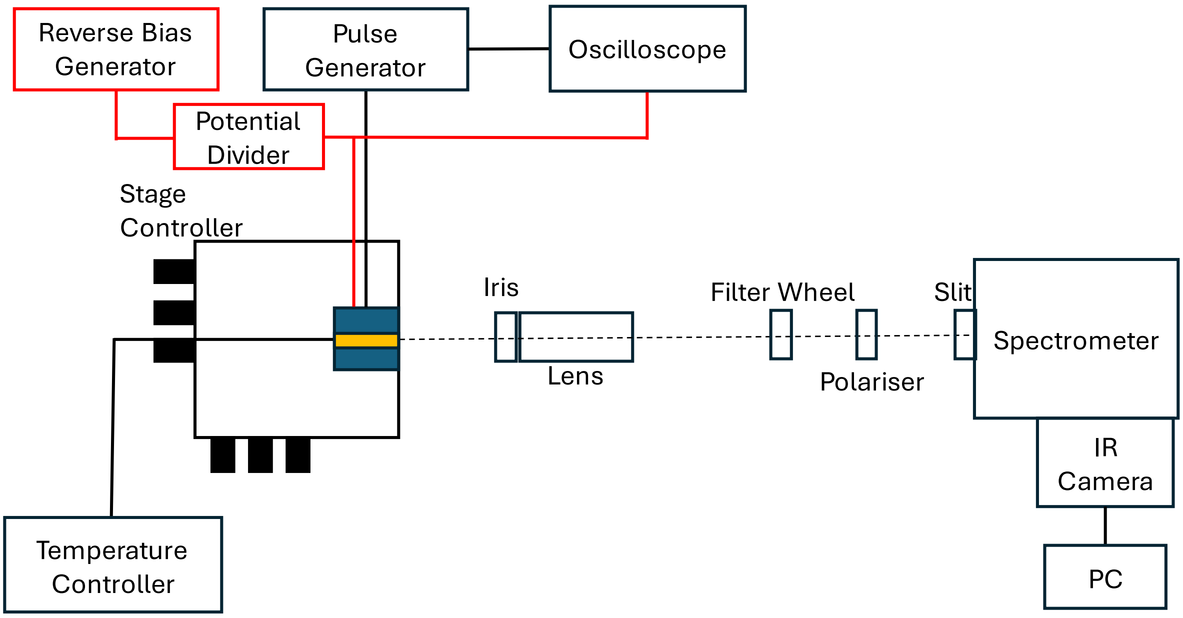

Figure 3.11: Schematic depiction of the SCM setup for reverse bias measurements.

The type of RB source had to be chosen with care, as a pulsed RB source led to significantly different absorption spectra than a direct RB source. The differences are depicted in Figure 3.12, for an applied bias of 5 V, the shift observed for the DC source was 38 nm, measuring from peak to peak, and 7 nm for the pulsed RB source. The shift is more than a fivefold higher for the DC bias source than for the pulsed bias source. The origin of those differences was attributed to heating effects caused by the DC bias source. More specifically, as the RB source was continuously pulling current from one section to another, it heated up the material, which led to an additional red shift. Thus, when using a direct RB source the expected red shift caused by the presence of an electric field was significantly overestimated, as it could not be separated from the red shift induced by the increased temperature of the dot material.

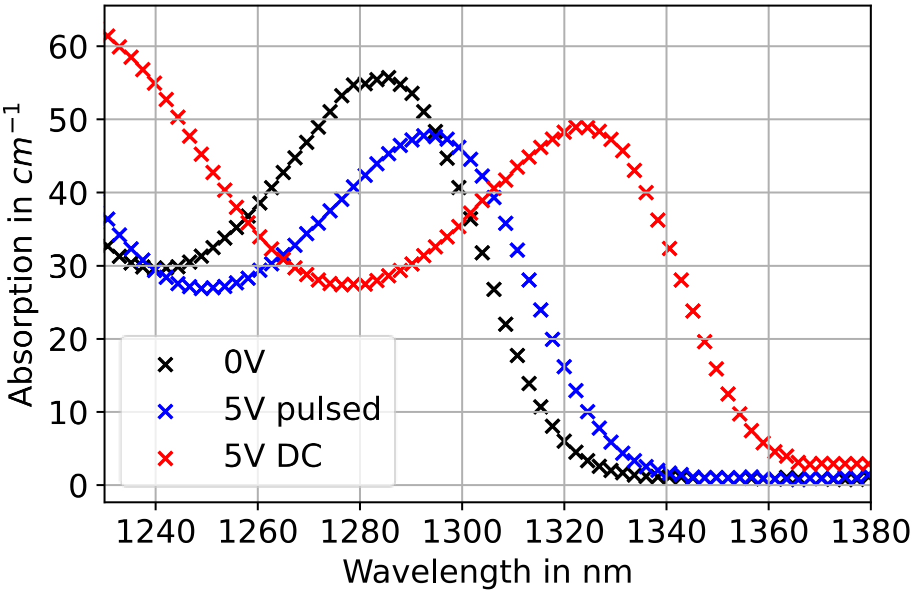

Figure 3.12: Depiction of difference in the absorption spectrum between pulsed (blue) and DC (red) RB source, for the same applied bias.

Care needed to be taken when changing from a direct RB source to a pulsed RB source. The pulsed source had a higher impedance than the DC source. This caused an issue when trying to maintain the reverse bias on one segment while forward biasing a different segment. Essentially, the pulsed RB signal across the segment significantly dropped in strength, when trying to collect the ASE of the other segment. This was caused by the higher impedance of the pulsed source in comparison to the DC source or the sample. This effect could be significantly reduced by including a potential divider at the output of the pulse RB source. As the name suggests a potential divider is commonly used to separate the voltage applied across the component, however in this case, it was used to effectively reduce the impedance of the pulsed generator. This then led to a stable RB signal on the device. A side effect of the potential divider was that the pulse RB source needed to output a significantly higher voltage to achieve the same bias strength across the segment. The equation relating the input voltage, V_{in}, and the output voltage, V_{out}, of the potential divider is given as,

$$V_{out} = \frac{R_2}{R_1 + R_2} V_{in} \tag{3.43}$$

Where R_1 and R_2 are the resistances of the resistors used to build the divider. A schematic diagram of the divider is given in Figure 3.13.

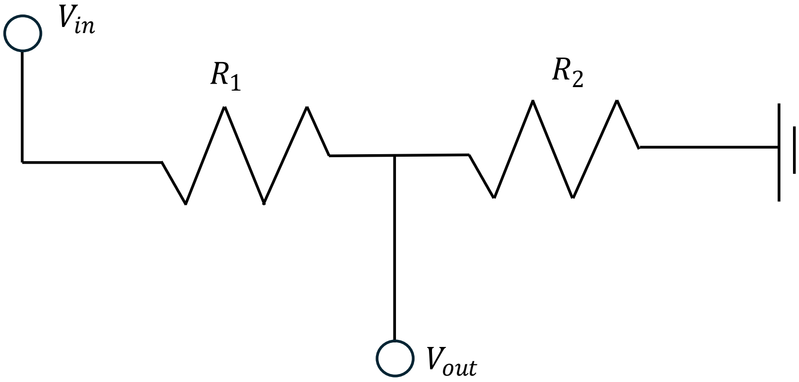

Figure 3.13: Schematic diagram of a potential divider.

For the following experiments thick film resistors, which could dissipate up to 150 W, was used, the resistance of R_1 was 47 Ω and the resistance of R_2 was 5 Ω. Thus, the input bias had to be 10.4 times larger than the output bias. To check if heating effects had been eliminated, the absorption was measured for different pulse widths. The resulting absorption spectra are depicted in Figure 3.14, which shows that the absorption hardly changed for the pulse widths of 1 µs, 5 µs and 10 µs, corresponding to duty cycled of 0.1 %, 0.5 %, and 1 %, respectively, except for a small reduction in absorption at around 1300 nm. The absorption then significantly shifts for a pulse width of 50 µs, which equates to a duty cycle of 5 %. Moreover, at 50 µs the absorption is nearly identical to the absorption measured with the DC bias source. Variations between the 50 µs and the DC bias[6] source were attributed to additional heating for the DC source, and alignment differences, which might have occurred since the measurements were not taken in the same measurement run. Figure 3.14 allows two

---

[6] In terms of Duty cycle this is equivalent to 5 % and 100 %, respectively.

conclusions to be drawn. First, it can be assumed that heating effects were successfully eliminated at 1 µs, as increasing the pulse width did not noticeably increase the red shift. Additionally, the shift in the absorption spectrum seemed to kick in nearly instantaneously, once a threshold pulse width was reached. This can be explained by the sample being allowed to cool down enough to regain its original state for short pulses. This is not the case for wider pulses. In this case the sample reaches a maximum shift leading to only minor additional changes when using a continuous RB.

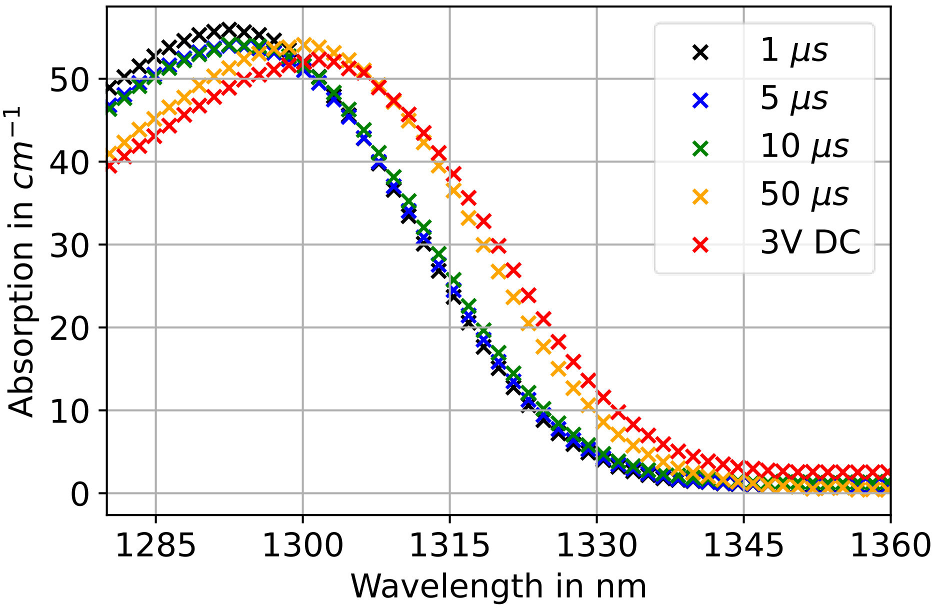

Figure 3.14: Depiction of the absorption under 3V RB for different pulse widths.

3.4. Summary

The implementation of the continuous mechanical strain using a staggered grid finite difference method was described. The identification of the piezoelectric potential from the identified strain field was detailed. The 8-band k.p model was established, exploring the discretisation needed to allow the use of the 8-band model for heterogeneous systems. Additionally, the appearance of spurious solutions was discussed as well as how to eliminate them for a finite difference model. Furthermore, the model for the identification of the occupation probability in the dots was described. The focus then shifts from the numerical implementation to experimental measurements. Discussing in detail the SCM and its use for the identification of modal gain and absorption. This included the theoretical background of the SCM, as well as the description of the experimental setup and the process of validating the obtained measurements. The changes made to the SCM setup allowing for accurate reverse bias measurements was also discussed, supported by measurements proving the suppression of heating effects.

4. **Simulating Absorption and Gain of Undoped InAs Dots Grown on GaAs**

The method leading to the simulation of modal absorption and gain spectra of InAs QDs on GaAs structures is described. This is achieved by combining the description of individual dots with the entire epitaxial structure. The results of the Strain solver, Schrödinger solver and Piezoelectric solver are presented and discussed. The reliability of the final absorption and gain spectra depends on the accuracy of the individual solvers. Each solver is independently tested and validated, and the resulting simulated spectra are subsequently compared with experimental measurements. Due to the inherently random nature of QDs the dot ensemble is calibrated to a single set of measurements before being used to simulate the gain and absorption of two more QD epitaxial structures. The calibration process is detailed and the results from the calibrated model are reported and discussed. The simulated modal gain and absorption spectra are directly compared to three distinct samples, resulting in good agreement between the implemented model and measurements.

The simulations in this chapter were run on a laptop with 32 GB of RAM and a 12th Gen Intel Core i7 processor, as well as a desktop computer with 128 GB of RAM and a 14th Gen Intel Core i9 processor. The strain and piezoelectric potential simulations took a few minutes to run, for a step size of 1 nm, and a simulation window of roughly 60 by 60 by 50, on both the laptop and the desktop computer. The 8-band k.p simulations took between 3-4 hours to run per QD, for a step size of 1 nm and a simulation window of roughly 40 by 40 by 30, using the desktop computer. A 1 nm step size was selected because it provides the required accuracy while keeping the simulation time manageable for individual dots. A smaller step size would significantly increase the compute time, a larger step size would lead to inaccurate simulation results. This is discussed in more detail in Section 4.1.4.

Photon Design's mode solver FIMMWAVE was used to identify the optical modes of the different QD epitaxial structures, which was then used to identify the modal absorption and modal gain. Photon Design's diode solver Harold was used to identify the occupation probability of the WL of the different samples, which were then used to identify the gain of the samples.

The QD sample investigated in this chapter were grown by UCL and by IQE using an MBE reactor. The contacts on the SCM samples were deposited by Dr. Sara-Jayne Gillgrass. Further sample preparation, which included cleaving the metal plated wafer and wire-bonding the cleaved sample to a 16-pin header, to which the sample was glued onto using silver epoxy, was conducted by Susanna Power and Noor Albittar.

4.1. Simulations of Individual Dots

To model an individual dot three distinct solvers were used, these are the Strain solver, the Piezoelectric solver, and the Schrödinger solver. Each of these solvers had to be validated separately to guarantee an accurate simulation of the modal gain and absorption spectra. The validation process relied on the physical understanding of the implemented theory, i.e., were the simulations physically reasonable and did they agree with what was expected from theory? Moreover, the simulated strain tensor, piezoelectric potential, energy levels and wavefunctions of individual QDs were compared to simulations conducted in the Literature.

The starting point for each solver was the physical representation of the individual dot. The most common description used for the shape of a QD in Literature is that of a lens or a pyramid. Thus, the model was set up to support either of these shapes. An example 15 nm wide and 5 nm high lens and pyramid are depicted in Figure 4.1, which include a 1 nm thick wetting layer (WL) as well as a 2 nm and 5 nm thick $In_{0.16}Ga_{0.84}As$ layer below and above the dots, respectively. These structures are commonly referred to as dots-in-a-well (DWELL) as the dots are surrounded by QW layers, which were in this case the $In_{0.16}Ga_{0.84}As$ layers. DWELL structures are commonly grown to reach wavelengths of 1.3 μm. The additional $In_{0.16}Ga_{0.84}As$ layers reduce the strain on the pure InAs used to grow the QDs, this allows for the growth of larger dots, which emit at longer wavelengths.

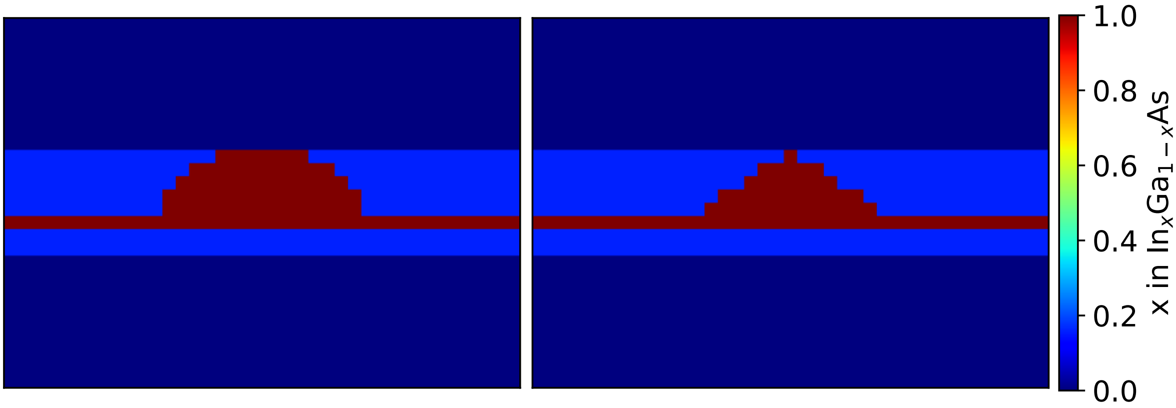

Figure 4.1: Schematic depiction of the discretised lens-shaped dot (left), and pyramid-shaped dot (right), sliced vertically through the middle of the structure.

For equal structural description, i.e., for an equal height and base width, the pyramid occupies a smaller volume[7]. The discretised dot description stores the material and strain information at each node, which were required as input values for the Strain, the Schrödinger, and the Piezoelectric solver. Unless stated otherwise the step size chosen for the discretisation of the model was 1 nm in all three directions. This step size was chosen to balance accuracy and compute time. More detail on the impact on accuracy as a function of step size is given in Section 4.1.4. The material parameters were extracted from the extensive Literature review by Vurgaftman et al. (2001) [57]. For ternary materials the material parameters were identified using a simple linear interpolation scheme,

$$p(A_xB_{1-x}C) = x \times p(AC) + (1-x) \times p(BC) \tag{4.1}$$

Where p is the material parameter of a given binary material AC, or BC, and x is the concentration of element A.

4.1.1. Validation of the Strain Solver

The strain field of the individual dot needed to be known for the identification of the deformations of the CB and the VB edges, which were inputs to the Schrödinger solver, and the Piezoelectric solver. The strain simulations were validated against the simulations done by Grundmann et al. (1995) [86], who relied on the same continuum

---

[7] For equal base and height the volume occupied by a pyramid shaped dot is $\frac{\pi}{2}$ smaller than that of a lens shaped dot.

mechanical description of strain as presented in Section 3.1. The simulated dot was described in detail, which was an InAs pyramid with a base of 12 nm and a height of 6 nm surrounded by GaAs, with a WL of 1.7 ML [86]. A direct comparison between the Literature and the implemented strain model is depicted in Figure 4.2. A step size of 0.5 nm was chosen, matching the step size selected by Grundmann et al. (1995) [86], with the dot being surrounded by 12 nm thick GaAs for the implemented model.

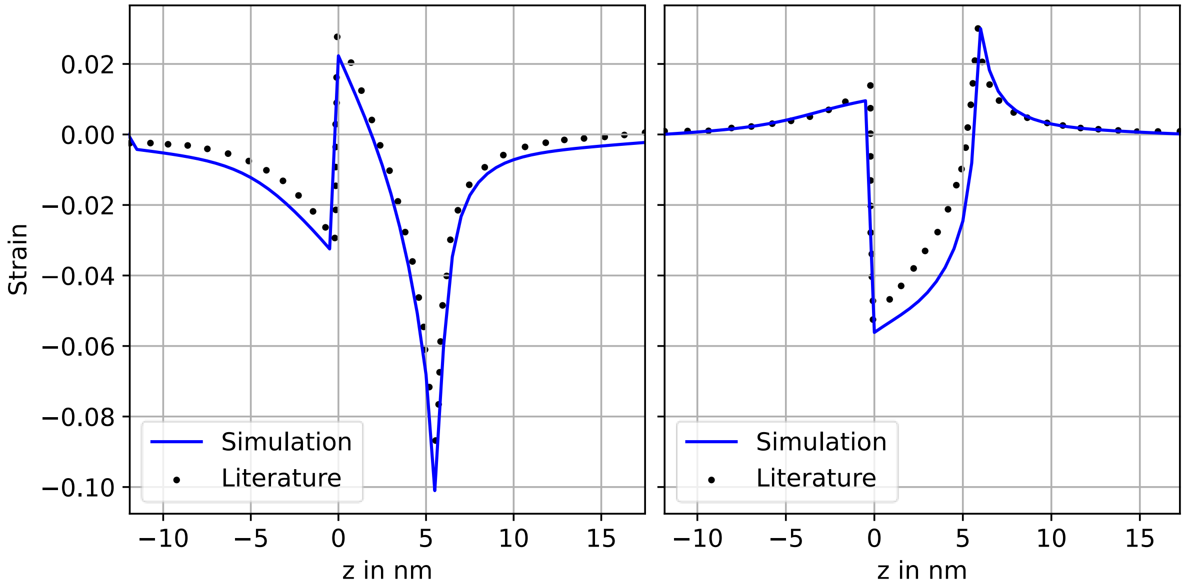

Figure 4.2: Depiction of ε_{zz} (LHS) and ε_{xx} (RHS) plotted for a line going vertically through the apex of the pyramid.

The simulations showed good agreement with the Literature employing the same theoretical framework. Small deviations were attributed to differences in the material parameters, and discretisation scheme, between the implemented model and the Literature, where the complete set of input parameters is not available.

The full strain field for the pyramid shaped dot of the above given dot structure is depicted in Figures 4.3 and 4.5. The depiction of the ε_{yy} is omitted as, due to the symmetry of the structure[8], it is identical to ε_{xx}. Here the xy-plane refers to the plane parallel to the growth direction, and xz- and yz-direction are the planes perpendicular to the growth direction.

---

[8] ε_{yy} = ε_{xx} when rotating by 90 degrees along the axis passing vertically through the centre of the structure.

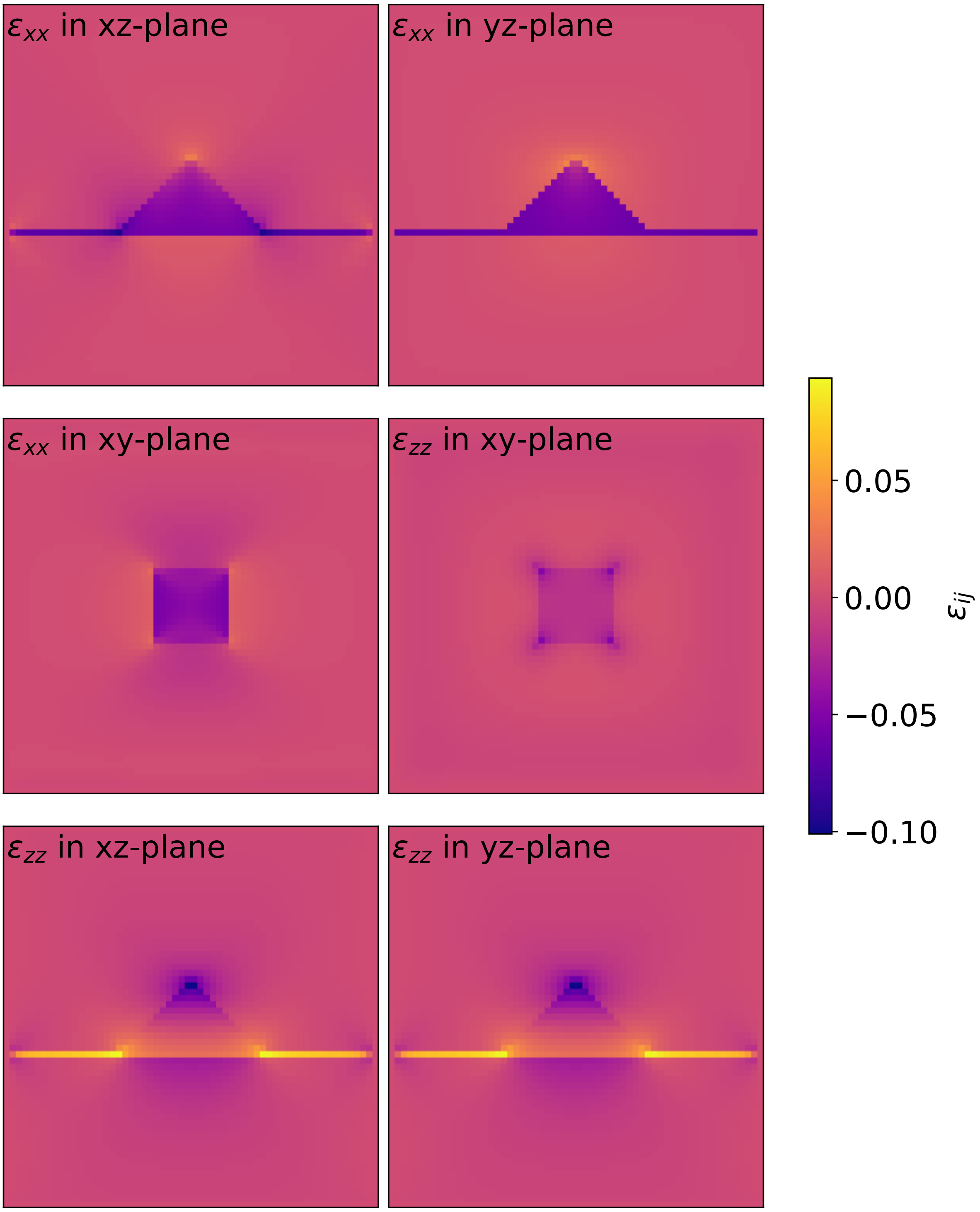

Figure 4.3: Depiction of the strain tensor plotted in the xz-plane and yz-plane going through the centre of the QD, and the xy-plane going through the centre of the QD.

The strain solver was set up such that there was a one node thick border around the computational window, visible in Figure 4.3. The strain was not identified for that region, leading to an abrupt drop to zero of the strain at the border of the dot structure. These border effects can potentially impact the overall strain of the structure. However, for an appropriate large barrier thickness, the impact of these boundary effects are negligeable. Additionally, GaAs was assumed to be the substrate material, whose lattice constant was used for the identification of the initial strain, as required by Equation 3.6.

From Figure 4.3 one can observe that the InAs atoms are compressed, in the x- and y-direction responding to the presence of GaAs. Additionally, the GaAs atoms are extended due to the presence of InAs. Compression is represented by negative strain and extension is represented by positive strain. In the z-direction the InAs atoms change from extension to compression. The WL is extended in the z-direction, and compressed in the x- and y-direction, which is commonly approximated by the pseudomorphic growth assumption, i.e., the lattice constant of the growth material conforms to the lattice constant of the substrate material. Similar behaviour of the strain in QD structures were been simulated by Belling et al. (2018) [44], who used a finite element model for the identification of the strain field. Equivalent simulations were conducted by Ahmed et al. (2015) [87], who relied on an atomistic strain model. The ability to qualitatively simulate the results obtained by different models is an indicator that the strain model was successfully implemented. While the focus lay on InAs QDs grown on GaAs, the strain solver is valid for any zinc-blende material composition or dot shape for which the necessary material parameters are known.

The main displacement, and therefore the highest strain, is located inside or in close proximity to the dot material. However, the strain also propagates deeply into the surrounding material. Plotting the hydrostatic and the biaxial strain highlights the depth of the strain propagation, as depicted in Figure 4.4. The hydrostatic strain is expressed as the trace of the strain tensor,

$$Tr(\varepsilon) = \varepsilon_{xx} + \varepsilon_{yy} + \varepsilon_{zz},$$

and the biaxial strain is expressed as,

$$Bi(\varepsilon) = \varepsilon_{xx} + \varepsilon_{yy} - 2\varepsilon_{zz}.$$

While the hydrostatic strain dissipates nearly instantly outside the dot, the biaxial strain propagates all the way through the simulated structure only slowly regaining its unstrained state. The wavelike behaviour of the biaxial strain in the x- (and y-) direction is caused by boundary effects. These can be eliminated by increasing the simulation window, as has been done for the following simulations within the work.

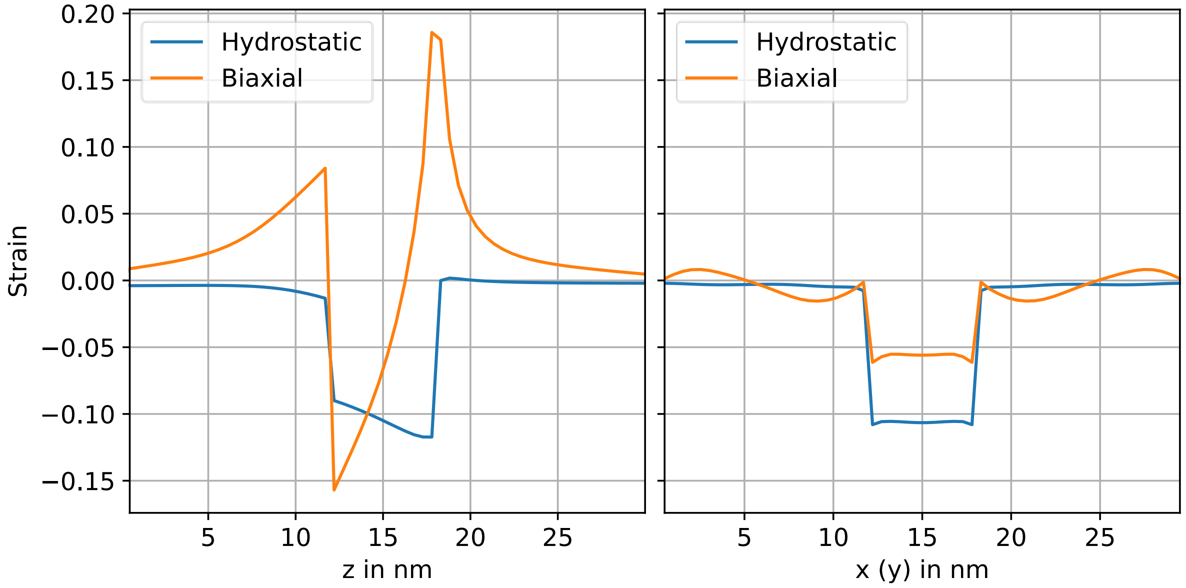

Figure 4.4: Hydrostatic and biaxial strain plotted along the axis going through the apex of the dot, from top to bottom (left) and the base of the of the pyramid, perpendicular to the growth direction (right).

The effect of the deep propagation of the strain was observed in grown QD samples, where the dot layers are separated by only a few nanometres [88]. Multiple dot layers are used to increase the effective number of dots. For these structures the dot growth can present as non-random, and is dependent on the location of the dots in the underlying layer. This is caused by the strain of the underlying dots not fully terminating, effectively reducing the strain just over the dot in the next layer. This leads to vertically aligned dots, which become larger and larger for each layer [89]. This configuration is a disadvantage if a uniform dot distribution is desired across all dot layers. This effect can be eliminated by separating the dot layers by at least a few tens of nanometres. Work done by Kim et al. (2009) [90] investigated the appearance of vertically aligned dots for varying capping layer thicknesses. Vertically aligned and randomly distributed dots were presented for GaAs capping layers of 9 nm and 49 nm, respectively [90]. The values of the capping thickness depends on the materials used during the growth. Thus, strain simulations can be used to tune the growth parameters to achieve an optimised epitaxial structure [91].

In contrast to the normal strain, the shear strain is located closer to the material interfaces, as is depicted in Figure 4.5. ε_{xy} in the yz-plane is identical to the ε_{xy} in the xz-plane, ε_{yz} in the yz-plane is the same as ε_{xz} in the xz-plane, and ε_{yz} in the xz-plane is equivalent to ε_{xz} in the yz-plane.

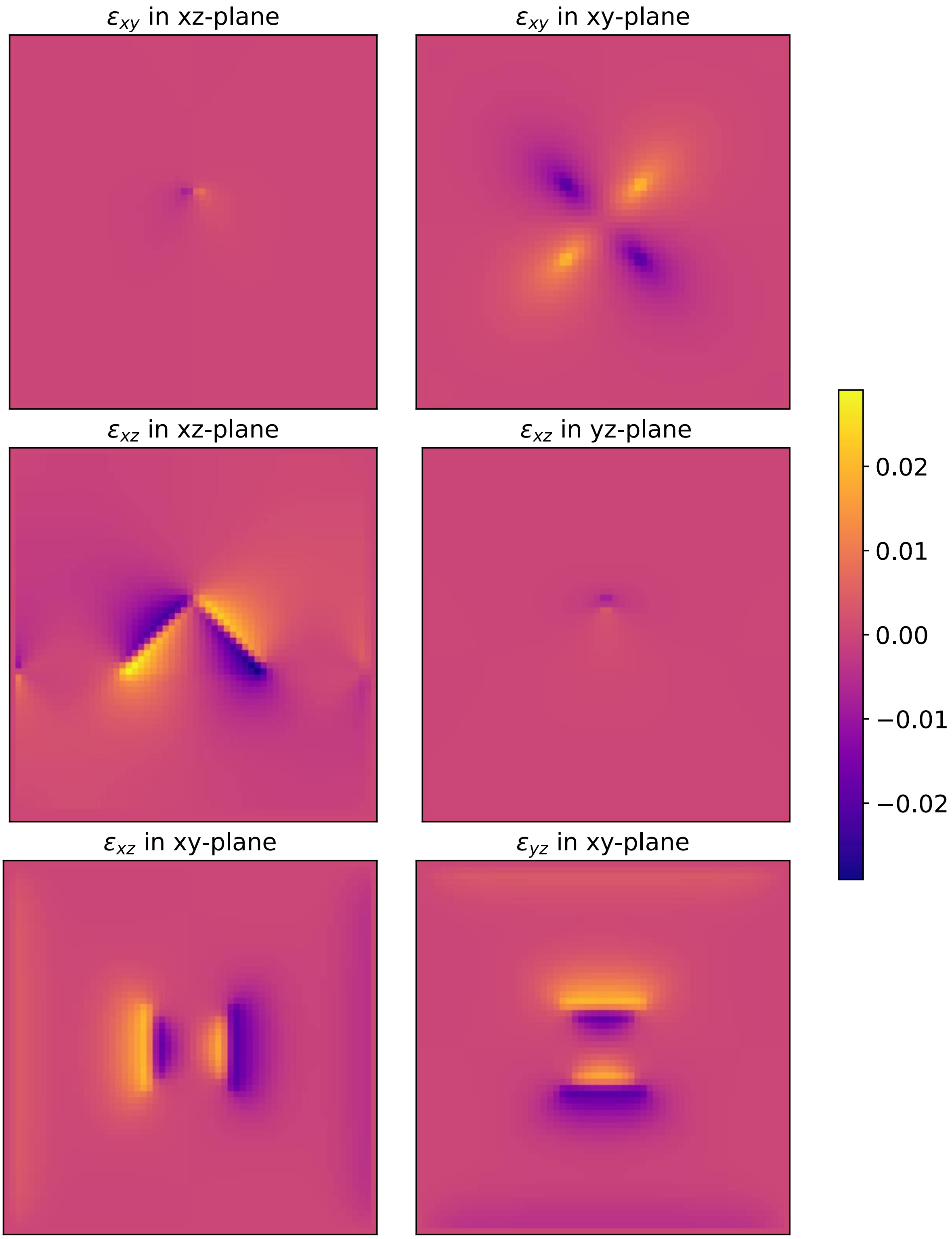

Figure 4.5: Depiction of the shear strain plotted in the xz-plane and yz-plane going through the centre of the QD, and the xy-plane going through the centre of the QD.

Once the strain was identified, its impact on the confining potential was analysed. The terms quantifying the effects on the confining potential due to shear strain and spin-orbit coupling lie on the off-diagonal of the 8-band k.p Hamiltonian. Therefore, to be able to identify the effect of strain on the confining potential, the Hamiltonian at each node needed to be diagonalised. This was not necessary for an unstrained potential, where the terms quantifying the confining potential lie on the diagonal of the Hamiltonian. The confining potential including strain deformation is compared to the strain-free confining potential in Figure 4.6.

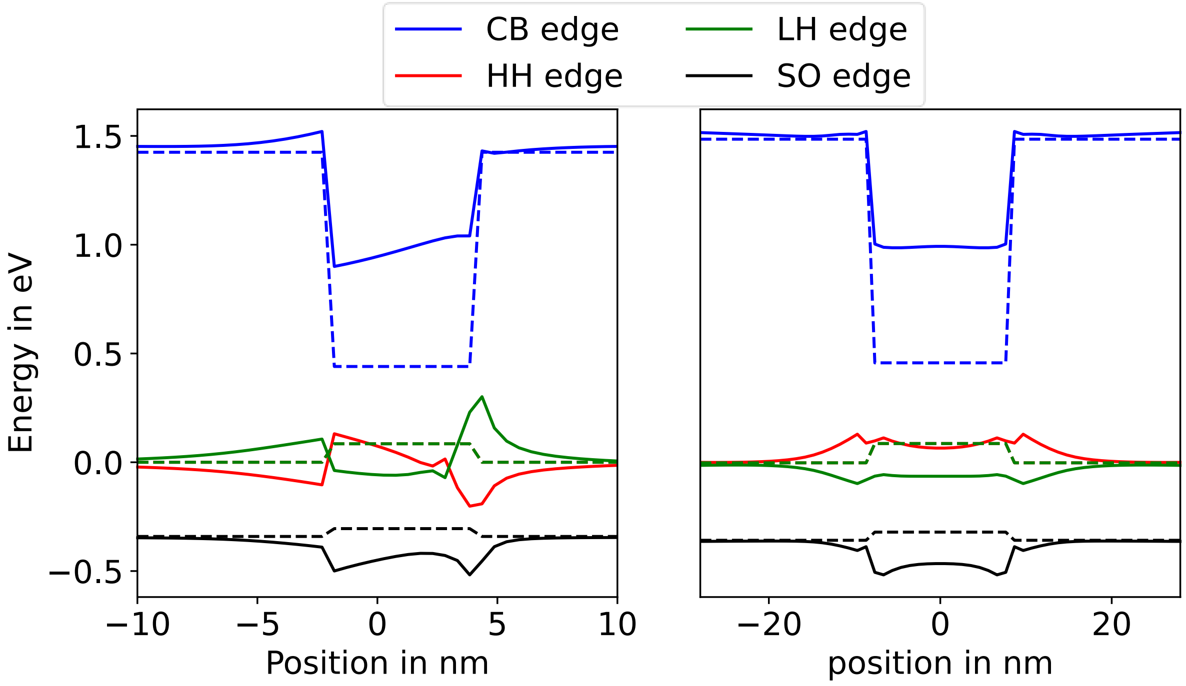

Figure 4.6: Representation of the unstrained (dashed) and strained (solid) confining potential of a dot structure. The potential is plotted along the axis going vertically (left) and horizontally (right) through the centre of the dot structure.

The piezoelectric potential was not included in the identification of the confining potential depicted in the above figure. Figure 4.6 highlights the impact of strain on the confining potential. Most notably is the impact on the bandgap, changing from 0.36 eV for an unstrained system to 0.60 eV for a strained dot. Additionally, the strain splits the degeneracy of the LH and HH bands. It should be noted that the band edges are labelled using the notion of heavy- and light-hole bands, however, due to the nature of the 8-band k.p model, band mixing is present, making the assignment of the "LH" and "HH" labels essentially arbitrary. Figure 4.6 emphasises the importance of the implementation of the strain solver to obtain an accurate representation of the confining potential of the dot structure. Not including strain effects on the confining potential impacts the possible accuracy achievable by the 8-band k.p solver.

The strain model was implemented and directly validated to the Literature for InAs on GaAs QDs. This allowed the identification of the strain field and its impact on the confining potential. While the results are only shown for InAs on GaAs QDs, the model is valid for any zinc blende material (assuming the material parameters are known).

4.1.2. Validation of the Schrödinger Solver

8-band k.p models are used to describe the energy levels and wavefunctions of individual charge carriers in semiconductor structures. In this instance they were used to quantify the confinement effect in QDs. This description was necessary to simulate macroscopic effects, such as absorption or gain spectra of the final active device.

In this section the simulation results of a 11.3 nm wide and 5.65 nm high InAs dot surrounded by GaAs, with a WL thickness of 1.5 ML were compared to the results presented by Jiang et al. (1997) [92]. The step size was set to 0.565 nm and 1.13 nm in the growth direction and the other directions, respectively. The dot dimensions and discretisation steps were chosen to be integer multiples of the GaAs lattice constant. This ensures that the model more closely reflects the atomic-scale structure of a real QD, with the material spacing in the simulation matching the uniform spacing found in the actual crystal. The strain was identified for the given description of the dot, before the energy levels of the CB and VB of the dot were simulated. The wavefunction and energy levels of the above described dot, obtained using the implemented 8-band k.p model are depicted in Figure 4.7.

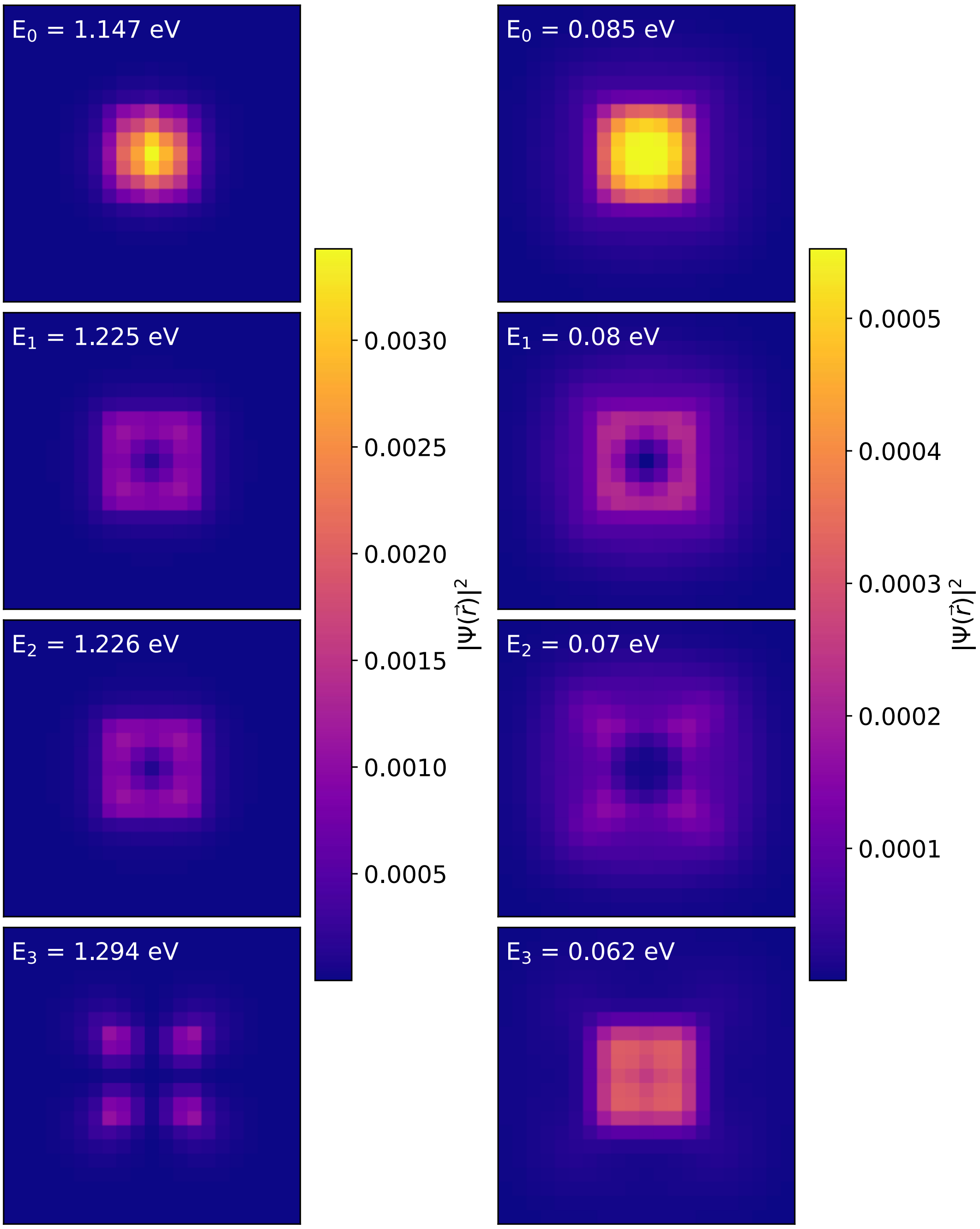

Figure 4.7: Probability distribution of the electrons in the CB (left) and the holes in the VB (right). The zero energy reference point is set to the VB edge of GaAs.

A transition energy of 1.063 eV and 1.145 eV for the ground state (GS) and the first excited state (ES) transition, respectively, was identified for the simulated pyramid-shaped dot. In comparison to the reported 1.045 eV and 1.159 eV for the GS and the 1st ES transition, respectively [92]. The authors of [92] did not report any uncertainties on the identified energy levels. Noting that while the simulated GS transition energy is larger than the energy reported in the Literature, the simulated 1st ES transition energy is lower. A discrepancy of a maximum of 18 meV was obtained from the implemented model, in comparison to the Literature. Deviations between the two models are attributed to differences in the discretisation technique, as well as the use of different material parameters. Interestingly, the Literature did not detail how, or even if, spurious solutions were encountered. This implies that different material parameters or discretisation techniques were implemented by Jiang et al. (1997) [92], which impacted the identification of the energy states. Nevertheless, the implementation of the Schrödinger solver allowed the identification of the energy levels and wavefunctions of electrons and holes in the CB and VB of a given dot structure, which qualitatively agree with simulation reported in the Literature [52,53,86,92]. While the Schrödinger solver was only validated for InAs QDs grown on GaAs, it can be used for arbitrary material compositions, and dot shapes. The solver is thus capable of reliably identifying, the energy and wavefunction of the CB and VB states, as well as the resulting transition energies, and wavefunction overlaps, for a wide range of different individual dot descriptions.

4.1.3. Validation of the Piezoelectric Solver

In addition to the confining potential deformation, the strain also induces a piezoelectric charge, which leads to a piezoelectric potential. Depending on the material the piezoelectric potential significantly impacts the wavefunction and energy level of the confined carriers. Utilising the description of the polarisation established in Section 3.1.1, the piezoelectric charge was obtained from the divergence of the polarisation, identified using a central difference discretisation and depicted in Figure 4.8. Both the linear and the quadratic polarisation were used to identify the piezoelectric charge, following the work done by Bester et al. (2006) [93], who highlighted the importance of including the quadratic part of the piezoelectricity, for a more accurate description of the piezoelectric effect.

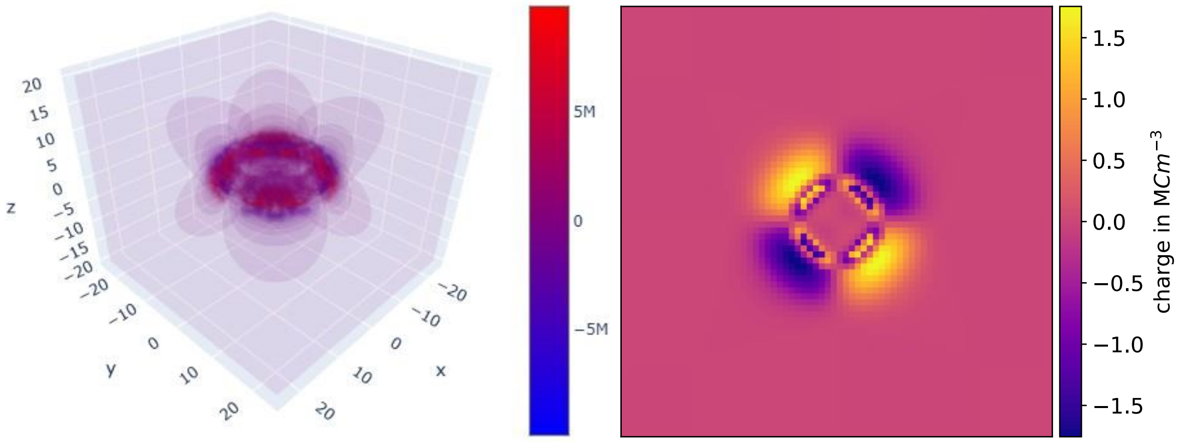

Figure 4.8: Depiction of the charge density for a lens-shaped dot (left). Slice of the charge density through the base of the dot (right).

The piezoelectric charge is predominantly located at the material interface, a direct consequence of its dependence on the shear strain. From the piezoelectric charge the potential can be identified by solving Poisson's equation, given by Equation 3.12, using a central finite difference discretisation. The resulting potential is depicted in Figure 4.9.

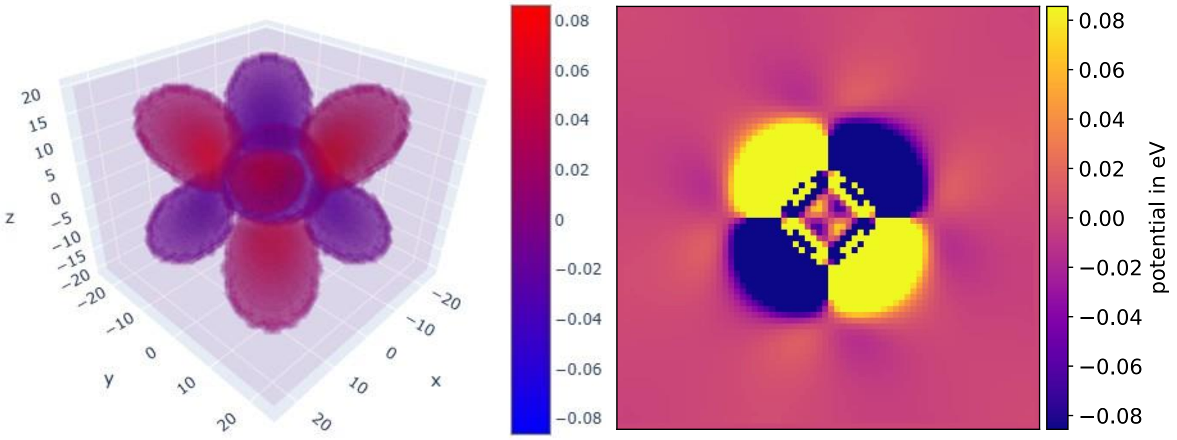

Figure 4.9: Representation of the piezoelectric potential for a lens-shaped dot (left). Slice of the piezoelectric potential through the base of the dot (right).

While the piezoelectric potential is comparatively small, with a maximum value of the order of 80 meV, leading to a small effect on the value of the confining potential, the piezoelectric potential has C_{2v} symmetry. The reduced symmetry of the confining potential impacts the symmetry of the final descriptive Hamiltonian. The overall symmetry was reduced from $C_{\infty v}$, for lens-shaped dots, and C_{4v} for pyramid- or truncated pyramid-shaped dots to C_{2v} for both lens- and pyramid-shaped dots. This impact was studied by Bester et al. (2006) [93] and by Schliwa et al. (2007) [94]. Each simulated the impact of piezoelectricity on the confining potential. Bester et al. (2006) used the linear combination of strained bulk bands model, and Schliwa et al. (2007) did not give a detailed descriptions of their dot structure, making a direct comparison between their obtained wavefunctions and energy levels and the herein implemented model impossible. However, they presented the obtained piezoelectric potential, which qualitatively agreed with the implemented model. Moreover, their overall conclusion, regarding the impact of the piezoelectric potential on the confined charge carriers was replicated. The effect of the piezoelectricity is only minor for the CB energy levels, with a maximum variation of around 3 meV. This effect is more pronounced for the VB states, with a maximum variation of around 8 meV. The piezoelectric effect is most noticeable in the shape of the wavefunctions, as can be seen in Figure 4.10, especially for the VB states. The wavefunction "loses" its $C_{\infty v}$ symmetry and assumes the C_{2v} symmetry of the piezoelectric potential. Additionally, the additional potential splits the 1st and 2nd ES, which is now separated by around 6 meV, instead of being degenerate.

While the effects on the energy levels are minimal this might only be the case for the herein investigated dot structures. Different materials can have stronger piezoelectric properties, which would lead to a more pronounced impact on the wavefunction and energy levels of the confined carriers. The established Piezoelectric solver is capable of resolving the piezoelectric potential for arbitrary zinc blende semiconductor QDs, assuming the material parameters are known.

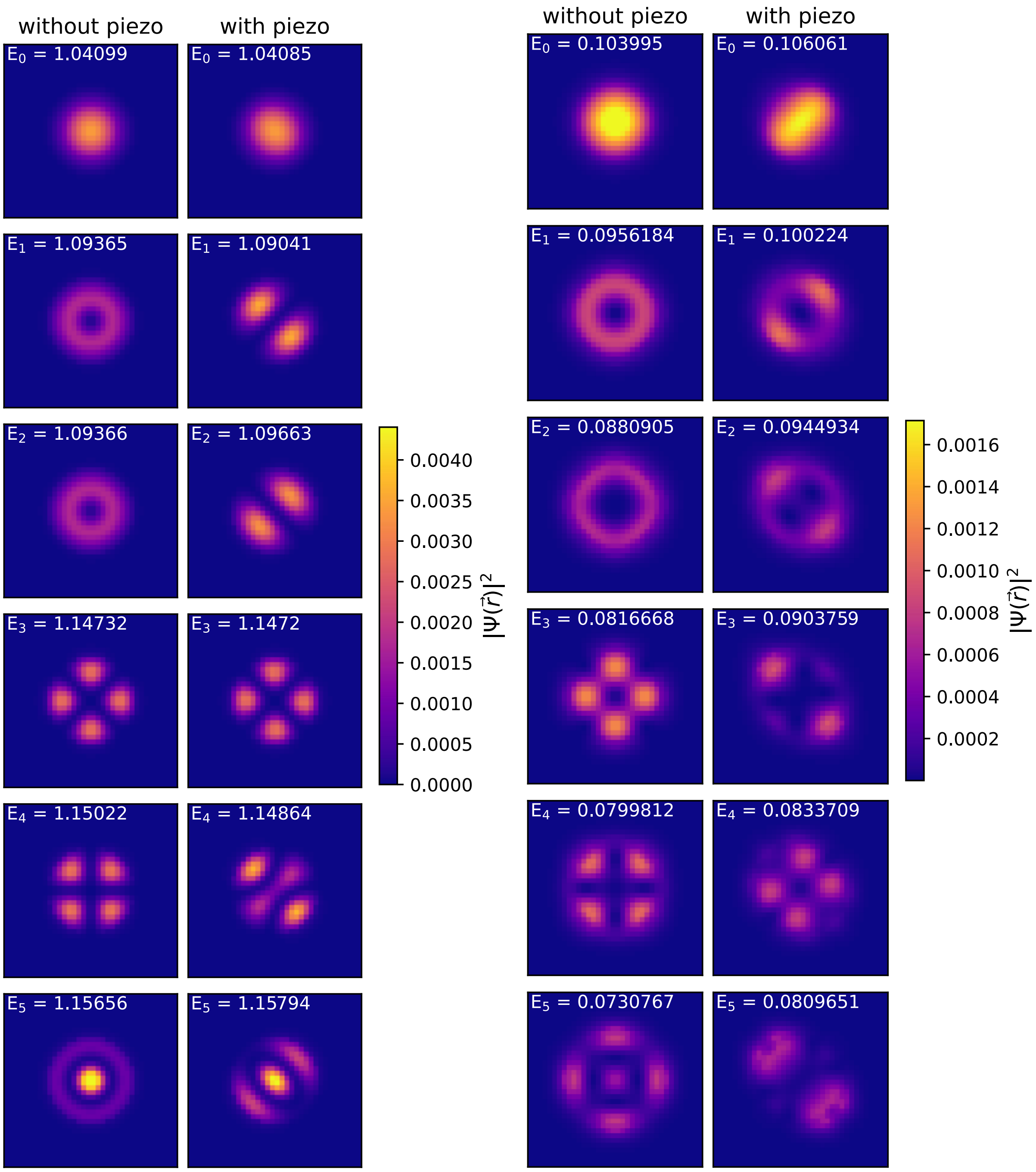

Figure 4.10: Depiction of the wavefunction of the 6 lowest states of the CB (left) and VB (right) of a 20 nm by 5 nm lens-shaped dot with (col. 2 and 4) and without (col. 1 and 3) the piezoelectric potential.

4.1.4. Additional Validation Tests

The model was additionally validated by simulating simple structures for which analytical solutions were available. This was done for the implemented QW and QD solver, for the 1D and 3D single band particle in a box. The analytical solutions of the 1D particle in a box can be solved for exactly, leading to the following expression for the energy of a confined carrier,

$$E_{1D}(n) = E_g + \frac{\hbar^2}{2m_e^*}\left(\frac{\pi n}{L}\right)^2 \tag{4.2}$$

Where E_g is the band gap of the material, m_e^* is the effective mass of the confined carrier, n is the principal quantum number, with $n = \{1, 2, 3, \ldots\}$ and L is the width of the well. The analytical solution of the energy of a particle confined in a 3D box is given by,

$$E_{3D}(n_x, n_y, n_z) = E_g + \frac{(2\hbar\pi)^2}{8m_e^*}\left[\left(\frac{n_x}{L_x}\right)^2 + \left(\frac{n_y}{L_y}\right)^2 + \left(\frac{n_z}{L_z}\right)^2\right] \tag{4.3}$$

Where L_i is the width of the box and the n_i is the principal quantum number in the i direction, with $i \in \{x, y, z\}$. The single band model was obtained from the 8-band model by setting the Kane parameter E_p to zero. This decouples the electron band from the valence bands, and eliminates any band mixing effects between the CB and the VBs. The error in the simulation was identified for a given 1D and 3D structure. The results of a 14 nm wide 1D box and of a 6 nm by 6 nm by 6 nm 3D box are depicted in Figure 4.11. For each model the reduction in the error with respect to the analytical solution decreases proportional to Δ^2, where Δ is the step size of the discretisation. This is expected for the implemented central difference discretisation scheme [95].

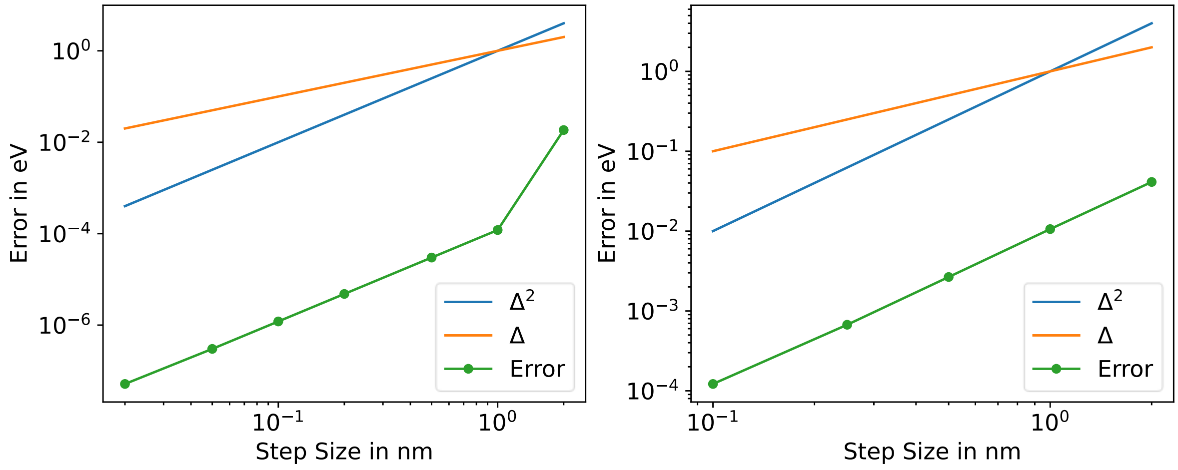

Figure 4.11: Depiction of convergence of implemented model to the analytical solution of 1D particle in a box (left) and 3D particle in a box (right).

The comparison to analytical solutions is restricted to simple structures. For band coupling, no analytical solutions exist. Confidence in the simulated results were obtained through convergence testing, which was conducted for all simulations within this work.

Numerical errors occur mainly due to two reasons, edge and resolution effects. The edge effects are caused when the simulation window is too small, such that the simulation cannot converge at the edge. For example, for the implemented 8-band k.p model, the wavefunctions should terminate fully at the edge of the simulation window. If that is not the case, the obtained results might not be reliable. This results in incorrect wavefunctions and energy levels. An exemplar wavefunction termination is shown in Figure 4.12, for a 20 nm wide and 5 nm high lens-shaped QD surrounded by GaAs.

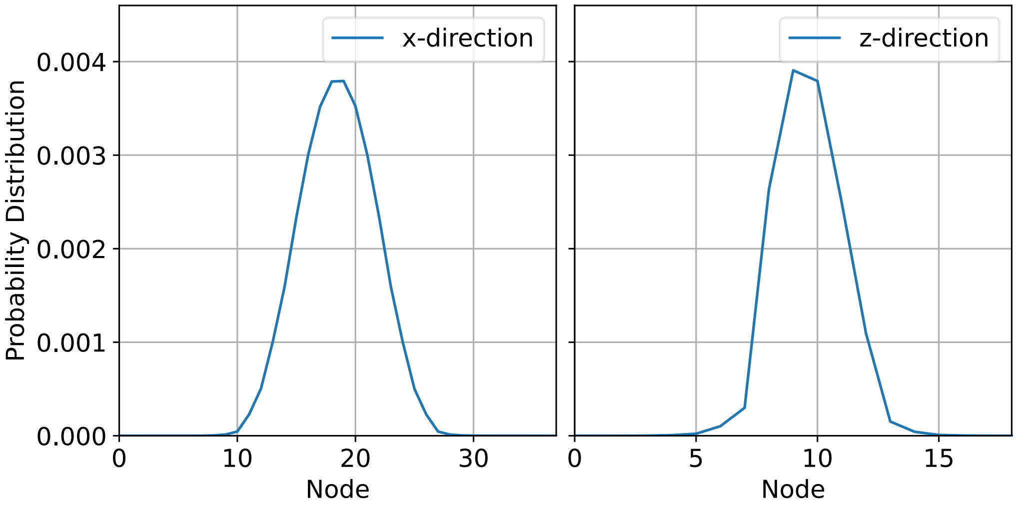

Figure 4.12: Wavefunction for a given QD along the axis going through the base of the dot perpendicular to the growth direction (left) and through the centre of the dot parallel to the growth direction (right).

Resolution effects appear when the discretisation step size is too large. The ideal step size can be obtained by simulating the same structure for different step sizes, noting the results, and observing how they change as a function of step size. Depending on the desired accuracy, the step size is then chosen such that the simulated results change less than the desired accuracy, between step sizes. For example, for the identification of energy levels of confined carriers, if the desired accuracy were 2 meV and the energy levels change by 1 meV when changing from 1 nm to 0.5 nm, then the ideal step size would be 1 nm. Ideally, this test would be done for each simulated structure; however, as this is extremely time intensive[9], the convergence can be done for a single structure, similar to those being simulated and extracting the ideal simulation parameters from the convergence test of these structures. These tests are put into place to eliminate numerical inaccuracies.

However, for the 8-band k.p simulations, increasing the resolution significantly increases the required computational resources. When these resources are not available the simulations have to run using a mesh that is too coarse. This inevitably introduces numerical inaccuracies. Test simulations for a mesh with a 1 nm and 0.5 nm step size was done to try and quantify the resulting numerical error when using a 1 nm step size. This was done for a QD which is asymmetric in the x- and y-direction. This dot lies on a 2 nm thick $In_{0.16}Ga_{0.84}As$ layer and topped by 5 nm of $In_{0.16}Ga_{0.84}As$, all of which is surrounded by GaAs. For this example the VB energies changed by ~0.5 meV and the CB energies by ~12 meV. Based on this convergence test an estimated error of 12 meV was identified for the transition energies. While this error is significant, the inaccuracies in the shape, size, and composition of the dot are more significant and a step size of 1 nm was deemed acceptable for the simulations completed in this work. This will hold for the simulations conducted in this work, as the geometries and dot sizes have not been significantly altered. If significantly larger or smaller dots are to be investigated additional convergence testing would be required.

4.2. **Description of Dot Ensemble**

Gain and absorption spectra of epitaxial structures can be used to obtain preliminary insights into the functionality of the resulting optoelectronic devices. A qualitative description of the material’s interaction with light allows the optimisation of the device’s design. For example, knowing the wavelength of the peak gain can be used to design the optical cavity of a laser such that the peak gain aligns with the optical mode. In this section, the process of identifying absorption and gain spectra from individual dots is detailed.

---

[9] Halving the step size in each direction increases the number of nodes by a factor of 8. For the implemented eigen solver, this will lead to an at least 8 times increase in compute time.

Depending on the growth, epitaxial QD stacks contain between 10^{10} dots per cm^2 and 10^{11} dots per cm^2 for each dot layer. To reduce the numerical cost only a selection of dots were simulated individually. From this given set of dots, a trend of dot size versus energy was established. By doing so the description of the transition energies of the full ensemble of dots, which might include a wide range of different dots of different size, composition, or height could be identified. This was necessary as solving the energy levels and wavefunction for each dot individually was futile, considering a single dot simulation can take multiple hours to run, depending on the size of the dot and resolution of the solver. For the example structure, the dots were assumed to be of equal height, shape, and composition, solely varying in width. The variation of dot width was assumed to be Gaussian, described by a given mean dot width and a standard deviation. Three different dot ensembles described by a mean dot width of 20 nm and of standard deviation of 1 nm, 2 nm and 3 nm is depicted in Figure 4.13. For aid of visualisation only 50 different dot widths are plotted, which would lead to a piecewise continuous absorption or gain spectrum, to obtain a smooth and realistic spectrum, at least 200 different dot widths should be used to describe the dot ensemble.

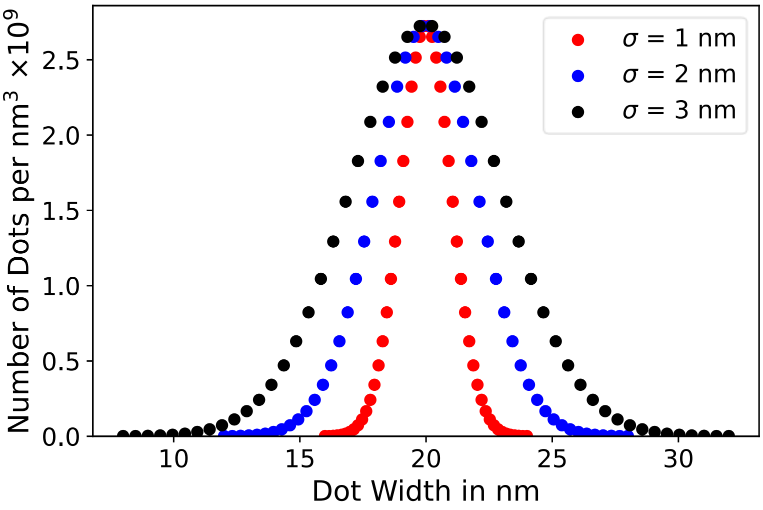

Figure 4.13: Depiction of Gaussian dot width distribution for three different standard deviations centred around a dot width of 20 nm.

To establish the relation between dot width and energy of the dot states a set of three dots were simulated. The energy of the CB monotonically decreases as the width of the dot increases, whereas the energy of the VB state monotonically increases as a function of dot width. Therefore, the change in transition energy vs dot width was fitted to the following equations,

$$ax^b \tag{4.4}$$

and,

$$aln(x) + b \tag{4.5}$$

where x is the width of the dot, and a and b are fitting parameters. Two equations have been chosen as that has led to the best fitting results. Equation 4.4 was used to fit the change in energy vs dot width of the CB states, with $b < 0$. Equation 4.5 was used to fit the change in energy vs dot width of the VB states. Care had to be taken when selecting which dots are used as the sample set. For the fitting to be as effective as possible the chosen set should cover the energy range over which the gain or absorption spectrum was identified, i.e., if the dot ensemble was set to be described by a mean dot width of 20 nm and a standard deviation of 1 nm, then a reasonable set of dot widths chosen for the simulation should be 18 nm, 20 nm, and 22 nm, assuming that the Gaussian distribution was cut-off at five standard deviations. While the above set would still require extrapolation of the energies at the tail of the Gaussian distribution, this was favourable, as dot widths at the tail of the Gaussian had a significantly lower impact on the spectrum as those closer to the mean dot width. This can be seen in Figure 4.14, where the simulated energies of dots of width of 18 nm, 20 nm, and 22 nm as well as the resulting interpolated energy and the Gaussian distribution is plotted. For an ensemble of 3 nm standard deviation, and only simulating a dot width of 18 nm, 20 nm and 22 nm requires significant extrapolation, which could lead to inaccuracies in the absorption and gain spectrum.

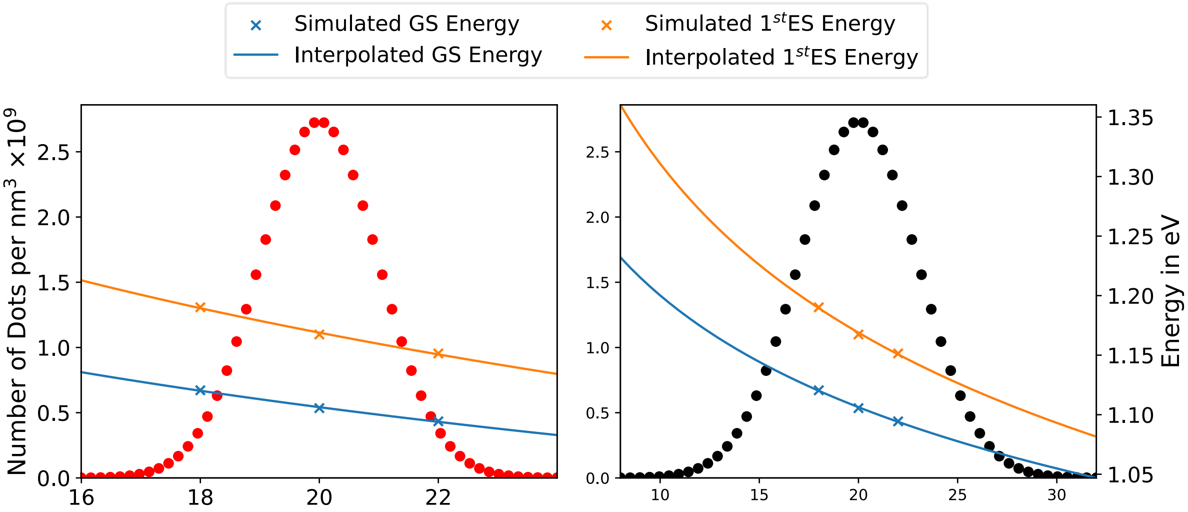

Figure 4.14: Depiction of simulated energy levels of individual dots (crosses), interpolated energy (solid line), and the Gaussian distribution of the dots in the ensemble (points) for a Gaussian distribution of 1 nm (left) and 3 nm (right).

4.2.1. Calibration of Dot Model

The description of individual dots and the dot ensemble needed to be known to be able to simulate the modal gain or absorption spectrum. However, as already discussed in Section 2.2.2, the description was not readily available. Despite this, a rough picture of the individual dots can be extracted from the available Literature. Based on various microscopy techniques, the dot widths lie between 10 nm to 30 nm wide, their height can range from 2 nm to 8 nm, the deposited dot material intermixes with the surrounding material, and the dots are most commonly described either by a lens, a pyramid, or a truncated-pyramid, and the dot density lies between 10^{10} cm^{-2} and 10^{11} cm^{-2}. This is specifically for InAs (or InGaAs) dots grown on GaAs, for functionality at 1.3 μm. Based on the vast number of free parameters that can be used to describe the dots, some preliminary assumptions had to be made, these were that the dot ensemble is described by lens-shaped dots each 5 nm high, which only vary in width, and whose change is described by a Gaussian distribution.

This dot ensemble is effectively described by the indium distribution inside the dot, a mean dot width, the standard deviation of the dot width, and the dot density. While it is possible to get a rough estimate of the dot density by leaving one of the dot layers uncapped and using AFM to scan the surface, the mean dot width, standard deviation, and indium composition of the dots cannot be known a priori. To be able to still compare the simulated results to experiments, the model had to be calibrated. The calibration entailed the identification of the dot density, standard deviation, and material composition of the individual dots.

The dot density was identified by matching the peak of the GS → GS transition of the simulated absorption to that of the measured absorption. The gain or absorption spectrum is proportional to the dot density, as depicted in Figure 4.15, for a standard deviation of 1 nm and a mean dot width of 20 nm. The 1st ES and the 2nd ES transitions are degenerate, leading to the an increased absorption at higher energies.

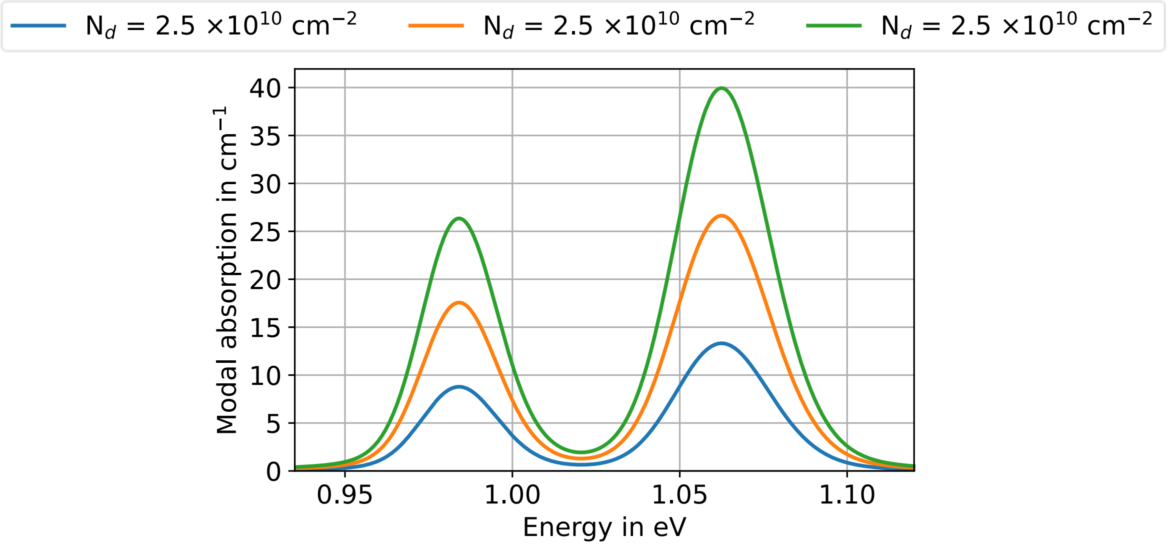

Figure 4.15: Impact of QD density on the absorption spectrum, including the GS → GS, 1st ES → 1st ES, and 2nd ES → 2nd ES transitions.

The standard deviation was identified by matching the low energy slope (slope of the GS transition peak) of the measured and simulated modal absorption, as there is no overlap with higher energy transitions. The impact of different standard deviations on the modal absorption is depicted in Figure 4.16. The absorption spectrum broadens for larger standard deviation, and the intensity of the absorption decreases.

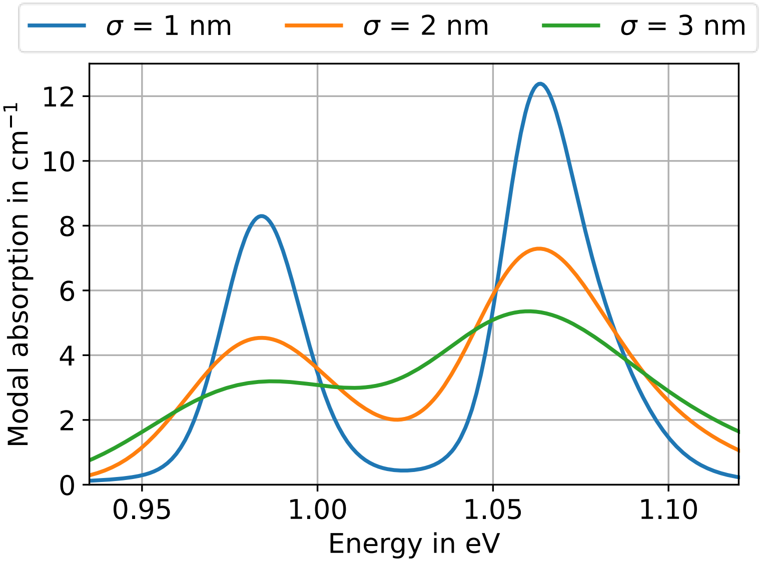

Figure 4.16: Impact of standard deviation of width on the absorption spectrum, including the GS → GS, 1st ES → 1st ES, and 2nd ES → 2nd ES transitions.

The mean width of the dot was identified such that the transition energy of the mean dot was equal to the energy of the peak of the measured GS → GS absorption peak. Increasing the mean dot width reduced the energy of the absorption peak of the GS → GS transitions, a trend depicted in Figure 4.17. The intensity of the modal absorption decreased as the width of the dot decreased, as it is dependent on the optical cross section. Additionally, the spectrum broadened as changes in the width led to bigger shifts in the energy for narrower dots, which also impacted the intensity of the absorption, with increasing absorption for wider dots.

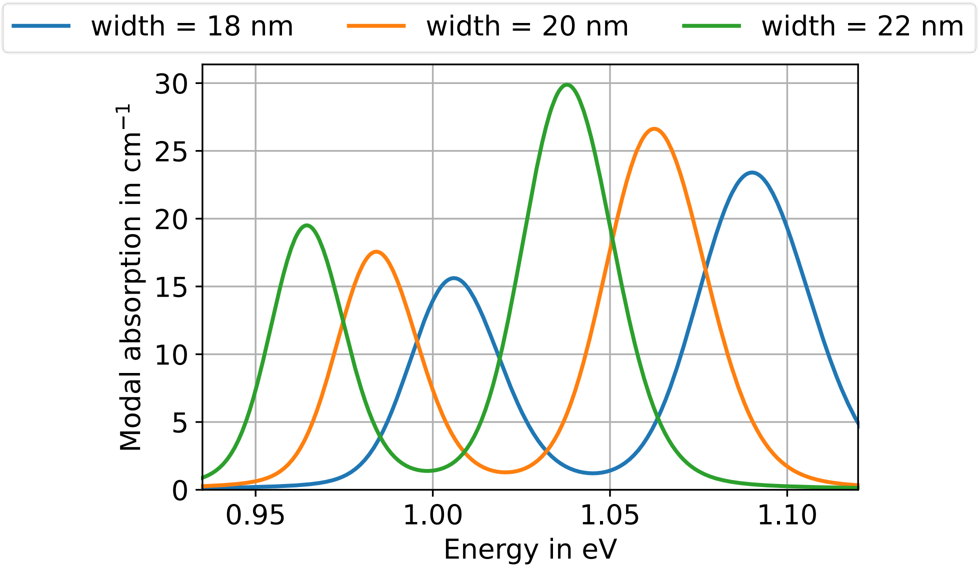

Figure 4.17: Depiction of the change in the absorption spectrum due to changes in the mean dot width, only including the GS → GS, 1st ES → 1st ES, and 2nd ES → 2nd ES transitions.

The material composition was identified based on the energy separation between the GS → GS absorption peak and the 1st ES → 1st ES and 2nd ES → 2nd ES absorption peak, referred to as peak-to-peak distance. The peak-to-peak distance is not directly linked to the material mixing, but rather to the width of the dot. However, the width of the dot was identified based on the GS → GS absorption peak, and depending on the identified width, the peak-to-peak distance could be inaccurate. This was adjusted by including material mixing effects. A kernel average smoothing algorithm was used to recreate the indium distribution of the grown dot structure. This algorithm was chosen because the distribution of indium during the dot growth was not well understood and no straightforward physical model was available; thus using a kernel average smoothing algorithm was easier and quicker to implement. Additionally, more freedom to adjust the extent of material mixing as required was obtained from the kernel smoothing algorithm. A kernel average smoother works as follows. For each node, a constant distance size (also referred to as kernel radius) is chosen, and a weighted average for all indium compositions closer than the kernel radius to the node is computed, as depicted in Figure 4.18. The larger the kernel size the more points are included in the kernel average smoothing. In the model, a larger kernel size indicates more material mixing.

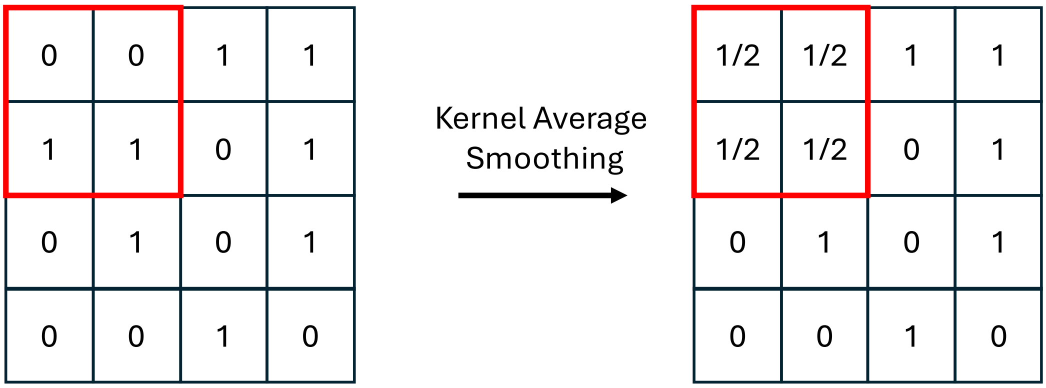

0	0	1	1
1	1	0	1
0	1	0	1
0	0	1	0

1/2	1/2	1	1
1/2	1/2	0	1
0	1	0	1
0	0	1	0

Figure 4.18: Schematic depiction of the kernel average smoothing algorithm.

Material mixing increases the bandgap of the dot material, requiring wider dots to match the measured GS → GS absorption peak, which in turn reduces the peak-to-peak distance. The effect of changes in kernel size are depicted in Figure 4.19. For comparison, the GS → GS transition energy was kept constant for varying kernel sizes. Leading to three dot ensembles described by a mean dot of width of 15 nm, 20 nm, and 28 nm. The indium distribution of the individual dots is given in Figure 4.20. As can be seen the peak-to-peak distance noticeably reduces as the kernel size and dot width increases. An additional effect is the narrowing of the spectrum due to larger kernel sizes. This is because the energy of wider dots is less affected by changes in the width, thus for the same standard deviation in width, a smaller deviation in energy is observed for wider dots.

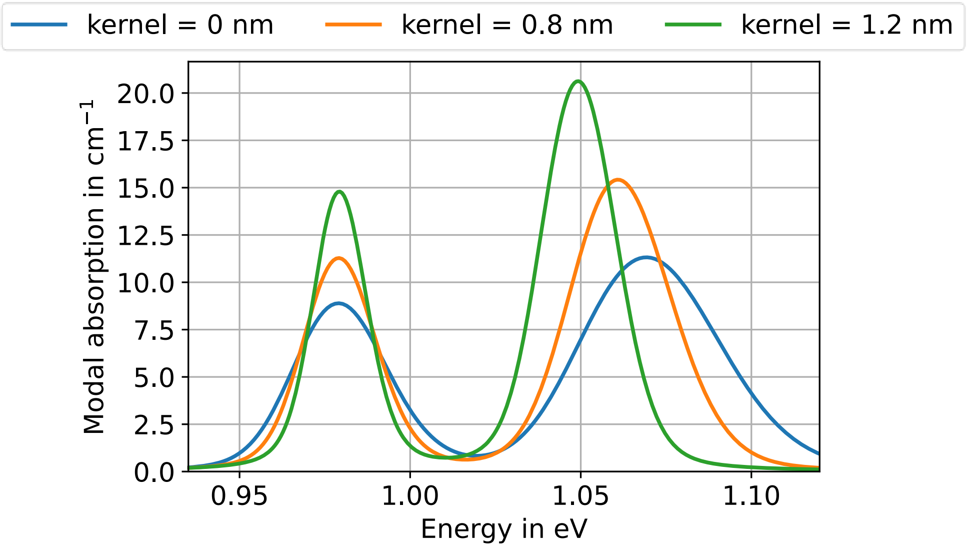

Figure 4.19: Depiction of effect on the absorption spectrum due to changes in the kernel size, only including the GS → GS, 1st ES → 1st ES, and 2nd ES → 2nd ES transitions.

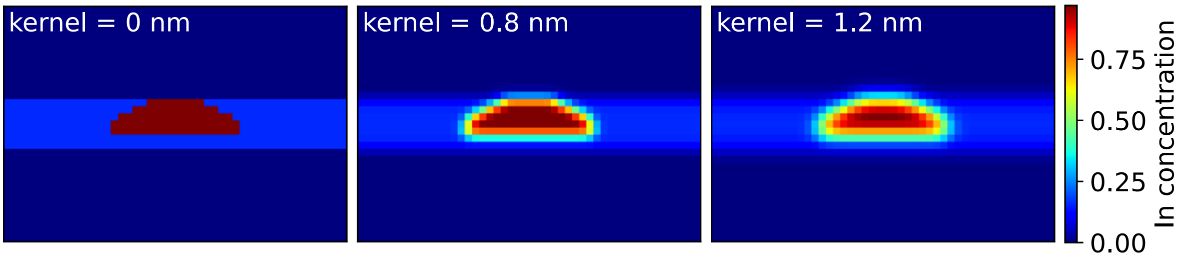

Figure 4.20: Depiction of indium distribution depending on the kernel size.

4.2.2. Simulating the Absorption Spectrum

The detailed calibration steps were used to simulate the modal absorption depicted in Figure 4.21.

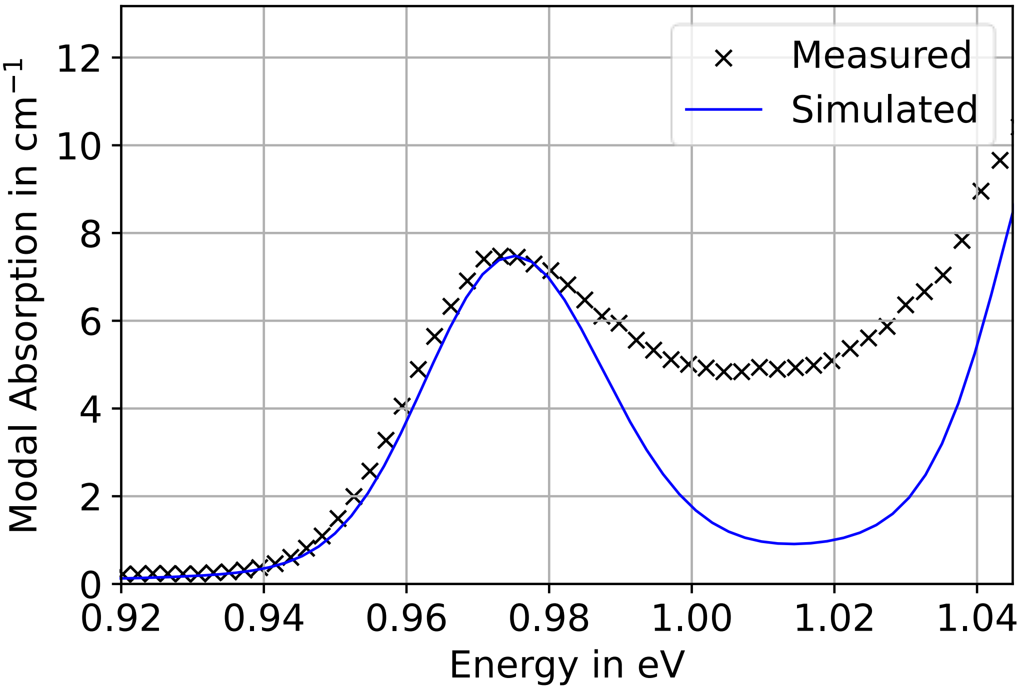

Figure 4.21: Depiction of simulated (solid line) and measured (crosses) modal absorption.

The modal absorption of the ensemble of dots in Figure 4.21 is described by a Gaussian distribution centred around a 20.9 nm wide and 5 nm high dot, a standard deviation of 1.2 nm, a dot density of 4.9×10^{10} cm^{-2}, and a kernel size of 0.8 nm. The piezoelectric effect was not included in the simulation of the individual dots. The simulated absorption only agrees with measurements for energies below 0.98 eV. A strong deviation from the measurements is visible for higher energies. The simulations predict a significant larger dip between the GS → GS and 1st ES → 1st ES absorption peaks than the measurements. Due to low signal to noise ratio (SNR) it became impossible to resolve the absorption at energies higher than 1.045 eV using the SCM. By taking edge photovoltage spectroscopy (ePVS) measurements, the absorption spectrum at higher energies can be observed, however, given in arbitrary units (a.u.), an example spectrum is depicted in Figure 4.22. The observed increase in photovoltage with excitation energy indicates that progressively higher-lying states in the quantum dots, as well as the wetting-layer (peak around 1.27 eV), become optically active.

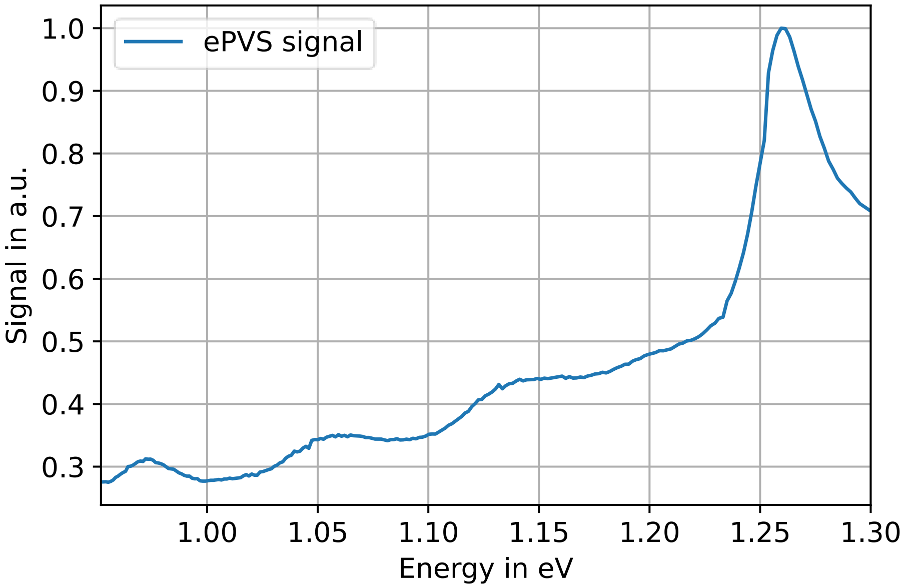

Figure 4.22: Depiction of the edge photovoltage spectroscopy spectrum of Sample A.

Two mechanisms were identified which do not present the “dip”, these are asymmetrical dots, and bimodal growth. Different shapes, such as pyramid-, truncated-pyramid-shaped, or oval-shaped dots were conducted leading to similar disagreements between measurements and simulations. Additionally, dot ensembled where the height was varied and the width was kept constant also failed to replicate the measured modal absorption. Similarly, simulations that included the piezoelectric effect did not lead to improved agreement between simulations and measurements.

“Asymmetric” is being used to describe dots which are asymmetric along the plane perpendicular to the growth plane, an example is given in Figure 4.23. This description was obtained by adjusting the ellipsoidal equation using the deformation constants, d_1, and d_2, as given by Equation 4.6.

$$d_1 \left(\frac{x}{a}\right)^2 + d_2 \left(\frac{y}{b}\right)^2 + \left(\frac{z}{c}\right)^2 = 1 \tag{4.6}$$

Where a, b, and c are the semi-axis describing the ellipsoid. The introduction of asymmetry directly impacts the wavefunction overlaps of the transitions. The change in wavefunction impacts the optical matrix element which affects the absorption spectrum.

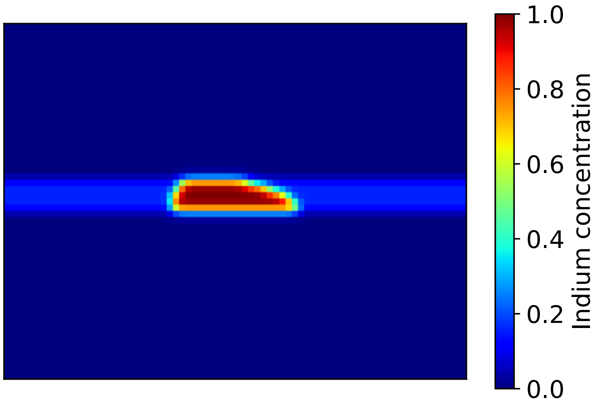

Figure 4.23: Schematic depiction of a 20 nm by 5 nm asymmetric dot and a kernel size of 1 nm.

The impact of the asymmetry is reflected in the wavefunctions, as depicted in Figure 4.24. The charge carriers favour being located in the area with higher indium concentration, thus shifting the probability distribution of the confined carriers. This will directly impact the wavefunction overlaps used for the identification of the absorption spectrum. The asymmetry also leads to a splitting of the 1st ES and 2nd ES states.

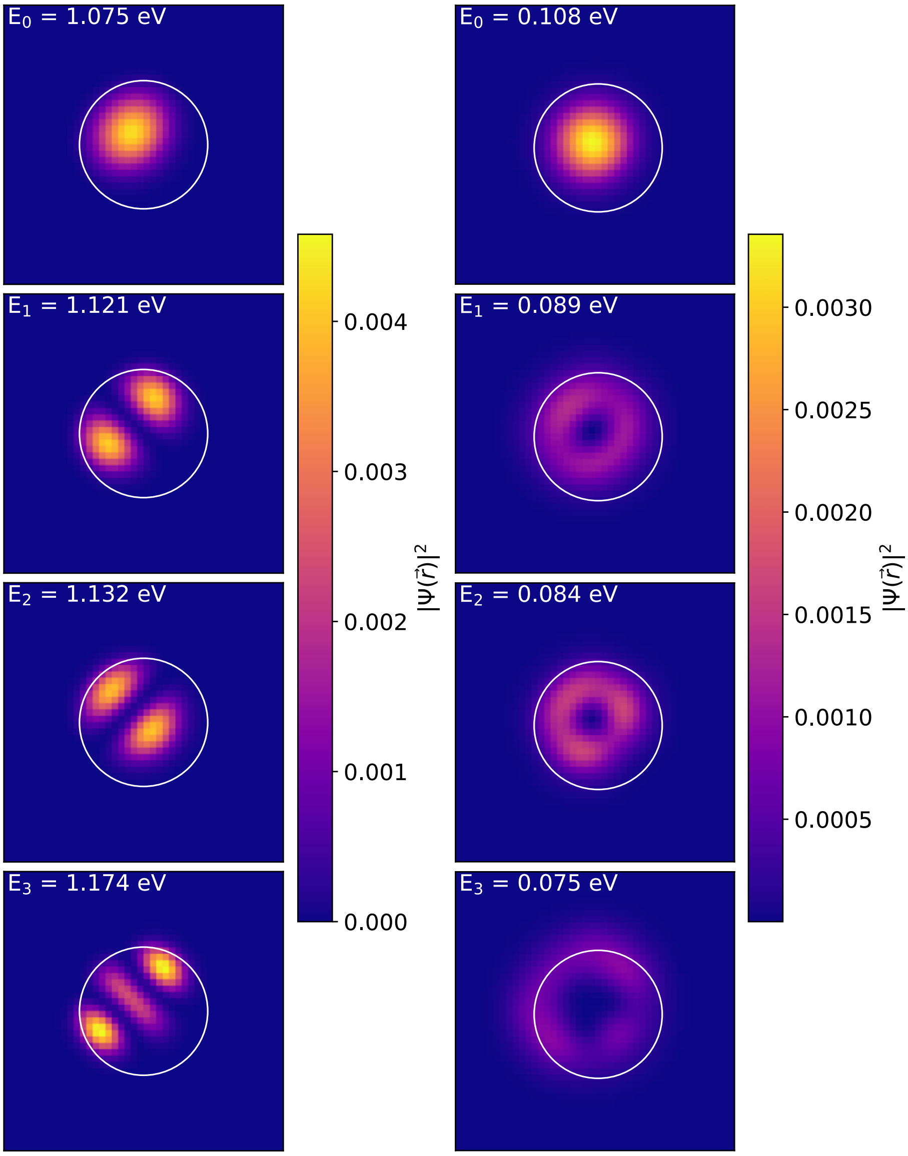

Figure 4.24: Depiction of the probability distribution of the confined carriers in asymmetric dots of electrons in the CB (left) and of holes in the VB (right). The white circle indicates the circumference of the base of the dot, used as a reference point to highlight the “shift” of the probability distribution.

In addition to having asymmetric dots, the standard deviation was increased. This lead to a worse agreement at lower energies, but improved the overall match between simulations and measurements, as depicted in Figure 4.25. The dot ensemble is described by a 22.8 nm wide and 5 nm high mean dot, a width standard deviation of 1.5 nm, a dot density of 3.6×10^{10} cm^{-2}, and a kernel size of 1 nm.

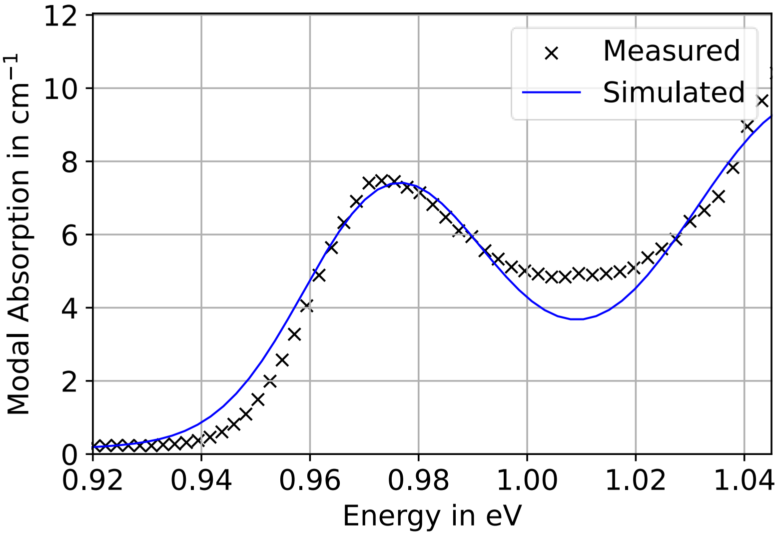

Figure 4.25: Comparison between measured (crosses) and simulated (solid line) modal absorption, assuming asymmetrical dots.

Asymmetric dots had been discussed in the Literature. Microscopic techniques, with nanometre accuracy were used and observed asymmetric dot shapes [96]. This asymmetric growth was attributed to the random nature of the dot formation [97]. Spencer et al. (2013) [98] argued that as the dots grow they transition from symmetric pyramid-shaped dots towards symmetric lens-shaped dots. During this transition, the pyramid sidewalls are covered at different times, the resulting dots become asymmetric [98]. Additionally, the formation of asymmetric dots were experimentally investigated for germanium dots on silicon [99,100].

Bimodal growth assumes that the dot ensemble can be described by two distinct dot distributions. In this instance the dot ensemble is described by two Gaussian distributions, each defined by a mean width, and standard deviation. The second distribution is then attributed with a mean GS → GS transition energy centred at the "dip". A comparison between the absorption spectrum with bimodal growth and measurements is depicted in Figure 4.26. The simulated absorption was described by two dot distributions, one given by a Gaussian distribution with a mean dot width of 17.7 nm, a standard deviation of 2 nm, and a dot density of 2.5×10^{10} cm^{-2}, and the other given by a Gaussian distribution with a mean dot width of a 21.1 nm, with a standard deviation of 1.2 nm and a dot density of 2.5×10^{10} cm^{-2}. Noting that the dot density is equal for either distribution. However, the modal absorption is larger for the wider dot distribution due to its dependence on the standard deviation.

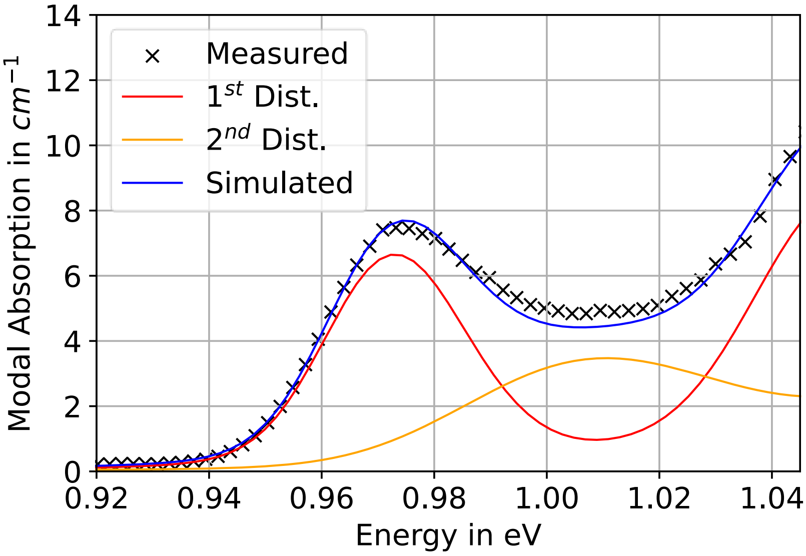

Figure 4.26: Comparison between measured (crosses) and simulated (solid line) absorption, assuming bimodal growth. Highlighting the absorption obtained from the two distributions of dots used to recreate the total absorption.

Similar to the notion of “asymmetric” dots, bimodal growth was discussed in the Literature. The appearance of bimodal growth was explained either due to the presence of two distinct dot formations [101], or due to the desorption of InAs from smaller dots by larger dots [102].

Both the asymmetric dot and the bimodal growth assumption were used to replicate the measured absorption. Neither method depicts a clear advantage over the other. Thus, one cannot conclude from the absorption simulations alone, whether the dots are asymmetric or bimodal. For each case the free parameters identified fall within the values expected from the Literature.

A match between a single set of measurements and a calibrated simulation is not decisive, to further validate the implemented model two more samples were characterised and compared to simulations, depicted in Figure 4.27 and Figure 4.28. The epitaxial structure of Sample B and C are depicted in Figure 4.29. For each simulated sample, the same set of dots have been used, adjusting the dot density, standard deviation and dot width.

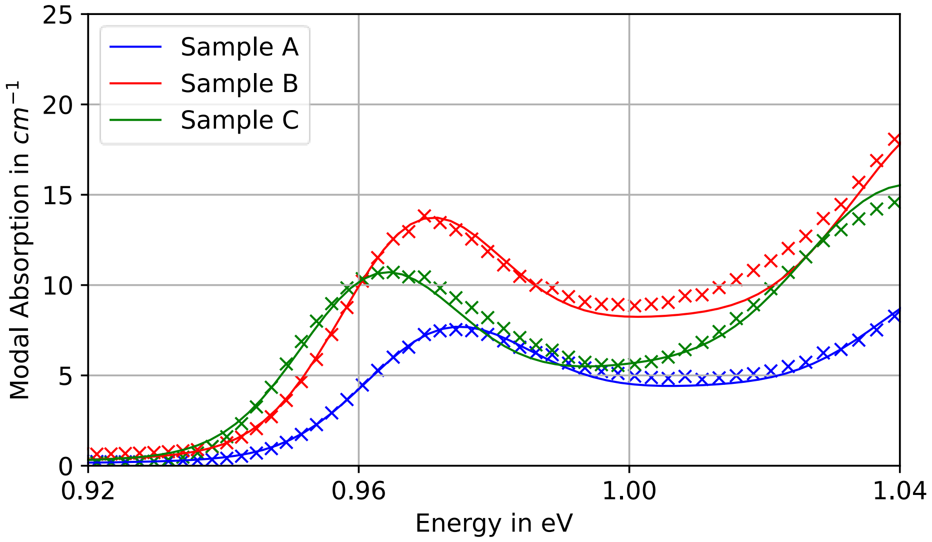

Figure 4.27: Measurements (crosses) and simulations (solid line) of absorption spectra, assuming bimodal growth.

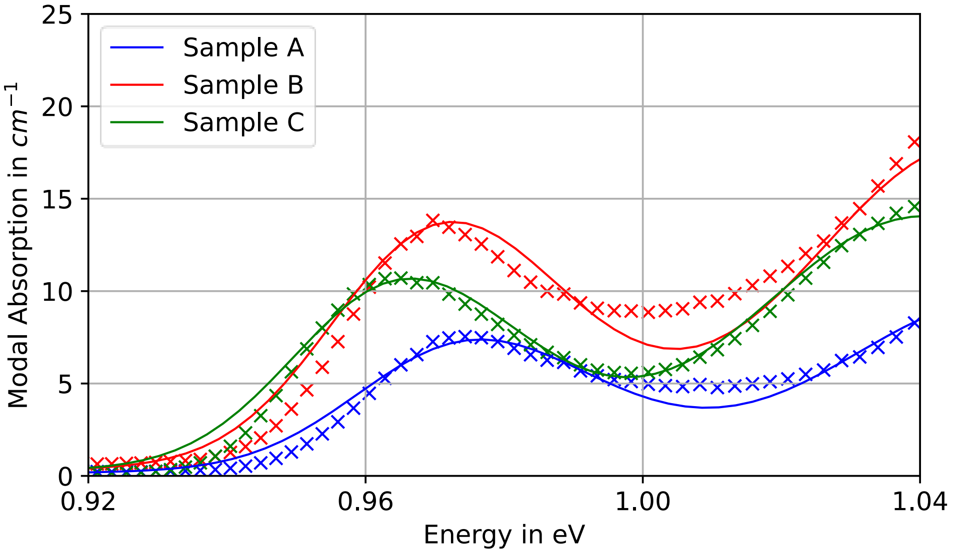

Figure 4.28: Measurements (crosses) and simulations (solid line) of absorption spectra, assuming asymmetric dots.

Material	Height (nm)	Repetition
GaAs	300	
GaAs	2.5	x10
$Al_{0.4}Ga_{0.6}As$	2.5	
$Al_{0.4}Ga_{0.6}As$	1400	
GaAs	1	x6
$Al_{0.4}Ga_{0.6}As$	1	
GaAs	36	
GaAs	39.5	x7
$In_{0.16}Ga_{0.84}As$	4.5	
InAs (QD)	3 ML	
$In_{0.16}Ga_{0.84}As$	2	
GaAs	75.5	
GaAs	1	x6
$Al_{0.4}Ga_{0.6}As$	1	
$Al_{0.4}Ga_{0.6}As$	1400	
GaAs	2.5	x10
$Al_{0.4}Ga_{0.6}As$	2.5	
GaAs	200	

Material	Height (nm)	Repetition
GaAs	300	
GaAs	2.5	x6
$Al_{0.4}Ga_{0.6}As$	2.5	
$Al_{0.4}Ga_{0.6}As$	1400	
GaAs	1	x10
$Al_{0.4}Ga_{0.6}As$	1	
GaAs	97.5	
GaAs	42.5	x7
$In_{0.16}Ga_{0.84}As$	5	
InAs (QD)	3 ML	
$In_{0.16}Ga_{0.84}As$	2	
GaAs	135	
GaAs	1	x10
$Al_{0.4}Ga_{0.6}As$	1	
$Al_{0.4}Ga_{0.6}As$	500	
$Al_{0.95}Ga_{0.05}As$	150	
$Al_{0.4}Ga_{0.6}As$	2.5	x6
$Al_{0.95}Ga_{0.05}As$	2.5	
$Al_{0.4}Ga_{0.6}As$	30	
GaAs	2.5	x6
$Al_{0.4}Ga_{0.6}As$	2.5	
GaAs	200	

Figure 4.29: Depiction of the epitaxial structure of Sample B (left) and Sample C (right). (ML ≡ monolayer)

All three samples have been grown using an MBE reactor. The main differences between Sample A, B, and C is the different aluminium content in the cladding layers. A fraction of 0.3, 0.4, and up to 0.95 was used for Sample A, B, and C, respectively. Sample A and B were grown by UCL four years apart, and Sample C was grown by IQE. The measurements of samples which were grown at different times and by different institutions indicate that the presence of absorption between the GS → GS and 1st ES → 1st ES peak is a universal feature of QD materials, and not sample dependent. Figure 4.27 and 4.28 show that both the asymmetric dot and the bimodal growth assumption led to an excellent agreement between measurements and simulations for the absorption of dot structures. The free parameters used to obtain the simulated absorption spectra are summarized in Table 4.1.

Table 4-1: Summary of the calibrated free parameters.

	Sample A	**Sample B**	**Sample C**
Asymmetric Dots:			
Dot width (nm)	22.7	23.2	23.7
Standard deviation (nm)	1.7	1.7	1.7
Dot density ($\times 10^{10}$ cm^{-2})	3.6	6.4	5.5
Bimodal growth:			
Dot width 1 (nm)	21.1	21.5	22.2
Standard deviation 1 (nm)	1.2	1.2	1.2
Dot density 1	2.5	4.2	3.8
Dot width 2 (nm)	17.7	18.1	18.5
Standard deviation 2 (nm)	2	2	2
Dot density 2 ($\times 10^{10}$ cm^{-2})	2.5	4.5	3.2

4.2.3. Simulating the Gain Spectrum

The occupation probability solver described in Section 3.2.3, established by O'Driscoll et al. (2010) [76], only includes the CB states of the dots. For the identification of gain the occupation probability of the VB states needs to be identified as well. This can be done by extending the rate equation model to also include the VB states. However, this method does not guarantee the dots to be charge neutral. An alternative approach was implemented, guaranteeing charge neutrality within individual dots. This was achieved by first identifying the occupation probability of the CB of the dots to obtain the number of electrons in each dot, using the rate equation model established by O'Driscoll et al. (2010) [76]. The number of electrons in each dot was then used to identify the quasi Fermi level of the VB needed to obtain an equivalent number of holes in the VB. Satisfying the following equality,

$$N_{e,w} = \sum_{i} f_{h,i} N_w \tag{4.7}$$

Where $N_{e,w}$ is the number of electrons for a given dot of width w, N_w is the number of dots of a given width w, and $f_{h,i}$ is the occupation probability of the i-th VB state, which is given by the Fermi-Dirac distribution,

$$f_{h,i} = \frac{1}{\exp\left(\frac{E_{v,i} - E_{fv}}{k_b T}\right) + 1} \tag{4.8}$$

Where $E_{v,i}$ is the energy level of state i, T is the temperature, k_b is Boltzmann's constant, and $E_{fv,i}$ is the quasi Fermi level. Due to the closely spaced VB states, a Fermi distribution was used to describe the VB states within each dot. This assumption is valid as long as $k_b T$ is larger than the energy between the VB states.

The established carrier distribution method is dependent on the description of the WL. Specifically, the model depends on the energy and the occupation probability of the electrons in the WL. Edge photovoltage spectroscopy (ePVS) was conducted to identify the transition energy of the WL. From the measurements a transition energy of 1.266 eV was identified. The 8-band k.p solver was used to simulate the transition energy of the WL. A WL thickness of 0.4 nm matched the measured transition energy. 0.4 nm equates to 1.3 ML of InAs for the WL, assuming one monolayer of InAs corresponds to half the lattice constant of InAs. This value agrees with WL thicknesses encountered in the Literature [103,104].

The occupation probability of the WL is identified using a commercial diode solver, Photon Design's Harold, which simulates the transport of carriers through the whole epitaxial structure for given input biases. As the dots were not taken into account by the diode solver, recombination between the WL and the dots were reproduced by assuming that the dot states act as deep states. In Harold, the rate at which this occurs was expressed by the Shockley-Read-Hall (SRH) recombination lifetime, τ_{SRH}. In this scenario, τ_{SRH} represents both, the capture lifetime from the WL into the dots, $\tau_{WL \to QD}$, as well as the capture lifetime into other deep states. The latter can be dependent on material parameters and growth quality and was assumed to be the same for the three different structures that were simulated. Harold was then used to identify the occupation probability of the WL state. Preliminary simulations suggested that the capture process of charge carriers from the WL into the dot were dependent on the injection current. Therefore, Sample A was used to calibrate τ_{SRH}, which was set to be equivalent to $\tau_{WL\rightarrow QD}$ defined in Section 3.2.3, as a function of current density. Utilising the calibrated $\tau_{SRH}(J)$ modal gain for Sample B and C were simulated. A flowchart of the implemented gain solver is depicted in Figure 4.30.

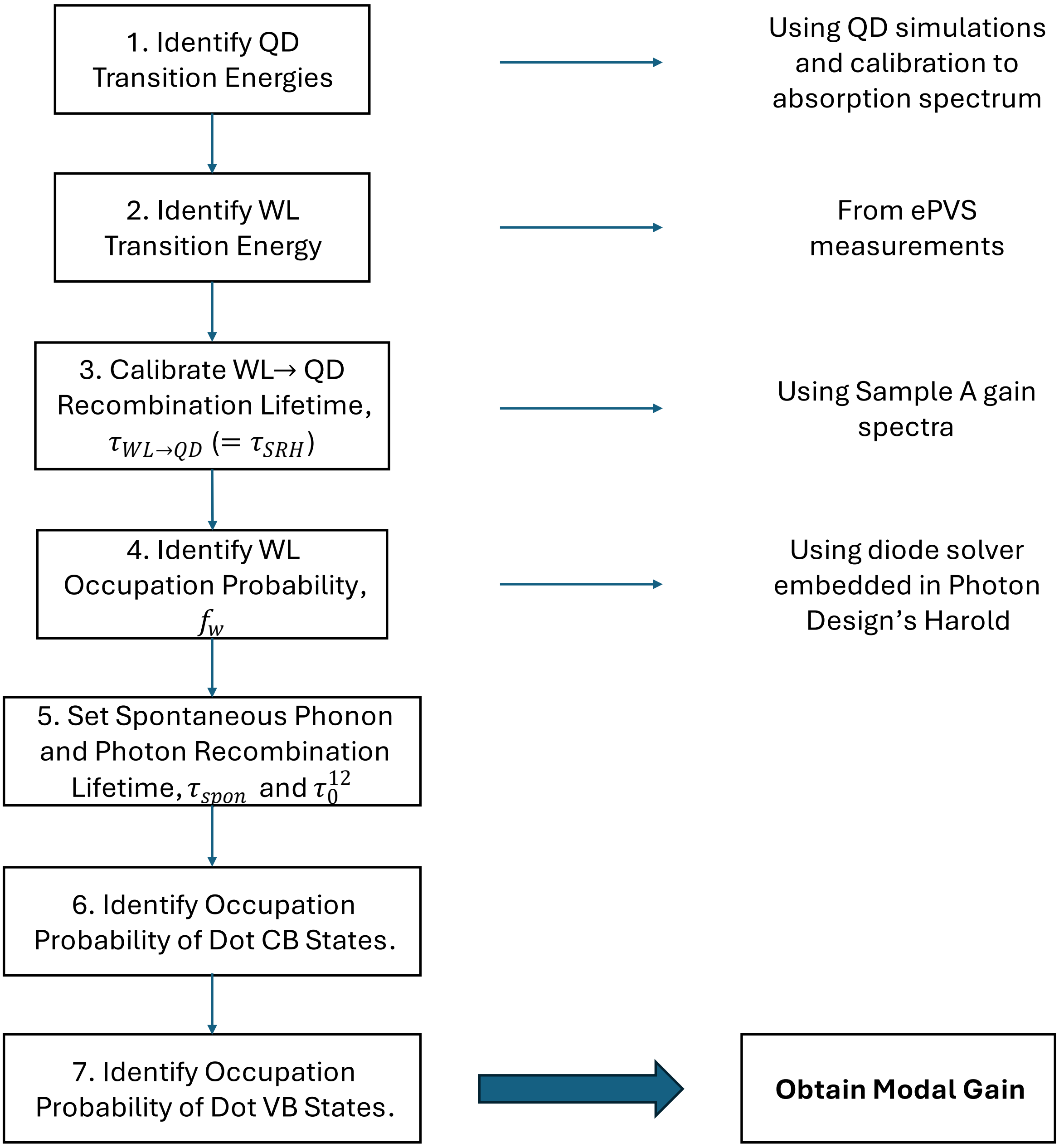

Figure 4.30: Depiction of flowchart of the established gain model.

Ideally, the recombination between the dot states and the WL state would be integrated directly into the diode solver, creating one single rate equation model instead of two distinct models. However, different current solvers can lead to different results based on their implementation, accuracy, material parameters used, and other factors. In this case, the current solver and the dot gain solver are connected through τ_{SRH} and should a different current solver be used, a different value for the τ_{SRH} will most likely need to be identified. The established QD gain solver can therefore be used for different drift-diffusion current solvers. The recombination rates identified in the rate equation model established in Section 3.2.3 are re-iterated in Figure 4.31.

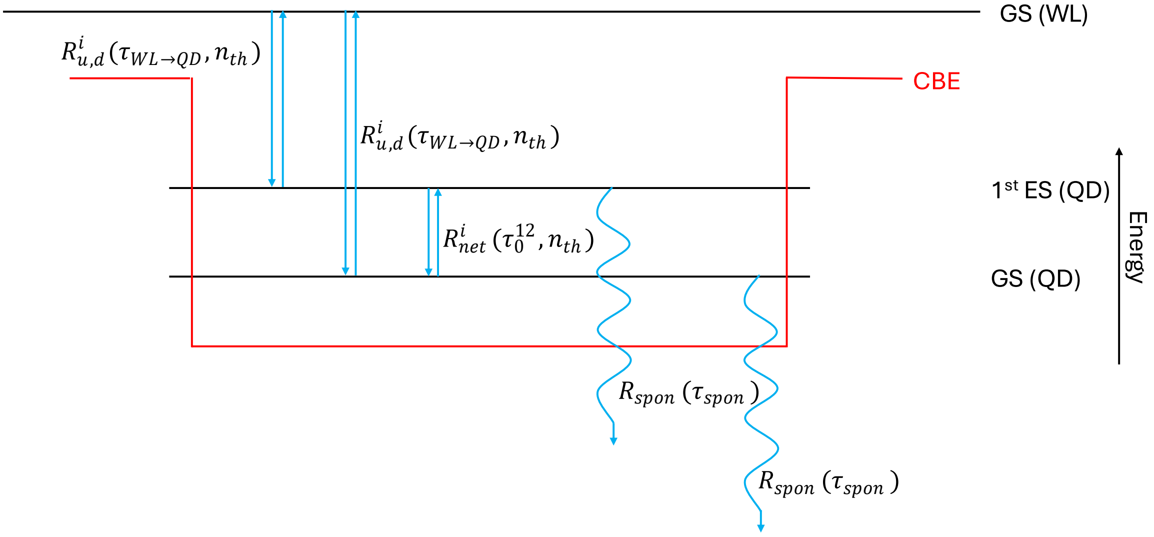

Figure 4.31: Depicting the possible recombination rates in an individual QD. (CBE ≡ conduction band edge)

The resulting calibrated gain spectra for Sample A are depicted in Figure 4.32. The simulations were calibrated to the change in gain as a function of input current density, effectively adjusting τ_{SRH} such that the simulated gain matches the measured gain. The homogeneous broadening, spontaneous recombination lifetime, τ_{spon}, and the dot to dot recombination lifetime, τ_0^{12} were kept constant under varying current densities. The spontaneous recombination lifetime, τ_{spon}, was set to 50 ns, and the spontaneous emission lifetime, τ_0^{12}, was set to 0.1 ns. Chosen to further improve the match between simulations and measurements for Sample A. Both these values are an order of magnitude larger than what is commonly found in the Literature [105,106]. The modal gain is inversely proportional to τ_{spon} and τ_0^{12}; larger lifetimes lead to a reduced gain.

Additionally, carrier-carrier interactions and their impact on the emission spectrum were taken into account. This was done by assuming a redshift of 1 meV per electron occupying the dot, as was identified from the Literature [107,108].

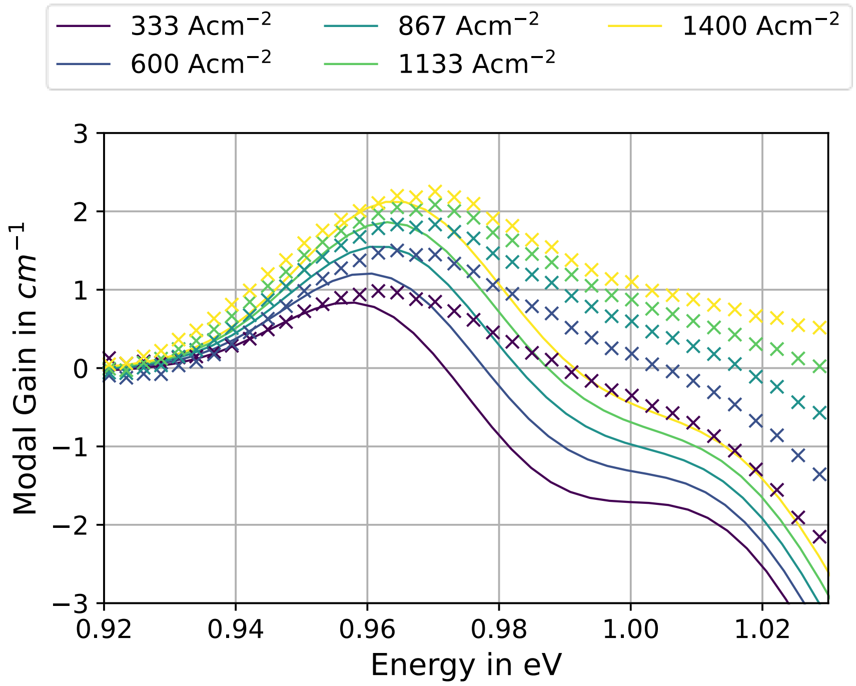

Figure 4.32: Depiction of simulated (left) and measured (right) modal gain for varying input current densities.

From the above calibration a linear relation between the WL-to-dot recombination lifetime[10], $\tau_{WL \to QD}$ and the injected current density was identified, as depicted in Figure 4.33.

---

[10] This is equal to the τ_{SRH} used in Harold.

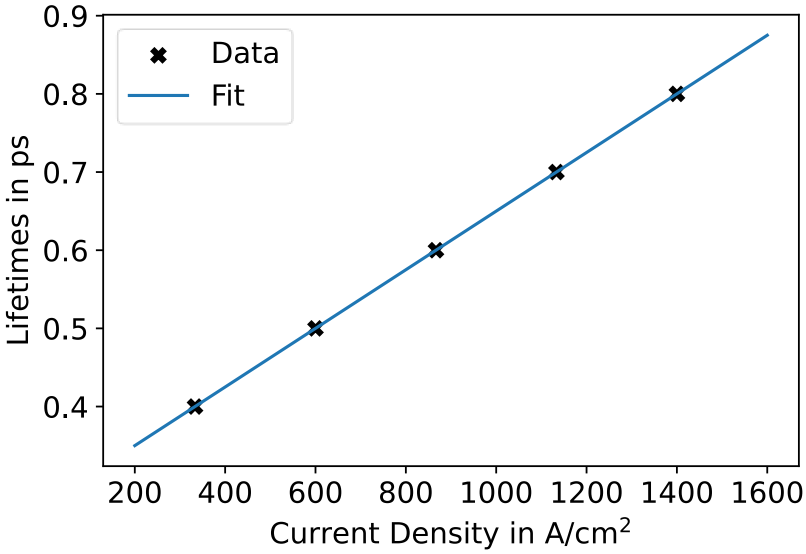

Figure 4.33: Depiction of calibrated WL to dot capture times (crosses) and fitted line (solid).

$\tau_{WL\rightarrow QD}$ is expressed as a function of injected carrier density by the following equation,

$$\tau_{WL\rightarrow QD}(J) = 3.75 \times 10^{-4} \times J + 0.275 \tag{4.9}$$

Where J is the injected current density. A linear increase of the recombination lifetime is obtained as a function of current density. Leading to a reduced recombination rate between the WL and dot states, however to an increased occupation probability of the WL state. The overall effect is an improved occupation probability of the QD CB states.

The identified relation between injection current and $\tau_{WL\rightarrow QD}$ was then used to simulate the gain at various current densities for Sample B and C, as depicted in Figure 4.34 and 4.35. The same set of dots was used for each sample, assuming asymmetric dots and using the ensemble descriptions identified based on the absorption spectra, as summarised in Section 4.2.2. The simulated and measured current densities are higher for Sample B and C than for Sample A, this is because the same injection current was used for the measurements, however, the segments of Sample B and C are half as long as those of Sample A, as mentioned in Section 3.3.2. The simulated gain spectra give good agreement to measurements for current densities lower than 1200 A/cm^{-2} and start to overestimate the gain at lower energies for higher current densities. This is attributed to the neglect of carrier-carrier scattering broadening in the simulations. Specifically, as more carriers are pumped into the device, the charge carriers begin to scatter among themselves. This broadens the gain spectrum and reduces the modal gain [109]. Additionally, the simulations predict a lower modal gain at higher energies (> 0.98 eV). Specifically the modal gain of the 1st ES → 1st ES transitions is consistently underestimated by the simulations. This is due to the assumption that the spontaneous recombination lifetimes, τ_{spon}, are equal for each transition. Attempts to rectify the spontaneous recombination lifetime led to the non-linear solver failing to converge, resulting in unusable occupation probabilities. However, the description of the spontaneous recombination lifetimes given in the Literature, show an energy dependency [65,76]. This strongly suggests that different spontaneous recombination lifetimes, for different transitions, should be used to obtain a better agreement with measurements. Specifically, a decrease in spontaneous emission lifetime as the transition energy increases should lead to a numerical model, able to better replicate the measurements.

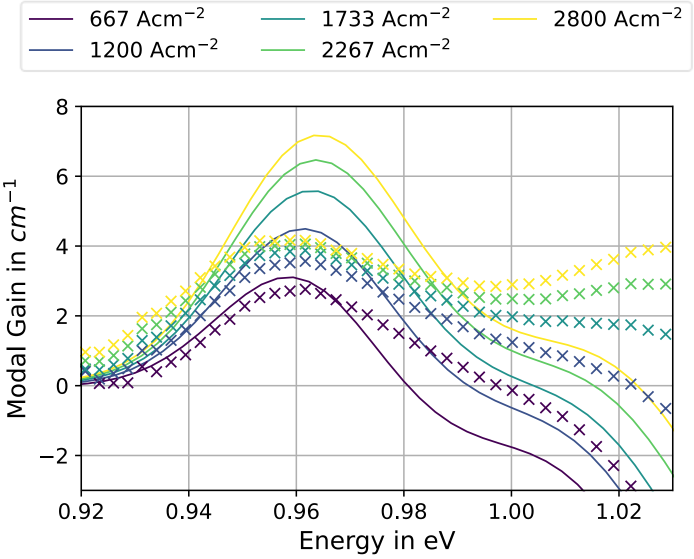

Figure 4.34: Depiction of simulated (left) and measured (right) modal gain of Sample B.

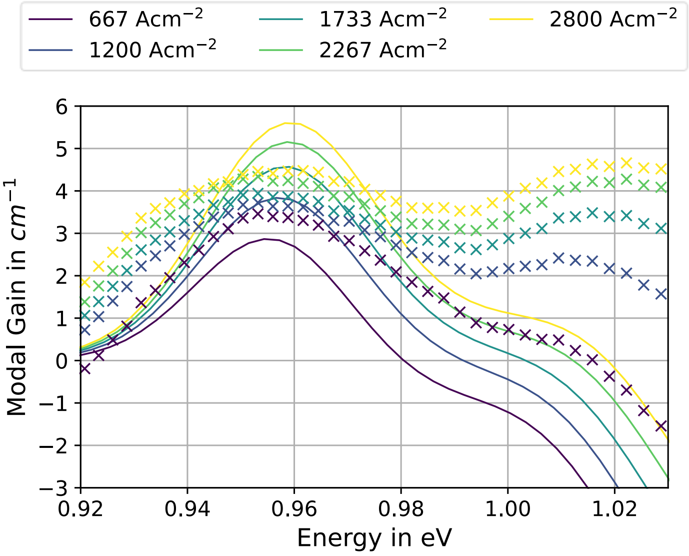

Figure 4.35: Depiction of simulated (left) and measured (right) modal gain of Sample C.

Based on the calibrated transition lifetime the gain model was used to simulate the gain of two additional samples, described by different epitaxial structures. The model allowed the simulation of different epitaxial structures, with good agreement to measurements for low current densities. This highlights the ability to use the implemented model for the simulation, and thus optimization, of various different QD epitaxial structures.

Additionally, the implemented gain model was used for different descriptions of individual dots. The modal gain of the ensemble of lens-shaped dots for the bimodal growth assumption in Section 4.2.2, was simulated, as depicted in Figure 4.36.

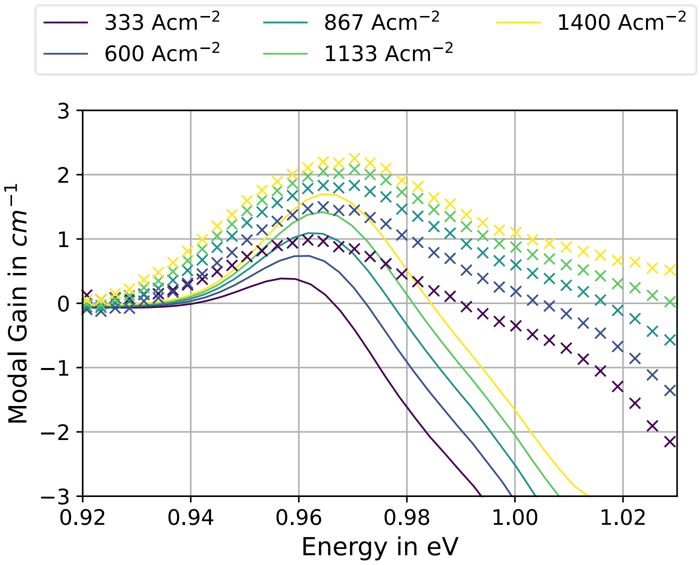

Figure 4.36: Depiction of simulated (left) and measured (right) modal gain of Sample A assuming bimodal growth.

From Figure 4.36 it is noticeable that while the gain is following the trend of the measured gain at lower energies (< 0.97 eV) significantly more deviation from the gain is observed at higher energies than for the asymmetric dots. This is caused by the 2nd distribution of the dot ensemble, which according to the implemented occupation probability solver is predominantly unoccupied, depicted in more detail in Figure 4.37. In this instance the 2nd distribution did not contribute to the gain, but actually absorbed light at energies larger than 0.98 eV.

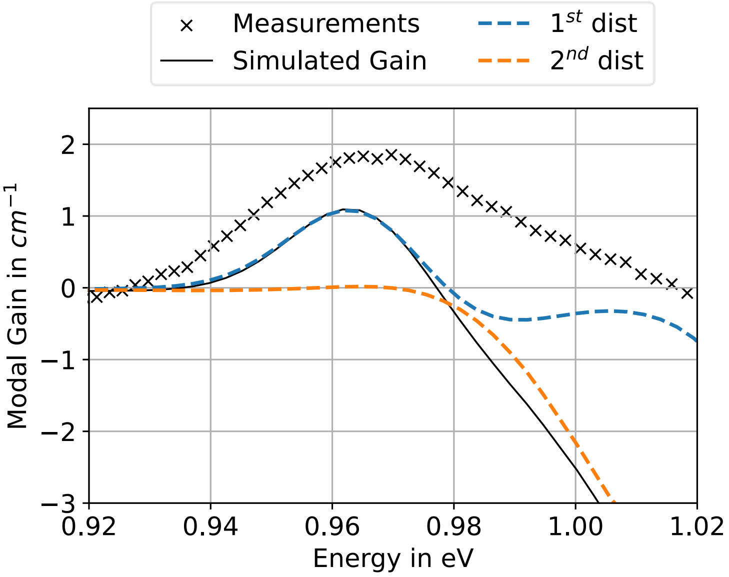

Figure 4.37: Depiction of the simulated (solid black) and measured (black crosses) modal gain at 130 mA. The gain is a sum of the gain from the 1^{st} (dashed blue) and 2^{nd} (dashed orange) distribution.

Distinct variations between the simulations and the measurements were observed for the modal gain. However, the overall trends of the gain of an epitaxial structure containing dots were well replicated, despite having to neglect non-radiative recombination and assume a constant spontaneous emission lifetime for different dot states. Good agreement between the simulation and measurement of the modal gain of three distinct samples described by significantly different epitaxial structures was achieved. Additionally, the implemented model was used for different descriptions of individual dots, having simulated the modal gain of lens-shaped dots as depicted in Figure 4.36. Even though the gain under bimodal growth assumptions led to a worse match with measurements, the implemented model allowed a realistic description of gain for different dot structures. This suggests that the measured dot ensembles are more likely to contain asymmetric dots.

Based on the successful validation of the implemented absorption and gain model, it is now possible to simulate macroscopic characteristics of different epitaxial structures as well as individual dot descriptions. Thus, successfully connecting the nanoscopic description of individual QDs to the microscopic description of entire epitaxial structures.

4.3 Summary

This chapter reviewed the Strain solver, the Piezoelectric solver, and the Schrödinger solver used to obtain a detailed description of the confined charge carriers in individual dots. The results from each solver were presented and validated against the Literature. Additional validation techniques, such as convergence testing and comparison to analytical results were discussed. While direct comparison to the Literature proved difficult, as crucial information about the structural description or material parameters were missing, each implemented solver was able to replicate the from the Literature predicted trends. Additionally, the identification of absorption spectra, relying on the combination of the individual solvers, was described. A fit between measured and simulated absorption was achieved by calibrating the model to measurements and by assuming either bimodal growth or asymmetric dots. For the simulation of gain the occupation probability of the individual dots was identified using a non-linear rate equation model. This model required the identification of the current density dependent capture lifetimes between the WL and the dots, which was done using one of the available gain measurements. The identified recombination as function of injection current density lifetime was then used to simulate the gain of different samples. The established gain model showed reasonable agreement with the measurements. The model allowed the identification of gain for varying epitaxial structures and different descriptions of individual dots.

5. Doping, Reverse Bias, and Temperature Effects in QDs

This chapter investigated additional avenues that are of interest in the context of simulating QD devices. Firstly, as QD-based photonic devices heat up under operation, the impact of increased temperature on the gain and absorption was investigated. Using appropriate parameters quantifying the impact of the increasing temperature on the QDs modal absorption and gain were simulated and compared to measurements. Secondly, QDs were investigated for potential application as electro-absorption modulators. To be able to simulate these devices, the response of QDs to an electric field needs to be identified; this was numerically and experimentally investigated. Thirdly, to improve the functionality of QD lasers, two doping schemes were researched. P-type modulation doping was simulated and directly compared to undoped structures. Additionally, the impact of n-doping on the transition energy and wavefunction on individual dots was numerically investigated, as well as the resulting impact on the modal gain spectrum.

The QD sample investigated in this chapter were grown by UCL and by IQE using an MBE reactor. The contacts on the SCM samples were deposited by Dr. Sara-Jayne Gillgrass. Further sample preparation, which included cleaving the metal plated wafer and wire-bonding the cleaved sample to a 16-pin header, to which the sample was glued onto using silver epoxy, was conducted by Susanna Power and Noor Albittar.

5.1. Temperature Effects in QDs

Inherently, electro-optic devices are haunted by thermal effects. These effects can become detrimental to their functionality. A common technique to avoid performance deterioration is to cool the device. A study on thermal management in data centres was done by Garimella et al. (2012), stating that cooling makes up 33 % of the total energy consumption [110]. It therefore follows that thermally stable devices, which would not require cooling, can significantly reduce energy consumption. Furthermore, this would also reduce the water usage needed for cooling, and reduce the overall environmental impact caused by cooling data centres.

Lasers using QDs as active material have shown excellent thermal stability. Specifically, the change of the threshold current as a function of temperature is significantly less than for bulk or QW active material. This stability is commonly quantified using the characteristic temperature, T_0[11]. Which can be identified using the following relation,

$$J_{th}(T) = J_{th,0} \exp\left(\frac{T}{T_0}\right) \tag{5.1}$$

Where J_{th} is the threshold current density, T is the temperature, and $J_{th,0}$ is an additional fitting parameter. For a large value of T_0 the temperature dependence of the threshold current density is low, i.e., a large T_0 is desirable [65]. Work done by Badcock et al. (2007) [111] showed improved temperature characteristics for p-type modulation doping in QD lasers emitting at 1.3 µm.

Commercially available lasers, advertised for use in telecommunication, present an operation temperature between 0 °C and 70 °C [112,113]. Over this temperature range Fathpour et al. (2004) [114] investigated fabricated QD lasers, presenting an infinite characteristic temperature. This indicates that no increase in threshold current was observed over this temperature range; both for on native [114] and on Si substrates [115]. These results highlight the viability of QD lasers for photonic application and their integration on existing silicon platforms.

From a simulation perspective it is therefore of interest to include temperature effects in the established model. This can be achieved based on the identification of individual dots, by analysing the change in material parameters as a function of temperature. From the Literature the most commonly analysed material parameter as a function of temperature is the band gap energy, which is fitted to the empirical Varshni form, given by,

$$E_g(T) = E_g(T = 0) - \frac{\alpha T^2}{T + \beta} \tag{5.2}$$

Where, α and β are fitting parameters, commonly referred to as Varshni parameters. These parameters are empirically identified by measuring the band gap energy at varying temperatures and fitting α and β to the resulting data. The Varshni parameters for various compound semiconductors are given in Vurgaftman et al. (2000) [57]. The

---

[11] N.B. Care has to be taken when identifying T_0 as it is dependent on the range of temperature over which it is identified and the magnitude of the threshold current density.

values of the Varshni parameters for GaAs and InAs are presented in Table 5.1. A large α value leads to a higher energy shift as a function of temperature. A large β value leads to a lower shift in energy as a function of temperature.

The impact of temperature on the lattice constant, $a_{lc}(T)$, was widely studied. The change in temperature is expressed as a linear relation, given by,

$$a_{lc}(T) = a_{lc}(T = 300K) + \gamma(T - 300) \tag{5.3}$$

Where γ is a fitting parameter. Similarly to the band gap, gamma is identified by measuring the lattice constant at varying temperatures and fitting γ to the data. For bulk GaAs and bulk InAs it is equal to 3.88×10^{-6} nm/K and 2.74×10^{-6} nm/K, respectively. The lattice constant increases for higher temperatures and decreases for lower temperatures; the larger γ is the faster this change occurs.

Material parameters, including the deformation potentials, a_c, a_v, b, and d, the Kane parameter E_p, the Luttinger parameters, γ_1, γ_2, and γ_3, spin-orbit split off energy, Δ_{SO}, the valence band offset, and the stiffness coefficients, C_{11}, C_{12}, and C_{44}, were assumed to be independent on temperature as very little discussion is available in the Literature.

5.1.1. Absorption Spectra as a Function of Temperature

Utilising the temperature dependent material parameters described in Equation 5.2 and 5.3, the absorption spectra at different temperatures were simulated. Figure 5.1 depicts the absorption spectra at 21.5 °C (ambient temperature), 40 °C, 60 °C, and 80°C, for 5 nm high lens-shaped dots, with an average width of 20 nm and no material mixing. For ease of comparison only the GS → GS, 1st ES → 1st ES, and 2nd ES → 2nd ES transitions[12] have been depicted. The simulations show minimal change (< 0.1 % for a 20 °C increase) in the wavefunction overlaps for different temperatures.

---

[12] The 1st ES and 2nd ES transition energies are degenerate for lens-shaped dots.

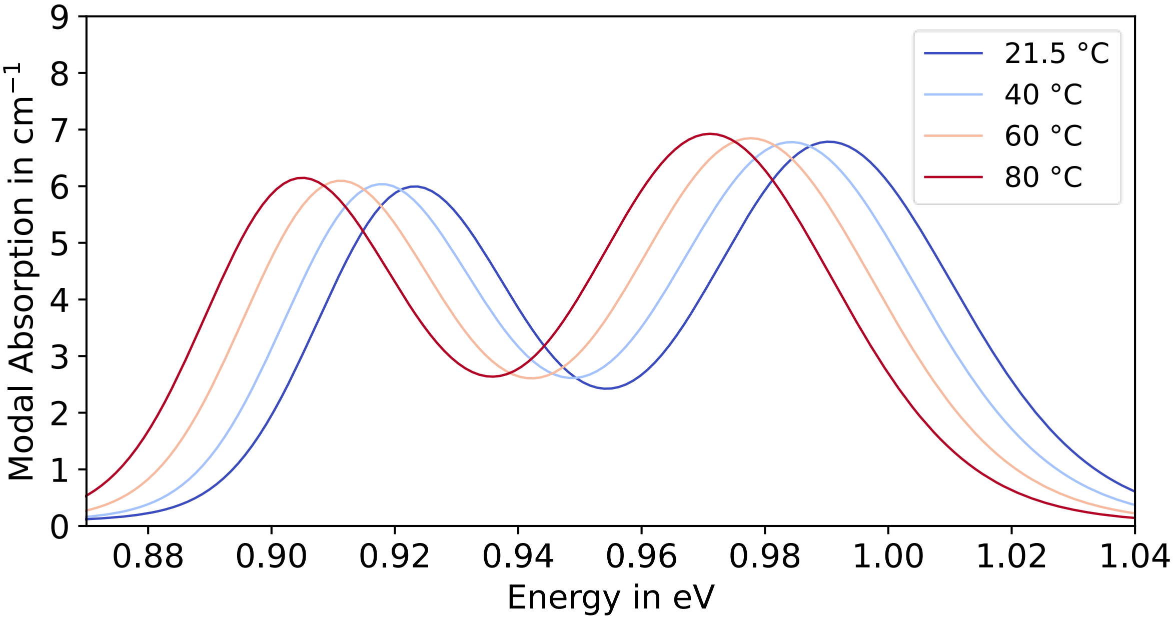

Figure 5.1: Simulation of modal absorption at 21.5 °C, 40 °C, 60 °C, and 80 °C.

From Figure 5.1, a red shift of the absorption spectra is observed with increasing temperature. This is due to the reduction in band gap energy as the temperature increases.

The SCM setup was used to measure changes in the modal gain and absorption spectra as a function of temperature. Measurements were taken at 21.5 °C, 40 °C, 60 °C, and 80 °C. The modal absorption of Sample A at these temperatures is depicted in Figure 5.2, along with simulations under these conditions. Figure 5.2 shows that the shift in the absorption spectra due to the variation in temperature were not recovered by the simulations. The simulations underestimated the shift in energy as a function of temperature. Conversely, for Sample B, the simulated absorption spectra shifted more than the measured spectra as a function of temperature, as can be observed in Figure 5.3. Lastly, the simulated absorption spectra for Sample C were in agreement with measurements, as depicted in Figure 5.4. This indicates that the shift in energy cannot simply be replicated by accounting for the shift in material parameters of the bulk material, or that the assumption that the other material parameters are not temperature dependent, is invalid. Instead, for QD ensembles, the structure should be described by its own set of Varshni parameters. These can be extracted from the measurements, by fitting Equation 5.2 to the collected data points. The fitted parameters may then be used to simulate the shift in energy as a function of temperature, to better reflect the change in transition energy as a function of temperature.

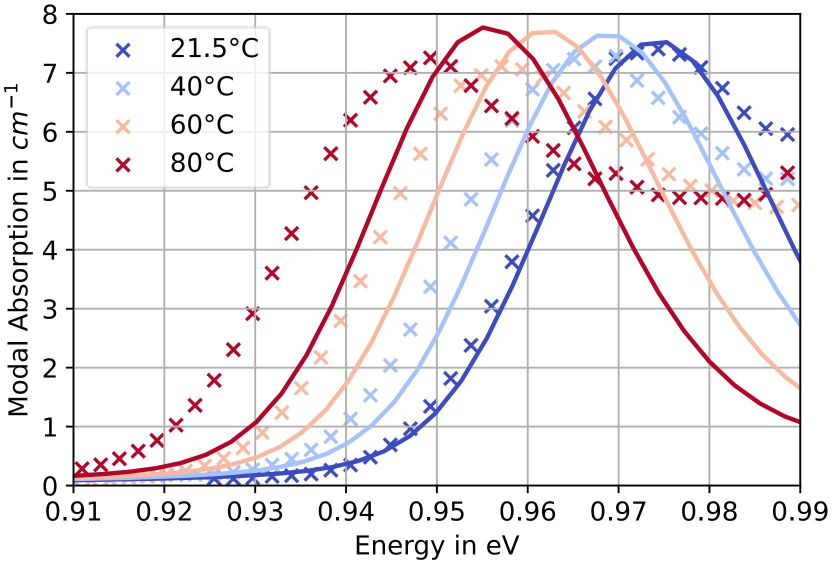

Figure 5.2: Depiction of the measured (crosses) and simulated (solid line) modal absorption at 21.5 °C (dark blue), 40 °C (light blue), 60 °C (salmon), and 80 °C (dark red) of Sample A.

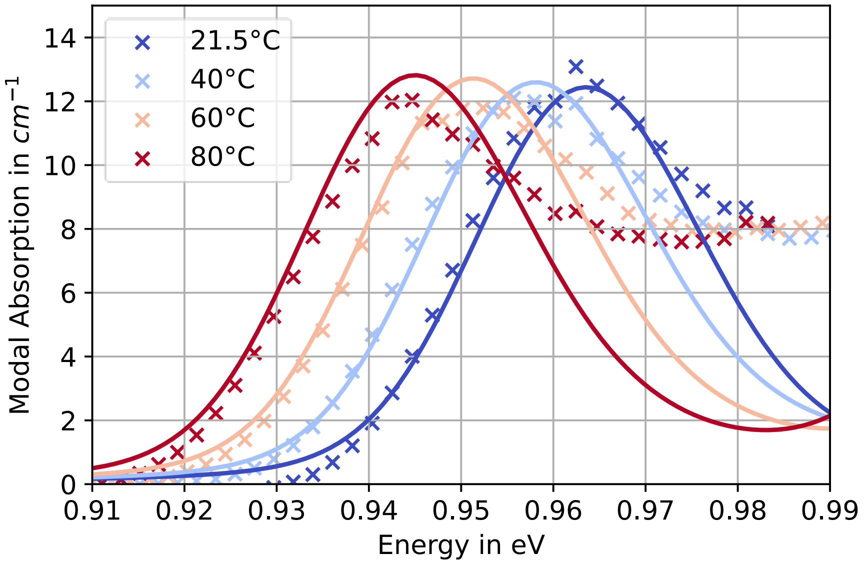

Figure 5.3: Depiction of the measured (crosses) and simulated (solid line) modal absorption at 21.5 °C (dark blue), 40 °C (light blue), 60 °C (salmon), and 80 °C (dark red) of Sample B.

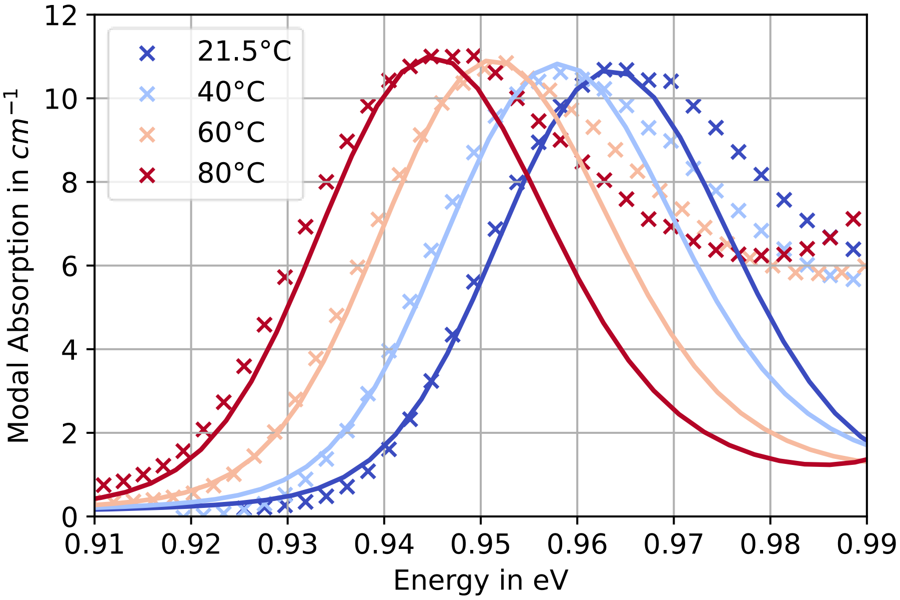

Figure 5.4: Depiction of the measured (crosses) and simulated (solid line) modal absorption at 21.5 °C (dark blue), 40 °C (light blue), 60 °C (salmon), and 80 °C (dark red) of Sample C.

Utilising these QD sample dependent Varshni parameters (summarised in Table 5.1), good agreement between each sample measurement and simulations was achieved, depicted in Figure 5.5, 5.6, and 5.7. The parameters were not tested for a broader temperature range. Based on the identified errors of the Varshni parameters the difference in the identified parameters between the three samples is not significant. Further data points would have to be collected to be able to obtain well determined Varshni parameters and allow for a valid comparison between the sample dependent Varshni parameters. However, for the purpose of simulating the measured shift in absorption as a function of temperature, over a temperature range from 20 °C to 80 °C, the identified Varshni parameters allow for a good fit between model and measurements.

While the model is unable to accurately describe the temperature induced shift in energy variations based on the temperature dependent bulk material parameters, the overall trend of the reduction in transition energy as the temperature increases is well replicated. Therefore, the model would still allow to collect preliminary insight into the shift of the absorption spectrum as a function of temperature, even if the exact Varshni parameters are not known.

Table 5-1: Summary of Varshni parameters of different QD samples, GaAs, and InAs.

	Sample A	**Sample B**	**Sample C**	**GaAs**	**InAs**
α in meV/K	0.48 ± 0.46	0.30 ± 0.33	0.35 ± 0.35	0.54	0.276
β in K	190 ± 902	100 ± 1210	120 ± 1053	204	93

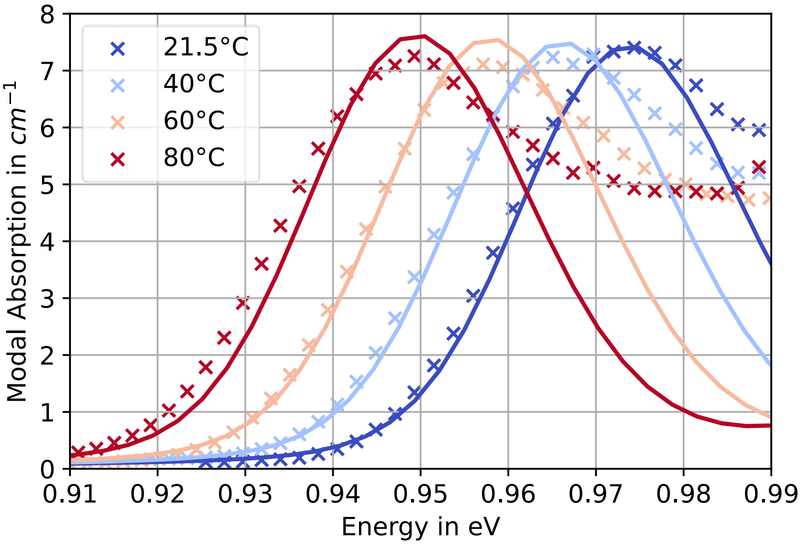

Figure 5.5: Depiction of the measured (crosses) and simulated (solid line) modal absorption at 21.5 °C (dark blue), 40 °C (light blue), 60 °C (salmon), and 80 °C (dark red) of Sample A, using QD sample dependent Varshni parameters.

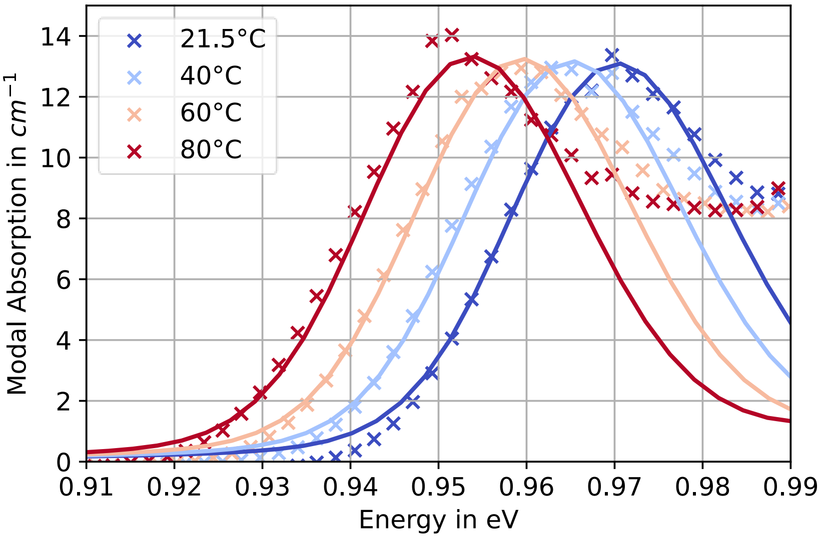

Figure 5.6: Depiction of the measured (crosses) and simulated (solid line) modal absorption at 21.5 °C (dark blue), 40 °C (light blue), 60 °C (salmon), and 80 °C (dark red) of Sample B, using QD sample dependent Varshni parameters.

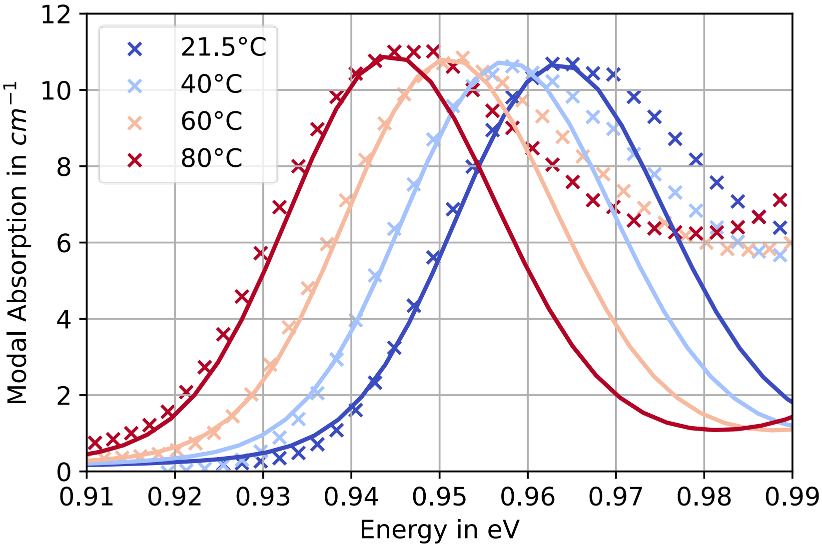

Figure 5.7: Depiction of the measured (crosses) and simulated (solid line) modal absorption at 21.5 °C (dark blue), 40 °C (light blue), 60 °C (salmon), and 80 °C (dark red) of Sample C, using QD sample dependent Varshni parameters.

5.1.2. Modal Gain Spectra as a Function of Temperature

The temperature effects on the gain spectra can be simulated using the identified Varshni parameters. ePVS measurements were conducted identifying the transition energy of the WL at 21.5 °C, 40 °C, 60 °C, and 80 °C (1.266 eV, 1.26 eV, 1.252 eV, and 1.246 eV, respectively). Using the established rate equation model in line with O'Driscoll et al. (2010) [76], three types of recombination occur, as described in Section 3.2.3. The recombination rates between WL states and QD states, $R^{i}_{d|u,w}$ and between QD states themselves, R^{i}_{net}, are phonon induced and therefore, their temperature dependence arises from and is calculated using the Bose-Einstein distribution. The dependence of the recombination rates to the Bose-Einstein distribution is highlighted in Figure 4.28. The impact of temperature on the spontaneous recombination, R_{spon}, must be included in a different way. This is achieved through adjusting the spontaneous photon recombination lifetime, $\tau_{spon}(T)$, such that the simulated gain peaks match the measured gain peak of the GS transition for Sample A at 21.5 °C, 40 °C, 60 °C, and 80 °C, at 600 Acm^{-2}. $\tau_{spon}(T)$ was used to tune the change in carrier density in the rate equation model established in Section 3.2.3. The same temperature dependent spontaneous photon recombination lifetime, $\tau_{spon}(T)$, was used for Sample A, B, and C. An updated flowchart (with respect to the flowchart detailed in Section 4.2.3) is depicted in Figure 5.8.

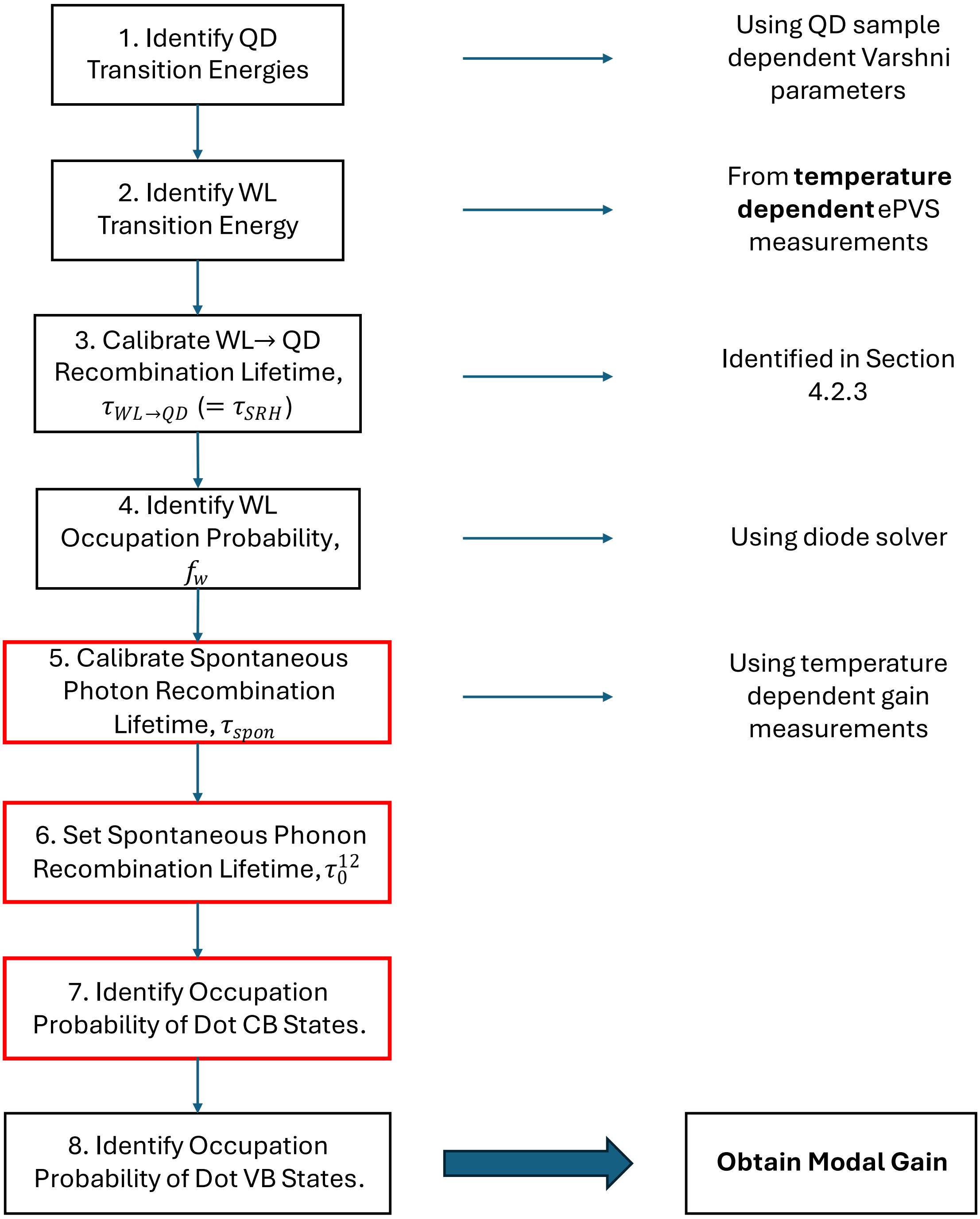

Figure 5.8: Flowchart describing the identification of temperature dependent modal gain. Highlighted in red are the different steps to the flow chart depicted in Section 4.2.3.

The increase in spontaneous recombination impacts the required occupation probabilities of the CB states at equilibrium, which in turn impacts the modal gain. A match between the simulated and measured gain was achieved for a spontaneous lifetime of 50 ns, 22 ns, 10 ns, and 5 ns, at 21.5 °C, 40 °C, 60 °C, and 80 °C, respectively. The trend shows a continuous reduction in spontaneous lifetime as a function of temperature. This in turn leads to an increased spontaneous photon recombination rate. Based on the calibration, the more spontaneous photon recombination occur, this leads to lower occupation probabilities of the dot states, leading to less modal gain.

The modal gain, at different current densities and different temperatures was simulated, for Sample A, B, and C, depicted in Figure 5.9.

Measurements demonstrated a reduction in modal gain as a function of temperature for all current densities for all three samples. The implemented calibrated model was capable of replicating the main features of the modal gain at varying temperatures and current densities. With this it should be possible to simulate QD based photonic devices at varying temperatures over the range of 20 °C to 80 °C. This should allow preliminary insights into the functionality of the QD based photonic device at different temperatures. The same conclusion holds even if the Varshni parameters are not empirically identified and the literature values are used.

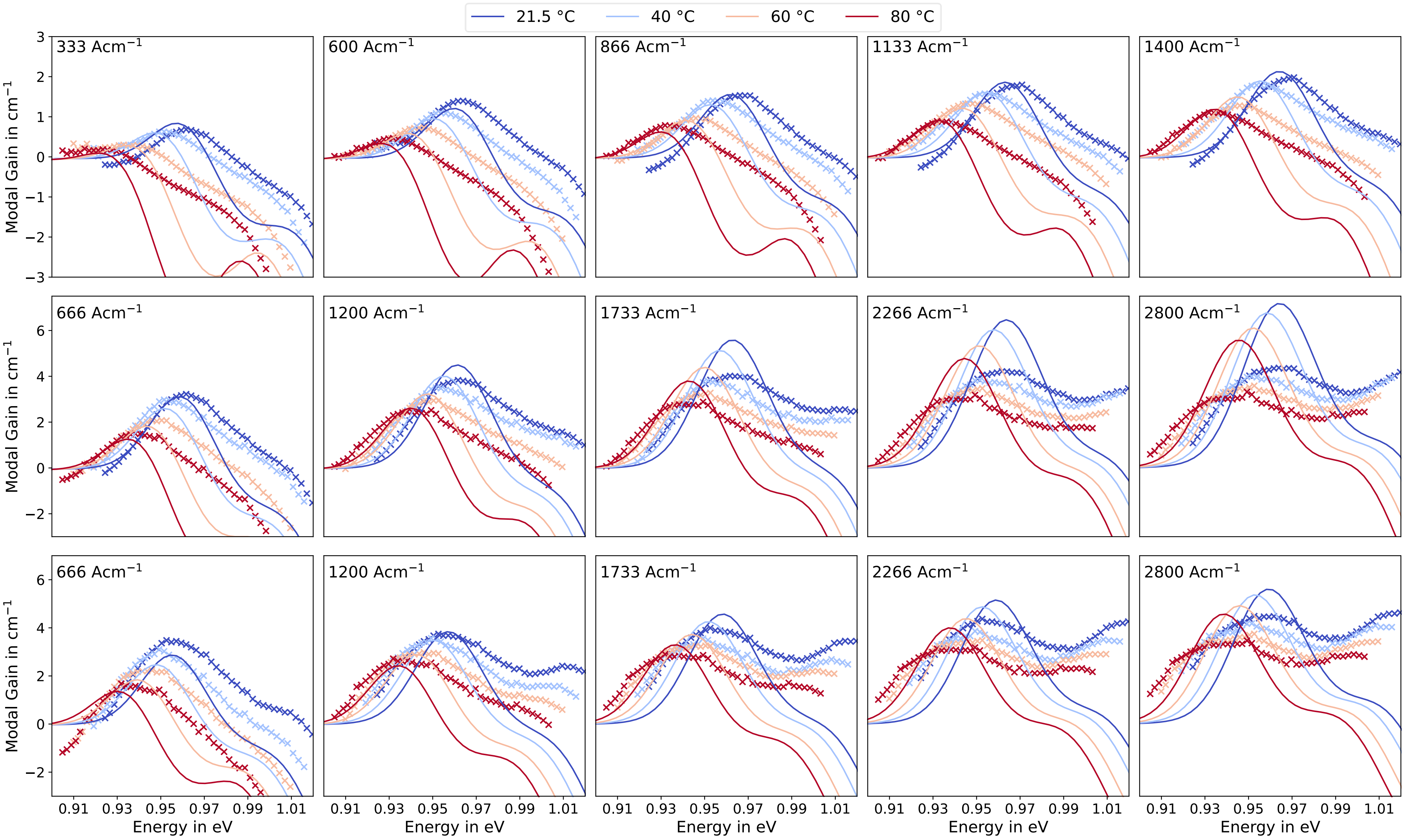

Figure 5.9: Depiction of the measured (crosses) and simulated (solid line) modal gain, at 21.5 °C (dark blue), 40 °C (light blue), 60 °C (salmon), 80 °C (dark red) for Sample A (first row), B (second row), and C (third row), for given current densities as stated in the top left corner of the subplots.

5.2. Reverse Bias Effects in QDs

The ability to control the characteristics of a signal is fundamental to data communication. For optical signals, the change in amplitude, phase, frequency, and polarization can be used to encode and transmit information. Devices capable of impacting or controlling these characteristics are called modulators. Improving the functionality of these modulators could have a huge impact in the field of telecommunication [116]. A potential candidate as active material for next-generation optical modulators are QDs; specifically for the use in electro-absorption modulators. QD modulators present low internal loss and improved chirping properties [117]. Additionally, QDs respond strongly to externally applied electric fields. Work done by Lin et al. (2011) demonstrated that QD based modulators can achieve similar functionality as well-established QW modulators, using dots whose epitaxial structure was not optimised for modulation [14]. Being able to optimise the QD stack prior to fabrication would therefore be of great interest. This requires a good understanding of the impact of an applied electric field on the confined charge carriers in QDs.

Applying an electric field across a structure confining carriers leads to the appearance of the quantum confined Stark effect (QCSE). Under increasing reverse bias, the strength of the electric field across the junction increases. The presence of the electric field impacts the confining potential, which in turn impacts the CB and VB states of the confined carriers. The change in confining potential is shown in Figure 5.10, for no bias and an E-field of 120 kV/cm in a 6 nm wide InAs QW surrounded by GaAs[13]. In this example, the transition energy was shifted by 5.9 meV. In addition to the shift in energy, the electric field induced change in the confining potential shifted the wavefunctions of the CB and the VB, leading to a change in the wavefunction overlap. For the example depicted in Figure 5.10, the overlap of the GS to GS transition was reduced from 0.96 to 0.85, when a 120 kV/cm strong E-field was applied. The change in wavefunction overlaps directly impacts the recombination efficiency of the charge carriers. For

---

[13] The strain in QWs is assumed to be pseudomorphic, meaning that the confining potential resembles a box-like shape, as depicted in Figure 5.10.

example, a reduction in wavefunction overlap between two transition states would directly result in a reduction in absorption.

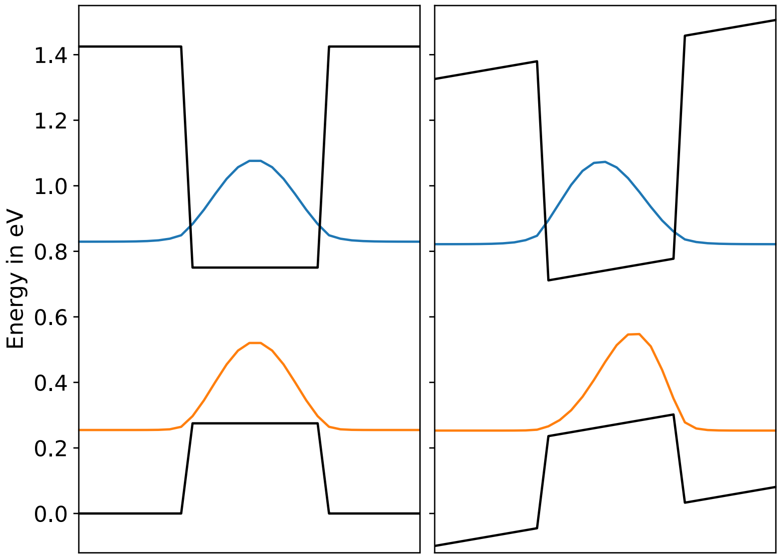

Figure 5.10: Depiction of the confining potential (black) of a QW and the GS of the CB (blue) and the VB (orange) under no bias (LHS) and an applied E-field of 120 kV/cm (RHS).

5.2.1. Simulating the Response of QDs to an Electric Field

The confining potential for dots is different to that for QWs, specifically, the potential is already tilted inside the QD, due to strain, as depicted in Figure 5.11. Therefore, depending on the direction of the E-field, the QCSE will impact the confined charges in QDs differently than in QWs. In the context of this work, a positive field points in the direction of the growth, from the n-type doped layer towards the p-type doped layer. In what follows, positive E-field corresponds to reverse bias and negative E-field corresponds to forward bias. The QD simulations do not directly include the internal built-in field, resulting from the p-n junction. However, a properly selected simulated electric field can replicate the influence of the built-in field on the confined charge carriers. The built-in field is identified using Photon Design’s Harold QCSE package.

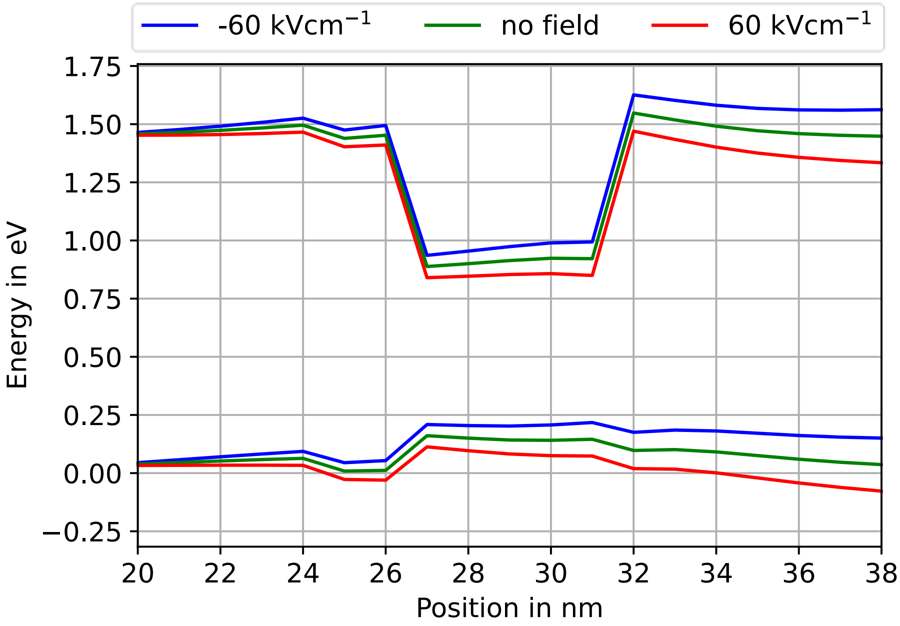

Figure 5.11: CB and VB edge for -60 kVcm^{-1} (blue), no field (green), and 60 kVcm^{-1} (red), along the axis going through the centre of the dot from the bottom to the top.

From Figure 5.11 it can be seen that both the CB and the VB band edge are not horizontal within the QD at zero internal field[14]. Focusing on the VB edge, one observes a maximum value at the bottom of the dot, which slowly decreases within the dot until it reaches the top. When then applying a negative E-field this tilt first needed to be "overcome" before similar behaviour as in the QW scenario was observed. This is reflected in the simulation of unmixed lens-shaped QD, as depicted in Figure 5.12.

---

[14] Indicating that there is no applied reverse bias and no internal field.

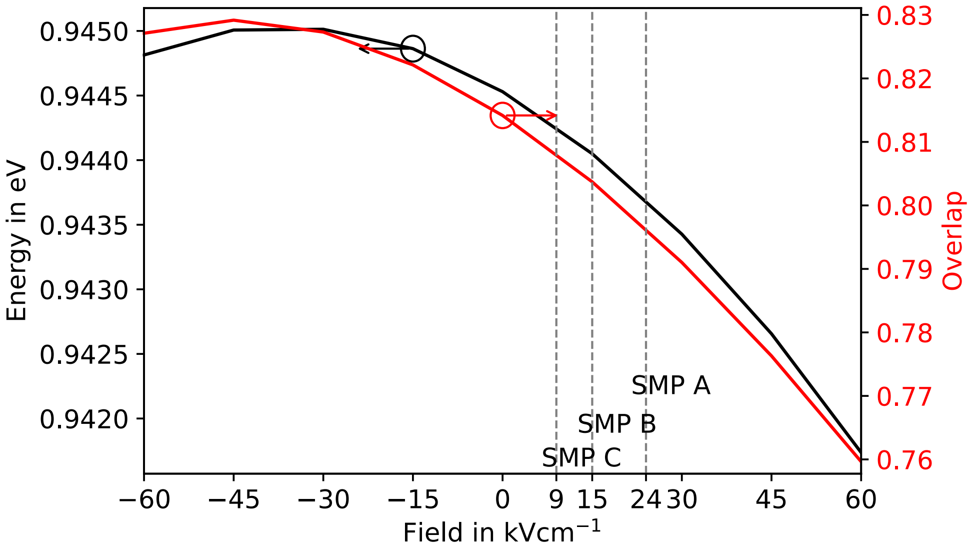

Figure 5.12: Depiction of the change in overlap (red) and transition energy (black) between the GS of the CB and VB for a 18 nm wide and 5 nm high lens-shaped QD. The dotted lines indicate the strength of the simulated built-in field for Sample (SMP) A, B, and C.

Figure 5.12 depicts how the transition energy first increases, until -30 kVcm^{-1}, as a function of field strength, before a reduction in energy is observed. Similarly for the overlap values between the GS of the CB and the VB, however, the overlap increases until the E-field is -45 kVcm^{-1}. Both the transition energy and the overlap decreases for increasing E-field. The same behaviour was observed for dots of different width (20 nm and 22 nm). The next set of simulations was used to investigate the response of the QD ground state, including material mixing, to an externally applied electric field. The material profile of the different dots is depicted in Figure 5.13.

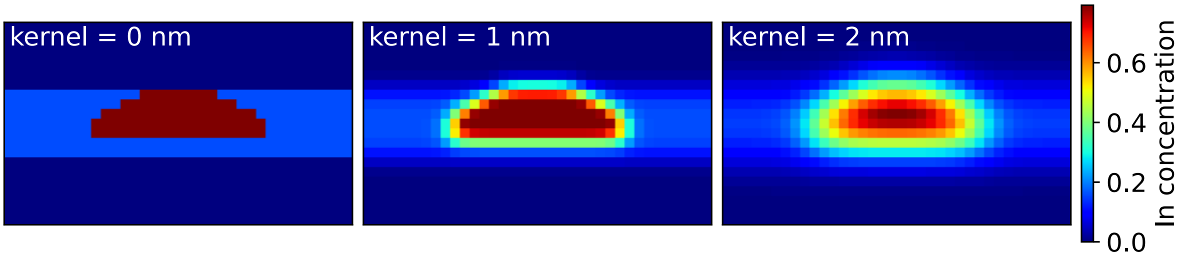

Figure 5.13: Depiction of material profile for different kernel sizes, used in the E-field simulations.

The change in the GS transition and overlap as a function of electric field, for a kernel size of 1 nm, is depicted in Figure 5.14. The behaviour of the GS transition energy and the overlap is qualitatively the same as for the pure InAs dot structure. However, the absolute shift in energy is slightly more pronounced, with a 2.8 meV and 3.1 meV for the pure InAs, and for the mixed InAs QD, respectively, when increasing the field from no bias to 60 kV/cm. This corresponds to a relative shift of 0.3 % for both the un-mixed and mixed structure.

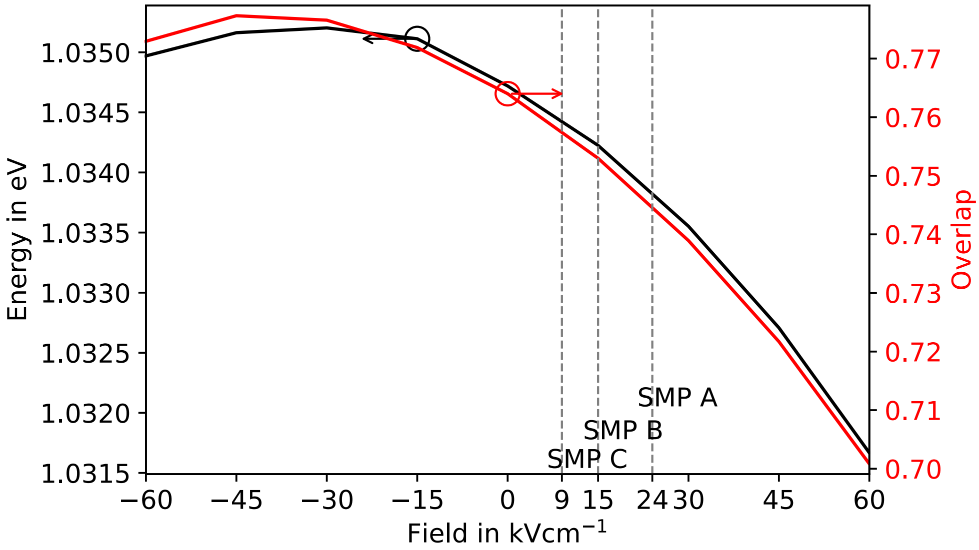

Figure 5.14: Depiction of the change in GS transition energy (black) and wavefunction overlap (red). The dotted lines indicate the strength of the simulated built-in field for Sample (SMP) A, B, and C.

Additional simulations with stronger material mixing, using a kernel size of 2 nm, were conducted. The change in GS wavefunction overlap and transition energy is depicted in Figure 5.15. The trend of the GS transition energy and overlap is the same as for the structures with no mixing and mixing with a 1 nm big kernel. However, the extent to which the transition energy changes is further emphasized for higher material mixing. With a shift of 5.8 meV, corresponding to a relative shift of 0.5 %, when increasing the field from no bias to 60 kV/cm, for a kernel size of 2 nm. Additionally, the absolute shift in wavefunction overlap increases for increasing kernel size, with a shift of 0.0545, 0.0738, and 0.157, for a kernel size of 0 nm, 1 nm, and 2 nm, respectively, for a shift in E-field from no bias to 60 kV/cm. This corresponds to a relative wavefunction overlap shift of 6.7 %, 8.3 %, and 23 %, for a kernel size of 0 nm, 1 nm, and 2 nm, respectively. This shows that while the relative shift only increases for high mixing, the wavefunction overlap shift increases as a function of material mixing.

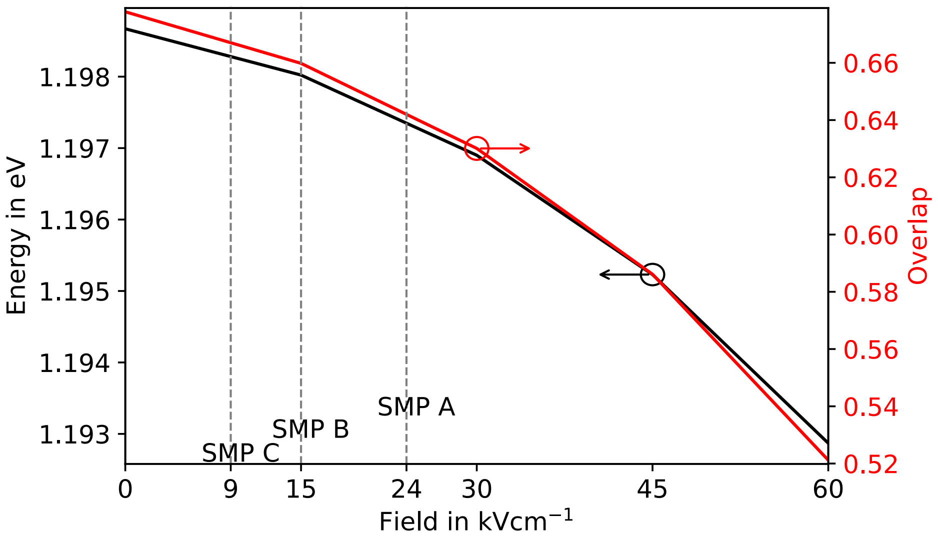

Figure 5.15: Depiction of changes in GS transition energy (black) and wavefunction overlap (red). The dotted lines indicate the strength of the simulated built-in field for Sample (SMP) A, B, and C.

Work done by Barker and O'Reilly [118,119], discussed the impact of changes in the E-field for dots described by a gradient indium distribution. Similar to the material composition investigated by Blokland et al. (2009) [28], discussed in Section 2.2. This type of indium distribution occurs during higher temperature InAs growth as the heavier indium segregates towards the top of the layer/dot [26,120]. The dot then presents a material composition of $In_xGa_{1-x}As$, where x is the indium concentration, at the bottom, which linearly increases to InAs at the top of the dot. Example structures presenting a gradient Indium distribution are depicted in Figure 5.16.

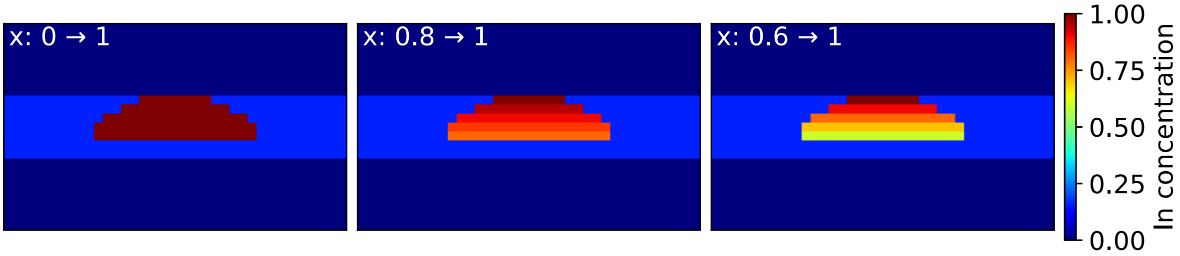

Figure 5.16: Depiction material profile for dots with a gradient shift due to indium segregation.

The graded dot structures were simulated for different E-fields, the results are presented in Figure 5.17. Similar to the un-graded and material-mixed dots the transition energy and wavefunction overlap decreases with increasing E-field. Presenting an absolute energy shift of 4.6 meV and an absolute overlap reduction of

0.097 for a field increased from no bias to 60 kV/cm. This corresponds to a relative shift of 0.4 % and 12.4 %, for the transition energy, and the overlap, respectively.

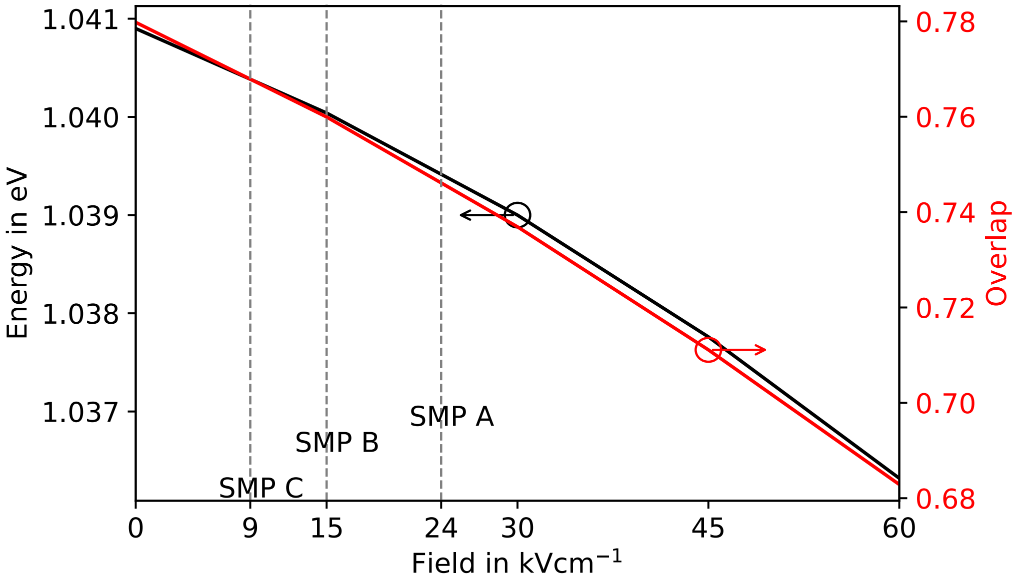

Figure 5.17: Depiction of change in GS transition energy (black) and wavefunction overlap (red). For a graded dot staring from $In_{0.8}Ga_{0.2}As$ at the bottom of the dot. The dotted lines indicate the strength of the simulated built-in field for Sample (SMP) A, B, and C.

The same simulations were conducted for the more highly graded dot structure, the results are presented in Figure 5.18.

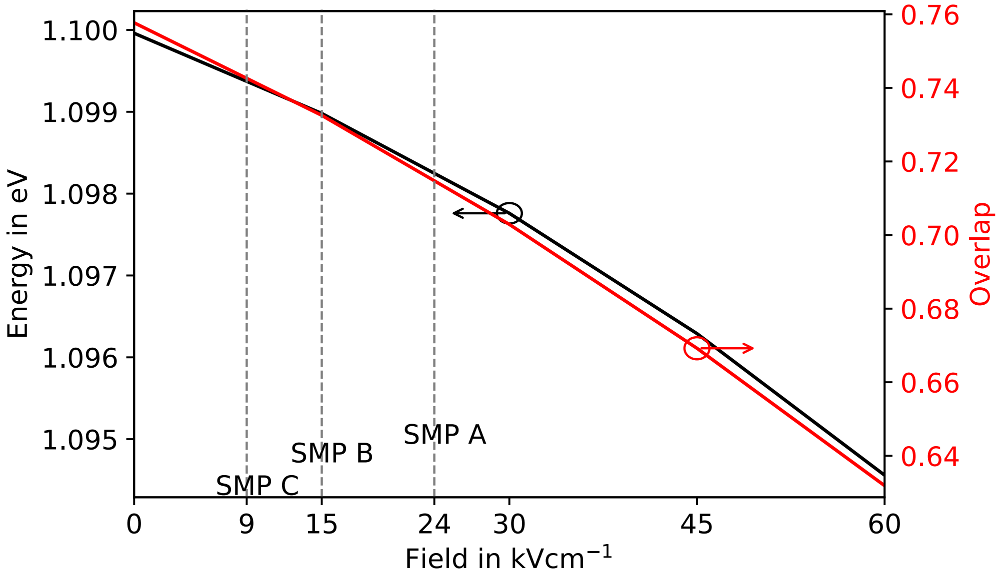

Figure 5.18: Depiction of change in GS transition energy (black) and wavefunction overlap (red). For a graded dot starting from $In_{0.6}Ga_{0.4}As$ at the bottom of the dot. The dotted lines indicate the strength of the simulated built-in field for Sample (SMP) A, B, and C.

Similar to the previous simulations, the GS transition energy and wavefunction overlap decreases with E-field strengths. Figure 5.18 presents an absolute GS energy shift of 5.4 meV and an absolute wavefunction overlap shift of 0.126, corresponding to a relative difference of 0.5 % and 19.9 %, for the GS transition energy and the wavefunction overlap, respectively. For the graded structure a continuous increase in shift, for both the GS transition energy and wavefunction, for increased indium gradient is observed.

In addition to the material composition, changes to the height of the dot and their responsiveness to an applied E-field were simulated. The dot height was set to 3 nm, 5 nm, and 7 nm, a visual representation of these dots is depicted in Figure 5.19.

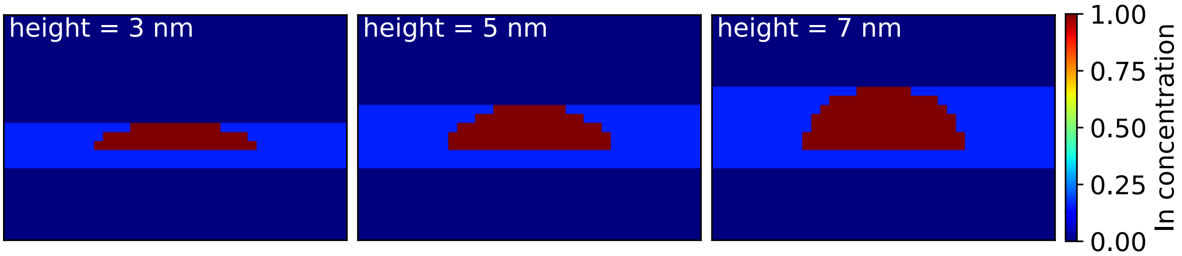

Figure 5.19: Depiction of a 3 nm (left), 5 nm (middle), and 7 nm (right) high lens-shaped dot.

The dot structures with different heights all show the same trend as the previously discussed structures, both the GS transition energy and the wavefunction overlap decreases as a function of increasing E-field, as can be seen in Figure 5.20 and 5.21. However, the QD presenting a height of 3 nm, shows a significantly smaller absolute and relative shift for both the energy and the overlap, as can be observed in Figure 5.20. When increasing the E-field from no field to 60 kV/cm an absolute shift of 0.6 meV and a relative shift of 0.066 % is observed for the transition energy, whereas an absolute shift of 0.012 and a relative shift of 1.3 % is observed for the wavefunction overlap. This shows how the change due to an applied field is significantly reduced for smaller dots. This is further supported by analysing the shift in GS transition energy and wavefunction overlap due to an applied E-field for the 7 nm tall dots. Here the exact opposite occurs observing a significantly stronger absolute and relative shift for the transition energy and the wavefunction overlap, as can be observed in Figure 5.21. A shift from no field to 60 kV/cm, induces an absolute shift of 6.7 meV and a relative shift of 0.7 % for the transition energy, and an absolute shift of 0.12 and a relative shift of 17 % for the wavefunction overlap.

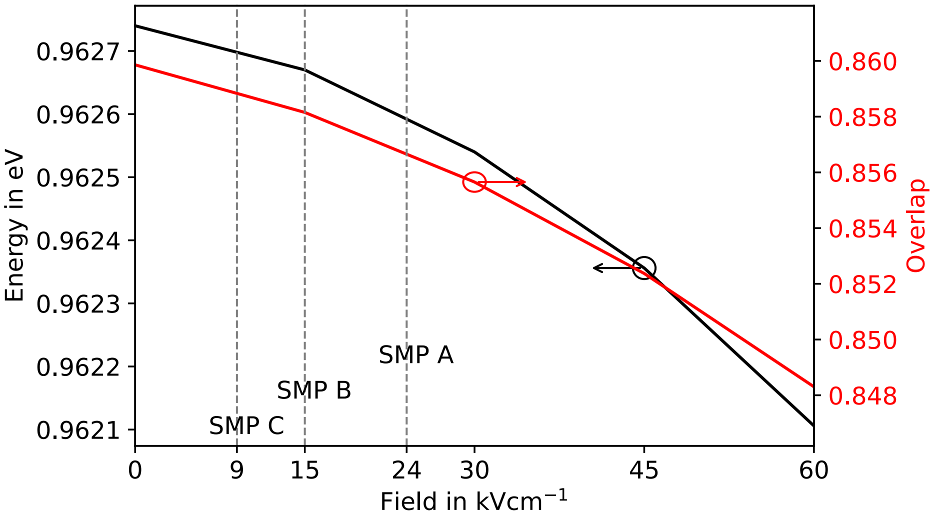

Figure 5.20: Depiction of the change in GS transition energy (black) and GS wavefunction overlap (red) as a function of E-field, for dots that are 3 nm high. The dotted lines indicate the strength of the simulated built-in field for Sample (SMP) A, B, and C.

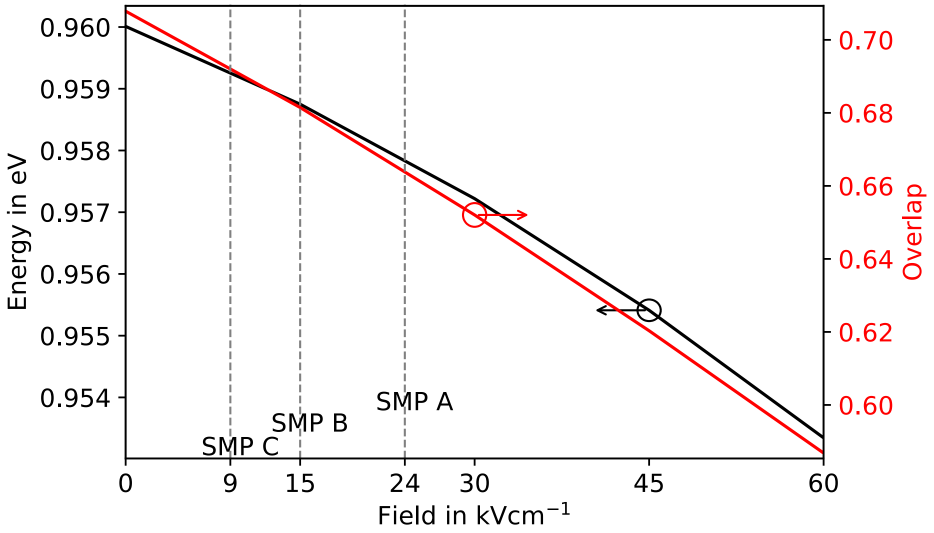

Figure 5.21: Depiction of the change in GS transition energy (black) and GS wavefunction overlap (red) as a function of E-field, for dots that are 7 nm high. The dotted lines indicate the strength of the simulated built-in field for Sample (SMP) A, B, and C.

5.2.2. Reverse Bias Measurements

The setup discussed in Section 3.3.6 was used to study the effect of reverse bias on the absorption spectra of Sample A, B, and C. For each sample the shift in energy of the GS modal absorption peak was identified as function of reverse bias. The shift in energy is identified based on the shift of the first absorption peak. By fitting a Gaussian function to the measured data, the energy of the first absorption peak is identified, given by the mean of the fitted Gaussian. The uncertainty in the peak energy is equal to the uncertainty of the mean obtained from the Gaussian fit. The energy of the different absorption peaks for Sample A, B, and C, under various RB conditions are presented in Figure 5.22, the errors on the values are too small to be visible[15].

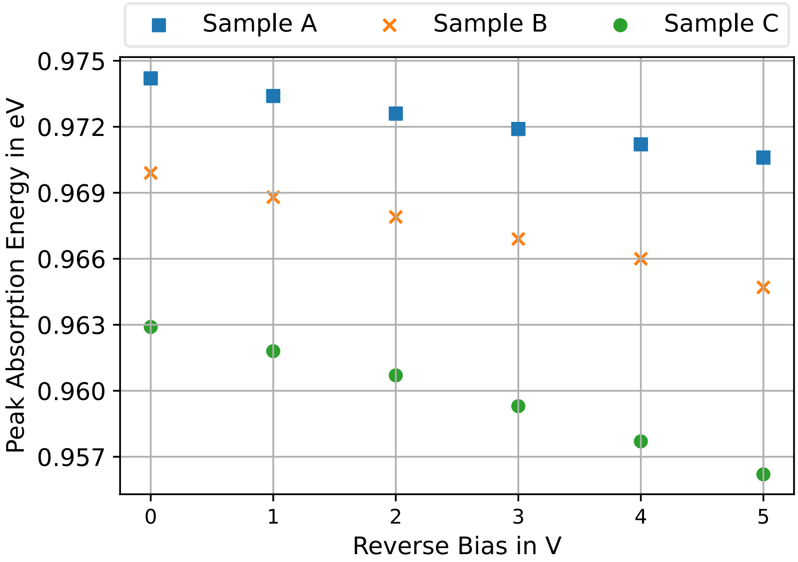

Figure 5.22: GS modal absorption peak as a function of reverse bias for Sample A (blue pentagons), B (orange squares), and C (green crosses).

A red shift in the absorption spectra for increasing RB is observed for all three samples. By tracking the peak of the GS absorption, the QCSE shift was quantified, the shift in energy as a function of RB is summarised in Table 5.2.

Table 5-2: Summary of the energy shifts for varying applied RB.

	0 V → 1 V	1 V → 2 V	2 V → 3 V	3 V → 4 V	4 V → 5 V
Sample A					
ΔE (in meV)	0.8	0.8	0.7	0.7	0.6
Sample B					
ΔE (in meV)	1.1	0.9	1	0.9	1.3
Sample C					
ΔE (in meV)	1.1	1.1	1.4	1.6	1.5

---

[15] The largest identified error was of 0.1 meV.

Table 5.2 and Figure 5.22 show that the energy shifts due to RB vary from sample to sample. Sample C shows the strongest shift of 6.7 meV, and Sample A presents the weakest shift of 3.6 meV for a 5 V swing. Sample B presents a shift of 5.2 meV for a 5 V swing.

Even though the QD structures were designed to emit at the same wavelength (~1.3 µm), differences in their responsiveness to an external bias were observed. The difference in energy shift to an external field bias amongst the three samples is ascribed to different descriptions of the individual dots. The shape, dimensions, and material composition of the QD impact their responsiveness to an electric field.

5.2.3. Comparison Between Simulations and Measurements

To be able to relate the simulated E-fields across the dots to the RB measurements, the resulting E-field due to a corresponding bias needed to be identified. This was done by simulating the different measured samples using Photon Design's Harold QCSE package. This allowed the simulation of reverse bias effects on the entire epitaxial structure. From the simulations the E-fields across the dot layers for 0 V up to 5 V RB were identified for the three different samples, the results are depicted in Figure 5.23. From Figure 5.23 it can be seen that the E-field is significantly different for each sample with Sample A presenting the highest E-field across the dot layer at each bias and Sample C presenting the lowest. This is partially attributed to the lower aluminium content in the cladding layer of Sample A, as more voltage is dropped across the layers with higher Al concentration. Additionally, Sample A presents the thinnest intrinsic part of the p-i-n junction, amongst the three samples. This leads to a larger built-in field as the electric field of the i-region is inversely proportional to its thickness [121].

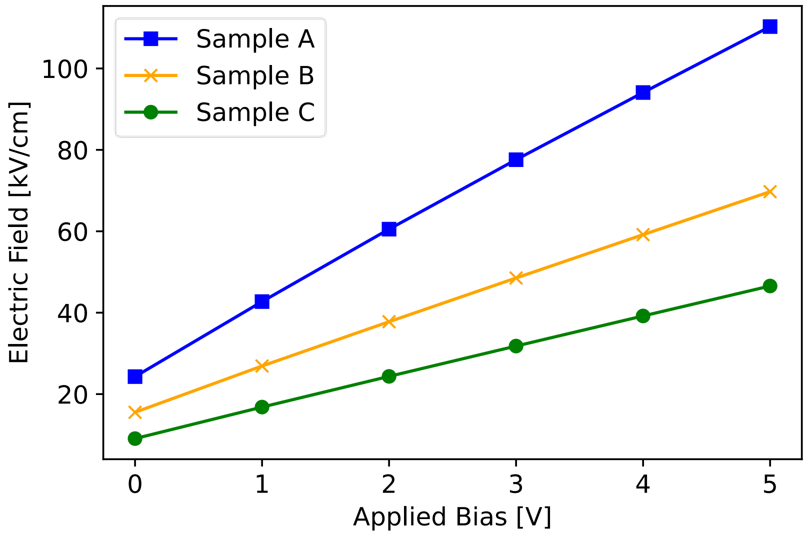

Figure 5.23: Depiction of the simulated electric field across the dot layer for Sample A (blue squares), Sample B (orange crosses), and Sample C (green dots).

With the knowledge of how the applied bias translates to an electric field, a closer comparison between the measured samples was conducted. To highlight the difference in responsiveness to the electric field of the three samples, the shift in energy for an equal shift in E-field was analysed. For an internal field shift from 24 kVcm^{-1} to 43 kVcm^{-1} for each sample an energy shift of 0.8 meV, 1.6 meV, and 3.5 meV was identified for Sample A, Sample B, and Sample C, respectively. While the exact energy shift at those values were not known for Sample B and C, they were linearly interpolated based on the available data. This highlights the significantly stronger experienced shift in energy due to an applied E-field of Sample C, in comparison to Sample A, and Sample B.

Furthermore, the transition energy as a function of electric field can be investigated, as depicted in Figure 5.24. The measured data points are fitted to a quadratic equation, $E_{GS} = a \times E^2 + b \times E + c$. Where E_{GS} is the GS transition energy, E is the strength of the electric field, and a, b, and c, and the fitting parameters.

Sample	Fitting Parameter a [eVcm^2/kV^2]	Fitting Parameter b [eVcm/kV]	Fitting Parameter c [eV]
Sample A	$4.3 \times 10^{-8} \pm 1.1 \times 10^{-8}$	$-4.8 \times 10^{-5} \pm 0.2 \times 10^{-5}$	0.9753 ± 0.0001
Sample B	$-2.2 \times 10^{-7} \pm 1.5 \times 10^{-7}$	$-7.5 \times 10^{-5} \pm 1.3 \times 10^{-5}$	0.9711 ± 0.0003
Sample C	$-1.4 \times 10^{-6} \pm 0.2 \times 10^{-6}$	$-1.0 \times 10^{-4} \pm 0.1 \times 10^{-4}$	0.9639 ± 0.0002

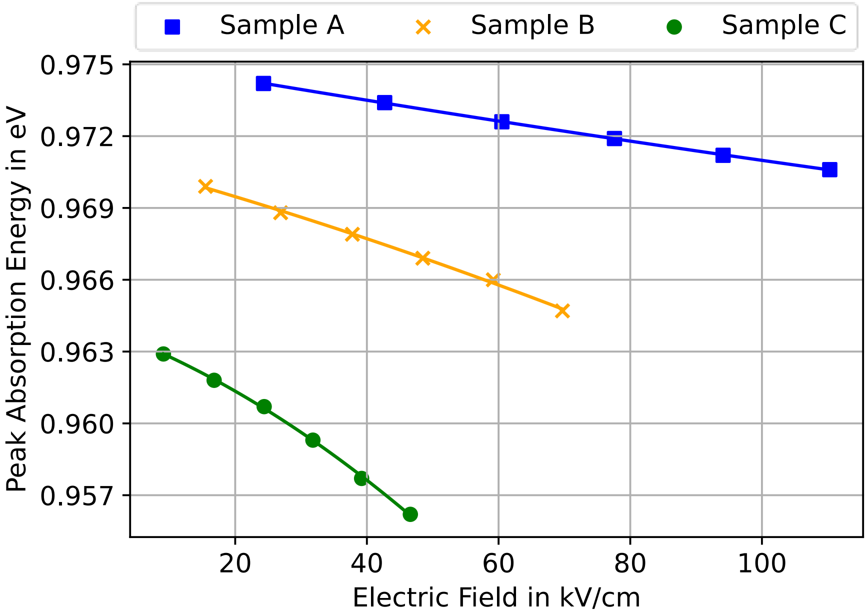

Figure 5.24: Depiction of GS transition energy as a function of electric field, for Sample A, B, and C.

The different samples are differently impacted by the influence of an applied electric field. The response to the electric field is strongest for Sample C and weakest for Sample A, this is supported by the identified fitting parameters, where the absolute value of the a and b fitting parameters are largest for Sample C, and lowest for Sample A. Interesting to note is that the sign of the fitting parameter a of Sample A is opposite to the sign of Sample B and C, further highlighting the difference in response to an electric field amongst the three different samples.

In addition to comparing the measured samples amongst each other, the simulated E-fields for a given RB can be used to directly compare the simulations of the dots to measurements.

For Sample A, applying 2 V RB led to an electric field of 60 kV/cm, increased from 24 kV/cm at 0 V. For this swing an absolute shift of 1.6 meV and a relative shift of 0.16 % was measured. This is the lowest measured relative swing amongst the three samples. However, looking at the dot structure of height of 3 nm, an even smaller relative shift, of 0.04%, was simulated for an E-field shift from 24 kV/cm to 60 kV/cm. This shows that the measurements can be matched by correctly adjusting the height of the dot structure.

For Sample B, applying a 4 V RB led to an electric field of 59 kV/cm, increased from 15 kV/cm at 0 V. For this swing an absolute shift of 3.9 meV and a relative shift of 0.4 % was measured. Similar relative shifts were obtained by the graded InAs dot structures, 0.29 % and 0.33 %, for the dot with 80 % indium at the base and 60 % indium at the base, respectively.

For Sample C, applying a 5 V RB led to an electric field of 47 kV/cm, increased from 9 kV/cm at 0 V. For this swing an absolute shift of 6.7 meV and a relative shift of 0.7 % is measured. None of the simulated structures presented a relative shift that matches the large measured shift of Sample C. Looking at the highly graded InAs dot, with a 60 % indium concentration at its base, a relative shift of 0.3 % is simulated, significantly smaller than the measured shift. Further simulations of using both material mixing and graded indium content were not able to increase the relative shift of the GS transition energy. Even the 7 nm high dot only presents a relative shift of 0.5 % for the applied RB shift. However, even taller dots or a combination of taller dots and more highly graded dots could replicate the measured shift.

While the above comparison shows that the simulations do not entirely capture the effects of RB on entire QD structures. The ability to simulate individual dots, with control over their shape and composition allows to make connections between the impact of the QCSE and the shape and composition of the individual dot. This can in theory be used to adjust the dot growth to tailor the response of the dot to an external bias. While indium segregation is difficult to suppress, techniques exist that can decrease or increase its extent [120], therefore presenting a degree of control over the gradient of the dot and with it also a control over its response to an electric field. A similar argument can be made for changing the height of the dot. Moreover, material mixing can be further increased in post-growth processes, using for example rapid thermal annealing [122]. This numerical analysis is not only restricted to individual dots, but can also be applied to entire epitaxial structures, which, in theory, can then be used for optimization of the epitaxial layers prior to fabrication for the design of opto-electronic modulators.

5.3. **Doping Strategies in QD Material**

Type III-V semiconductor lasers are described by a light electron mass in the CB and a heavy electron-hole mass in the VB. This has the consequence that during carrier inversion the lower excited levels of the VB are less likely to be empty than it is for the lower excited states of the CB to be filled, i.e., under lasing condition, the electrons transition from filled CB states to almost filled lower states [123]. The imbalance between individual transition states, e.g. the GS of the CB and the GS of the VB, as depicted in Figure 5.25, impedes lasing. This directly reduces gain, as it is proportional to the inversion, $f_c - f_v$, with a maximum value of 1, under full inversion. A first attempt at maximising the inversion is to introduce additional free spaces in the VB for the electrons to transition to. This can be achieved through p-type modulation doping.

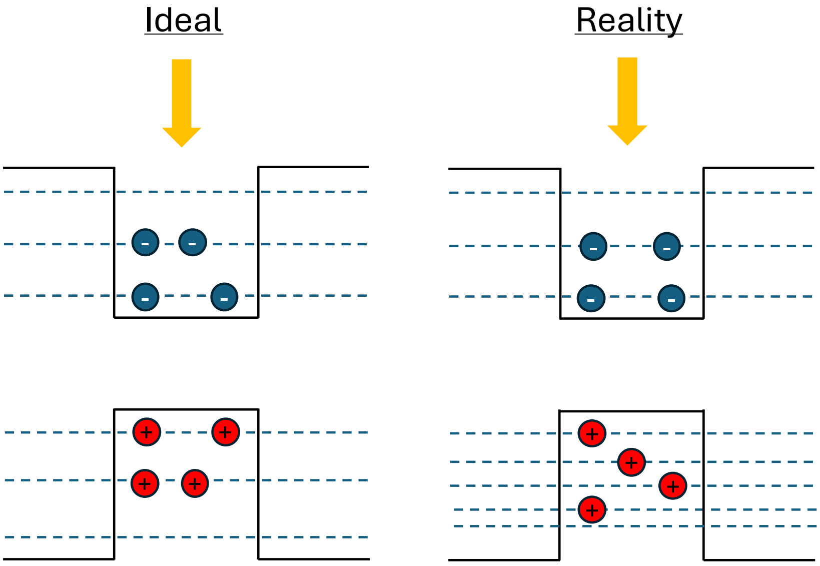

Figure 5.25: Schematic depiction of the distribution of electrons (blue, negative sign) and electron-holes (red, plus sign) inside a QD under forward bias (indicated by the yellow arrow), for the ideal (left) and real scenario (right). The dashed line represent the available energy levels inside the CB and VB.

P-type doping is the process of introducing an element with a lower number of covalent electrons into the system. For example, in GaAs the introduction of Beryllium leads to the presence of an element with two valence electrons[16], creating empty covalent bonding positions [124]. These empty positions effectively increase the number of sites that can be occupied by electrons, as is desired for type III-V semiconductor lasers. For

---

[16] Compared to Ga with three valance electrons and As with five valence electrons.

QD based semiconductor lasers, this has been implemented using p-type modulation doping. This technique introduces p-type dopants not directly in the active material, instead in a layer in proximity to the dots. Effectively separating the carrier holes, which migrate inside the dot, and the ionized dopants [125]. A schematic representation of p-type modulation doping is given in Figure 5.26. This technique has been widely studied. For example, Shchekin and Deppe (2002) used p-type modulation to improve the performance of QD lasers, arguing that their devices were competitive with the commercially available InP lasers of the time [126]. Further research was done directly comparing undoped and p-type modulation doping. Sandall et al. (2006) studied three dot stacks with varying doping levels. They concluded that p-type doping leads to an increase in maximum modal gain at fixed quasi-Fermi level separation. Furthermore, the presence of additional charge carriers had no impact on the internal loss of the structure. However, the doping also led to an increase in non-radiative recombination [127]. A similar conclusion was obtained by Zhang et al. (2018) [128], who included gain simulations to further support their argument that p-type modulation doping can not only improve gain, but also present higher differential gain, which is desirable for directly modulated lasers, mode-locked lasers, and narrow linewidth lasers. However, they had also concluded that p-type modulation doping increased non-radiative recombination [128]. Additional investigations were conducted to further improve the functionality of QD devices, leading to direct n-type doping.

Similar to p-type doping additional charge carriers are introduced into the structure by adding elements presenting a different number of valence electrons. For example, silicon, which has four valence electrons, can be used to dope InAs, by occupying sites which are usually occupied by indium, which has three valence electrons. This effectively increases the number of electron carriers in the system [124]. A schematic representation is given in Figure 5.26. This technique has been used in QD active material to improve opto-electronic device performance. This was shown by Wang et al. (2012), who reported improved output power when using n-type doped QDs [129]. Additionally Zun-Ren et al. (1997) reported better lasing efficiency and a reduced threshold current density for n-type doped QD lasers [130].

While p-type modulation does not affect the dot growth, it makes it difficult to control the carrier concentration inside the dots [131]. Direct n-type doping allows improved control of the carrier concentration within the individual dots. However, the introduction of Si directly into the dot material effects the growth of the QDs, which in turn impacts the emission spectra of the dots [132]. Furthermore, the presence of a dopant inside the dot alters the confining potential, additionally impacting the emission spectra of the dot [133]. This has the undesired effect that the dot growth needs to be “recalibrated” to obtain the desired emission spectra. Additionally, the introduction of donor dopants was shown to be consistent with the passivation of non-radiative recombination [134]. Work done by Deng et al. (2022) [135], directly compared the effects of p-type modulation doping, and direct n-type doping to undoped dots in the context of QD lasers. In this work, PL spectra of each sample was measured and, supported by simulations, it was shown that n-type doping led to changes in the transition energy of the dots. Low temperature PL investigations in combination with AFM measurements indicated that the reduction in PL emission is due to increased dot sizes [134,136]. Additionally, the threshold current of lasers, fabricated using the three different active material were taken at different temperatures. At room temperature, the n-type doping presented a lower threshold current than both the undoped and p-type doped structures. Interestingly, the undoped structure presented a lower threshold current than the p-type doped structure, which was argued to be due to the increase of non-radiative recombination. Additionally, the emission wavelength of the laser was studied for different temperatures. The measurements showed that the n-type doped laser jumped to ES lasing at lower temperatures, than for the undoped and p-type doped structures. The change in lasing wavelength is an undesirable effect as the emission wavelength is ideally constant under any operation conditions [135]; highlighting another advantage of p-type doping.

With both p-type doping and n-type doping presenting improvements to QD active material, the next logical step is to use both in the same dot structure. This was implemented by Wang et al. (2023) [137], who fabricated ridge waveguide lasers using co-doped and p-type modulation doping. The comparison between the two structures clearly showed that the co-doped material led to lasers, which possessed a lower threshold current, higher output power, and better temperature stability [137]. Similar conclusions were obtained by Deng et al. (2024) [138], who compared co-doped lasers to undoped, n-type, and p-type modulation doping, and concluded that the co-doped laser presented the best performance in terms of threshold current density with a wide operating temperature range up to 165 °C. Further work on high temperature lasing was done by Mishra et al. (2025), who used co-doped QDs, achieving a lasing temperature up to 202 °C under pulsed operations, outperforming undoped QD lasers by 20 °C [6].

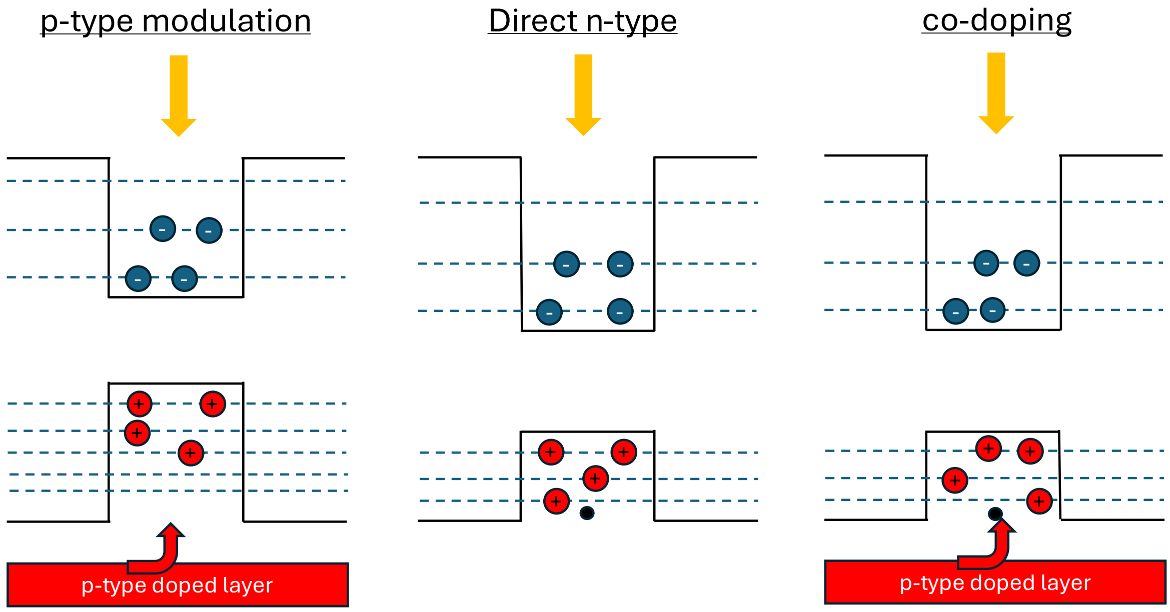

Figure 5.26: Schematic depiction of charge carrier within a QD for p-type modulation doping (left), direct n-type doping (middle), and co-doping (right). The black dot is used to indicate the ionised donor.

Due to the possible improvements that can be obtained from doped structures, it is of interest to be able to simulate n-type doping and p-type modulation doping. For both p-type and n-type doping the additional charge carriers impact the carrier distribution. This change can be tracked through the Fermi level of the system. For an intrinsic material, the Fermi level is identified based on the charge neutrality condition, i.e., equal number of electrons and holes in the structure $n = p = n_i$, where n, and p are the density of electrons and holes, respectively, and n_i is the intrinsic charge carrier density. The same condition applies for doping, however, the charge density now also depends on the ionized dopant concentration, using, N_D^+, to refer to the ionized donor concentration, and N_A^-, to describe the ionized acceptor concentration. Ionized, here refers to the possibility that not all dopants are ionized, depending on the current state of the system. For a given dopant density, material system, and temperature, the Fermi-level can be identified. The exact details are covered in Chapter 1 of "Physics of Semiconductor Devices" by Sze & Ng [139].

5.3.1. P-type Modulation Doping

P-type doping for QDs is done through modulation, i.e., the dopants are not located in the active material, the effect on the Fermi level due to the presence of the additional charge carriers is accounted for by the solver used to identify the carrier distribution in the epitaxial structure. Therefore, the same strategy as implemented in Section 4.2.3 was used to simulate p-type modulation doping without any modifications to the individual dots. Additionally, it was assumed that the lifetimes are unaffected by the presence of p-type modulation, as well as associating any empirically observed increases in non-radiative recombination as a biproduct of a reduced growth quality. The effect of p-type modulation doping was investigated by comparing the simulated gain spectra to that of the three samples investigated in Section 4.2.3, where the only difference was replacing a 10 nm thick undoped GaAs layer with a 10 nm thick doped GaAs layer. The doped layer was placed 15 nm above the active dot material, beryllium was used as dopant, with a dopant density of $4.5\times10^{17}\text{cm}^{-3}$, which equates to about ten additional holes per dot for each sample. The following figures all show a significant increase in modal gain with the addition of p-type dopants. Based on the implemented model a favourable occupation probability of the QD states is obtained, leading to increased modal gain.

The QD gain model replicates the conclusion of Zhang et al. (2018) [128], who empirically and numerically observed an increase in modal gain for p-type modulation doping. A similar increase in modal gain was numerically predicted by Deppe et al. (2002) [140], as well as work done by Smowton et al. (2007) [141], who measured improved gain characteristics for p-type modulated structures.

In addition to the modal gain, the differential gain, G', was investigated. While G' is commonly given as the ratio of change in gain and change in carrier density, in this context it was identified as the change in gain divided by the change in current density, i.e., $G' = dG/dJ$. This was done to give a more direct correlation between change in gain due to changes in the injected current. G' is commonly investigated as it not only gives an insight into how the gain is affected by the bias input, but can also be used to identify the linewidth enhancement factor (LEF). The differential gain for the undoped and p-type modulation doped structures are summarised in Table 5.4, 5.5, and 5.6. For p-type modulation a clear increase in differential gain is observed, except for Sample B at high currents, where the occupation probability of the GS is already nearly fully occupied at 1733 Acm^{-2}. This agrees with the work done by Kim et al. (2006) [142], who empirically investigated the differential gain of p-type modulation doped QD structures. The simulations recreated the desired outcome of p-type modulation doping, an increase in modal gain and an increase in differential gain. The increase in gain can be used to fabricate lasers with lower threshold current. Additionally, a better differential gain would lead to a lower LEF, which effectively improves the stability of the emission. Furthermore, the model is now able to further investigate the impact on doping density and location of the modulation layer on the gain spectrum. Effectively, allowing the optimisation of the doping conditions prior to fabrication of the QD device.

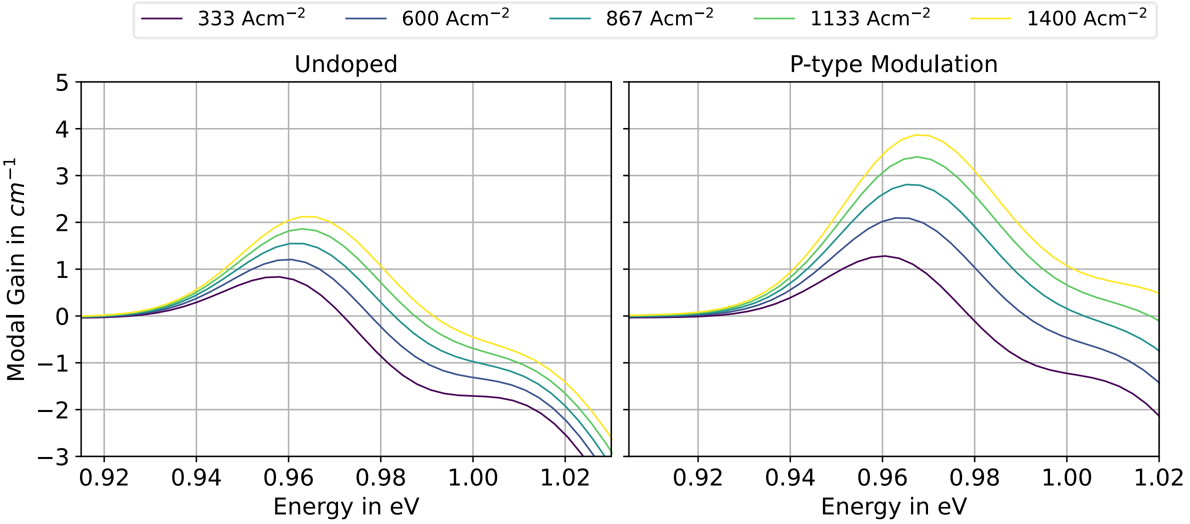

Figure 5.27: Depiction of modal gain for undoped (LHS) and p-type modulation doping (RHS) of Sample A.

Table 5-4: Summary of simulated differential gain of Sample A for undoped and p-type modulation doping.

dG/dJ in cmA^{-1}	**Undoped**	**p-type modulation**
333 Acm^{-2} → 600 Acm^{-2}	0.0014	0.0031
600 Acm^{-2} → 867 Acm^{-2}	0.0013	0.0027
867 Acm^{-2} → 1133 Acm^{-2}	0.0012	0.0022
1133 Acm^{-2} → 1400 Acm^{-2}	0.0010	0.0018

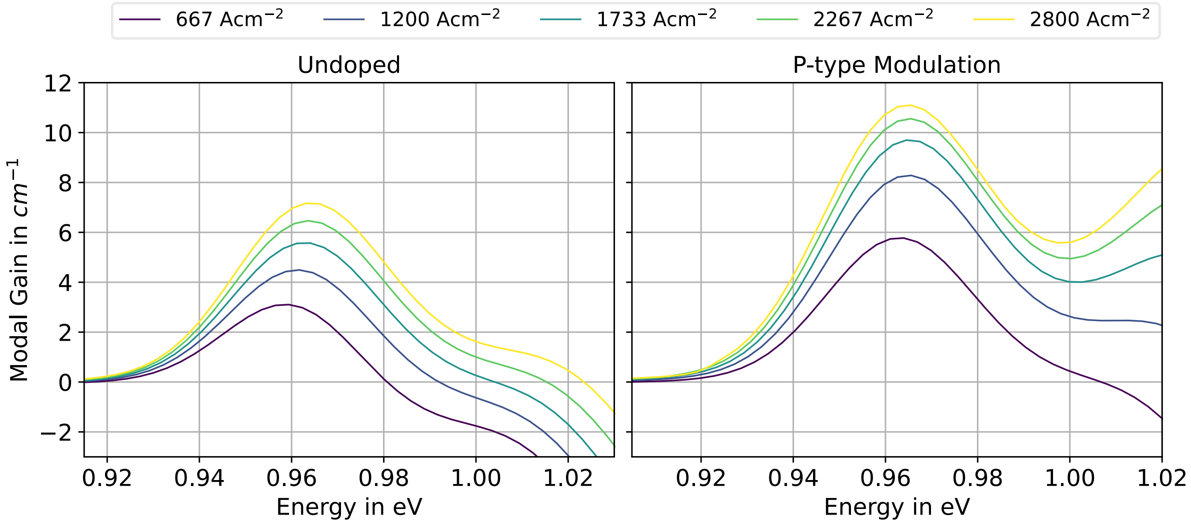

Figure 5.28: Depiction of modal gain for undoped (LHS) and p-type modulation doping (RHS) of Sample B.

Table 5-5: Summary of simulated differential gain of Sample A for undoped and p-type modulation doping.

	Undoped	**p-type modulation**
667 Acm^{-2} → 1200 Acm^{-2}	0.0026	0.0047
1200 Acm^{-2} → 1733 Acm^{-2}	0.0020	0.0027
1733 Acm^{-2} → 2267 Acm^{-2}	0.0017	0.0016
2267 Acm^{-2} → 2800 Acm^{-2}	0.0013	0.0010

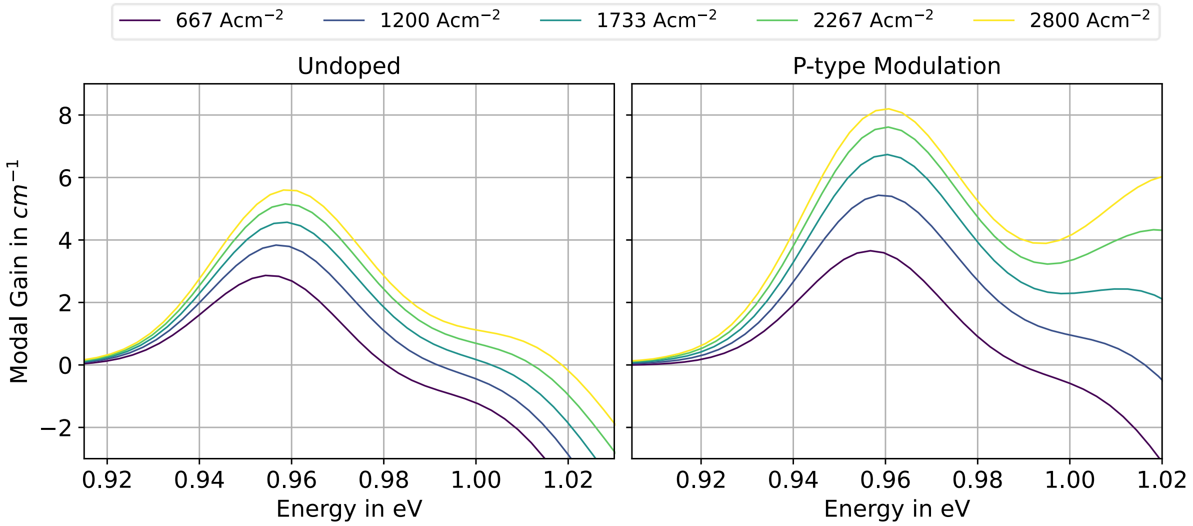

Figure 5.29: Depiction of modal gain for undoped (LHS) and p-type modulation doping (RHS) of Sample C.

Table 5-6: Summary of simulated differential gain of Sample A for undoped and p-type modulation doping.

	Undoped	**p-type modulation**
667 Acm^{-2} → 1200 Acm^{-2}	0.0018	0.0033
1200 Acm^{-2} → 1733 Acm^{-2}	0.0014	0.0025
1733 Acm^{-2} → 2267 Acm^{-2}	0.0011	0.0017
2267 Acm^{-2} → 2800 Acm^{-2}	0.0008	0.0011

5.3.2. Description of N-doping in QDs

There are two factors that impact the emission spectrum of n-doped dots. The first one is the increase in dot size, leading to a redshift, and the second is the presence of the dopants themselves, whose impact is discussed in more detail. At room temperature and higher, the dopant is very likely to be ionized, affecting the confining potential of the QD. The presence of ionised charges in the dot create a potential energy, which needs to be accounted for. Debye screening can be used to identify the potential caused by the presence of ions in semiconducting material [143]. Debye screening was originally established for quasi-neutral plasmas, for semiconductors, the covalent electrons and the core atoms replicate similar conditions. The charge potential, $V(\boldsymbol{r})$ is then given by,

$$V(\boldsymbol{r}) = \frac{q}{4\pi\varepsilon|\boldsymbol{r}|}e^{-\frac{|\boldsymbol{r}|}{\lambda_D}} \tag{5.4}$$

Where q is the charge of the ion, ε is the material dependent dielectric constant, and λ_D is the Debye screening length, which is given by,

$$\lambda_D = \sqrt{\frac{\varepsilon k_b T}{e^2 n}} \tag{5.5}$$

Where k_b is Boltzmann's constant, T is the temperature, and n is the electron density. For bulk material the carrier density is readily identified, with $n = 2\left(\frac{m_e k_b T}{2\pi\hbar^2}\right)^{3/2}$. For InAs material at room temperature the Debye screening length is 14.3 nm. However, the carrier density in QDs differs significantly from that in the bulk. In this work a low unconfined carrier density (<10^{17} cm^{-3}) was assumed for QDs. Under this assumption the Debye screening length is large compared to the dot dimension, effectively turning the screened charge potential into an unscreened charge potential. For the following simulations of n-doped QDs the charge potential due to an ionized dopant is given by the potential due to a point charge,

$$V(\boldsymbol{r}) = \frac{e}{4\pi\varepsilon\boldsymbol{r}} \tag{5.6}$$

Care needs to be taken when implementing the above expression due to the singularity at $r = 0$. To avoid this it was assumed that the charge is uniformly distributed over a sphere of radius R. The radius of the sphere is set to the atomic radius of the dopant, for example, for a silicon dopant the atomic radius is 111 pm. The final description of the charge potential due to a dopant is then given by,

$$V(\boldsymbol{r}) = \begin{cases} \dfrac{e}{4\pi\varepsilon r} & \text{for } r > R \\ \dfrac{e}{8\pi\varepsilon R}\left(3 - \dfrac{r^2}{R^2}\right) & \text{for } r \leq R \end{cases} \tag{5.7}$$

An example of the charge potential resulting from a single silicon dopant is depicted in Figure 5.30. Based on the resulting potential its impact on the confined charge carriers can be identified.

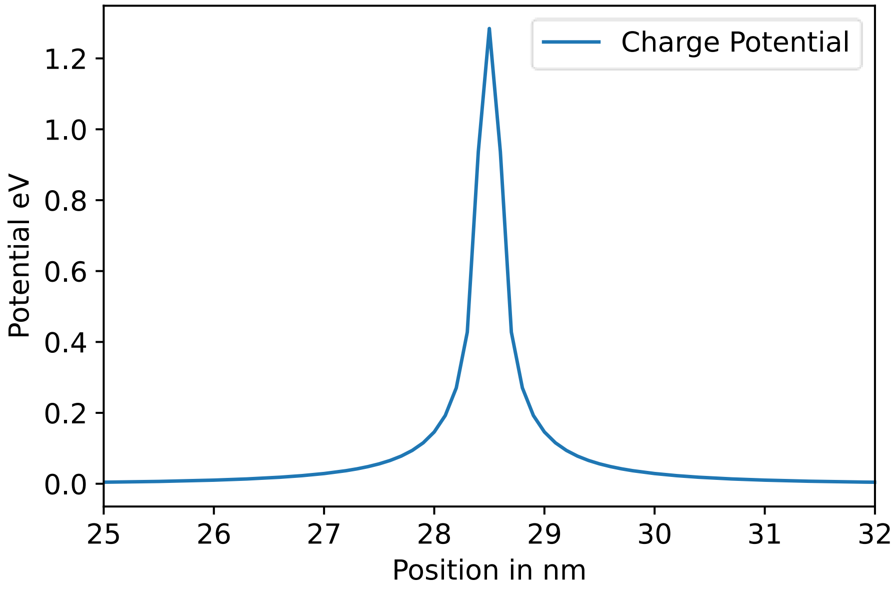

Figure 5.30: Depiction of the charge potential due to an ionized Si dopant.

For multiple dopants the charge potential is equivalent to the sum of the charge potential resulting from the individual dopants.

5.3.3. Impact of N-dopant on QD Confined Charge Carriers

The presence of an ionized dopant has a significant impact on the confining potential of the dots. This in turn impacts the energy level and the wavefunction of the confined charge carriers. The exact impact was investigated for various positions of the dopant for a 20 nm wide and 5 nm high lens-shaped QD. The locations of the dopant is visible in Figure 5.31, depicting the confining potential of the CB of the aforementioned dot structure. The dopant was not placed exactly in the centre of the dot. The dopants distance between the centre of the dot was not the same for the dots depicted in c) and d) in Figure 5.31, with the dopant in d) being 1 nm closer to the centre.

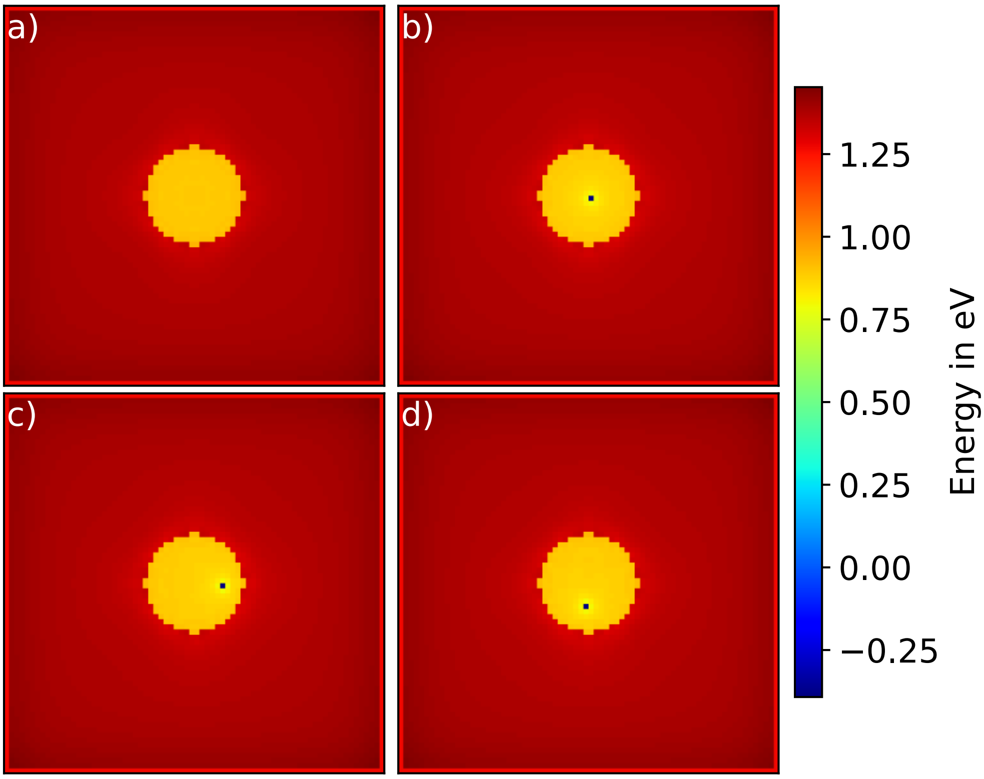

Figure 5.31: Depiction of the CB confining potential of an undoped dot (a), doped dot located 1 nm off-centre from the dot (b), 6 nm to the x-direction from the centre of the dot (c), and 5 nm in the y-direction from the centre of the dot (d).

The resulting energy and probability densities are depicted in Figure 5.32, for the CB states and in Figure 5.33 for the VB states, in each case showing the GS, 1st ES, and 2nd ES of the dot structures depicted in Figure 5.31. From Figure 5.32 and 5.33 a couple of observations can be made. Firstly, the energies reduce due to the presence of the dopant. The location of the dopant within the dot impacts the extent of which the energy changes. Specifically, the closer the dopant is to the centre, the more the energy of the states in the CB and VB are affected. Secondly, the dopant has a visible impact on the wavefunction of the confined states. The presence of the dopant splits the degeneracy of the 1st ES and 2nd ES of the CB, which is also dependent on the location of the dopant. The impact of the dopant on the wavefunctions is reflected in the wavefunction overlap values. The overlap between the GS of the CB and the VB reduces from 0.84 to 0.71 for the undoped and doped dot, respectively. This is expected as the electron is attracted by the dopant and the hole is repulsed. Thirdly, while the CB states and VB states reduce in energy the overall transition energy increases for the doped dots. The undoped dot presents a transition energy of 0.922 eV, which increases to 0.928 eV for the central dopant. The transition energy changes less for the non-central dopants, with a transition energy of 0.922 eV and 0.923 eV for c) and d), respectively.

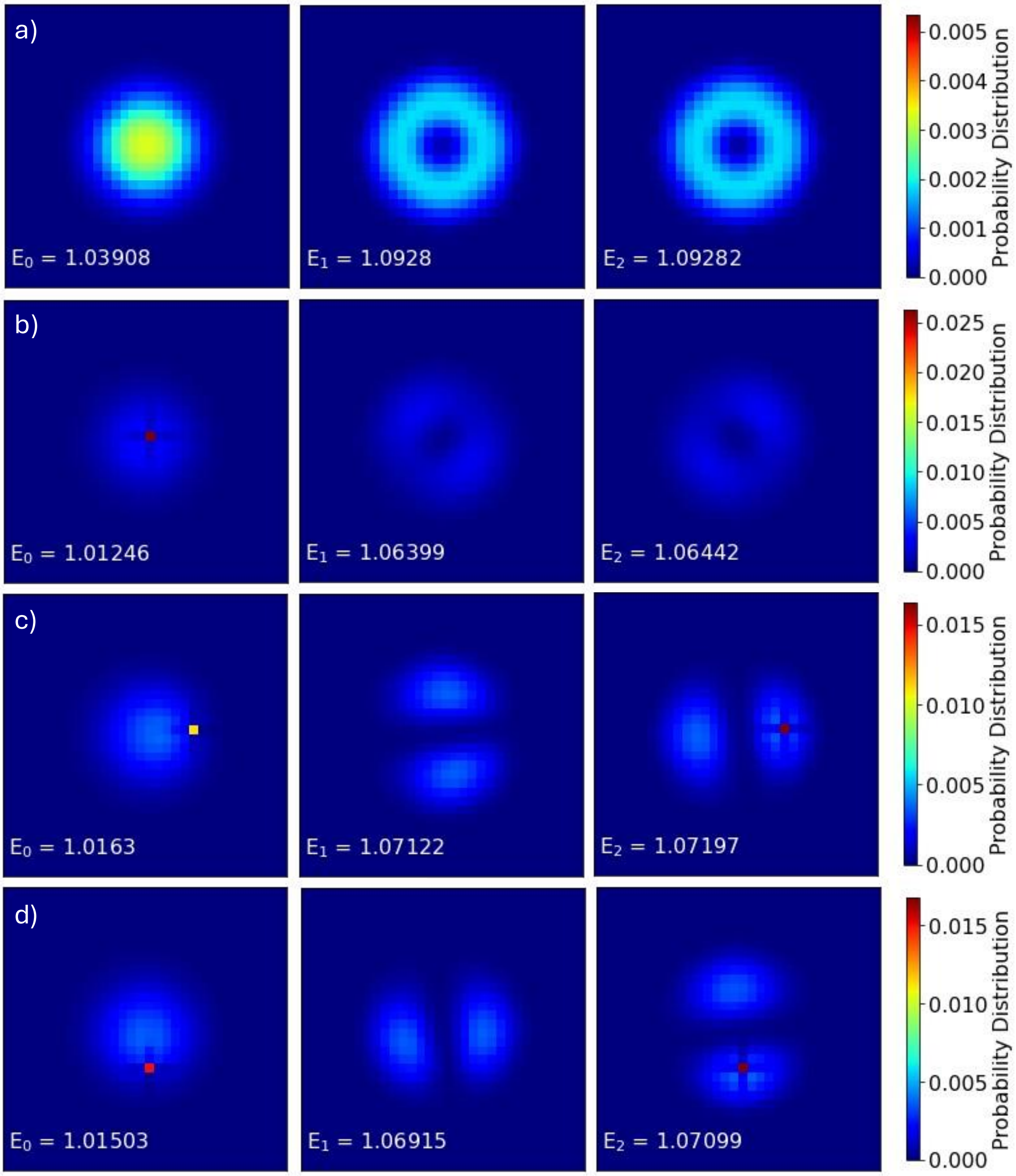

Figure 5.32: Depiction of energy and probability density of the GS, 1st ES and 2nd ES energy states of the CB of an undoped dot (a), dot with dopant 1 nm off-centre (b), dot with dopant 6 nm in the x-direction from the centre (c), dot with dopant 5 nm in the y-direction from the centre (d).

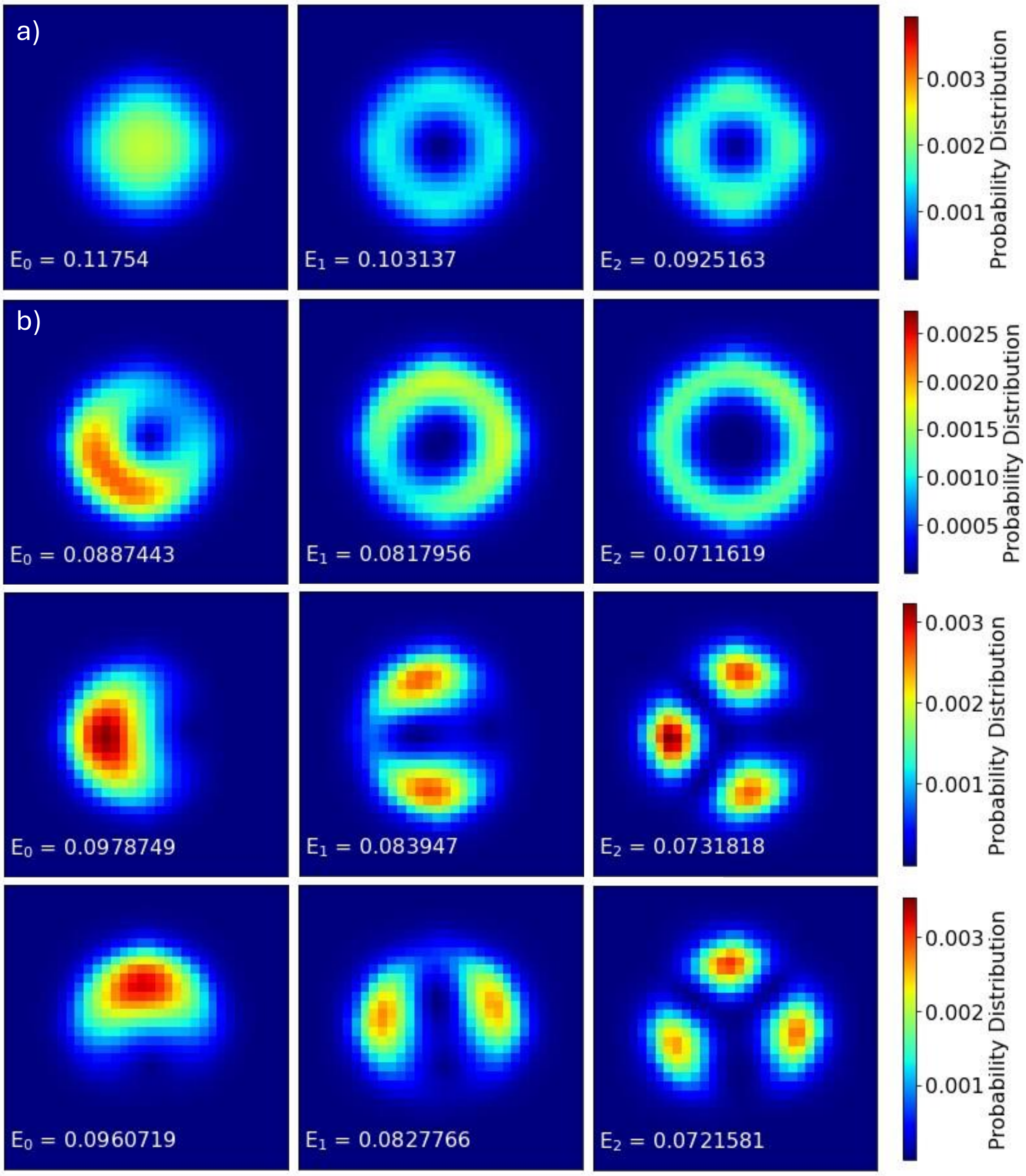

Figure 5.33: Depiction of energy and probability density of the GS, 1st ES and 2nd ES energy states of the VB of an undoped dot (a), dot with dopant 1 nm off-centre (b), dot with dopant 6 nm in the x-direction from the centre (c), dot with dopant 5 nm in the y-direction from the centre (d).

From the simulation of the different dopants an interesting insight into the location of the dopant can be made. Since the position of the ion within the dot impacts its transition energy one would expect additional broadening of the absorption or gain spectrum, if the ion was randomly distributed within the dot. This, however, was not encountered in the Literature. Work done by Wang et al. (2012) [144] investigated the PL spectra for n-doped dots with varying doping densities. They first observed a reduction in FWHM of the spectrum due to doping, before it started to broaden for higher doping densities. This would suggest that the dopant is located in the same location for each dot. Meaning that there is a physical reason for this phenomena, with, for example, the dopant facilitating the nucleation of the dot, and thus being predominantly located at the centre of the dot.

5.3.4. Impact of N-type Doping on Gain

Following the procedure implemented in Section 4.2.3 the gain for three different n-doped dot ensembles was simulated. To allow for direct comparison, the exact same epitaxial structure (as used in Harold) as those for Sample A, B, and C was used as in Section 4.2.3, with the addition of n-dopants in the WL. Additionally, the same dot description (used in the Schrödinger Solver) was used except for the presence of a single positive ion, located at the centre of the dot. No changes to the recombination lifetimes were made. The simulated gain for n-doped dots was directly compared to the undoped gain simulations, as presented in Section 4.2.3. The simulations are depicted in Figure 5.34, 5.35, and 5.36.

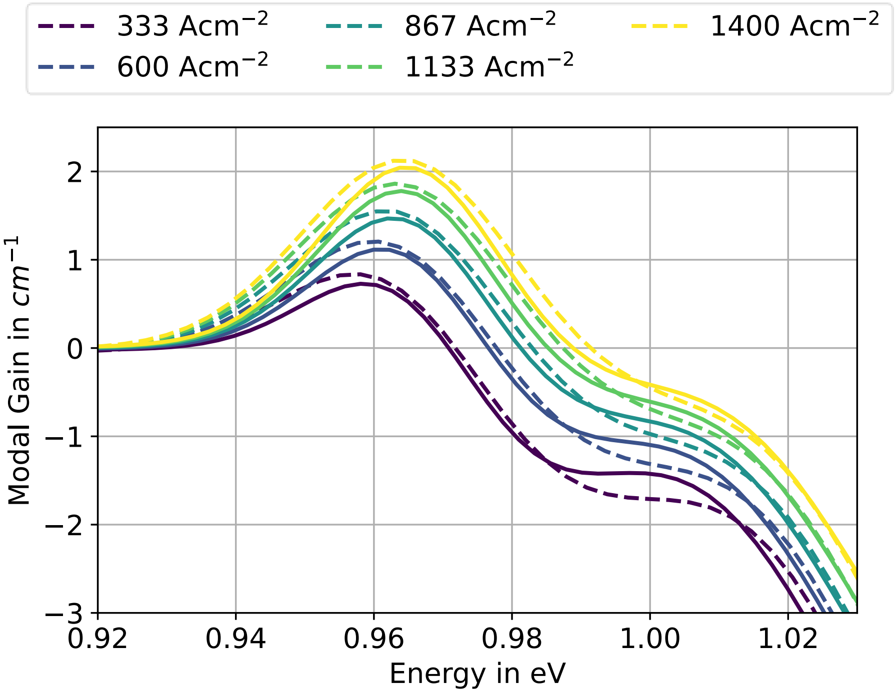

Figure 5.34: Depiction of modal gain for undoped (dashed) and n-doped (solid) dot ensemble of Sample A.

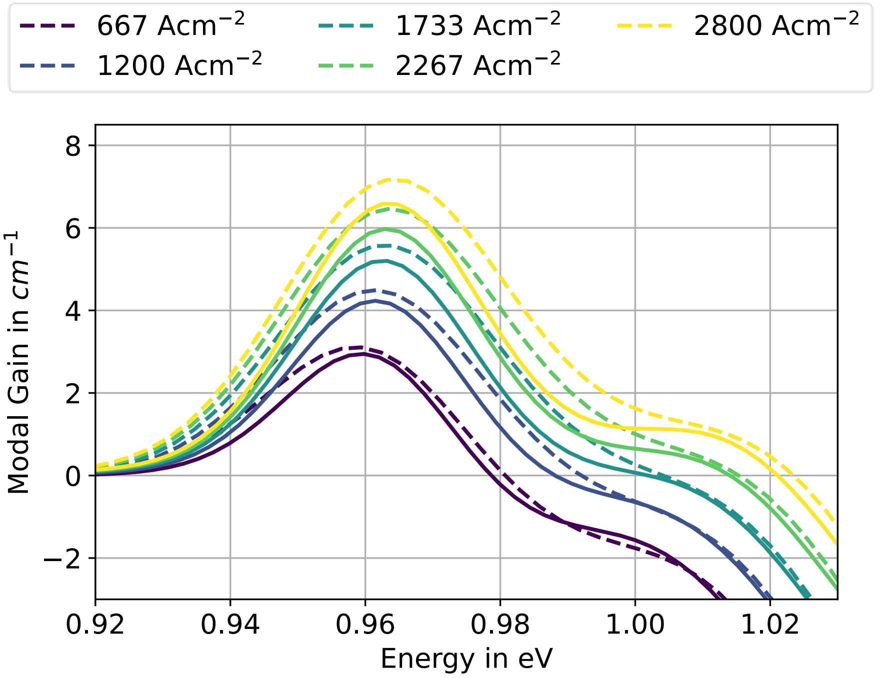

Figure 5.35: Depiction of modal gain for undoped (dashed) and n-doped (solid) dot ensemble of Sample B.

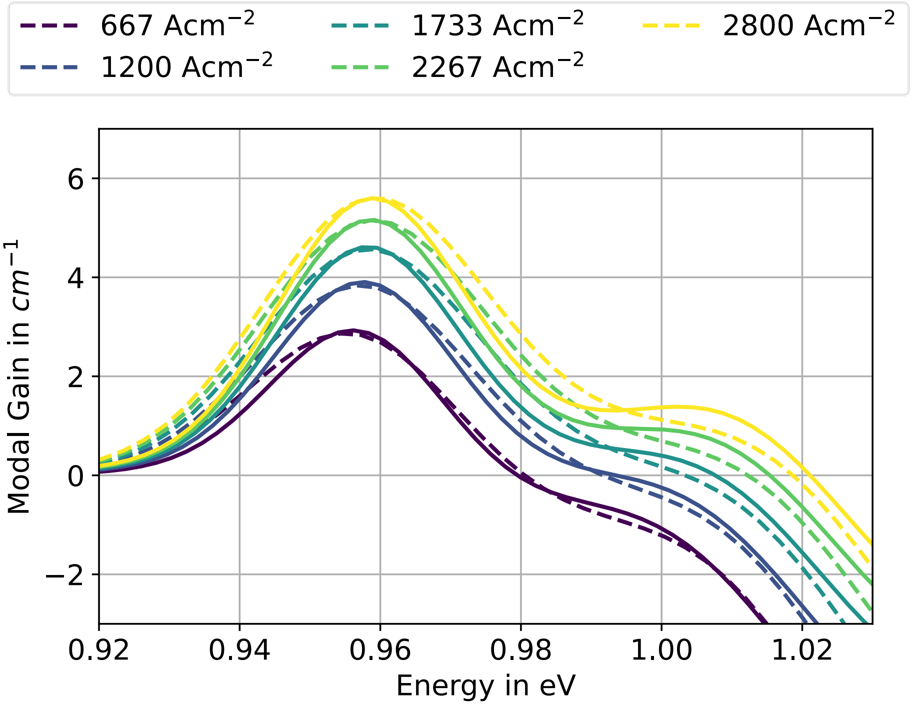

Figure 5.36: Depiction of modal gain for undoped (dashed) and n-doped (solid) dot ensemble of Sample C.

From Figure 5.34 and 5.35, the n-doped QDs present a reduced modal gain for Sample A and B. From Figure 5.36 an increase in modal gain is presented for the n-doped dots in Sample C.

From the occupation probabilities of the dot states the inversion of the dots can be investigated for the undoped and n-doped case. Inversion, I, is defined by Equation 5.8,

$$I = f_e + f_h - 1 \tag{5.8}$$

Where f_e is the occupation probability of the electron in the CB, and f_h is the occupation probability of the hole in the VB. For lasing a high inversion is desired, with a maximum value of 1. The inversion of the mean dot of Sample A, B, and C at different currents is depicted in Figure 5.37.

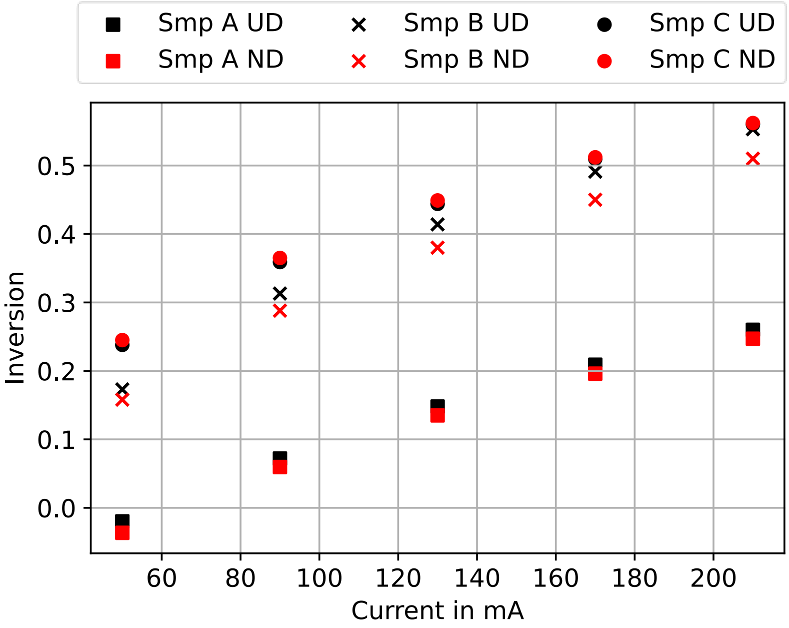

Figure 5.37: Inversion of the mean QD of dot ensemble describing Sample A (squares), B (crosses), and C (points), for undoped (UD, black) and n-doped (ND, red) QDs.

From Figure 5.37 it can be seen that the inversion decreases for Sample A and B, however, increases for Sample C. This is due to the slightly larger difference in dot width between the undoped and n-doped dots for Sample C, where the n-doped dots are 0.5 nm wider than the undoped dots. For Sample A and B the dots widen by 0.4 nm, due to n-doping. Holes in wider dots are less confined, which facilitates the occupation of holes in the VB, Sample C, therefore, presents a higher occupation probability of the VB GS in comparison to Sample A and B, leading to a higher inversion, as no change in the

CB occupation probability was observed. However, in neither case is the difference in inversion significant and has little to no impact on the modal gain. Two additional n-doping effects impact the modal gain. Firstly, the presence of the n-dopant reduces the wavefunction overlap between the CB and VB states of the dots. A simulated GS overlap of 0.79 for the undoped dots is reduced to 0.69 for n-doped dots, a 13 % reduction in overlap value. This reduction in overlap results in an overall decrease of 23.7% in both the modal gain and the absorption. However, this reduction is not visible in the simulated gain spectra, as the reduction in modal gain is countered by the increase in dot width. The GS transition energy increases due to the n-dopant. Therefore, for the doped dots to emit at the same energy as the undoped dots, the doped dots need to be wider than the undoped dots. The mean dot of Sample A increases from 22.7 nm to 23.1 nm, for undoped and n-doped dots, respectively. The mean dot of Sample B increases from 23.2 nm to 23.6 nm, for undoped and n-doped dots, respectively. The mean dot of Sample C increases from 23.7 nm to 24.2 nm, for undoped and n-doped dots, respectively. Less energy broadening occurs for wider dots for equal standard deviation, leading to a narrower gain spectra and an increase in modal gain, as the same standard deviation was used for the doped and undoped dot ensembles.

The model was adjusted to include direct n-doping into the description of individual QDs. The energy levels and wavefunctions of the doped dots are used to identify the modal gain. These simulations were done for three distinct epitaxial structures. N-doping presented minimal overall impact on the gain spectra of the three samples. For the implemented rate equation model, n-type doping shows no significant change in the inversion, I. The presence of the dopant leads to a reduction in wavefunction overlap between the CB and the VB states of the dots. The reduction in modal gain is, however, countered by the narrowing of the gain spectrum due to an ensemble described by wider dots for equal standard deviation. Therefore, under the assumption that the recombination lifetimes are equal for undoped and n-doped dots, and that non-radiative recombination is negligeable, no significant impact of n-doping on the modal gain was observed for the implemented dot simulations. However, if n-doping were to improve non-radiative recombination, as discussed in the Literature [134], favourable gain conditions would be observed. Under those conditions, n-doping would lead to improved lasing conditions.

5.4 Summary

This chapter covered various additional circumstances, which from the perspective of device fabrication are of interest. Since devices can heat up under operation, the impact of increased temperature on the absorption and gain spectra was investigated. Preliminary comparison, where the material parameters were represented as a function of temperature based on their behaviour in bulk material, has proven to be insufficient to account for the experimentally identified changes in absorption spectra due to changes in temperature. By relying on QD sample dependent Varshni parameters the shift in the absorption spectra was replicated. Additionally, the gain model established in Chapter 4 was used to simulate the gain of three different dot samples and the results were compared to measurements. Good agreement between simulations and measurements were achieved for a range of 21.5 °C to 80 °C for all three samples at all measured current densities.

Additionally, QD material were investigated for the use of optoelectronic modulation. In that regard the changes to the ground state transition energy was investigated under various electric field directions and strengths. Various dots described by different dimensions and material profiles were simulated. Furthermore, reverse bias measurements were conducted to identify the impact on the absorption spectra due to changes of the E-field. The experiment showed that the responsiveness to an E-field is sample dependent. A very low shift in transition energy was observed for Sample A, which matched the simulated QCSE shift for short QDs. The simulated shift for 5 nm high dots with either material mixing or graded indium composition, matched the experimental shifts observed for Sample B. Sample C presented the highest measured RB shift, which was not directly matched by simulations. However, taller dots and additional grading in the indium concentration are predicted to replicate the measured shift.

Lastly, the effects of p-type modulation doping and direct n-type doping were investigated. Various gain spectra were simulated for p-type modulation doping, which predicted increased modal gain and differential gain. The simulated p-type modulation structures clearly follow the trends presented in the Literature. Further investigation into the n-type doping were discussed. Focusing on the impact of an ionized dopant on the energy levels and the wavefunctions of the confined carriers, as well as the overall impact on the modal gain. A clear impact on the energy levels and wavefunctions was observed. The ionized n-dopant increases the confinement of the CB states and reduces the confinement of the VB states, the overall effect leads to an increase in transition energy. Additionally a reduction in wavefunction overlap is observed between the GS of the CB and the GS of the VB. The overall impact of n-doping on the modal gain, however, is minimal. Based on the implemented rate equation model, no significant impact on the occupation probability of the QD states is observed. Furthermore, the reduction in GS transition overlap is nearly fully cancelled out by the narrowing of the modal gain spectrum.

6. **Conclusions and Future Work**

In this work, the 8-band k.p model, and the continuous mechanical strain model, including the strain induced piezoelectric potential, were implemented for the description of charge carriers in individual InAs dots grown on $In_xGa_{1-x}As/GaAs$. In combination with a rate equation model, for the identification of the occupation probability of the individual dots, and commercially available software, describing the current distribution, entire epitaxial structures were simulated under varying bias conditions. Further investigations were focused on the simulation of temperature effects, reverse bias effects, and the impact of p-type modulation doping, and direct n-type doping on the absorption and gain spectra of QD material.

The simulation results of the individual dot descriptions were directly compared to work done in the Literature. Additionally, simulated absorption and gain spectra were validated using experimental measurements. Through appropriate adjustments to the experimental setup, heating effects, caused by using a DC current source, were minimised and reverse bias measurements were conducted.

6.1. Conclusion to This Work

Various models for the description of confined charge carriers in QDs were discussed. The 8-band k.p model was identified as the ideal model for the simulation of confined charge carriers in individual dots, based on a combination of requirements, including being limited to desktop level computational resource, ease of implementation, and having a detailed description of the underlying physics at play. While the 8-band k.p model is commonly used, surprisingly little Literature is available detailing the appearance of spurious solutions. The reason for their appearance and the chosen procedure to eliminate them was presented here. The final description of the charge carriers was obtained through a central finite difference scheme, leading to an eigenvalue problem. Solving the eigenvalue problem allowed the identification of the description of the energy levels and wavefunction of electrons in the CB and electron-holes in the VB of dots. While the focus was on lens-shaped InAs QDs grown on GaAs, the implemented model can, in theory, identify the energy levels and wavefunctions of dots of arbitrary shape and material composition.

To match the continuous description of 8-band k.p model used for the charge carriers, the continuous mechanical strain description, which also gives an accurate physical description, was used to identify the strain tensor of 3D dot structures. To account for abrupt material interfaces in the dot heterostructure a staggered grid mesh in combination with the central difference approximation was used. A 3D Poisson solver was implemented to obtain the piezoelectric potential resulting from the strained zinc blende material. The resulting impacts on the confining potential of the dot were incorporated into the 8-band k.p solver. The presence of piezoelectricity impacted the energy levels of the charge carriers by a few meV for InAs QDs and reduced the symmetry of the system down to C_{2v}.

Further steps were taken to obtain the modal absorption of an ensemble of dots for a given epitaxial structure. This was achieved by sampling individual dots and relaying changes in their energy to changes in parameters used for the description of the dot ensemble. In this work, this was done for changes in energy of the CB and VB states of the dot as a function of the width of the dot. Additionally, the momentum matrix elements were identified for the case of the 8-band k.p model. In combination with the description of the fundamental transverse electric mode, identified using Photon Design's FIMMWAVE, the modal absorption was simulated.

Due to limited knowledge about the description of the individual dots, the simulation had to be calibrated to measurements, as well as making assumptions about the height and shape of the dot. Initial calibration still showed significant variations between the simulations and the measurements, with simulations predicting a significantly lower dip in modal absorption between the GS to GS and the 1st ES to 1st ES absorption peak. Further investigations showed that to be able to match simulations to measurements the dot ensemble had to be either described by asymmetric dots or by a bimodal dot distribution. Both of these assumptions were used to further simulate the modal absorption of two distinct dot structures. In either case an excellent agreement between measurements and simulations was achieved for both samples.

Similar to the absorption spectrum, the modal gain spectrum was identified, with the addition of the identification of the occupation probabilities of the energy states of the dots. This was achieved by implementing a rate equation model described in the Literature, and using a Fermi-Dirac distribution for the occupation probability of the VB states. This rate equation model requires the description of the charge distribution throughout the entire epitaxial structure, which was obtained from Photon Design's Harold package. To connect the QDs to the 3D dot structure within Harold, the dots were assumed to act as deep states within a QW, meaning that the transition between the surrounding material and the dots is controlled through the SRH lifetime of the quantum well. Additional calibration of the SRH lifetime with respect to the injection current density was conducted on Sample A, leading to a current density dependent lifetime that was used for two additional samples. This allowed the simulation of the gain of various dot structures described by different epitaxial layers and dot with different shapes and material composition. While the modal gain of the dot samples was not exactly replicated, with a significant underestimation of the 1st electron ES to 1st hole ES gain, the trends of the gain as a function of injection current density was well replicated. Any mismatch between experiments and simulations was attributed to the model not including carrier-carrier coulomb effects, as well as using the same spontaneous transition lifetime for all transitions. Based on the successful implementation of the gain model, the model was fully integrated into one of Photon Design's software packages. After validating the calculated absorption and gain spectra across three distinct quantum-dot samples, the framework is now robust enough to support the simulation and optimisation of QD epitaxial structures, linking a nanoscopic description of individual dots with a microscopic representation of the full heterostructure.

In addition to ambient conditions, the dot structure was investigated at temperatures up to 80 °C. Preliminary simulations of changing just the bandgap and the lattice constant as a function of temperature failed to replicate the measured shift of the absorption spectra. Additionally, the extent of the shift in temperature differed amongst the three measured samples. Only by using sample dependent Varshni parameters, for the shift in energy as a function of temperature, can the measured shift in temperature be replicated by the simulations. This lead to the conclusion that the energy shift of the spectra was dependent on the material surrounding the dot and not just the material of the dot itself. To be able to simulate the change in gain as a function of temperature additional calibration of the spontaneous transition lifetime was conducted. The calibration was done for a single injection current density at different temperatures. The temperature dependent spontaneous lifetime was then used in combination with the identified Varshni parameters to simulate the gain spectra for the three different samples at RT, 40 °C, 60 °C, and 80 °C. The calibrated model can be used to investigate the absorption and gain spectra of different QD structures over the temperature range of 20 °C up to 80 °C.

In the Literature, QD material was investigated as a potential candidate as active material in electro-optic modulators. This motivated a numerical and experimental investigation into reverse bias effects of QD structures. Using an updated measurement setup, which minimised heating effects, the shift in energy due to an applied reverse bias for three different samples was investigated. The measurements showed significant variation of the reverse bias effect on the different dot samples. The inconsistent impact of the changes in the electric field was numerically investigated. It was shown that the material composition and the height of the dot can significantly impact the RB shift. Simulations suggested that small (in height) dots with little material mixing are less responsive to changes in the E-field. Tall dots, and dots presenting an indium graded material composition, on the other hand, showed a higher shift in transition energy as a function of applied reverse bias. Through additional simulations of the electric field profile across the entire epitaxial structure, it was possible to correlate the simulated individual dots to the measured modal absorption under different reverse biases. Thus combining the epitaxial structure and the individual dots for different reverse biases. This in turn, will allow the optimization of the epitaxial structure and individual dots for the design of QD-based opto-electronic modulators.

Doping effects had been the recent centre of attention in investigations to further improve the QD material used in state-of-the-art lasers. Specifically focusing on p-type modulation doping, direct n-type doping, and both, which is commonly referred to as co-doping. Therefore, it is of interest for the established model to be able to include these doping strategies. This was achieved for both p-type modulation doping and direct n-type doping. The improved carrier occupation due to p-type modulation doping showed a significant increase in the modal gain, as well as the differential gain. For n-type doping additional simulations were conducted to identify the impact of the location of the dopant on the QD transition energies and wavefunctions of the confined carriers. This showed that the location of the dopant within the dot alters the emission spectrum, therefore indicating that random distribution of the dot should lead to a broadened absorption or emission spectrum. This however was not observed in the Literature, therefore indicating that the location of the dopant within the dot is the same in each dot. Additionally, the modal gain was only minorly affected by the presence of the n-dopants. The implemented model can now simulate the gain spectra for various doping techniques, and can, in theory, be used to optimise the doping conditions prior to fabrication.

6.2. Future Work

Symmetry arguments during the identification of charge carriers of individual dots could be investigated. Disregarding piezoelectric effects, the symmetry of the lens- or pyramid-shaped dots can be used to reduce the size of the simulation window by a factor of 4. Even if the piezoelectric effect is included, the simulation window could be reduced by a factor of 2, significantly reducing the necessary computational costs. If the 8-band k.p model is kept, this would significantly speed up simulation times. However, this could also be used to improve the accuracy of the solver by incorporating additional bands, without increasing the simulation runtime. This would be necessary for dot material possessing additional bands which are energetically closely spaced, for example material including nitrogen.

Further investigations into the occupation probability of the energy levels of individual dots under varying biases might lead to a better match for higher excited transitions. Specifically, focusing on a theoretical description and empirical identification of the transition lifetimes and creating an improved non-linear solver, which can handle a wider range of input parameters without failing to converge. As well as including non-radiative recombination, potentially leading to a gain model which does not require additional calibration of the recombination rates between the dots and the wetting layer.

Further investigations could use the implemented model for the optimisation of modal gain for a QD epitaxial structure. Carrying out numerically investigations to improve epitaxial structures and dot descriptions leading to enhanced device functionality. Furthermore, it would be of interest to test the implemented model for different material compositions outside of $In_xGa_{1-x}As$, for example InAs grown on InP, which are of interest due to their emission spectra around 1550 nm. Additionally, taking the implemented model to simulate photonic devices and compare them to measurements could further validate the implemented model.

The study could benefit from additional experimental characterisation. For example, temperature induced changes in the spectrum were shown to be sample dependent, being able to identify what exactly causes that would allow for a more reliable and more widely applicable temperature dependent model. Similarly for the investigation into reverse bias effects. While the measured effects were replicated for different dot structures, having additional experimental data to support the simulation would give more confidence in the implemented model. Furthermore, while different doping strategies were numerically investigated, they could benefit from direct comparison to measurements.

References:

1. H. Fröhlich, "Die spezifische wärme der elektronen kleiner metallteilchen bei tiefen temperaturen," Physica **4**, 406–412 (1937).

2. M. Fox and R. Ispasoiu, "Quantum wells, superlattices, and band-gap engineering," Springer Handbooks 1 (2017).

3. L. E. Brus, "Electron–electron and electron-hole interactions in small semiconductor crystallites: The size dependence of the lowest excited electronic state," J Chem Phys **80**, 4403–4409 (1984).

4. J. C. Norman, R. P. Mirin, and J. E. Bowers, "Quantum dot lasers—History and future prospects," Journal of Vacuum Science & Technology A: Vacuum, Surfaces, and Films **39**, (2021).

5. Z. I. Alferov, "Nobel Lecture: The double heterostructure concept and its applications in physics, electronics, and technology," Rev Mod Phys **73**, 767–782 (2001).

6. P. Mishra, L. Jarvis, C. Hodges, A. Enderson, F. Albeladi, S.-J. Gillgrass, G. M. Jandu, R. Forrest, C. P. Allford, H. Deng, M. Tang, H. Liu, S. Shutts, and P. M. Smowton, "High Temperature Operation of Co-Doped InAs Quantum Dot Laser for O-Band Emission," IEEE Photonics J **17**, 1–6 (2025).

7. J. C. Norman, R. P. Mirin, and J. E. Bowers, "Quantum dot lasers—History and future prospects," Journal of Vacuum Science & Technology A: Vacuum, Surfaces, and Films **39**, (2021).

8. S. Melnik, G. Huyet, and A. Uskov, "The linewidth enhancement factor α of quantum dot semiconductor lasers," Opt Express **14**, 2950 (2006).

9. S. O'Hara, "The degradation of semiconductor light-emitting diodes, high-radiance lamps and lasers," J Phys D Appl Phys **10**, 409–430 (1977).

10. J. C. Norman, D. Jung, Z. Zhang, Y. Wan, S. Liu, C. Shang, R. W. Herrick, W. W. Chow, A. C. Gossard, and J. E. Bowers, "A Review of High-Performance Quantum Dot Lasers on Silicon," IEEE J Quantum Electron **55**, 1–11 (2019).

11. S. Y. Siew, B. Li, F. Gao, H. Y. Zheng, W. Zhang, P. Guo, S. W. Xie, A. Song, B. Dong, L. W. Luo, C. Li, X. Luo, and G.-Q. Lo, "Review of Silicon Photonics Technology and Platform Development," Journal of Lightwave Technology **39**, 4374–4389 (2021).

12. Z. Zhou, B. Yin, and J. Michel, "On-chip light sources for silicon photonics," Light Sci Appl **4**, e358–e358 (2015).

13. S. Chen, W. Li, J. Wu, Q. Jiang, M. Tang, S. Shutts, S. N. Elliott, A. Sobiesierski, A. J. Seeds, I. Ross, P. M. Smowton, and H. Liu, "Electrically pumped continuous-wave III–V quantum dot lasers on silicon," Nat Photonics **10**, 307–311 (2016).

14. C. H. Lin, J. P. Wu, Y. Z. Kuo, Y. J. Chiu, T. E. Tzeng, and T. S. Lay, "InGaAs self-assembly quantum dot for high-speed 1300 nm electroabsorption modulator," J Cryst Growth **323**, 473–476 (2011).

15. "Optical Simulation and Design Software | Ansys Optics," https://www.ansys.com/products/optics.

16. "Your source of photonics CAD tools | Photon Design," https://photond.com/.

17. J. Pond, G. S. C. Lamant, and R. Goldman, "Software tools for integrated photonics," Optical Fiber Telecommunications VII 195–231 (2020).

18. O. Hess and E. Gehrig, *Photonics of Quantum-Dot Nanomaterials and Devices: Theory and Modelling* (Imperial College Press, 2012).

19. P. M. Petroff and S. P. DenBaars, "MBE and MOCVD growth and properties of self-assembling quantum dot arrays in III-V semiconductor structures," Superlattices Microstruct **15**, 15 (1994).

20. K. Shimomura, T. Shirasaka, D. M. Tex, F. Yamada, and I. Kamiya, "RHEED transients during InAs quantum dot growth by MBE," Journal of Vacuum Science & Technology B, Nanotechnology and Microelectronics: Materials, Processing, Measurement, and Phenomena **30**, (2012).

21. R. Hogg, "Technology focus: Epitaxy semiconductorTODAY Material characteristics for MBE Comparison between MBE and MOCVD technologies," **19**, (n.d.).

22. P. M. Petroff, A. Lorke, and A. Imamoglu, "Epitaxially Self-Assembled Quantum Dots," Phys Today **54**, 46–52 (2001).

23. I. N. Stranski and L. Krastanow, "Zur Theorie der orientierten Ausscheidung von Ionenkristallen aufeinander," Monatsh Chem **71**, 351–364 (1937).

24. H. Y. Liu, M. Hopkinson, C. N. Harrison, M. J. Steer, R. Frith, I. R. Sellers, D. J. Mowbray, and M. S. Skolnick, "Optimizing the growth of 1.3 μm InAs/InGaAs dots-in-a-well structure," J Appl Phys **93**, 2931–2936 (2003).

25. G. T. Liu, A. Stintz, H. Li, T. C. Newell, A. L. Gray, P. M. Varangis, K. J. Malloy, and L. F. Lester, "The influence of quantum-well composition on the performance of quantum dot lasers using InAs-InGaAs dots-in-a-well (DWELL) structures," IEEE J Quantum Electron **36**, 1272–1279 (2000).

26. T. Walther, "Role of Interdiffusion and Segregation during the Life of Indium Gallium Arsenide Quantum Dots, from Cradle to Grave," Nanomaterials **12**, 3850 (2022).

27. A. D. Giddings, J. G. Keizer, M. Hara, G. J. Hamhuis, H. Yuasa, H. Fukuzawa, and P. M. Koenraad, "Composition profiling of InAs quantum dots and wetting layers by atom probe tomography and cross-sectional scanning tunneling microscopy," Phys Rev B **83**, 205308 (2011).

28. J. H. Blokland, M. Bozkurt, J. M. Ulloa, D. Reuter, A. D. Wieck, P. M. Koenraad, P. C. M. Christianen, and J. C. Maan, "Ellipsoidal InAs quantum dots observed by cross-sectional scanning tunneling microscopy," Appl Phys Lett **94**, (2009).

29. R. Y. Tanaka, N. M. Abe, E. C. F. da Silva, A. A. Quivy, and A. Passaro, "Modeling the 3D In profile of InxGa1-xAs/GaAs quantum dots," J Phys D Appl Phys **49**, 215101 (2016).

30. C. Y. Ngo, S. F. Yoon, C. Z. Tong, W. K. Loke, and S. J. Chua, "An investigation of growth temperature on the surface morphology and optical properties of 1.3 μm InAs/InGaAs/GaAs quantum dot structures," Nanotechnology **18**, 365708 (2007).

31. T. V Hakkarainen, J. Tommila, A. Schramm, A. Tukiainen, R. Ahorinta, M. Dumitrescu, and M. Guina, "Structural characterization of InAs quantum dot chains grown by molecular beam epitaxy on nanoimprint lithography patterned GaAs(100)," Nanotechnology **22**, 295604 (2011).

32. L. E. Franken, K. Grünewald, E. J. Boekema, and M. C. A. Stuart, "A Technical Introduction to Transmission Electron Microscopy for Soft-Matter: Imaging, Possibilities, Choices, and Technical Developments," Small **16**, (2020).

33. P. D. Siverns, S. Malik, G. McPherson, D. Childs, C. Roberts, R. Murray, B. A. Joyce, and H. Davock, "Scanning transmission-electron microscopy study of InAs/GaAs quantum dots," Phys Rev B **58**, R10127–R10130 (1998).

34. R. Murray, S. Malik, P. Childs, C. Roberts, B. Joyce, and H. Davock, "Scanning Transmission Electron Microscopy (STEM) Study of InAs/GaAs Quantum Dots," Jpn J Appl Phys **38**, 496 (1999).

35. A. Mikkelsen, N. Sköld, L. Ouattara, M. Borgström, J. N. Andersen, L. Samuelson, W. Seifert, and E. Lundgren, "Direct imaging of the atomic structure inside a nanowire by scanning tunnelling microscopy," Nat Mater **3**, 519–523 (2004).

36. I. Mal, D. P. Panda, B. Tongbram, D. P. Samajdar, and S. Chakrabarti, "Analytical modeling of temperature and power dependent photoluminescence (PL) spectra of InAs/GaAs quantum dots," J Appl Phys **124**, (2018).

37. S. Gaan, G. He, R. M. Feenstra, J. Walker, and E. Towe, "Size, shape, composition, and electronic properties of InAs/GaAs quantum dots by scanning tunneling microscopy and spectroscopy," J Appl Phys **108**, (2010).

38. R. Murray, S. Malik, P. Childs, C. Roberts, B. Joyce, and H. Davock, "Scanning Transmission Electron Microscopy (STEM) Study of InAs/GaAs Quantum Dots," Jpn J Appl Phys **38**, 496 (1999).

39. R. Heitz, O. Stier, I. Mukhametzhanov, A. Madhukar, and D. Bimberg, "Quantum size effect in self-organized InAs/GaAs quantum dots," Phys Rev B **62**, 11017–11028 (2000).

40. P. Offermans, P. M. Koenraad, J. H. Wolter, K. Pierz, M. Roy, and P. A. Maksym, "Atomic-scale structure and photoluminescence of InAs quantum dots in GaAs and AlAs," Phys Rev B **72**, 165332 (2005).

41. D. Poulin, A. Qarry, R. Somma, and F. Verstraete, "Quantum Simulation of Time-Dependent Hamiltonians and the Convenient Illusion of Hilbert Space," (2011).

42. P. Y. Yu and M. Cardona, "Vibrational Properties of Semiconductors, and Electron-Phonon Interactions," in *Fundamental of Semiconductors* (2010), pp. 107–158.

43. O. Stier, M. Grundmann, and D. Bimberg, "Electronic and optical properties of strained quantum dots modeled by 8-band k·p theory," Phys Rev B **59**, 5688–5701 (1999).

44. S. W. Belling, H. L. Cihak, and W. Li, "Finite element analysis of strain effects on symmetry reduction of semiconductor quantum dots," Superlattices Microstruct **120**, 22–30 (2018).

45. M. Ehrhardt and T. Koprucki, *Multi-Band Effective Mass Approximations : Advanced Mathematical Models and Numerical Techniques*, Lecture Notes in Computational Science and Engineering ; 94 (Springer, 2014).

46. Y. Li, O. Voskoboynikov, C. P. Lee, and S. M. Sze, "Computer simulation of electron energy levels for different shape InAs/GaAs semiconductor quantum dots," Comput Phys Commun **141**, 66–72 (2001).

47. C. Pryor, "Eight-band calculations of strained InAs/GaAs quantum dots compared with one-, four-, and six-band approximations," Phys Rev B **57**, 7190–7195 (1998).

48. M. G. Burt, "Fundamentals of envelope function theory for electronic states and photonic modes in nanostructures," Journal of Physics: Condensed Matter **11**, 53–83 (1999).

49. B. Maglio, L. Jarvis, M. Tang, H. Liu, and P. M. Smowton, "Modelling the effects of p-modulation doping in InAs/InGaAs quantum dot devices," Opt Quantum Electron **56**, 687 (2024).

50. M. Jaouane, R. Arraoui, A. Ed-Dahmouny, A. Fakkahi, K. El-Bakkari, H. Azmi, and A. Sali, "Finite element method simulation of electronic and optical properties in multi-InAs/GaAs quantum dots," The European Physical Journal Plus **139**, 222 (2024).

51. P. Harrison and A. Valavanis, "Quantum wells, wires and dots : theoretical and computational physics of semiconductor nanostructures," Comput Phys Commun **133**, 137–138 (2000).

52. A. Mittelstädt, A. Schliwa, and P. Klenovský, "Modeling electronic and optical properties of III–V quantum dots—selected recent developments," Light Sci Appl **11**, 17 (2022).

53. P. Sengupta, H. Ryu, S. Lee, Y. Tan, and G. Klimeck, "Numerical guidelines for setting up a k.p simulator with applications to quantum dot heterostructures and topological insulators," J Comput Electron **15**, 115–128 (2016).

54. H. Fu, L. W. Wang, and A. Zunger, "Applicability of the method to the electronic structure of quantum dots," Phys Rev B Condens Matter Mater Phys **57**, 9971–9987 (1998).

55. G. Klimeck, R. Chris Bowen, T. B. Boykin, and T. A. Cwik, "sp3s*Tight-binding parameters for transport simulations in compound semiconductors," Superlattices Microstruct **27**, 519–524 (2000).

56. M. Zieliński, "Including strain in atomistic tight-binding Hamiltonians: An application to self-assembled InAs/GaAs and InAs/InP quantum dots," Phys Rev B **86**, 115424 (2012).

57. I. Vurgaftman, J. R. Meyer, and L. R. Ram-Mohan, "Band parameters for III–V compound semiconductors and their alloys," J Appl Phys **89**, 5815–5875 (2001).

58. A. Sawamura, T. Kato, and S. Souma, "Improved tight-binding parameters of III–V semiconductor alloys and their application to type-II superlattices," Jpn J Appl Phys **61**, 021004 (2022).

59. Y. Tan, M. Povolotskyi, T. Kubis, T. B. Boykin, and G. Klimeck, "Transferable tight-binding model for strained group IV and III-V materials and heterostructures," Phys Rev B **94**, 045311 (2016).

60. W. Kohn, "Nobel Lecture: Electronic structure of matter—wave functions and density functionals," Rev Mod Phys **71**, 1253–1266 (1999).

61. L. W. Wang, A. J. Williamson, A. Zunger, H. Jiang, and J. Singh, "Comparison of the k·p and direct diagonalization approaches to the electronic structure of InAs/GaAs quantum dots," Appl Phys Lett **76**, 339–341 (2000).

62. C. Carmesin, "Tight-Binding based Investigation of Semiconductor Quantum Dots and Molybdenum Disulfide Nanobubbles : From Atomic Structure to Optical Spectra," (2018).

63. Crosslight, "Self-consistent quantum dot model demonstrated," .

64. nextnano, "Energy levels in a pyramidal shaped InAs/GaAs quantum dot including strain and piezoelectric fields," .

65. P. Blood, *Quantum Confined Laser Devices*, First edition., Oxford Master Series in Physics (Oxford University Press, 2015), Vol. 23.

66. A. Beya-Wakata, P.-Y. Prodhomme, and G. Bester, "First- and second-order piezoelectricity in III-V semiconductors," Phys Rev B **84**, 195207 (2011).

67. G. Bester, A. Zunger, X. Wu, and D. Vanderbilt, "Effects of linear and nonlinear piezoelectricity on the electronic properties of InAs/GaAs quantum dots," Phys Rev B **74**, 081305 (2006).

68. G. Bester, X. Wu, D. Vanderbilt, and A. Zunger, "Importance of Second-Order Piezoelectric Effects in Zinc-Blende Semiconductors," Phys Rev Lett **96**, 187602 (2006).

69. M. G. Burt, "The justification for applying the effective-mass approximation to microstructures," Journal of Physics: Condensed Matter **4**, 6651–6690 (1992).

70. T. Eissfeller, "Theory of the Electronic Structure of Quantum Dots in External Fields," Technischen Universität München (2012).

71. R. G. Veprek, S. Steiger, and B. Witzigmann, "Ellipticity and the spurious solution problem of k.p envelope equations," Phys Rev B **76**, 165320 (2007).

72. B. A. Foreman, "Effective-mass Hamiltonian and boundary conditions for the valence bands of semiconductor microstructures," Phys Rev B **48**, 4964–4967 (1993).

73. B. A. Foreman, "Elimination of spurious solutions from eight-band k·p theory," Phys Rev B **56**, R12748–R12751 (1997).

74. V. Anjan Kumar, N. B. Pendyala, and A. Banerjee, "Simulating the spectral response of quantum dot-in-well infrared photodetectors from eight band k.p method," J Appl Phys **116**, (2014).

75. D. Gershoni, C. H. Henry, and G. A. Baraff, "Calculating the optical properties of multidimensional heterostructures: Application to the modeling of quaternary quantum well lasers," IEEE J Quantum Electron **29**, 2433–2450 (1993).

76. I. O'Driscoll, P. Blood, and P. M. Smowton, "Random Population of Quantum Dots in InAs–GaAs Laser Structures," IEEE J Quantum Electron **46**, 525–532 (2010).

77. T. P. Felici and D. F. G. Gallagher, "On propagation through long step tapers," Special Issue of Optical and Quantum Electronics (2001).

78. R. A. Perez-Herrera, P. Roldan-Varona, M. Galarza, S. Sañudo-Lasagabaster, L. Rodriguez-Cobo, J. M. Lopez-Higuera, and M. Lopez-Amo, "Hybrid Raman-erbium random fiber laser with a half open cavity assisted by artificially controlled backscattering fiber reflectors," Scientific Reports 2021 11:1 **11**, 1–8 (2021).

79. L. A. Coldren, "Diode Lasers and Photonic Integrated Circuits," Optical Engineering **36**, 616 (1997).

80. B. W. Hakki and T. L. Paoli, "Gain spectra in GaAs double−heterostructure injection lasers," J Appl Phys **46**, 1299–1306 (1975).

81. K. L. Shaklee and R. F. Leheny, "DIRECT DETERMINATION OF OPTICAL GAIN IN SEMICONDUCTOR CRYSTALS," Appl Phys Lett **18**, 475–477 (1971).

82. P. Blood, G. M. Lewis, P. M. Smowton, H. Summers, J. Thomson, and J. Lutti, "Characterization of semiconductor laser gain media by the segmented contact method," IEEE Journal of Selected Topics in Quantum Electronics **9**, 1275–1282 (2003).

83. J. D. Thomson, H. D. Summers, P. J. Hulyer, P. M. Smowton, and P. Blood, "Determination of single-pass optical gain and internal loss using a multisection device," Appl Phys Lett **75**, 2527–2529 (1999).

84. G. M. Lewis, P. M. Smowton, J. D. Thomson, H. D. Summers, and P. Blood, "Measurement of true spontaneous emission spectra from the facet of diode laser structures," Appl Phys Lett **80**, 1–3 (2002).

85. H. H. Ku, "Notes on the Use of Propagation of Error Formulas," (1966).

86. M. Grundmann, O. Stier, and D. Bimberg, "InAs/GaAs pyramidal quantum dots: Strain distribution, optical phonons, and electronic structure," Phys Rev B **52**, 11969–11981 (1995).

87. S. Ahmed, S. Sundaresan, H. Ryu, and M. Usman, "Multimillion-atom modeling of InAs/GaAs quantum dots: interplay of geometry, quantization, atomicity, strain, and linear and quadratic polarization fields," J Comput Electron **14**, 543–556 (2015).

88. M. A. Migliorato, L. R. Wilson, D. J. Mowbray, M. S. Skolnick, M. Al-Khafaji, A. G. Cullis, and M. Hopkinson, "Structural and optical studies of vertically aligned InAs/GaAs self-assembled quantum dots," J Appl Phys **90**, 6374–6378 (2001).

89. H. Heidemeyer, S. Kiravittaya, C. Müller, N. Y. Jin-Phillipp, and O. G. Schmidt, "Closely stacked InAs/GaAs quantum dots grown at low growth rate," Appl Phys Lett **80**, 1544–1546 (2002).

90. H. S. Kim, J. H. Suh, C. G. Park, S. J. Lee, S. K. Noh, J. D. Song, Y. J. Park, W. J. Choi, and J. Il Lee, "Effects of the thickness of GaAs spacer layers on the structure of multilayer stacked InAs quantum dots," J Cryst Growth **311**, 258–262 (2009).

91. X. B. Niu, Y.-J. Lee, R. E. Caflisch, and C. Ratsch, "Optimal Capping Layer Thickness for Stacked Quantum Dots," (2007).

92. H. Jiang and J. Singh, "Conduction band spectra in self-assembled InAs/GaAs dots: A comparison of effective mass and an eight-band approach," Appl Phys Lett **71**, 3239–3241 (1997).

93. G. Bester, A. Zunger, X. Wu, and D. Vanderbilt, "Effects of linear and nonlinear piezoelectricity on the electronic properties of InAs/GaAs quantum dots," Phys Rev B **74**, 081305 (2006).

94. A. Schliwa, M. Winkelnkemper, and D. Bimberg, "Impact of size, shape, and composition on piezoelectric effects and electronic properties of In(Ga)As/GaAs quantum dots," Phys Rev B **76**, 205324 (2007).

95. S. Mazumder, "The Finite Difference Method," Numer Methods Partial Differ Equ 51–101 (2016).

96. M. C. Xu, Y. Temko, T. Suzuki, and K. Jacobi, "Shape transition of self-assembled InAs quantum dots on GaAs(114)A," Phys Rev B **71**, 075314 (2005).

97. B. Tongbram, J. Saha, S. Sengupta, and S. Chakrabarti, "Metamorphosis of self-assembled InAs quantum dot through variation of growth rates," J Alloys Compd **824**, 153870 (2020).

98. B. J. Spencer and J. Tersoff, "Symmetry breaking in shape transitions of epitaxial quantum dots," Phys Rev B **87**, 161301 (2013).

99. U. Denker, A. Rastelli, M. Stoffel, J. Tersoff, G. Katsaros, G. Costantini, K. Kern, N. Y. Jin-Phillipp, D. E. Jesson, and O. G. Schmidt, "Lateral Motion of SiGe Islands Driven by Surface-Mediated Alloying," Phys Rev Lett **94**, 216103 (2005).

100. G. Katsaros, A. Rastelli, M. Stoffel, G. Isella, H. von Känel, A. M. Bittner, J. Tersoff, U. Denker, O. G. Schmidt, G. Costantini, and K. Kern, "Investigating the lateral motion of SiGe islands by selective chemical etching," Surf Sci **600**, 2608–2613 (2006).

101. B. Bansal, M. R. Gokhale, A. Bhattacharya, and B. M. Arora, "InAs/InP quantum dots with bimodal size distribution: Two evolution pathways," J Appl Phys **101**, (2007).

102. H. Lee, R. R. Lowe-Webb, W. Yang, and P. C. Sercel, "Formation of InAs/GaAs quantum dots by molecular beam epitaxy: Reversibility of the islanding transition," Appl Phys Lett **71**, 2325–2327 (1997).

103. M. Hugues, M. Teisseire, J.-M. Chauveau, B. Vinter, B. Damilano, J.-Y. Duboz, and J. Massies, "Optical determination of the effective wetting layer thickness and composition in InAs/Ga(In)As quantum dots," Phys Rev B **76**, 075335 (2007).

104. G. Sęk, P. Poloczek, K. Ryczko, J. Misiewicz, A. Löffler, J. P. Reithmaier, and A. Forchel, "Photoreflectance determination of the wetting layer thickness in the InxGa1−xAs/GaAs quantum dot system for a broad indium content range of 0.3–1," J Appl Phys **100**, (2006).

105. T. S. Sosnowski, T. B. Norris, H. Jiang, J. Singh, K. Kamath, and P. Bhattacharya, "Rapid carrier relaxation in In0.4Ga0.6As/GaAs quantum dots characterized by differential transmission spectroscopy," Phys Rev B **57**, R9423–R9426 (1998).

106. T. Müller, F. F. Schrey, G. Strasser, and K. Unterrainer, "Ultrafast intraband spectroscopy of electron capture and relaxation in InAs/GaAs quantum dots," Appl Phys Lett **83**, 3572–3574 (2003).

107. I. O'Driscoll, M. Hutchings, P. M. Smowton, and P. Blood, "Many-body effects in InAs/GaAs quantum dot laser structures," Appl Phys Lett **97**, (2010).

108. H. C. Schneider, W. W. Chow, and S. W. Koch, "Many-body effects in the gain spectra of highly excited quantum-dot lasers," Phys Rev B **64**, 115315 (2001).

109. H. Haug and S. W. Koch, "Semiconductor laser theory with many-body effects," Phys Rev A (Coll Park) **39**, 1887–1898 (1989).

110. S. V. Garimella, L. T. Yeh, and T. Persoons, "Thermal management challenges in telecommunication systems and data centers," IEEE Trans Compon Packaging Manuf Technol **2**, 1307–1316 (2012).

111. T. J. Badcock, R. J. Royce, D. J. Mowbray, M. S. Skolnick, H. Y. Liu, M. Hopkinson, K. M. Groom, and Q. Jiang, "Low threshold current density and negative characteristic temperature 1.3μm InAs self-assembled quantum dot lasers," Appl Phys Lett **90**, (2007).

112. "EMLs | Lumentum Operations LLC," https://www.lumentum.com/en/optical-communications/products/source-lasers-ics-and-photodiodes/emls.

113. "850nm Laser Diode, 1mW Output Power from Finisar," https://www.laserdiodesource.com/laser-diode-product-page/850nm-1mW-TO-can-ball-lens-VCSEL-1-25Gbps-Finisar.

114. S. Fathpour, Z. Mi, P. Bhattacharya, A. R. Kovsh, S. S. Mikhrin, I. L. Krestnikov, A. V. Kozhukhov, and N. N. Ledentsov, "The role of Auger recombination in the temperature-dependent output characteristics (T=∞) of p-doped 1.3 μm quantum dot lasers," Appl Phys Lett **85**, 5164–5166 (2004).

115. Z. Lv, Z. Lv, S. Wang, S. Wang, S. Wang, S. Wang, H. Chai, H. Chai, L. Meng, L. Meng, X. Yang, X. Yang, X. Yang, T. Yang, and T. Yang, "Ultra-high thermal stability InAs/GaAs quantum dot lasers grown on on-axis Si (001) with a record-high continuous-wave operating temperature of 150 °C," Optics Express, Vol. 31, Issue 15, pp. 24173-24182 **31**, 24173–24182 (2023).

116. X. Cai and M. Xu, "Advances in integrated ultra-wideband electro-optic modulators [Invited]," Optics Express, Vol. 30, Issue 5, pp. 7253-7274 **30**, 7253–7274 (2022).

117. R. Sahara, M. Matsuda, H. Shoji, K. Morito, and H. Soda, "Proposal for quantum-dot electroabsorption modulator," IEEE Photonics Technology Letters **8**, 1477–1479 (1996).

118. T. Murphy, C. A. Broderick, F. H. Peters, and E. P. O'Reilly, "Lateral Quantum-Confined Stark Effect for Integrated Quantum Dot Electroabsorption Modulators," IEEE Journal of Selected Topics in Quantum Electronics **31**, (2025).

119. J. Barker and E. O'Reilly, "Theoretical analysis of electron-hole alignment in InAs-GaAs quantum dots," Phys Rev B **61**, 13840 (2000).

120. Z. Deng, Y. Jiang, W. Wang, L. Cheng, W. Li, W. Lu, H. Jia, W. Liu, J. Zhou, and H. Chen, "Indium segregation measured in InGaN quantum well layer," (2014).

121. Mark. Fox, "Optical properties of solids," 396 (2010).

122. S. Malik, C. Roberts, R. Murray, and M. Pate, "Tuning self-assembled InAs quantum dots by rapid thermal annealing," Appl Phys Lett **71**, 1987–1989 (1997).

123. E. Yablonovitch and E. Kane, "Reduction of lasing threshold current density by the lowering of valence band effective mass," Journal of Lightwave Technology **4**, 504–506 (1986).

124. D. A. . Neamen and Dhrubes. Biswas, "Semiconductor physics and devices," 500 (2020).

125. T. Suemitsu, "GaAs- and InP-Based High-Electron-Mobility Transistors," Comprehensive Semiconductor Science and Technology **1–6**, 84–113 (2011).

126. O. B. Shchekin and D. G. Deppe, "Low-threshold high-T0 1.3-μm InAs quantum-dot lasers due to p-type modulation doping of the active region," IEEE Photonics Technology Letters **14**, 1231–1233 (2002).

127. I. C. Sandall, P. M. Smowton, C. L. Walker, T. Badcock, D. J. Mowbray, H. Y. Liu, and M. Hopkinson, "The effect of p doping in InAs quantum dot lasers," Appl Phys Lett **88**, 111113 (2006).

128. Z. Zhang, D. Jung, J. C. Norman, P. Patel, W. W. Chow, and J. E. Bowers, "Effects of modulation p doping in InAs quantum dot lasers on silicon," Appl Phys Lett **113**, 61105 (2018).

129. H. Wang, Z.-R. Lv, Z.-K. Zhang, Y.-Y. Ding, H.-M. Wang, X.-G. Yang, T. Yang, and A. Phys Lett, "Enhanced performance of InAs/GaAs quantum dot superluminescent diodes by direct Si-doping," Appl. Phys. Lett **23**, 45202 (1997).

130. Z. R. Lv, Z. K. Zhang, X. G. Yang, and T. Yang, "Improved performance of 1.3- μ m InAs/GaAs quantum dot lasers by direct Si doping," Appl Phys Lett **113**, 23 (2018).

131. T. Inoue, S. Kido, K. Sasayama, T. Kita, and O. Wada, "Impurity doping in self-assembled InAs/GaAs quantum dots by selection of growth steps," J Appl Phys **108**, 26 (2010).

132. H. Deng, "Doping Strategies of InAs/GaAs Quantum Dot Lasers," University College London (2023).

133. B. C. Maglio, "Electroabsorption modulators and laser diodes for free space optics and on-chip applications," Cardiff University (2022).

134. T. Kita, R. Hasagawa, and T. Inoue, "Suppression of nonradiative recombination process in directly Si-doped InAs/GaAs quantum dots," J Appl Phys **110**, 103511 (2011).

135. H. Deng, L. Jarvis, Z. Li, Z. Liu, M. Tang, K. Li, J. Yang, B. Maglio, S. Shutts, J. Yu, L. Wang, S. Chen, C. Jin, A. Seeds, H. Liu, and P. M. Smowton, "The role of different types of dopants in 1.3 μm InAs/GaAs quantum-dot lasers," J Phys D Appl Phys **55**, 215105 (2022).

136. T. Inoue, S. Kido, K. Sasayama, T. Kita, and O. Wada, "Impurity doping in self-assembled InAs/GaAs quantum dots by selection of growth steps," J Appl Phys **108**, (2010).

137. S. Wang, Z. Lv, S. Wang, H. Chai, L. Meng, X. Yang, and T. Yang, "Significantly enhanced performance of InAs/GaAs quantum dot lasers on Si(001) via spatially separated co-doping," Opt Express **31**, 20449 (2023).

138. H. Deng, J. Park, X. Yu, Z. Liu, H. Jia, H. Zeng, J. Yang, S. Pan, S. Chen, A. Seeds, M. Tang, P. Smowton, and H. Liu, "1.3 μm InAs/GaAs Quantum-Dot Lasers with p-Type, n-Type, and Co-Doped Modulation," Advanced Physics Research **3**, (2024).

139. S. M. Sze and K. K. Ng, "Physics and Properties of Semiconductors—A Review," Physics of Semiconductor Devices 5–75 (2006).

140. D. G. Deppe, H. Huang, and O. B. Shchekin, "Modulation characteristics of quantum-dot lasers: the influence of p-type doping and the electronic density of states on obtaining high speed," IEEE J Quantum Electron **38**, 1587–1593 (2002).

141. P. M. Smowton, I. C. Sandall, H. Y. Liu, and M. Hopkinson, "Gain in p-doped quantum dot lasers," J Appl Phys **101**, (2007).

142. J. Kim and S. L. Chuang, "Theoretical and Experimental Study of Optical Gain, Refractive Index Change, and Linewidth Enhancement Factor of p-Doped Quantum-Dot Lasers," IEEE J Quantum Electron **42**, 942–952 (2006).

143. D. M. Larsen, "Screening by fixed charges in compensated semiconductors," Phys Rev B **11**, 3904–3909 (1975).

144. K.-F. Wang, Y. Gu, X. Yang, T. Yang, and Z. Wang, "Si delta doping inside InAs/GaAs quantum dots with different doping densities," Journal of Vacuum Science & Technology B, Nanotechnology and Microelectronics: Materials, Processing, Measurement, and Phenomena **30**, (2012).